The Morphology of the Milky Way

Constructing a map of the Galaxy from numerical simulations and synthetic observations

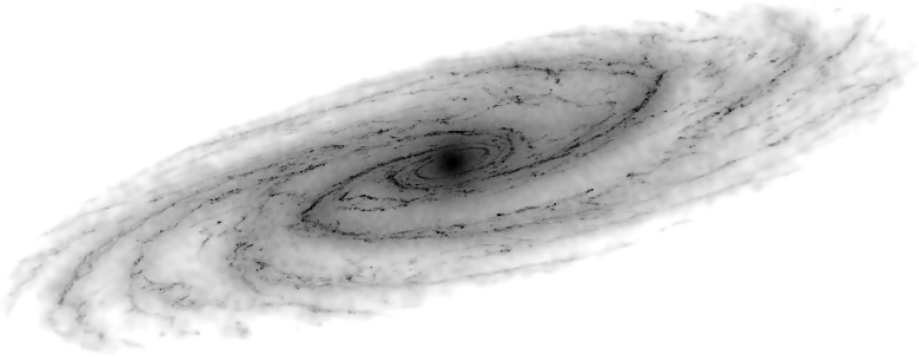

Alexander Robert Pettitt

Submitted by Mr Pettitt to the University of Exeter as a thesis for the degree of Doctor of Philosophy in Physics, August, 2014.

Signed: .....
Mr A. R. Pettitt

Date: .....

Abstract

This thesis presents an investigation into the morphological features of the Milky Way, the exact structure of which is somewhat of an unknown. We begin with a discussion of the problem at hand, and a review of the literature and methodology associated with determining Galactic structure (Chapter 1). The methodology of the investigation is to use numerical simulations to reproduce the structure of the interstellar medium (ISM) gas under the effect of gravitational forces that represent possible morphologies of the Milky Way, such as spiral arms and inner bars. The ISM is simulated using smoothed particle hydrodynamics (SPH), which has been tailored to ISM scales by the inclusion of cooling, heating and a simple chemical network, discussed in Chapter 2.

The Milky Way is first assumed to be grand design in nature, with analytic potentials representing the various arm and bar components. Simulations are then compared to longitude velocity CO emission observations to assess the quality of the reproduction of Galactic morphology. These results are shown in Chapter 3, where best fitting models have a bar pattern speed within $50 - 60\mathrm{km\,s^{-1}\,kpc^{-1}}$, an arm pattern speed of approximately $20\mathrm{km\,s^{-1}\,kpc^{-1}}$, a bar orientation of approximately $45°$ and arm pitch angle between $10° - 15°$. While nearly all observed emission features are reproducible, there is no model that reproduces all simultaneously. Using both bar and arm components together we find a better match to the data, but still no perfect reproduction. Models with two arms lack many of the observed features, but models with four arms produce too much local emission in the inner quadrants. Chapter 4 shows more sophisticated synthetic observations, created using a radiative transfer code. Resulting emission features are broadly in keeping with those seen in observations, the strength of which appears a strong function of gas surface density.

The analytic potentials are then replaced by a set of discretised mass components that represent the stellar system, which is the subject of Chapter 5. Using a live N-body disc then allows for the dynamic creation of bar and arm features, from which further synthetic observations are produced. Transient arm and bar features are relatively easy to produce, though not necessarily simultaneously. Arm patterns showing two to five arms and some with an effectively flocculent structure are created, with pitch angles around $20°$. The pattern speed of which tends to decrease with radius, highlighting that the arms are material rather than wave-like in nature. Best fitting synthetic observations show that a four-armed spiral pattern provides good agreement with observations, more so than that of the fixed potentials, with clear reproduction of nearly all arm features. However, an inner bar appears necessary to remove excess emission seen towards the Galactic centre, which was not present in these models.

Contents

List of Figures

List of Tables

Declaration

This thesis contains work published or pending publication as papers. The work in Chapters 3 and 4 form the basis of the work the paper Pettitt, Dobbs, Acreman & Price 2014a which has been accepted by the Monthly Notices of the Royal Astronomical Society (MNRAS) and is due for publication. Chapter 5 forms a separate paper; Pettitt, Dobbs, Acreman & Price 2014b, which is in preparation and will be submitted to MNRAS in the months following the submission of this thesis. I am first author in both of these works, and performed the majority of the work myself with insights, advice and code development aid from my co-authors; C. Dobbs, D. Acreman and D. Price. This work is also included in the conference proceedings of Pettitt et al. 2013 (IAUS 298) and Dobbs & Pettitt 2014 (*Lessons from the Local Group*). Other work as part of my PhD contributed to the papers of Tremblin et al. (2014) and Wilson et al. (2014).

A variety of codes were used in this thesis that are the work of other authors. These include the SPH codes PHANTOM, SPHNG and the radiative transfer code TORUS that are primarily developed by D. Price, M. Bate and T. Harries respectively (and collaborators). SPHNG and PHANTOM have already been somewhat adapted for Galactic scale simulations by C. Dobbs and D. Price.

Acknowledgements

Dear intrepid reader,

There are few thanks to give out here, so bear with me. One of the biggest acknowledgements has to go to my supervisor Clare. It's no small understatement to say you wouldn't be reading this without her help. Beyond the aid acknowledged from a standard student-supervisor point of view, she also stepped in and offered me a project when I was found wanting. I can only imagine taking on a PhD student with baggage is not an ideal first student, but I am myself at least very happy with the way things turned out.

To my fellow Exeter students, office mates, and post-docs, thank you very much for making this experience all the more enjoyable, and listening to my rants and rages from time to time: Tom, Emily, Alex, Maria, Paul, Lee, Rob, Nawal, Cat, Hannah, David, Claire and the rest! As you are probably aware reading this, I had somewhat of a shift in topics eighteen months into my PhD. During which time I sought advice and solace from a great many people, and again later on when looking for advice with regards to post-doc positions. I'd like to thank Tim N., Isabelle, Nathan, Tim H., Aude, Matthew, Pete V., Daniel P., Jenny H. and David S. A special thanks to those who kindly agreed to let me have some of the extra monies floating around so I could effectively remove everything related to extra-solar planets from this thesis. I feel a thank you must be given to Frédéric, without whom I wouldn't be in Exeter in the first place, and for indirectly teaching me some life lessons.

Thanks to all the users of Zen, who rarely (if ever) complained at my incessant abuse of resources, and Dave and Daniel for all their help with the computing side of things. Thanks too to all the crew of LOCALSTAR, it has been a pleasure to work with you, and I hope to continue to do so in the future. This thesis makes extensive use of previous observational studies, in particular those of Dame et al. (2001) and Kalberla et al. (2005), to which I am grateful for their work and making the data publicly available. Also, thanks to the STFC, for footing the bill for my PhD!

Thanks to my parents, who have been encouraging and supportive throughout my PhD, both the good times and the not so good. Finally, an innumerable amount of thanks to Katrina. She has been with me throughout most of my time in Exeter and is constant source of support and a never faltering smile. I couldn't imagine doing this any other way.

Unquantifiable thanks to all,

Alex Pettitt

4th August 2014

1

The Milky Way Galaxy

"I know not the true face of the mountain, for I am in its midst"
– Su Shi (1037-1101)

1.1 The Galaxy: seeing the forest for the trees

The Milky Way galaxy is the home of the Solar system and planet Earth, and yet we know disturbingly little regarding what it actually looks like. Simply by looking up into the night sky we observe the bright stream of stars and gas that is Milky Way, from which it is logical to assume the host of the Solar System is a flattened structure (see Figure 1.1). Such thoughts were postulated as early as the seventeenth century by Galileo Galilei, observing that the Milky Way actually consisted of numerous individual stars rather than a continuous "celestial fluid" (Binney & Merrifield 1998). Later work by Thomas Wright and Immanuel Kant in the eighteenth century developed this idea by proposing the Milky Way was effectively an upscale Solar System, with stellar bodies orbiting the central point on near-circular orbits, counter-acting the immense gravitational forces of the combined stellar stellar system. Kant also proposed that sources that were seen to be more nebulous and blurred out, rather than point like, could be analogues to our own Milky Way, or "island universes" (Kant 1755).

In the later eighteenth century Charles Messier and William Herschel undertook a systematic cataloguing and measuring of celestial sources. Herschel produced a diagram of the entire night's sky (right, Figure 1.2), including many more fuzzy nebulae (Herschel 1785), believing these were indeed island universes postulated by Kant as he was able to resolve discrete sources within them. Some of the first observations of spiral structure in the night sky were made by William Parsons, the Third Earl of Rosse, in 1845 using his appropriately named *Leviathan of*

Figure 1.1: Panoramic view of the Milky Way viewed from Earth. Credit: ESO/S. Brunier.

Parsonstown (Bailey et al. 2005), discovering nebulae both disc-like and spheroidal in nature, and clear spiral/whirlpool like patterns in nebulae such as M51 (left, Figure 1.2), adding further support to the notion that nebulae undergo large scale rotation.

In the early twentieth century a large global network of calibrators led by Jacobus Kapteyn employed the use of photographic plates and proper motions to produce a three-dimensional map of the Milky Way (Kapteyn 1922). Kapteyn proposed a disc-like Milky Way, 8kpc in radius, with a drop in stellar density towards the edges, with the Solar distance being only around 0.6kpc from the centre. The seemingly unlikely placement of the sun in the centre of the Milky Way was a troubling one. Kapteyn's measurements were undermined by the presence of an interstellar medium (ISM, specifically dust) that subdued the light from the Milky Way stars, thereby exaggerating their distances from the Earth. This caused a net preference for a strong drop off in stellar density from the Earth which could be misinterpreted as a heliocentric view of the Milky Way. Kapteyn's work also indicated the existence of two distinct stellar streams, i.e. that the motion of stars was not random, but rather moved in two streams moving in opposite directions, further endorsing the theory of Galactic rotation. Work around the same time by Harlow Shapley presented a radically different view of the Milky Way's structure based on distance measurements of globular star clusters and Cepheid variables (Shapley 1918a,b,c and other papers in this series). Shapley's analysis indicated that clusters were not uniformly distributed in the plane of the Milky Way, suggesting instead that the Solar System was significantly displaced from the centre, by some 15kpc, and that the Milky Way was nearly 100kpc in diameter. The Kapteyn and Shapley universes differed in many regards, both being the victims of the effect of inter-stellar absorption, the full importance of which was not quantified until the work of Trumpler (1930), who discovered that open stellar clusters at large distances were much fainter than they should be for their apparent size. This absorbing effect heavily undermines the distance determinations underpinning both Galactic models.

Shapley's ideas surrounding the structure of the Milky Way extended to those on external spiral nebulae, which he believed must be small constituent components of the Milky Way itself due its apparent huge size. This view was not accepted by all, with some preferring the smaller

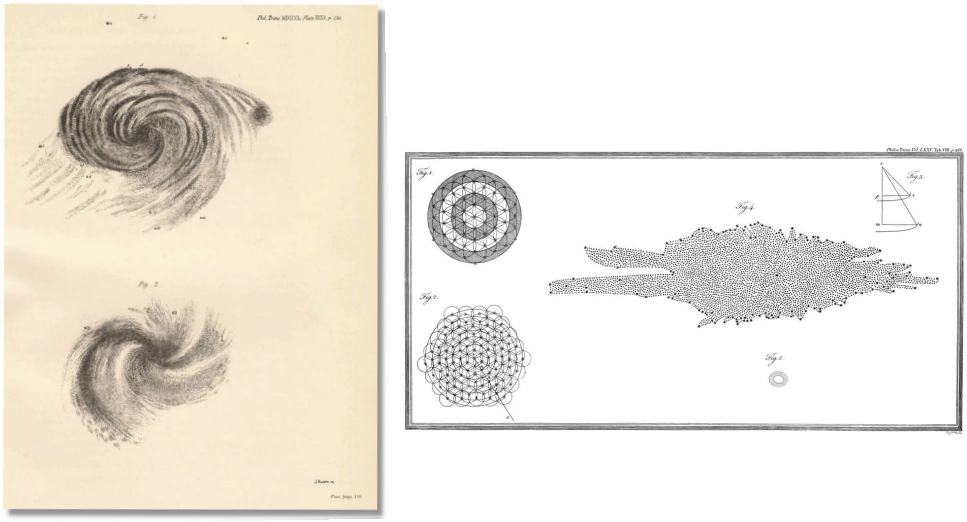

Figure 1.2: Left: sketches of M5 (top) and M99 (bottom) by Lord Rosse in 1850 from Bailey et al. (2005). Right: William Herschel's map of the Milky Way (Fig. 4 insert) from Herschel (1785). The Earth is located at the bright dot near the centre.

Kapteyn model of the Milky Way, with spiral nebulae existing as entirely separate entities. The conflicting models were pitted against each other at the so-called "Great Debate" in 1920, where Heber Curtis was given the challenge of standing for the "island universe" paradigm against Shapley, though there was no clear winner (Hoskin 1976).

In the advent of galactic spectroscopy it became apparent that nebulae shared very similar characteristics with stellar spectra, with full spectra that resembled that of the integrated Milky Way, backing the "island universe" view. Additionally, Doppler shifts gave the relative velocity of these systems, which seemed to be much higher than the stars in the plane of the Milky Way, further supporting the idea that nebulae were dynamically uncoupled to our Galaxy. Support for the Shapley model was hinged on a lack of knowledge about the absorbing properties of the ISM. He questioned if the Milky Way was like spiral nebulae, then why is it significantly darker and redder? Missing from the Shapley model was the absorbing ISM that has a tendency to absorb in the blue and would diminish the total luminosity of the galactic disc when viewed from the Earth.

The Great Debate was not truly settled until Edwin Hubble's observations in the mid 1920's. By resolving Cepheid variables inside these nebulae it was possible to determine their distances. It turned out they were far too distant to be considered part of the Milky Way itself and thus these collections of stars lying external to the Milky Way became known as galaxies. Around the same time efforts were also being made into measuring the kinematic properties of stars in the Milky Way. Bertil Lindblad and Jan Oort discerned that stars in the Solar vicinity are rotating in a highly flattened disc with velocities between 200-300 $\mathrm{km\,s^{-1}}$ (too high to remain bound in Kapteyn's smaller Milky Way).

Further insights into the structure of the Milky Way came from the discovery of the H I 21cm emission line (see Section 1.4), predicted by Hulst in 1941 and not seen until 1951 by a number of observers (see Binney & Merrifield 1998). This line was well separated from other spectral features, allowing for precise measurements of line-shifts. The biggest benefit of this line

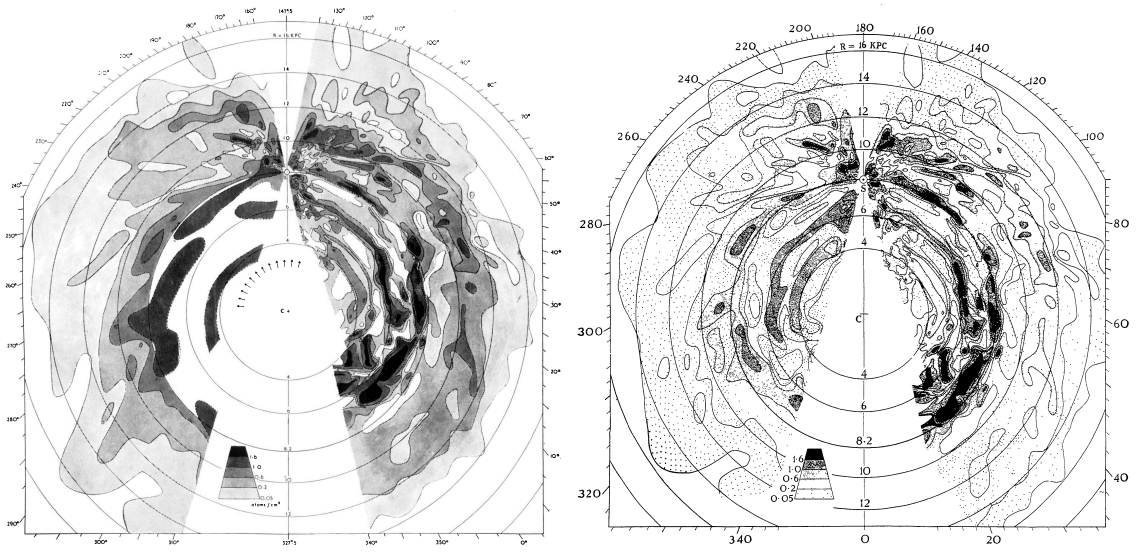

Figure 1.3: Top-down H I 21-cm emission maps of the Milky Way from Oort et al. (1958) on the left and Kerr (1962) on the right. The sun is located approximately two thirds from the bottom of each figure in the centre.

was its position in the radio regime, far from the dust absorption that hampered so many previous works, providing a tracer capable of mapping much deeper in the Galactic disc. This enabled Oort et al. (1958) to build a near-full map of the Galactic plane (left, Figure 1.3). Clearly the map is asymmetric, which could be a pointer towards spiral structure, but on average displayed a uniform density with azimuth. Note the over-abundance of material towards our Solar System, located approximately two-thirds up the y-axis. This is because the map assumes circular orbits, and spiral perturbations could cause non circularity giving the tendency of gas to point towards the observer. In later maps you can begin to see clearer spiral structure in the H I gas (Kerr 1962, right Figure 1.3).

The evidence outlined above leads to the categorisation of the Milky Way as a disc galaxy with net rotation and a diameter of 20-30kpc. However, inferring anything more concrete than this has been a point of contest for researchers for the past decades. While the existence of *some* spiral structure is widely undisputed, the exact morphology and kinematics are still shrouded in confusion. The problem is inherent to our position within the Galactic disc. As we lie within it there is no easy way to construct a full top-down map with irrefutable accuracy (and it is highly unlikely we will ever travel far enough out of it to do otherwise!). As can be seen from Figure 1.3, it is possible to infer some structure. However, the underlying calculations rely upon difficult distance determinations with large uncertainties and rely on some assumed rotation model. Even then, it is nigh impossible to apply these methods to behind the Galactic centre due to the extreme brightness in the entire electromagnetic (EM) spectrum.

The topic of this thesis is to constrain the morphology of the Milky Way through numerical simulations, reverse engineering them to reproduce observations seen here on Earth. Exactly how this is done will be discussed later in this Chapter, before which we will discuss some key points regarding galactic morphology and inter-stellar physics.

Figure 1.4: A collection of disc galaxies with clear morphological features. Top row from left to right shows three spiral galaxies; M51 (“Whirlpool”), M101 (“Pinwheel”) and NGC 4414. The bottom row shows three barred galaxies; UGC 12158, NGC 1672 and NGC 1300. Images credit; NASA, ESA, and The Hubble Heritage Team (STScI/AURA).

1.2 The galaxy zoo

Galaxies come in a whole host of morphologies, ranging from flattened spheroids to grand design spirals. They can generally be classified into one of three categories; disc, elliptical or irregular (the latter being anything that can’t be classified as the former). While the exact morphology is uncertain, our own Milky Way is generally accepted to be a multi-armed disc galaxy. Spiral armed galaxies are characterised by their winding arms, and often have an extended bar structure in the inner disc, from which arms can propagate. Figure 1.4 shows some of the more striking spiral galaxies observed by the Hubble telescope, with varying morphologies. M51 is the poster child for galactic spiral structure, whose arms are believed to have been produced by interaction with the nearby companion galaxy NGC 5195. The arms of M101 are less clearly defined and more numerous. NGC 4414 displays very flocculent spiral structure, with no distinct arm number. Three examples of barred galaxies are shown in the lower row of Figure 1.4, with arm morphology and inner gas/dust features. While NGC 1672 and NGC 1300 have a very dominant bar structure, UGC 12158 has only a weak inner bar, with multi-armed spiral features dominating the outer disc. Edwin Hubble attempted to classify these many different galaxies using a “tuning fork” diagram (Figure 1.5), where spiral galaxies are either classified as barred, SB, or unbarred, S (Hubble 1936). This is then followed by an index defining the features of the spiral pattern. Sa spirals have tightly wound arms, Sb intermediately wound arms and Sc very loosely wound arms. The size of the central bulge decreases from Sa to Sc. Sa spirals have poorly resolved arms and relatively little gas compared to the Sc’s (similarly for SB barred spirals). The actual number of spiral arms observed in external galaxies varies from 2-6, though as the number of arms increases the galaxies tend to be described as flocculent, showing arm-like features but either too disperse or too numerous to clearly quantify.

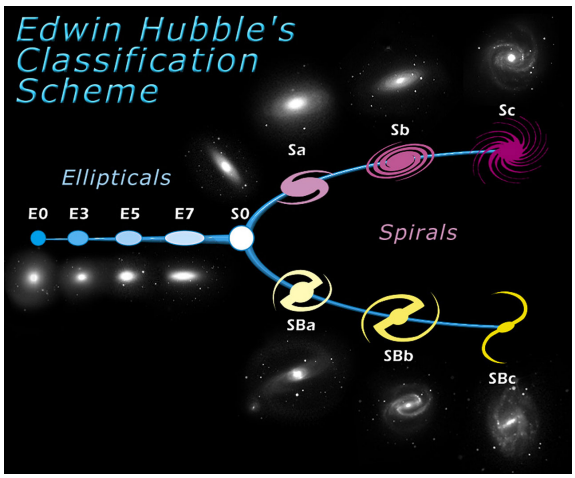

Figure 1.5: Hubble tuning fork diagram categorising the morphology of elliptical and spiral galaxies. Adapted from http://www.spacetelescope.org/images/heic9902o/ (credit: NASA and ESA).

While spiral galaxies form circular rotating discs, elliptical galaxies are spherically symmetric, oblate, prolate, or triaxial structures and have no clear surface patterns. The degree of spherical symmetry is categorised by the number of the elliptical, e.g. an E0 elliptical is completely spherically symmetric while an E7 is strongly prolate. The link between the elliptical and spiral classes is a lenticular class (or S0's), which are essentially spirals with no patterned features and a low gas content, though their exact relation between the elliptical and spiral galaxies is not entirely clear (see Sandage 2005 for a discussion). When studying the Hubble sequence one could be lead to the belief that the ellipticals evolved into the spirals over time, with the rotation flattening out the initially spherical stellar distribution into compact discs. This is however not the case, and no direct evolutionary path is implied by these classification schemes. "Early" and "late" type galaxies refers instead to evolution of morphological complexity in classification schemes (Binney & Merrifield 1998).

As well as their general outward morphology, elliptical and spiral galaxies have very different populations and internal structure. Elliptical galaxies are made up of much older stars (Population II[1]) with less ISM gas than spirals and as a result are redder in colour. The brightness decays slowly with radius by; $I(R) \propto \exp(-R^{0.25})$ (de Vaucouleurs 1948). The orbits of the stars inside the ellipticals are usually randomly orientated with no net rotation. If they are do exhibit a net rotation, it is slower than that in seen spirals.

Spiral galaxies on the other hand are mainly composed of Population I stars and have a large proportion of their mass in ISM gas and dust. They are often visually distinctive with their strong spirals emanating from the galactic centre with occasional bar like inner structures such as those in Figure 1.4 (see later in this chapter for more detail on the spiral and bar patterns). The surface brightness in the disc is characterised by an exponential drop off from the centre; $I(R) \propto \exp(-R)$, a steeper drop than that of Ellipticals (Freeman 1970; Binney & Tremaine 1987). Spiral galaxies tend to have a spherical inner nucleus, known as a bulge, which is very similar to

[1]Stars can generally be classified as either Population I or II. The former are young, hot, metal rich stars found in galactic discs. The latter are cooler, metal poor, often late in age and are found in globular star clusters.

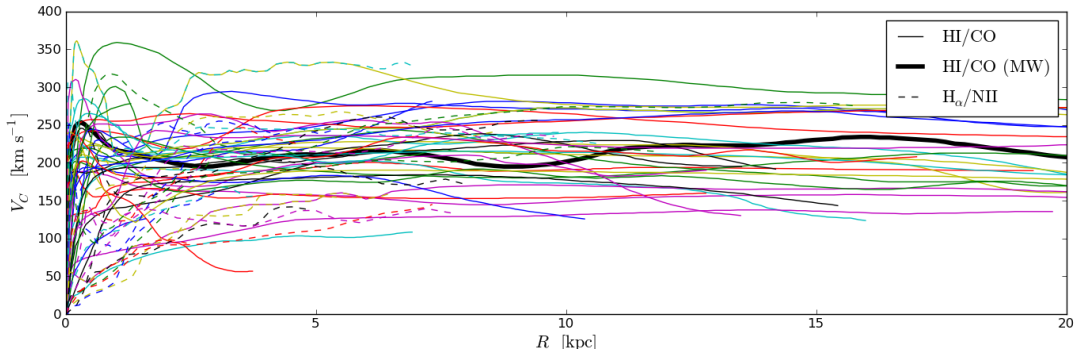

Figure 1.6: A selection of rotation curves from (Sofue & Rubin 2001) for spiral 52 spiral galaxies including the Milky Way (thick black line). Data is either from the CO 2.6mm, H I 21cm, H_α 656nm and N II 122μm emission lines.

a small elliptical galaxy. The bulge has random rotation and is composed of mostly Population II stars with little ISM gas and dust. The velocity distribution of the stars inside the disc tends to be roughly flat with radius; the rotation of spiral galaxies is constant as you move away from the galactic centre. Figure 1.6 shows the rotation curves for 52 spiral galaxies using a variety of different data sources from Sofue & Rubin (2001), showing flat rotation in most cases. The flat nature of the disc galaxy rotation curves presented a problem for galactic mass determinations, and is in many ways still an unsolved problem even in the 80 years since its first detection by Oort (1932). If the stars in galaxies were to orbit like objects in our own Solar System then they should obey Kepler's third law. That is, the orbital period should increase, and the speed decrease, as you move away from the galactic centre (the blue line in the left panel of Fig. 1.7). If it were a solid body-like rotation then velocity would have to increase as you move from the larger radii to stop the disc form breaking apart. However, studies began to show that galaxies had neither Keplarian nor solid body rotation. This is seemingly at odds with the luminosity profiles of disc galaxies, which clearly decay with increasing radii, indicating some material was contributing to the mass of the system but not to the luminosity. Evidence of so-called "dark matter" was seen in observations of individual stars (Rubin et al. 1980), galaxy clusters (Zwicky 1933), individual galaxies (Ostriker et al. 1974) and also in elliptical and dwarf galaxies (see the review of Trimble 1987 for a full discussion of evidence).

However, this dark matter has still yet to be observed in any direct way due to its indifference towards all regions of the EM spectrum. Figure 1.7 shows rotation curve measurements for the Milky Way from Sofue (2012). In the right panel a combination of an inner bulge and disc cannot reproduce a flat curve without some extra outer mass component. By including a spherically symmetric outer massive halo the rotation curve can then be flattened. The matter needed to do this, regardless of geometry of the halo, would imply that dark matter would outweigh regular matter by nearly an order of magnitude (Fich & Tremaine 1991; Battaglia et al. 2005). The spatial distribution of the dark matter is often assumed to be spherical, though the exact morphology is yet another unkown. Even 30 years after its original postulation, we can tell little more about dark matter other than the gravitational force it exerts.

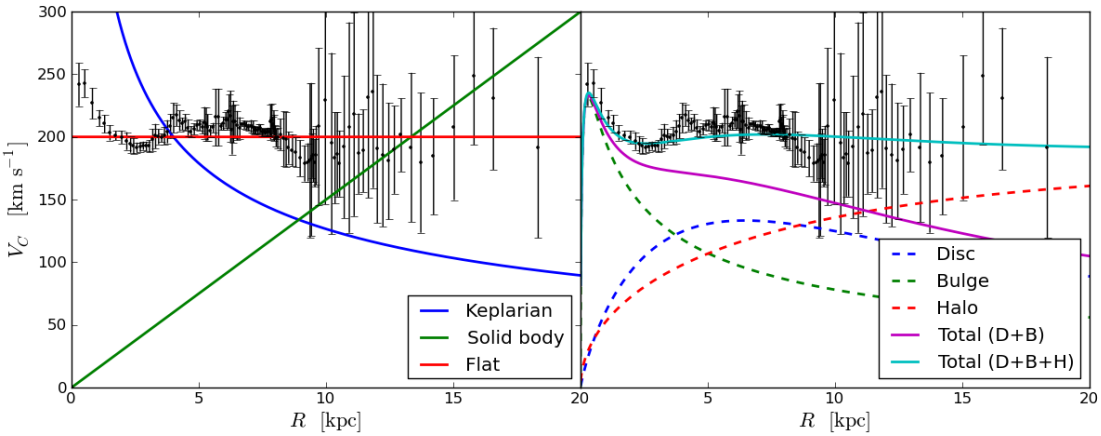

Figure 1.7: Left: rotation curve data for the Galaxy from Sofue (2012) with a Keplarian, solid body and flat model curve. Right: The same data with a flat model curve reproduced from combining a circular disc, spheroidal bulge and spherical halo of material.

1.3 Spiral and bar structure

While spiral patterns appear in no short supply in disc galaxies, upon first discovery there was considerable confusion as to what the underlying physics was behind them. One of the biggest conundrums was why the spirals were seen at all. If disc galaxies had flat rotation curves (as most do, see Fig. 1.6), then any pattern seen on the disc would not stay the same as the disc rotated (see the solid body curve in Fig. 1.7). For a flat rotation curve rotation frequency scales as $\Omega \propto 1/R$, and so the inside of an observed pattern would move at a much faster angular speed than the pattern at large radii. This effect, known as the "winding problem", meant that any spiral pattern would wind up into nothing after a few galactic rotations, and yet many disc galaxies at various redshifts are seen to have strong spiral features, indicating that galaxies either maintained their spirality or continuously reformed spiral arms.

Some of the earliest advances in understanding spiral structure were made by Lindblad in the early twentieth century. Lindblad developed the idea that spiral structure resulted from stellar and gaseous gravitational interactions during their orbits around the galactic centre. His idea was that spiral structure was seeded by leading spiral arms born at the edge of the stellar disc, with eccentric stellar orbits driving $m = 2$ spiral modes. Lindblad's work was underpinned by his theories of stellar orbits, which became a mainstay of future spiral models (see Pasha 2004a and Pasha 2004b for a review of Lindblad and early spiral structure theory). Consider stars/gas moving in some axisymmetric potential, such as that of a disc galaxy, in a near-circular orbit at a frequency of Ω. The equations of motion of the material are given by those of a circular orbit with perturbing terms; $R(t) = R_g + r'(t)$ and $\theta(t) = \Omega t + \theta'(t)$ where R_g is the average radius of the nearly circular orbit with $r'(t)$ and $\theta(t)'$ the deviations from a circular orbit in the radial and azimuthal directions respectively. The resulting equations of motion for the radial offset is $\ddot{r}' = -\kappa^2 r'$ (see Combes et al. 1995 for a derivation). As the equation of motion is only solved to first order this is known as the *epicycle approximation*. The frequency of radial oscillation, κ, is referred to as the epicycle

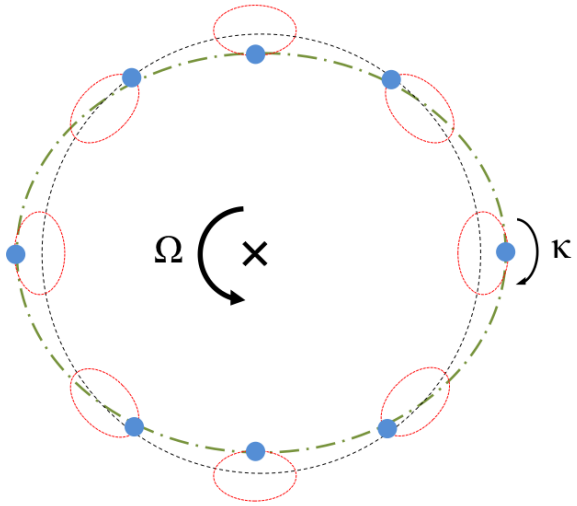

Figure 1.8: The orbital path of a star (blue dot) around the galactic centre with epicycle frequency of $\kappa = 2\Omega$. The epicycle, circular and resulting full orbital path are shown by the red, black and green lines.

frequency, and is given by

$$\kappa^2 = \frac{\partial^2 \Phi_{\rm axs}}{\partial R} + 3\Omega^2 \equiv R\frac{{\rm d}\Omega^2}{{\rm d}R} + 4\Omega^2 \equiv \frac{2\Omega}{R}\frac{\rm d}{{\rm d}R}R^2\Omega, \tag{1.1}$$

where $\Phi_{\rm axs}$ is the axisymmetric potential of the stellar system. While orbiting the galactic centre at Ω, the star is also rotating in a small ellipse in the rotating reference frame with radial frequency κ, where the combined orbit has the general shape of a rosette. The magnitude of κ is dependent on the rotation curve. For example, in the galactic centre the rotation curve is as a solid body, $V_c \propto R$, and so $\kappa = 2\Omega$. In the outer disc the rotation is differential, $V_c = $ const., so $\kappa = \sqrt{2}$. In general, $\Omega < \kappa < 2\Omega$, so the material completes an epicycle before it completes a full orbit. Figure 1.8 shows a star orbiting the galactic centre with an epicycle frequency of $\kappa = 2\Omega$, and the resulting effectively elliptical closed orbit.

The shortcomings of spiral models to fully solve the winding problem led to the postulation in the 1950's that large scale magnetic fields were the driving force of spiral structure. Observations of the field strengths in galaxies however indicated that field strengths were simply too weak to be responsible for large scale arm features (see Binney & Tremaine 1987).

1.3.1 Density wave theory

The work of Lindblad lead to one of the most popular theories of spiral structure. The spiral density wave theory of Lin & Shu (1964) formulated the spiral features not as a specific collection of stars, but rather a density wave that propagates azimuthally through the galactic disc. The spiral arms would manifest as over-densities in the stellar population, with stars passing into and then out of the density wave rather than spending their entire lifetimes within the arm. An often used analogy is that of a traffic jam on a road. Cars enter and leave the traffic jam, creating an over-density in cars at a certain point. The jam is still moving, albeit at a different speed to the cars,

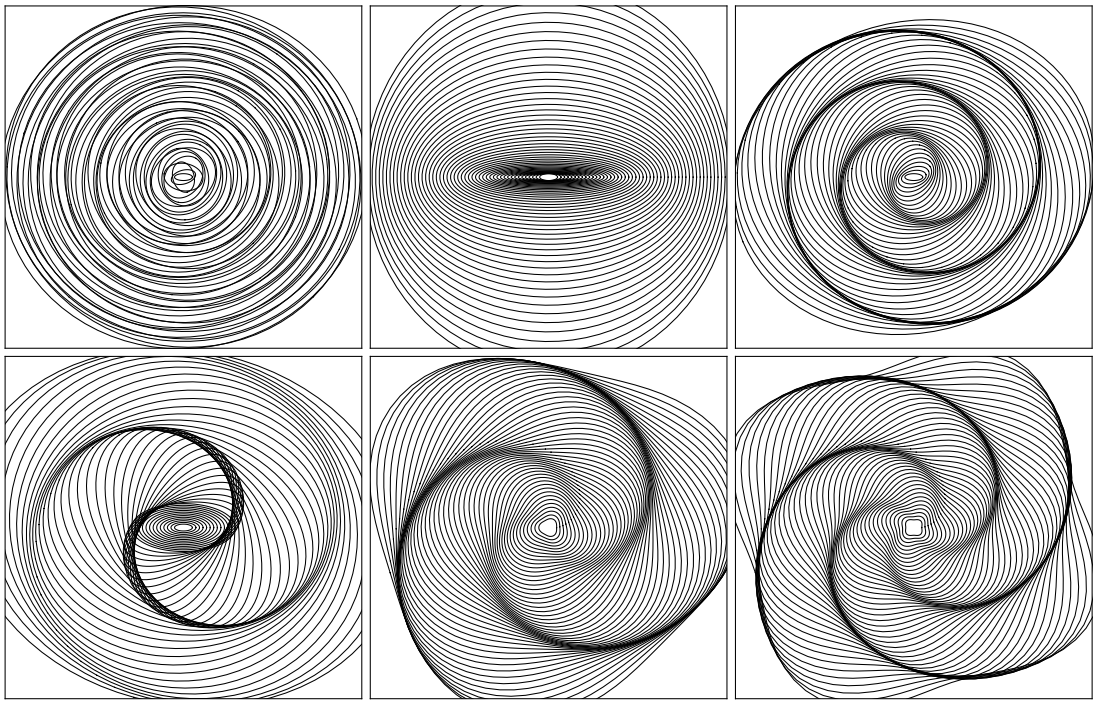

Figure 1.9: Illustration of the how the superposition of numerous stellar orbits can create bar and spiral patterns. Top left shows that random alignments of elliptical orbits creates no pattern, resulting in disc only structures. Top centre is a continuous superposition of ellipses aligned horizontally, creating a bar-like inner structure. The spiral pattern in the top right is made by simply incrementing the offset of each orbit steadily with increasing semi-major axis. Bottom left is a combination of a bar and 2 armed spiral through a simple combination of ellipses. The 3 and 4 armed spirals require non-elliptical orbits and for the masses to complete 3 or 4 complete radial oscillations during a full orbit (3/1 or 4/1 opposed to an ellipse's 2/1).

which enter and leave the jam over time. In this sense the traffic jam is a density wave, and cars do not reside in a single jam forever. With a steady spiral density wave it is possible to create any number of arm or bar structures, to have both leading and trailing arms, and avoid the winding problem.

The resulting stellar perturbation caused by this density wave is represented as a surface density of the form[2]

$$\Sigma_{sp}(R, \phi, t) = A_{sp}(R) \cos\left[m\phi + f(R) + \Omega_p t\right] \tag{1.2}$$

where A_{sp} defines the spiral radial strength, m the order of the spiral (i.e. number of arms), Ω_p the rotation frequency of the density wave and $f(R)$ the *shape function* of the arms. The shape function defines the morphology of the arms, whether it be a logarithmic, Archimedean, or hyperbolic spiral. The most common shape function is that of a logarithmic spiral, which has the form

$$f(R) = \ln\left(r/r_\circ\right) \cot(\alpha) \tag{1.3}$$

where $r_\circ$ is some constant and α is the pitch angle; the angle the arm makes with a tangent to a

[2]This can also be expressed as $\exp(i[m\phi + f(R) + \Omega t])$.

circle of constant radius. An example of how these spirals relate to actual stellar orbits is shown in Figure 1.9 (based on a similar diagram of Kalnajs 1973). In the first panel we show a set of elliptical orbits, closed such that $\kappa = 2\Omega$. The orbits are randomly rotated with radii, showing no distinct pattern. In the second panel we leave all orbits aligned with the x-axis, forming a bar-like feature in the inner disc. By then rotating each orbit with increasing radius we can form spiral patterns similar to those seen in disc galaxies. Multi-arm structures can be created by increasing the epicycle frequency, e.g. $\kappa = 3\Omega$ (or $\kappa = 3\Omega/2$) and $\kappa = 4\Omega$, creating 3 and 4 armed spiral patterns.

A dispersion relation for the spiral structure can also be formulated, but depends on a few key assumptions. The spiral must be sufficiently tightly wound. This simplifies the computation of long range gravitational forces in the disc, as it ensures there is some local density perturbation providing the majority of the gravitational force[3]. The spirals are also assumed to rotate as a rigid body and do not deform in shape over time (Ω_p and α are constant). The arms are said to be quasi-stationary spiral structures; QSSS (Dobbs & Baba 2014). This results in a dispersion relation of the form

$$(\omega - m\Omega)^2 = \kappa^2 - 2\pi G\Sigma|k| \tag{1.4}$$

where k is the radial wavenumber of the spiral density wave, ω is its angular frequency and Σ the surface density of the disc (Toomre 1964). The dispersion relation for a hot gas disc (the above is for a cold gas disc) was provided by Lin & Shu (1964) and requires an additional term of $c_s^2k^2$ added to the RHS of Equation 1.4, where c_s is the sound speed of the gas. A stellar dispersion relation is similar also to Equation 1.4, except with an additional multiplication factor added to the Σ term which is a summation of Bessel functions of Ω, ω, κ, k and the radial velocity dispersion of the stars, σ (Kalnajs 1965; Lin & Shu 1966). The pattern speed is related to the arm angular frequency by $\omega = m\Omega_p$. From these dispersion relations two key stability criteria can be found, referred to as Toomre Q parameters. If the terms on the RHS of Equation 1.4 are > 0 then a solution exists where Ω_p is real, and hence Equation 1.2 holds and the disc is stable. If, however, the LHS of Equation 1.4 is < 0 then Ω_p is complex, and Equation 1.2 will then contain an exponentially increasing factor, hence making the disc unstable (Binney & Tremaine 1987; Dobbs & Baba 2014). By extension to warm stellar and gaseous discs the respective Q parameters can be defined as

$$Q_g = \frac{\kappa c_s}{\pi G\Sigma} \tag{1.5}$$

and

$$Q_s = \frac{\kappa\sigma}{3.36G\Sigma}. \tag{1.6}$$

Stability of the discs requires $Q > 1$, and instability is present when $Q < 1$. Physically, Q can be thought of as the balance between the disc pressure forces (driven by velocity dispersion in stars or thermal dispersion in gas) and gravitational attraction of the disc of surface density Σ. Values in the Solar neighbourhood are approximately $Q_s \approx 2.7$ and $Q_g \approx 1.5$ implying the Solar neighbourhood is stable, but not by a large margin in the gas (Binney & Tremaine 1987).

There exists some regions of special interest when considering Equation 1.4. When epicycle

[3]This is also referred to the tight-winding, or WKB, approximation (Binney & Tremaine 1987).

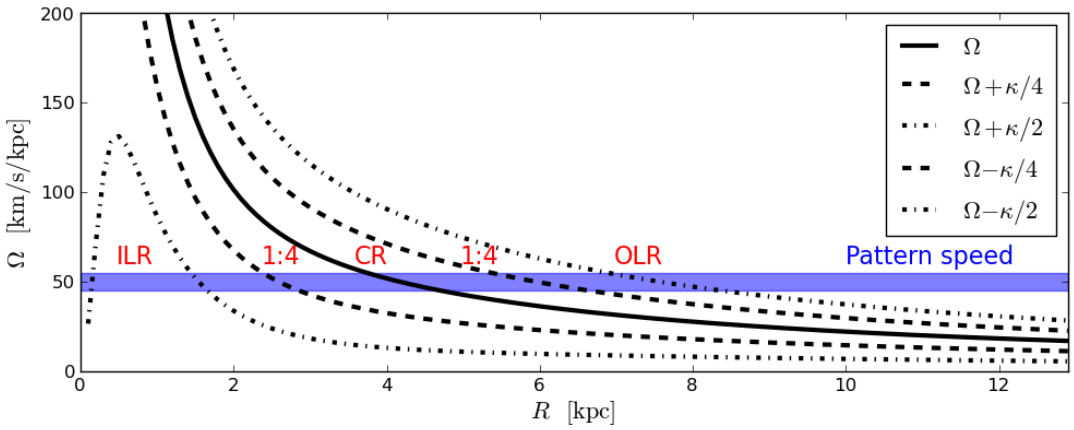

Figure 1.10: Rotation speeds for a Milky Way-like rotation curve. The dashed and dot-dashed lines show the 4:1 and 2:1 resonances calculated from the epicycle frequency, κ. The shaded region shows the the location of the pattern speed, which is in keeping with that of the Milky Way bar.

orbits close as some fraction of the orbital frequency we obtain the relation

$$\Omega - \Omega_p = \pm\frac{\kappa}{m} \tag{1.7}$$

where m is some integer, representing the number of arms. This equation is only satisfied at two radii for each m which are known as the inner and outer Lindblad resonances (ILR and OLR), usually defined with reference to $m = 2$. At the ILR and OLR the orbiting material orbits such that it encounters the density wave at the same point in the orbit each rotation, and experiences a resonance as a result. There also exists an intermediate radius where $\Omega = \Omega_p$, the co-rotation radius (CR). At the ILR the material moves faster than the perturbation, with the perturbation at CR, and slower than it at the OLR. Some examples of these different resonances are shown in Figure 1.10, where the ILR, OLR, and CR are shown for a Milky Way like rotation curve. The shaded region shows the pattern speed of some imposed perturbing density wave ($\Omega_p = 50\mathrm{km\,s^{-1}\,kpc^{-1}}$, which is closer to the bar pattern speed than that of the arms, but the principle is the same). Where Ω_p crosses the different resonant lines $\Omega \pm \kappa/m$ dictates the location of the resonance features. In this example there are actually two ILR due to the shape of the rotation curve near the galactic centre caused by the bulge.

The waves described by the dispersion relation above will in fact migrate radially, at some group velocity given by

$$v_g = \frac{\mathrm{d}\omega(k)}{\mathrm{d}k} = \pm\frac{|k|c_s^2 - \pi G\Sigma}{m(\Omega_p - \Omega)} \tag{1.8}$$

first formulated by Toomre (1969). As waves propagating radially they reverse direction when they come close to the CR, as k decreases R increases and vice-versa, and are reflected (or damped[4]) when they approach the Lindblad resonances. Density waves are thus not permitted to pass the

[4]Damping at the ILR can be reduced, and transformed into reflection if Q increases significantly at the ILR, creating a so-called Q-barrier. This is believed to occur in the Milky Way, and a Q barrier is seen in our calculations in Chapter 5.

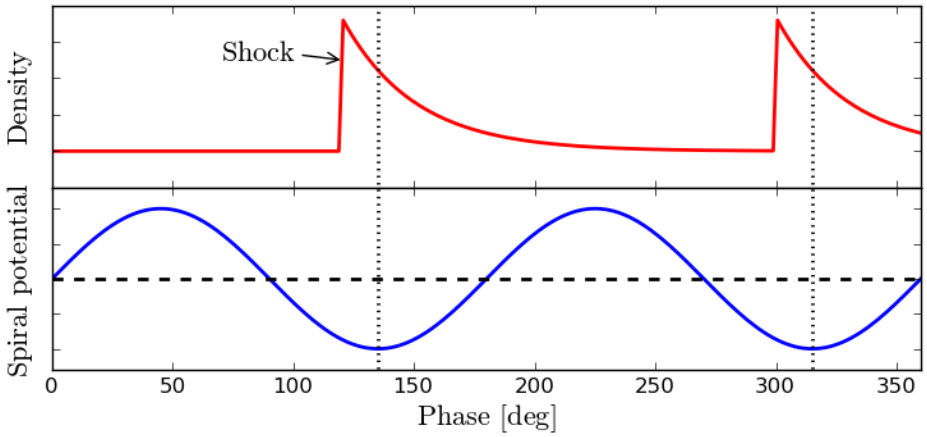

Figure 1.11: Position of ISM shock (top) resulting from passage into spiral potential (2-armed, bottom). The position of the shock, signified by compression and increase in density, is offset from the bottom of the spiral potential well. Based upon work by Roberts (1969).

ILR and OLR, where a build up or reflection of wave packets occurs (see Binney & Tremaine 1987, Combes et al. 1995 and Dobbs & Baba 2014 for further details). As a result of a non-zero group velocity, the wavenumber increases. This causes a tightly wound trailing wave to unwind, and eventually transition into a loose leading wave, which then winds up. The winding is much slower than material arms, but still presented a problem for theorists, as the whole point of density waves is that they are supposed to not be susceptible to the winding problem.

As density waves can be propagated through the disc, and as a result be dissipated over time, systems of re-seeding density waves need to be present. Such a solution is the theory of "swing amplification", which will be discussed in Section 1.3.2.

Spiral shocks

Soon after models of spiral structure emerged, theories of the spirals effect on the interstellar gas also surfaced. Galaxies such as NGC 5383 and M81 display striking dust lanes aligned along their spiral arms, suggesting compression of gas/dust caused by shocks induced by the spiral density waves. Fujimoto (1968) and Roberts (1969) postulated that a supersonic gas flow into a spiral density wave experiences a shock as a result of the rapid deceleration. This would occur *before* reaching the spiral minima, shown in Figure 1.11, and gas would accelerate once more as it leaves the arm/shock and travels towards the next. The sudden compression of gas at these spiral shocks is theorised to act as a trigger for star formation due to the accumulation of molecular gas in regions of high density. Young stars will then be seen to trail the spiral potential, as will ionised H II regions.

The offset of the peak gas and stellar densities as shown in Fig. 1.11 is not universally accepted however. Wada et al. (2011a) and Dobbs & Bonnell (2008) find that gas shocks do not appear to be offset from the stellar spiral potential well in calculations with dynamic stellar spiral potentials, where the structures are not long-lived, and so gas will develop with the arm and travel with it, rather than traverse through a well established density wave. Conversely, calculations

with fixed potentials tend to observe offsets between spiral minima and ISM shocks (Yuan & Grosbol 1981), though not always necessarily leading the arm (Gittins & Clarke 2004; Elmegreen & Thomasson 1993).

The actual response of ISM gas to a spiral perturbation is much more complex than a single shock front leading the arms. Numerical simulations including ISM heating and cooling show instabilities and shock fronts that are no means uniform across the arms (Shetty & Ostriker 2006; Wada 2008; Dobbs et al. 2008; Smith et al. 2014). This non-uniform response creates spurs and feathering features trailing from the spiral arms[5]. Wada & Koda (2004) believe these features are caused by a 'Wiggle-instability', essentially a manifestation of the Kelvin-Helmholtz instability, while Dobbs et al. (2008) theorise that they are simply caused by the amplification of cloud-scale substructures as they pass into the spiral shock.

1.3.2 Flocculent/dynamic spirals

While the density wave theory does solve some standing issues for galactic spirality, there is one major caveat. Thus far no direct evidence, be it observational or numerical, has been able to confirm the theory. Spiral arms can be seen in numerical simulations, but they are not persistent, rather transient and recurrent (see Sellwood 2011 for a review of spiral longevity). Material populates these arms for the lifetime of the arm itself, rather than flowing into and out of the perturbation as in density wave theory (see Wada et al. 2011b; Baba et al. 2013; Grand et al. 2013). Spiral arms in N-body simulations have two key differences to those of the density wave theory. They are material in nature, rather than propagating density waves, and they are recurrent, being victim to the winding problem. As the disc rotates the arms become sheared apart as they wind up, only for them to join different arm structures formed in their wake. While some authors find long lasting modes (e.g. Sellwood & Carlberg 2014), these arms are still transient with no fixed pattern speed. Arm features tend to only recur for a certain time, after which the disc tends to become featureless, or strongly barred (see Section 1.3.4). As the system evolves from initialisation, Q rises making the disc more stable to perturbations, eventually leading to the dissipation of spiral features (Sellwood & Carlberg 1984). The loss of spirality is even more severe with lower number of particles, implying it may also be a resolution effect (Fujii et al. 2011).

A key mechanism for generating these spiral features is "swing amplification". Numerical simulations of Toomre (1981) showed that a leading wavepacket could become significantly amplified as it transforms into a trailing wave and back into a leading wave. The transient trailing wave is even stronger still than the final leading wave, creating an amplification effect (Binney & Tremaine 1987). In order to set this swing amplification mechanism the initial leading spiral wave must be generated. Certain mechanisms for this have been theorised, such as a lack of ILR or reflection of density waves from a hard edge of the disc, though neither of these are likely in

[5]The terms branches, feathers and spurs are used interchangeably in the literature, but here we adopt the convention of Dobbs & Baba (2014). Branches are long, secondary arm features, resulting from bifurcation (e.g. the Local Arm in the Milky Way). Spurs and feathers and morphologically similar, which are smaller scale and more numerous, inter-arm features. Some define spurs as the star formation sites, and feathers as the dust lanes. In the work in this thesis there is no distinction between the latter two due to a resolution lacking to model star formation, and so we use spur and feather interchangeably.

the Milky Way (see Binney & Tremaine 1987 for a discussion). Swing amplification could also be responsible for the seemingly easy creation of bars in numerical simulations (Combes & Sanders 1981; Sparke & Sellwood 1987; Raha et al. 1991; Baba et al. 2009; Shen et al. 2010). See Chapter 5 for some examples of this phenomenon in our work.

The dominant mode of the swing-amplified spiral pattern is given by

$$m = \frac{\kappa^2 R}{2\pi G \Sigma X} \approx \frac{\kappa^2 R}{4\pi G \Sigma} \tag{1.9}$$

where $1 < X < 2$ generates spiral features, and $X = 2$ is a nominally adopted value (Fujii et al. 2011; Dobbs & Baba 2014). Equation 1.9 shows that the number of spiral arms is a strong function of the disc mass, with systems with high disc-to-halo mass ratios forming only a few strong spiral arms, whereas low mass discs form numerous but weaker arms (Carlberg & Freedman 1985). The dominant arm mode is also directly coupled to the Q parameter (Equation 1.6), and so seeding a disc with a very low Q will lower the expected m. Equation 1.9 only predicts the dominant mode, and any single simulation will have other spiral modes of comparable strength, and even then the dominant mode will increase with radius.

Further details on this mechanism of spiral formation will be presented in Chapter 5 where we show calculations using N-body stellar systems and their effect on the molecular content of the ISM.

1.3.3 Perturber/tidal induced spirals

The interaction between a galactic disc and some companion object can also seed arm structure. The poster child of spiral structure, M51 (top left, Fig. 1.4), is believed to have been seeded by such an encounter. Other notable examples include the Mice and Antennae galaxies, NGC 2207, and even our own Milky Way to a minor extent with the nearby L/SMC (Purcell et al. 2011). Encounters of this form drive bimodality in the disc at large distances, with severe disruption occurring as the companion nears the edge of the host (Combes et al. 1995). The attraction of the companion elongates orbits, effectively driving an epicyclic oscillation, which in turn will wind up due to the disc rotation creating spiral structures. These arms do not even require self-gravity in the stellar disc to become apparent, but it is required to ensure the tidal features are propagated to the centre of the disc as in M51 (Toomre 1981). Galactic tides may also be responsible in some part for disc warps, with the Milky Way's warp at $R > 9$kpc caused by the nearby L/SMC (Kalberla & Kerp 2009).

One of the first in depth simulations of interacting galaxies was performed by Toomre & Toomre (1972)[6]. Using only 120 particles the authors showed the relative ease of reproducing arm features (bridges, features connecting bodies, and tails, features approximately 180° offset to bridges). An example of these is shown in Fig. 1.12 where a companion, 1/4 the mass of the host galaxy, approaches on a parabolic orbit, distorting the disc into arm features similar to Arp 82,

[6]Worth mentioning is the study by Holmberg (1941), who "simulated" the interaction between two galaxies using lightbulbs, where the amount of light at any point represented the gravitational field of the combined galaxy system. Photocells measured the intensity of the light (which obeyed a $1/r^2$ law as gravity does), which was used to update the gravitational forces.

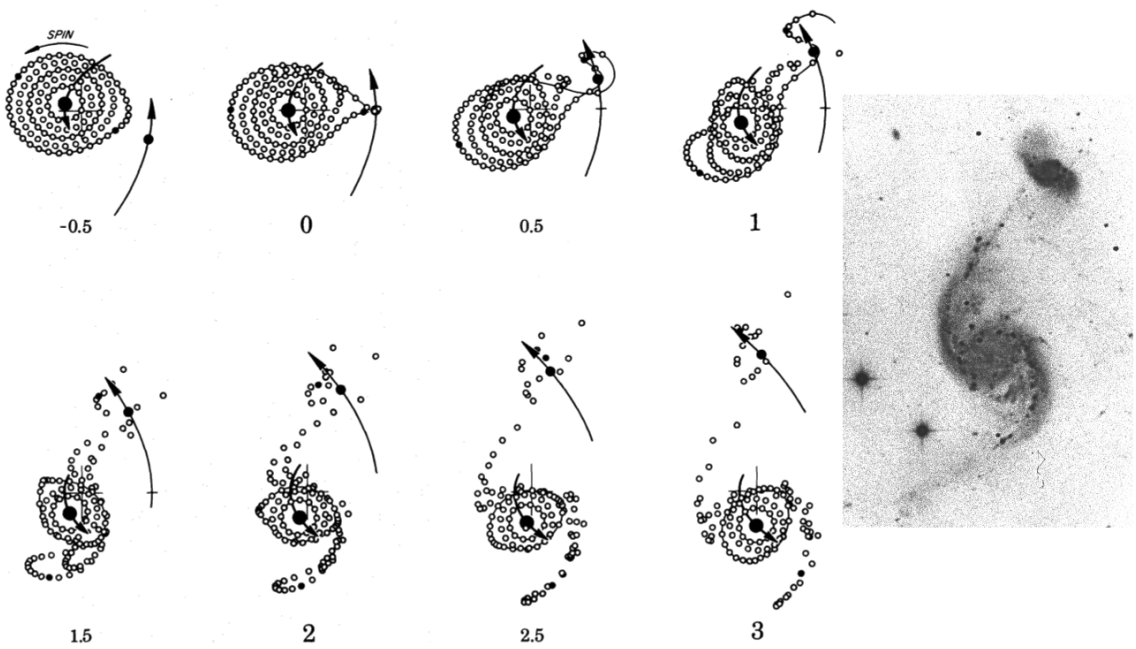

Figure 1.12: Interaction of a point mass companion with an N-body disc adapted from Figure 4 of Toomre & Toomre (1972). The initial perturber trajectory is parabolic with a mass 25% that of the primary galaxy, and the system is shown evolving in time from -0.5 to 3 in units of 100Myr (0 being perigalacticon passage). Clear bridge and tail features can be seen caused by gravitational attraction with the perturber. The right insert shows the Arp 82 system (a.k.a NGC 2535 and NGC 2536) from Arp (1966) showing similar tidal features.

shown in the insert.

The structures formed by these interactions are a mix of kinematic density waves (self-gravity in the stars is not required, Ω_p not fixed but winding slower than material arms), material waves (arms flow with the disc, $\Omega_p = \Omega(R)$), and density waves as in Section 1.3.1 (Ω_p = const.). The tails and bridges tend to be material arms and dissipate rapidly. Arms formed in simulations tend to have a pattern speed decreasing with radius, and are subject to winding up over time (Oh et al. 2008; Dobbs et al. 2010; Struck et al. 2011). Many examples now exist in the literature of tidally induced spirals, predominantly of the $m = 2$ mode (Elmegreen et al. 1991; Barnes 1992; Barnes & Hernquist 1996; Oh et al. 2008; Dobbs et al. 2010; Purcell et al. 2011; Struck et al. 2011). These successfully reproduce many observed galactic tidal encounters and computational resources are sufficient to also track the gas evolution, and the effect of a companion with an extended mass distribution.

1.3.4 Bar structure

Bars exist in many observed disc galaxies, as abundant as 30-50% (Binney & Tremaine 1987), being composed predominately of the old and red stellar population. They either dominate the disc structure as in NGC 1300 (SB class) or only extending to intermediate radii as in UGC 12158 (SAB class) or our own Milky Way. The bars themselves vary in dimensions, but are often very elongated and quite dissimilar morphologically to elliptical galaxies with axis ratios ranging from

Figure 1.13: Boxy/peanut bulges in the disc galaxies of Hickson Compact Group 87 (Credit: The Hubble Heritage Team, AURA/STScI/NASA, top) and NGC 5746 (credit: Palomar DSS, bottom).

2:1 to 5:1 (Combes et al. 1995). While ellipticals have a strong surface brightness drop-off away from their centre, bars have a near-constant surface brightness across their length. The vertical structure of bars is harder to assess, due to the difficulty in identifying bars in discs orientated edge-on. Numerical simulations suggest that a barred galaxy will display a boxy, or peanut, shaped bulge with lobes corresponding to the ends of the bar. Two examples of galaxies with such bulges are shown in Figure 1.13. Elliptical bulges are then either bar-free, or have a bar along the line-of-sight (Binney & Merrifield 1998).

While the density wave theory has had no irrefutable evidence supporting a single fixed pattern speed for the spiral arms, the pattern speed of bars does appear constant in simulations. The pattern speed of the bar is encompassed by the parameter $\mathcal{R}$, which relates the bar major axis to co-rotation radius, $R_{\rm CR}$, by

$$\mathcal{R} = R_{\rm CR}/a \tag{1.10}$$

where "slow" bars are defined by $\mathcal{R} \gg 1$ and "fast" bars have $\mathcal{R} \approx 1$. The co-rotation radius is in turn directly coupled to the pattern speed of the bar, and the pattern speed can be either measured directly using methods such as that of Tremaine & Weinberg (1984), or by comparison with simulations. The co-rotation and major axis of the bars follow a linear slope in many barred galaxies, with $0.9 < \mathcal{R} < 1.3$, and lie near $\mathcal{R} \approx 1$ within errors, making observed bars "fast" rotators (Binney & Tremaine 1987).

The equivalent equipotential surface of a simple barred gravitational potential is shown in the left panel of Figure 1.14 (i.e. in a reference frame rotating at the bar pattern speed; $\Phi_{eq} = \Phi_{bar} - \Omega_p^2 R^2/2$). There are five Lagrangian points; one at the centre, two unstable saddle points (red crosses) and two maxima (green crosses). Stars can oscillate around the maxima points at κ, and all the Lagrangian points combined outline the coronation zone (Combes et al. 1995). In the right panel of Fig. 1.14 the orbits in such a potential are shown, calculated by Contopoulos & Papayannopoulos (1980), showing several interesting features. At the centre of the bar a set of

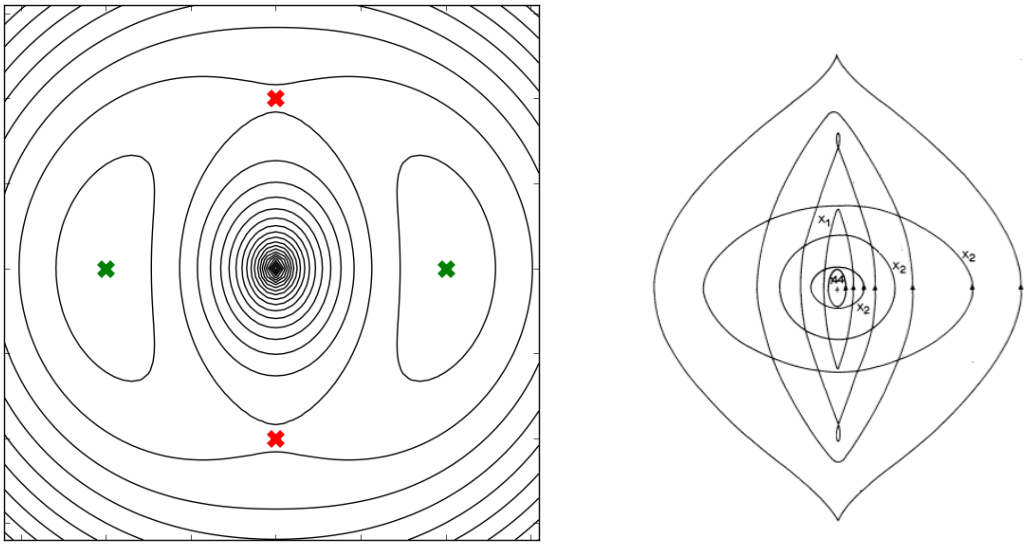

Figure 1.14: Left; orbits inside a simple biaxial potential representing a bar, from Binney & Tremaine (1987). Right; stable orbits inside such a potential, taken from Contopoulos & Papayannopoulos (1980). The bar is aligned vertically in both cases.

orbits parallel to the bar exist, denoted x_1 orbits. Beyond the CR the x_1 orbits now display lobes at their extremities. These orbits form the majority of the bar structure itself due to their stability and presence inside the CR. The x_2 family of orbits exist *perpendicular* to the bar major axis, and only exist between ILRs if they exist, which may not be the case for some disc structures. A further set of orbits exist around the lobe Lagrangian points (green crosses), that do not orbit the bar's centre. Well outside the CR orbits become circular again.

The above holds primarily for weak bars. For the strong case (SB class) orbits lie effectively only on the x_1 family (Contopoulos & Papayannopoulos 1980; Athanassoula 1992a). Modelling the orbits in these bars is more difficult, and they are usually studied via numerical simulations of unstable discs (Sparke & Sellwood 1987).

Numerical simulations have shown that while steady spiral structures are difficult to maintain, stable bars are easily created (e.g. Ostriker & Peebles 1973; Sparke & Sellwood 1987; Combes et al. 1990; Baba et al. 2009; Shen et al. 2010; Grand et al. 2012). The problem is not so much how to form bars, but rather how to hinder their formation to reproduce spiral galaxies with no bar component. The easiest way is to simply raise the stability of the disc by raising Q_s, which is easiest done by lowering the the disc to halo mass ratio, which also suppresses the swing amplification that helps further enforce the bar. A second way of suppressing bar formation is by ensuring the rotation curve has an ILR. As described in the previous section, an ILR stops trailing waves passing through the centre and forming leading waves on the opposite side of the disc (hence why arms are only formed outside of the ILR). While flat rotation curves are common in disc galaxies, this does not ensure an ILR, but the inclusion of a large central concentration will do (i.e. a bulge, as in Fig. 1.10). A criterion for bar formation was found by Efstathiou et al. (1982) of the form

$$\epsilon_b = \frac{V_{\max}}{\sqrt{GM_d/R_d}} \tag{1.11}$$

where $V_{\max}$ is the maximum velocity of the full rotation curve, M_d and R_d are the disc mass and scale-length respectively with bar formation requiring $\epsilon < 1.1$.

Bars are seen to have strong dust/gas lanes lying along either major axis, and often only on the leading side (see NGC 1300 in Fig. 1.4). The offset of these lanes to the bar itself, and their degree of curvature, is a related to the $\mathcal{R}$ parameter (Athanassoula 1992b). These then wind up near the galactic centre, forming nuclear rings around the central bulge. This transport of material results in a net gain of gas to the galactic centre, and accumulates at the inner x_2 orbits inside the outer ILR (Binney & Tremaine 1987). Star formation is seen at the bar ends rather than these parallel dust lanes, and bar ends are also the site of high density enhancements in simulations (Athanassoula 1992b).

Bar induced spiral arms

Bar and spiral arms often come hand in hand in nature, with $m = 2$ spirals extending from the ends of the inner bar. How and why the bar and spiral features are coupled is not clear, i.e. whether they inherently result from the same mechanism with identical pattern speeds, or whether they are dynamically separate entities. For instance, there is evidence that the bar and spiral features in our Galaxy have very different pattern speeds with the bar rotating at least twice the speed of the arms (see Gerhard 2011 and references therein). In the case where bars and arms share the same pattern speed, the arms trail directly off the bar ends and extend out to the OLR of the bar. These arms are seen in many numerical simulations of gas responding to some barred potential (Athanassoula 1992b; Englmaier & Gerhard 1999; Patsis & Athanassoula 2000; Wada & Koda 2001; Rodriguez-Fernandez & Combes 2008; Mel'Nik & Rautiainen 2009). While stellar orbits lie either parallel or perpendicular to a bar, the dissipative forces experienced by the gas allow for offset elliptical orbits caused by bar rotation. This causes orbits to trail, creating spiral arms in the gas emanating from the bar ends (Dobbs & Baba 2014). Eventually these arms in the gas will wind up to form rings at the OLR after the order 10 bar rotations (Schwarz 1981; Mel'Nik & Rautiainen 2009). Gas is evacuated from the CR region and is migrated to the ILR and OLR features. Having outer rings is not uncommon in observed galaxies (M95, NGC 1291), and neither are galaxies with arms transitioning into rings similar to those seen in simulations (NGC 3504, NGC 7479). The fact that all observed barred galaxies do not have outer rings indicates that the time-scale for bar formation and arm winding is of order of the age of the universe (Combes et al. 1995). There is some, though not much, evidence for decoupled arm and bar features in simulations, namely Sellwood & Sparke (1988) and Rautiainen & Salo (1999). Sellwood & Sparke (1988) find two distinct pattern speeds in their simulations, and observe the bar and arm features to disconnect and reform during rotation. Rautiainen & Salo (1999) find two different pattern speeds in *some* of their calculations, but not all, finding a decoupling that is epoch dependent. Grand et al. (2012) find distinct bar and spiral pattern speeds, but the arms are effectively material and rotate with the disc (having $\Omega_p \propto R^{-1}$).

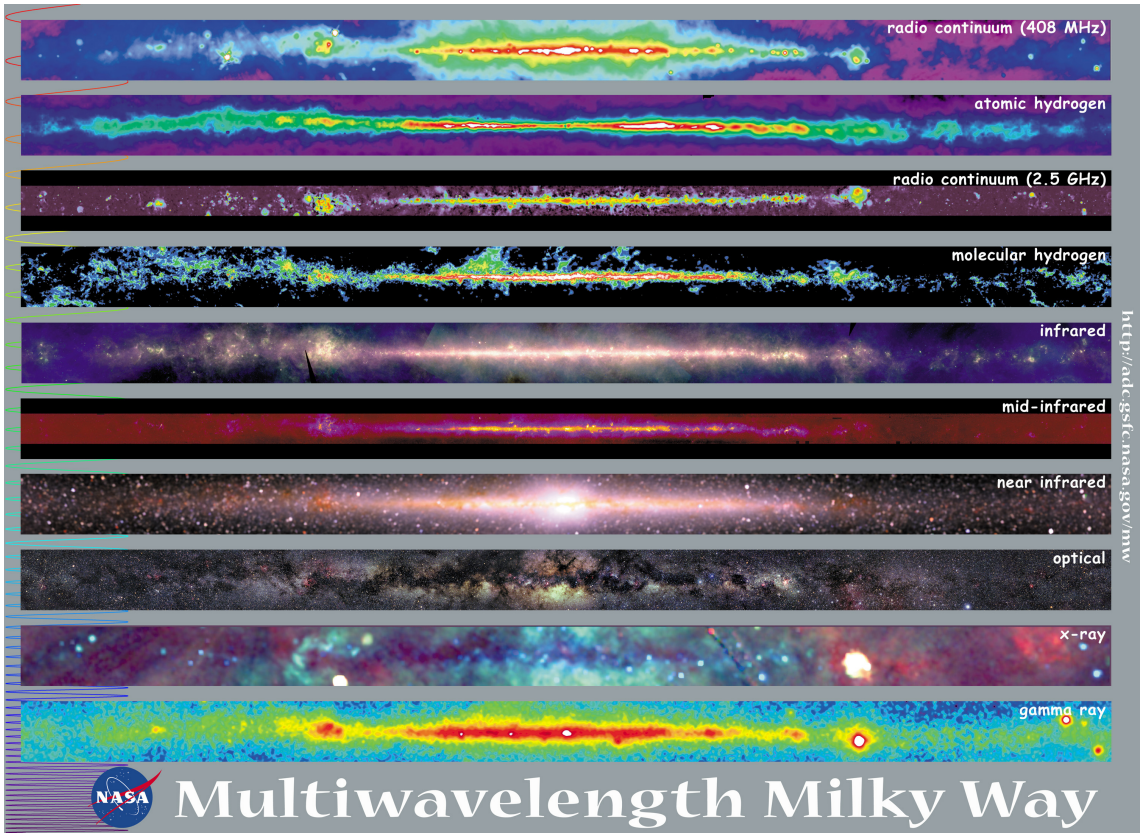

Figure 1.15: Observations of the Galactic plane traced by multiple sources: radio, H I, CO, infrared, optical, X-ray, and gamma rays. Image taken from; http://mwmw.gsfc.nasa.gov/mmw_product.html.

1.4 The Interstellar Medium

Aside from stars, galactic discs are composed primarily of the inter-stellar medium (ISM), a mix of material, primarily consisting of gas and dust. Simply by looking through the plane of our Galaxy (Fig. 1.1) or the disc of M51 (Fig. 1.4) shows dark absorbing material, the ISM dust specifically, that appears to be blocking out the starlight. Figure 1.15 shows the disc of the Milky Way at various wavelengths, each of which corresponding to a different galactic source; including several ISM species. Of specific interest are the second, third, fourth and fifth panels showing emission from H I, H II, H_2 (i.e. CO) and dust. In general the ISM is extremely tenuous, with densities approximately twenty orders of magnitude lower than the Earth's atmosphere.

Various chemical and cooling processes in the ISM that are relevant to the work in this thesis will be discussed in detail in Section 2.3, while here we only give a short overview. Many molecular species are present in the ISM, including but certainly not limited to, H_2, CO, CH, CN, CS, OH, HCN, NH_3 and H_2CO, with some tracing slightly different ISM populations (De Becker 2013). For the purposes of the work in this thesis, we are interested in CO and H_2.

H I

Atomic hydrogen, H I, is the simplest and most abundant element in the known universe and is the dominant component of the ISM. It is commonplace in disc galaxies and scarce in ellipticals, with total mass fractions ranging from 1-30% (elliptical-disc-irregular, Balkowski 1973). The primary electronic transition is the Lyman α line, seen in the UV, which can be used to map local galactic emission (Jenkins & Savage 1974; Shull & van Steenberg 1985), but at larger distances increased dust extinction makes observing this transition impossible.

A clear feature in the radio owing to the 21-cm spin-flip hyperfine transition[7] makes observing atomic gas throughout a galactic disc possible and was independently first detected by Ewen & Purcell (1951) and Muller & Oort (1951). This transition is one of the most important tools for ISM and galactic scale observations as it allows for the tracing of the interstellar gas component with minimal effects of dust extinction. The temperature required for the transition is much below that of the ISM. While the Einstein-A coefficient is very low (indicating a very long lifetime) the H I is so abundant that the transition line is easily detected. The H I traces spiral features strongly in external galaxies in the outer disc, though it tends to be scarcer in the galactic centres (e.g. M31; Chemin et al. 2009 and M81; Rots & Shane 1975). Atomic H I can be used to trace spiral features in our Galaxy(Nakanishi & Sofue 2003; Levine et al. 2006), though exact distance determinations of arms from H I are subject to some uncertainty (Burton 1973). The 21-cm line is seen in both emission, absorption (seen as gaps in the radio continuum), and self-absorption (shows cold H I absorbing 21-cm emission from warmer H I component).

Results from various surveys of Galactic H I will be discussed later in this chapter, the chemical network relevant to this work is discussed in Chapter 2 and the specifics behind simulation of the 21-cm emission line in Chapter 4.

H II

Singularly ionised hydrogen (H II) is also observed in galactic discs, and has been primarily ionised by the most massive and luminous of stars of O or B classification. H II is also seen in planetary nebulae and supernovae remnants. The H II is observed in the UV, visible and IR stemming from collisional excitation and recombination effects. H II can be observed in the optical, mostly by the Balmer lines (Hα, Hβ and Hγ) seen as hot ionised gas in the process of stabilising an electron to a ground state. These are seen in spiral galaxies as bright, condensed features within spiral arms and are believed to trace sites of star formation (see the red globules along the arms of M51 in Fig. 1.4). They are especially useful in mapping out our own Galactic structure due to their discrete nature and association with arms (Georgelin & Georgelin 1976; Russeil 2003; Hou et al. 2009).

[7]Hyperfine structure splitting stems from the split in the F quantum number, where $F = J + I$. J is the electronic angular momentum, $J = L + S$ and I is the nuclear spin which is 1/2 for H I. For the lowest energy state of H I we have one p^+ ($I = +1/2$), and an e^- in the ground state ($n = 1$). As such $L = 0$ ($L \leq n - 1$) so $J = \pm 1/2$ as $S = \pm 1/2$ for e^-'s. H I can either have $F = 1$ for e^- and p^+ parallel spins ($I = J = S = +1/2$) or $F = 0$ for antiparallel spins ($I = +1/2$, $S = J = -1/2$). The change in e^- spin causes the $\Delta F = 1$ hyperfine split, with the upper and lower states having slightly different energies, producing the 21-cm transition with an Einstein-A co-efficient of $\approx 10^{-15}\ s^{-1}$ (Combes et al. 1995).

H_2

The most abundant molecule in the ISM is molecular hydrogen (H_2). It is in the unfortunate position of being axisymmetric and therefore having no inherent dipole moment. This means there are no molecular $\Delta J = \pm 1$ transitions. There is no fine or hyperfine structure, making it effectively invisible in the radio or IR and difficult to observe with the effects of interstellar dust extinction (Field et al. 1966). Molecular hydrogen transitions don't appear until the rotational quadrupole regime of $\Delta J = \pm 2$ in the μm region, where higher energies are required to start a transition, requiring greater surrounding temperatures (around 500K, which can possibly be seen in shocked regions, Timmermann et al. 1996). This is high for typical molecular clouds, and so molecular hydrogen transitions are hard to spot, even then they are easily hidden by atmospheric water transitions. Even the ro-vibrational levels (requiring a vibrational transition in ν_1) fail to give anything more detectable. Molecular hydrogen can be observed at certain transitions such as electronic transitions in the UV and optical (e.g. *Copernicus*, Savage et al. 1977, and *FUSE*, Rachford et al. 2002). These observations, however, do not probe very deep into the ISM due to the effects of dust extinction (see Shull & Beckwith 1982 for a review). Tracing the molecular component of the ISM thus falls to the second most abundant species, CO (see next subsection).

The question of the formation of H_2 is still not entirely solved, but the current consensus is that it relies heavily on dust grains acting as a catalyst. H I is captured by the grains (if the grains are sufficiently cold) which is then allowed to tunnel through the surface to a stable point. In this hydrogen "sink" it sits until another H I interacts with it, bonds to the H I on the grain, and then easily breaks the bond to the surface, escaping into the ISM (Gould & Salpeter 1963; Hollenbach & Salpeter 1971). This process occurs inside dark clouds, with sufficient dust to catalyse the formation, and shielding both by dust and other H_2 molecules against immediate photo-destruction (Draine & Bertoldi 1996). There are also possibilities for chemically creating molecular hydrogen in the pure gas phase (Dalgarno & McCray 1973). Most of this requires either high ion supply (as in the early universe) or high temperatures, and is much less efficient in cold clouds where H_2 is easier maintained.

The amount of molecular hydrogen is measured by the H_2 fraction, which is quantified as

$$f_{H_2} = 2N(H_2)/\left[N(\mathrm{H\,I}) + 2N(H_2)\right] \approx 2N(H_2)/N(H_{tot}) \tag{1.12}$$

ranging from 10^{-7} to near 0.8 depending on environment (Binney & Merrifield 1998). The f_{H_2} ratio is a strong function of column ISM density, where diffuse clouds with insufficient UV shielding cannot protect their molecular content from photo-destruction (Spitzer et al. 1973).

CO

The task of tracing the molecular content of the ISM then falls to the next most abundant molecule; carbon monoxide ($CO/H_2 \approx 6\times10^{-5}$, Combes et al. 1995). Due to its asymmetry, CO has a readily detectable rotational transition ($J = 1 \rightarrow 0$) at a low enough energy, 2.6mm, to be seen in fairly cold clouds at 5.5K (the $J = 2 \rightarrow 1$ transition is also visible). This makes it the best tracer of molecular regions, due to the relative clarity of the radio regime. The higher strength of this

transition compared to the 21-cm H I line compensates for the much lower abundance of CO in relation to H I (Binney & Merrifield 1998).

The CO is assumed to spatially coexist with H_2. A conversion factor, $X_{CO} = N_{H_2}/I_{CO}$ is used to infer the amount of molecular hydrogen rather than observing it directly. It is defined as (Strong et al. 1988; Scoville et al. 1987)

$$X_{\rm CO} = N_{\rm H_2}/I_{\rm CO} \approx 2 \times 10^{20}\,{\rm cm^{-2}\,K^{-1}\,km^{-1}\,s} \tag{1.13}$$

where $I_{\rm CO}$ is integrated CO brightness temperature (K km/s), and N is the column density. While the $X_{\rm CO}$ value is assumed to be constant across the Milky Way, this value is subject to some variation with metallicity and density in different galaxies (Binney & Merrifield 1998; Narayanan et al. 2012).

CO itself is formed primarily through gas-phase transitions, with other C, H and O species. The isotopologues are also useful tracers, in case the CO itself becomes too optically thick. $C^{13}O$ is especially useful for temperature determinations (12CO/13CO ≈ 60-90). In the densest regions the photon from the CO rotational transition can be re-absorbed, and so masking the transition to observations, and observers can turn to the more optically thin 13CO to trace the densest cores (Combes 1991).

The study of CO has given observers their main window on cold molecular clouds, with temperatures in the range 5-20K (Young & Scoville 1991), Molecular material in general also traces out the global spiral structure of galaxies (e.g. M51; Schinnerer et al. 2013, various external galaxies; Helfer et al. 2003, and the review of Young & Scoville 1991). CO has the added advantage of having a much higher arm-interarm contrast than H I, which is present throughout the Galactic plane (Dame et al. 1986; Grabelsky et al. 1987), allowing for the finer tracing of arm features than the atomic gas.

Dust

Dust accounts for most of the attenuation effects in disc galaxies and also plays a key role in the star and planet formation processes. The term dust encompasses solid phase material that ranges in size from a few molecules to substances up to a few microns in size that cannot be considered in the atomic gas stage. This includes silicates, carbonaceous materials and polycyclic aromatic hydrocarbons[8] (PAHs) (Draine 2003). This dust acts to absorb and scatter away starlight, blocking out much of our own Galaxy from optical observations (see Fig. 1.1). As can be seen from Figure 1.15, dark dust bands appear in the optical and X-ray, but diminish in effectiveness as wavelengths move further into the infrared, and to greater wavelengths. The extinction (the collective term for dust scattering and absorption) caused by this dust is referred to as "redenning", due to the dust primarily absorbing in the blue end of the optical spectrum, the strong effect of which was not truly appreciated until the work of Trumpler (1930). The effects of dust on molecular ISM chemistry will be discussed in Section 2.3.

[8]PAH's are simply a hydrocarbons composed of carbon rings with outer hydrogen atoms. See Tielens (2008) for a review.

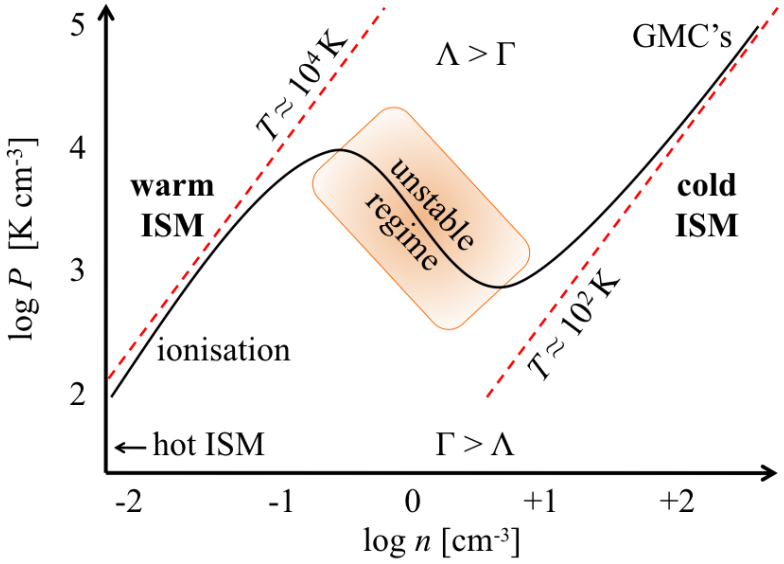

Figure 1.16: ISM phase diagram of pressure and density, based on the work of Field et al. (1969). Stable warm and cold ISM components exit with temperatures of the order 10000K and 100K respectively, joined by an unstable regime where runaway cooling/heating will return the gas to a stable regime. The various other phases, such as a very cold molecular phase and hot ionised phase, are not included in this diagram.

1.4.1 Phases of the ISM

The ISM is a very complex place, with numerous different astrophysical, radiative, and chemical processes continuously changing its thermodynamical properties. The processes relevant to the ISM gas on a galactic scale will be discussed in detail in Section 2.3. These include photoelectric heating on dust grains, cosmic ray heating, fine structure cooling, collisional ionisation, recombination cooling and molecular cooling. When all these cooling and heating effects are incorporated, a phase diagram can be produced of the ISM, similar to that shown in Figure 1.16, based on diagrams of Field et al. (1969); Wolfire et al. (1995); Liszt (2002); Cox (2005). The specifics of such a phase curve are not universal, and the exact shape is defined by the location, defining the various metallicities, abundances and fluxes that dictate the strength of individual cooling/heating rates (Wolfire et al. 1995; Liszt 2002). The diagram shows two distinct branches, indicating the two phases of the original Field et al. (1969) model; the cold neutral medium (CNM) and warm neutral medium (WNM). Each of these regions has approximately stable temperatures (of the order $<$ 100K and 10000K respectively). They are separated by an unstable region[9], with temperatures ranging from 200K to approximately 5000K (Cox 2005). In this region the gas experiences runaway cooling/heating until it joins one of the aforementioned stable branches.

This model helped explain the apparent discrepancy between observations of ISM gas with

[9]This is caused by the negative gradient in the "loss function", defined as the net heating/cooling rates; $\dot{E} = \Gamma + \Lambda$. The derivate of this function (i.e. the second derivative of the change in energy) defines the location of an unstable/stable equilibrium state. For example, $d\dot{E}/dn > 0$ signifies a stable point, while $d\dot{E}/dn < 0$ an unstable point.

Component	T [K]	n [cm^{-3}]	Notes
Molecular (MM)	10-20	10^2-10^6	Dominated by H_2 and CO, observed in radio
Cold atomic (CNM)	50-100	20-50	H I dominated, moderate density, H I absorption
Warm atomic (WNM)	6000-10000	0.2-0.5	H I dominated, diffuse, H I emission
Warm ionised (WIM)	≈ 8000	0.2-0.5	H II dominated, observed in H_α
Hot ionised (HIM)	$\approx 10^6$	$\approx 10^{-3}$	H II and ionised metals, observed in X-ray and UV

Table 1.1: Properties of the five main ISM phases believed to be present in the Galactic ISM, ordered by temperature. Adapted from Ferrière (2001).

contrasting temperatures and pressures. This two-phase model was then expanded to incorporate hot ionised media which are a result of supernovae winds heating up the surrounding ISM, creating H II "bubbles" (Cox & Smith 1974; McKee & Ostriker 1977). The warm medium was expanded to include both ionised and neutral components, with comparable densities and pressures. These multi-phase models are not without their flaws however. Models by Slavin & Cox (1993) found that the size of supernova bubbles may have been somewhat overestimated in the McKee & Ostriker (1977) multiphase model, undermining their importance in ISM thermal structure. The key assumption of local thermal pressure balance between the various phases may also be an incorrect one, and various other pressure sources such as magnetic fields and cosmic rays radiation pressure may be important (e.g. large thermal pressure variations were seen in the local ISM by Bowyer et al. 1995). Observations and simulations have also seen that the unstable regime shown in Figure 1.16 can be surprisingly well populated, despite the expected instability (e.g. Heiles & Troland 2003).

Nethertheless, the multiphase model of the ISM is still one of the better formulations of the ISM's various components (Cox 2005). The properties of the generally accepted 5-phases of the ISM are given in Table 1.1 (adapted from Ferrière 2001). The components are a cold and warm neutral medium (C/WNM), a warm ionised medium (WIM), which between them contain most of the galactic gas mass budget. The WIM traces gas that is subject to OB star UV fields. The hot ionised medium (HIM) traces the hottest gas components resulting from supernovae winds, and is found in bubbles and fountains far out of the galactic plane. Finally there is the molecular medium (MM) where the cold, dense clouds are found and are the sites of star formation.

Stars themselves have a strong influence on the ISM though various feedback mechanisms. The term feedback constitutes a variety of physical processes depending on the scale, but primarily it refers to either supernovae or stellar winds form OB stars injecting large amounts of energy into the adjacent pockets of ISM gas. The effect of feedback is to blow apart ISM gas, dissociating molecular gas in photodissociation regions (PDRs) and ionising gas in H II/HIM regions. Feedback also creates holes in the H I distribution (e.g. seen in IC 2574 by Walter & Brinks 1999 and M31 by Brinks & Bajaja 1986), and imparts thermal energy allowing for the expansion of shells into the ambient ISM. These expanding shells can eventually cool at sufficient distances from the feedback source, and can then host cold and dense gas. This could eventually host further star formation (e.g. Cioffi et al. 1988, McCray & Kafatos 1987), though winds could also act to break apart and destroy clouds and inhibit star formation (Dale et al. 2013).

1.5 Determining Galactic structure

Despite the difficulty in doing so, studies of the global structure of the Milky Way have been numerous in the past five decades. Due to the position of the Earth within the Galaxy many techniques have been used to try and circumvent the problem of discerning the shape of the body whilst inside it. In this section we briefly outline some of the main techniques used in the literature for determining galactic structure. Key findings based on these methods will be discussed in the next section.

1.5.1 Methods of structure determination

Method 1: Determine actual or kinematic distances

The most obvious method of determining Galactic structure is to simply measure the distance to sources in the Galaxy across various Galactic longitudes. For example through stellar parallaxes (distance and magnitude limited), trigonometric parallaxes (if close enough to the Earth), OB star standard candles, main sequence fitting, or through Cepheid variables. The problem is that many of these cannot be assumed to be tracing spiral structure, simply just the global disc-like structure of the Milky Way. The objects this is actually possible for is minimal and distances are only accurate to approximately 10%, making the larger distances more uncertain (Elmegreen 1985). Nevertheless, some spirality can clearly be seen in these measurements (Becker & Fenkart 1971; Vogt & Moffat 1975).

The more widely applicable method of determining distances is to use the velocity information of the source to calculate a kinematic distance. By using the velocities from emission lines of ISM gas complexes such as H I and CO a distance can be calculated so long as some velocity field of the Galaxy is known, which can be calculated from the rotation curve. The line-of-sight velocity, v_{los}, measured from the emission profile as a function of galactic longitude, l is

$$v_{los}(l) = R_\circ \sin(l) \left[\Omega(R) - \Omega_\circ\right], \tag{1.14}$$

where the gas is located at a radius R from the galactic centre (Shu 1982) and $\Omega_\circ$ is the angular velocity at the Solar position. If we simply substitute for the rotation frequency $\Omega(r) = V(R)/R$ we can re-arrange to give the Galactocentric radius of the emitting gas,

$$R = R_\circ \sin(l) \frac{V(R)}{v_{los} + V_\circ \sin l} \tag{1.15}$$

where v_{los} can be directly obtained from the emission profile, l, $R_\circ$ and $V_\circ$ are known (the position and velocity of the Earth's position) and $V(R)$ can be either taken from the known rotation curve or directly evaluated from emission profiles[10]. Fortunately the Galactic rotation curve is fairly well

[10]First evaluate Equation 1.14 for the smallest radius possible along the line of sight which is equivalent to $r_{\min} = R_\circ \sin l$. Then Equation 1.14 becomes $v_{los}^{\min}(l) = r_{\min}\Omega(r_{\min}) - V_\circ \sin(l)$ giving $V(r_{\min}) = v_{los}^{\min}(l) + V_\circ \sin(l)$. This gives a $v - r$ pair for the rotation curve, providing you can obtain the maxiumum line of sight velocity (corresponding to minimum radius) from the emission profile. This is done simply by observing where the emission sharply drops off at velocity extrema (Binney & Merrifield 1998).

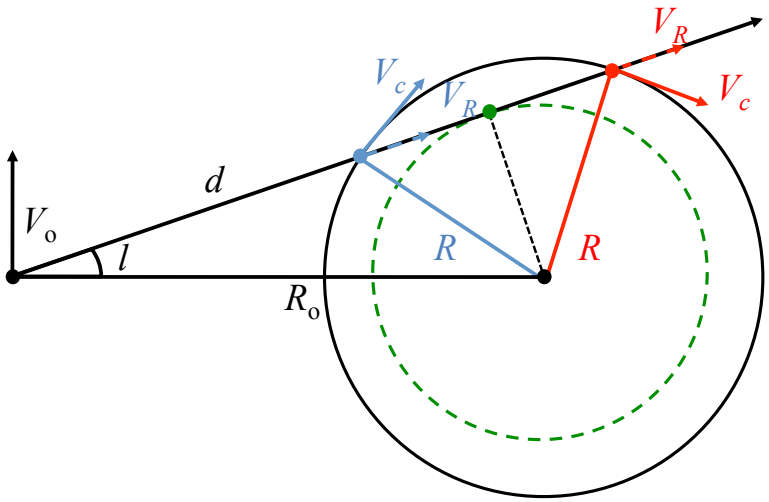

Figure 1.17: Kinematic distance problem in our Galaxy when observing gas with a radial velocity of V_r and circular velocity of V_c at some distance R from the Galactic centre. At any point a single radius and radial velocity corresponds to two separate distances from the Earth (red and blue lines intersection with the d line). Based on Figure 1 of Roman-Duval et al. (2009).

measured, and is approximately axisymmetric (Brand & Blitz 1993). While this method works well for calculating distances outside of the Solar circle, there is a degeneracy in distance when looking inside. Figure 1.17 illustrates this "distance ambiguity". There are two points that have the correct observed line-of-sight velocity calculated from the emission profile, one at a near (blue line, Fig. 1.17) and one near distance (red line) compared to the the smallest possible Galactic radius (dashed line) and point of maximum velocity observed from the profile. By simply calculating the distance, d, to the emitting gas shown in Fig. 1.17 you see that there are two distinct solutions;

$$d = R_\circ \cos(l) \pm \sqrt{R^2 - R_\circ^2 \sin^2(l)} \tag{1.16}$$

where d is the distance from the observer to the point of maximum velocity.

There have been numerous different techniques developed to break this degeneracy. Observations of H II regions by Downes et al. (1980) also measured OH or H_2CO absorption lines towards the same direction as the sources. If the shift in these lines implied a velocity much larger than the H II region they assumed the emission is from different sources and the emission from the H II travelled from the larger kinematic distance through OH/H_2CO. If the difference in velocities is small it is still somewhat ambiguous, due to streaming velocities and random dispersions possibly causing the small offset (Elmegreen 1985). Kolpak et al. (2003) use this method by using additional observations of H I in their H II survey to map out the Galaxy inwards of the Solar circle and Roman-Duval et al. (2009) use H I self-absorption (HISA) to eliminate the ambiguity in their CO survey, where additional HISA would be seen for the far-kinematic distance as opposed to the near distance. This method is widely employed for a number of different tracers (Araya et al. 2002; Russeil 2003; Sewilo et al. 2004; Watson et al. 2003; Fish et al. 2003; Paladini et al. 2004; Pandian et al. 2008). Another method requires the construction of theoretical density maps of the Milky Way, that are then used to estimate the column density viewed from Earth, from which we

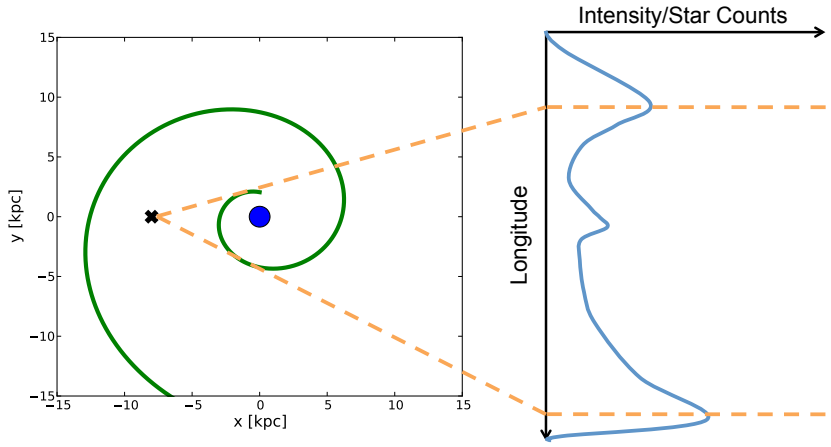

Figure 1.18: Tangency method for determining spiral structure. On the left is the top-down structure with the observer at the black cross in a galaxy with a one-armed spiral over-density. On the right is the star count/emission profile as a function of longitude, with over-densities caused by the spiral arm tangents appearing as peaks in the distribution. This is a simplified case, and in reality an exponential disc profile is seen superimposed in the observed profile.

can infer what distance the material lies (Nakanishi & Sofue 2003, 2006; Levine et al. 2006).

The main source of error is the uncertainty in the rotation curve, local velocity dispersion in the gas, or steaming at velocities significantly different to those implied by the global rotation, and is of the order 10-20% (Elmegreen 1985). The relatively large uncertainties and numerous different approaches that exist in the literature for solving the distance ambiguity make structure determinations from kinematic distances open to interpretation.

Somewhat troublingly; kinematic and direct distance determinations can yield different results, highlighting uncertainties in any distance determinations. For instance, Moisés et al. (2011) found that for a selection of H II regions trigonometric distances tended to be smaller than the kinematic distances. Using a simulated Galactic disc Gómez (2006) showed that kinematic distances return a distorted and spurious Galactic structure. While they also showed that a better reproduction could be made using the full Galactic velocity field, this is much more difficult to obtain than a simple axisymmetric rotation curve. The rotation models used to determine these distances fail to take into account large scale shocks and the effect of spiral/barred structure on the velocity field, which can result in large departures from an axisymmetric model.

Method 2: Tangencies

A non-kinematic method for determining Galactic structure is to use star counts or emission strength as a function of longtiude. In cases where stellar distances are not known the non-symmetric nature of the stellar distribution or dust emission with longitude can show over dense regions that can correspond to spiral/bar features. These spikes in the galactic emission profile stem from spiral arm tangencies seen from Earth and result from an increased density when looking down a long, continuous stretch of arm. By identifying the same arm in two separate quadrants we can also directly compute the pitch angle (Drimmel 2000). Another advantage of these kind of

observations is that by matching the global shape of the emission/star counts we can reverse engineer a surface density of the galactic disc, bulge and bar. These models can be then used directly in numerical simulations to set up the galactic stellar distribution (Benjamin 2008).

This method is illustrated in Figure 1.18. To the left is a top-down view of a simple one-armed spiral galaxy, where the observer is placed at the black cross. To the right is the emission/star count profile as a function of longitude in the inner galaxy. Peaks exist in the distribution when looking along an arm tangency, i.e. when orientated down a sight line that spans the longest stretch of spiral arm. A peak is also shown for the Galactic centre. This method is obviously only suitable for observations in the inner disc, and in reality the profile of the entire stellar disc will also be seen, as a steady decay in counts/emission as we look away from the Galactic centre. Bars are expected to appear as asymmetries around the Galactic centre, provided that the bar is angled far from the perpendicular to the line-of-sight to the Galactic centre.

Method 3: Longitude-velocity maps

A method of determining Galactic structure that is free from model assumptions, yet still allows for the tracing of spiral arms is to map out the position of sources in velocity space. An example of one of these longitude-velocity, *l*-*v* , diagrams is shown in Figure 1.19. In the left panel a simple disc galaxy is shown, with the observer placed at the black cross within some disc of material (grey circle). Two spiral arms have been included for illustration of the method (red and green lines). In the right panel is the corresponding *l*-*v* map, constructed using the same rotation model as that of the right panel of Fig. 1.7. The over-densities at the spiral arms will appear against the continuum of the disc, from which pitch angles can be directly measured. Spiral arm tangencies should also be seen as bright concentrations near peak velocities with longitude (if measuring emission). The terminal velocity curve can also be used to determine the rotation curve of the inner Galaxy independently for the first and fourth quadrants, assuming $R_\circ$ and $V_\circ$ are known (Binney & Merrifield 1998). Rings, bars, arms, expanding features, and non-circular motions will all impact the *l*-*v* plot, making the determination of the exact morphology of the underlying feature somewhat ambiguous.

This method has been used with a variety of different tracers including H I (Burton & Shane 1970; Weaver 1970; Henderson 1977; Hartmann & Burton 1997; Kalberla et al. 2005), CO (Cohen et al. 1980; Solomon et al. 1985; Dame et al. 1986; Grabelsky et al. 1987; Dame et al. 1987, 2001), H II (Lockman 1979; Downes et al. 1980) and $C^{13}O$ (Stark & Lee 2006; Bally et al. 1987). One of the main advantages of using gas emission is that the intensity as a function of *l*-*v* can provide additional information, as opposed to say the position of discrete sources such as H II regions in *l*-*v* space. The structure of emission as a function of latitude can also provide information on the scale of specific structures, highlighting features that may otherwise be missed in an integrated map (e.g. Dame & Thaddeus 2011). Full surveys of the Galactic plane require large amounts of observing time, so it is more common to find studies concentrating on certain regions, such as the Galactic centre. A top-down map can be constructed from these *l*-*v* observations but will again require a Galactic rotation model .

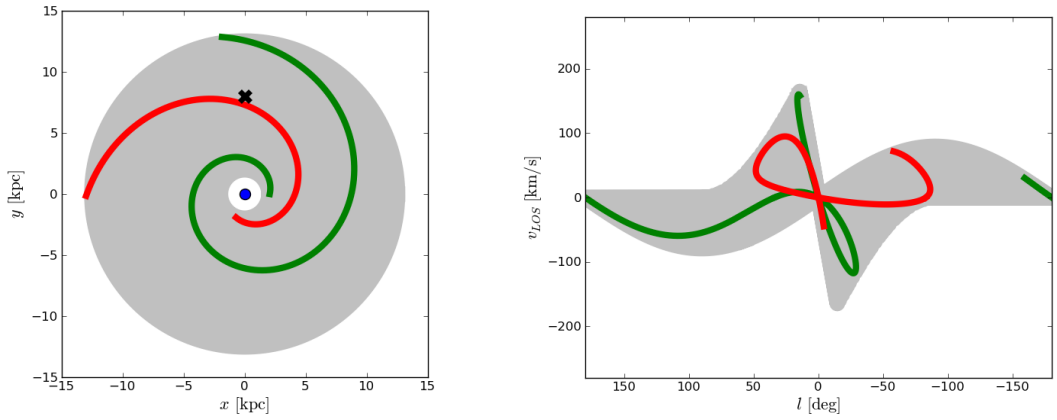

Figure 1.19: Projection of a Milky Way like disc and spiral arms from $x - y$ (left) onto $l - v$ (right) space using the rotation curve of the right panel of Fig. 1.7. The spiral arms appear as over-densities in $l - v$ space on the backdrop of the axisymmetric disc (shown in grey). Two spiral arms are shown, the arm in green has $\alpha = 13°$ and the red arm has $\alpha = 20°$, both are logarithmic in shape. The observer is placed at the black cross in the left panel with $l = 0°$ directed towards the Galactic centre.

As some of the results from the above methods are open to interpretation, numerical simulations are often used to attempt to reproduce the observations. If a model can be made that sufficiently reproduces the observations then the Galactic morphology underlying the model is a good representation of the Galaxy. This is in essence the approach adopted in this thesis, and will be discussed in detail later in this chapter.

1.6 Observational studies of Milky Way morphology

Many investigations into the structure of the Milky Way have been under-taken in the past half-century. While a combination of observational and computational studies have made progress by constraining arm and barred structure there is still no clear consensus on the Galactic morphology. The current best-guess is that the Milky Way is a four-armed spiral with a pitch angle of $10° - 20°$. The wide range of pitch angle depends on Galactic radius, with wider pitch angles inferred from the outer disc (e.g. Levine et al. 2006). There is however some support for a two-armed model, in which case the pitch angle is better fit by a much lower value. There is believed to be at least one inner bar, and some studies suggest a second with a different morphology and orientation. Finally some suggest a ring of molecular material may exist around $R = 5$kpc, though observational evidence could be due to an arm instead (e.g. Dobbs & Burkert 2012). In this section we will recount some of the major and more convincing evidence for these morphological features. For a more in depth take on all the studies in the literature the reader is directed to the works of Elmegreen (1985), Vallée (1995, 2002, 2005, 2008), Efremov (2011) and the proceedings of Benjamin (2008).

1.6.1 Structure: top-down reconstructions

Early investigations focusing on the distribution of hydrogen seemed to disagree from the outset. Weaver (1970) favoured a 2-armed, 12.5°structure in their analysis of H I, though this requires the existence of numerous spurs minor interarm features. However, the Parkes H I survey suggests a much tighter multi-armed structure (Kerr 1969a,b), with the singular agreement between these two studies being the positions of spiral tangents (Simonson 1970). The seminal ionised hydrogen maps of Georgelin & Georgelin (1976) (hereafter GG76) also favour a 4-armed spiral fit (of 12°), though largely based on kinematic distances. This model became the standard for the Galactic spiral map for some time, owing to the strong correlation of H II features with a spiral model (as opposed to H I maps at the time that often have a large amount of off-arm material). A variant of this model is shown in the left panel of Figure 1.20, showing the kink in the arms near the Solar position. Some studies even suggested a middle ground solution, such as the analysis of existing H I data in *l*-*v* space by Simonson (1976) who favoured a 2-armed 6-8° inner spiral branching into a 4-armed 16° spiral outside of the Solar circle.

The study of Caswell & Haynes (1987) finds that H II regions measured within $l = 0 - 180°$ are a reasonable match to the 4-armed model of GG76. Dame et al. (1986) find that measured CO cloud complexes within the first quadrant fit a multi-armed spiral structure with pitch angles between 5-12°. In another study of molecular clouds by Grabelsky et al. (1988) in the inner Galaxy, the authors determine that CO features are well matched by a single 10° logarithmic spiral, though their range of longitudes is somewhat limited. Worthy of note are the several studies that are not focused on various ISM gases. For instance, the works of Vallee (1988), Simard-Normandin & Kronberg (1980) and Han & Qiao (1994) use pulsar and extragalactic rotation measures[11] (RM) to discern the shape of the Galaxy's magnetic field. They tentatively show that the magnetic field is directed in a logarithmic spiral pattern, rather than a series of concentric rings, with Han et al. (1999) and Indrani & Deshpande (1999) specifically favouring a 4-armed spiral configuration. In a similar vein, Taylor & Cordes (1993) (hereafter TC93) construct a map of free electrons using the model of GG76, and show that using this they can obtain pulsar *dispersion measures* leading to pulsar distance measurements that are a very good match to actual measured distances, which in turn give further credibility to the 4-armed model. The spiral arm model adopted in their work superceedes that of GG76 as the literature standard for comparisons in other works, and is shown in the left of Figure 1.20 (see also Cordes & Lazio 2002 and Drimmel et al. 2003). An important point to note is that many studies of morphology are heavily influenced by the existing literature, for instance the TC93 model is a refinement of the GG76 model. In many cases studies will simply show a distribution is good by-eye match for the "standard" 4-armed case, with little consideration given to other possibilities. Amaral & Lepine (1997) use the positions of nearby open clusters to try and discern between a 2 and 4 arm structure. They find that a 2-armed (inner) superimposed on a 4-armed (outer) structure of 14°can match the positions and bridge the 2/4-armed discrepancies. Their modelling is only confined to the Solar neighbourhood however, and many clusters lie in the

[11] Rotation measures are a a radio astronomical tool for measuring the strength of magnetic fields. When light passes through a region with a non-negligible magnetic field the light becomes polarised. The effect of the light polarisation is proportional to the strength of the field along the line-of-sight, and the number density of free electrons: $\mathrm{RM} \propto \int n_e \vec{B} \cdot \mathrm{d}\vec{s}$.

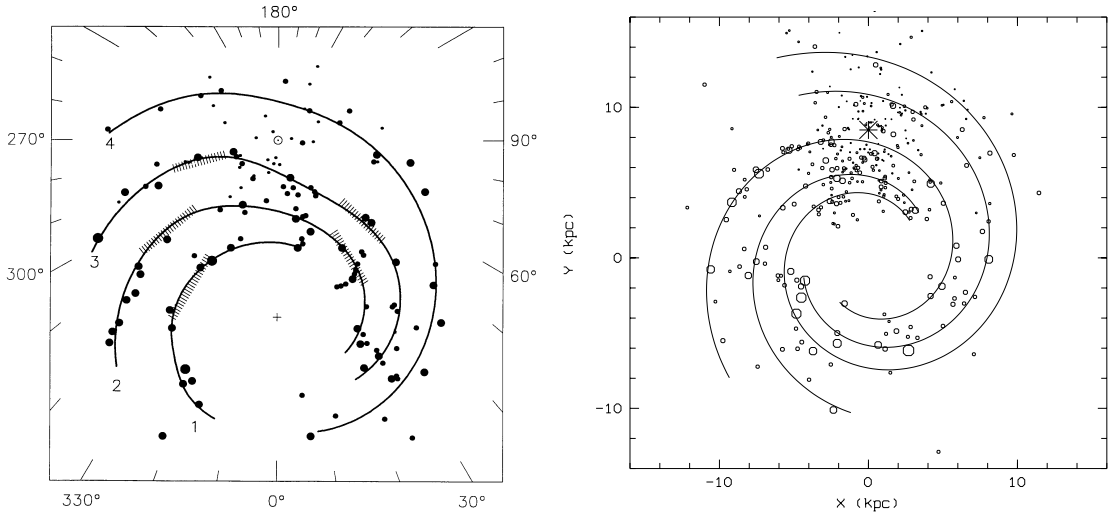

Figure 1.20: Two studies of distance determinations in the Galaxy. Left: H II regions mapped by Taylor & Cordes (1993) shown with a variant of the arm model of Georgelin & Georgelin (1976). Tangencies are shown as hatched regions. Right: star forming complexes (H II, CO, OB stars) mapped by Russeil (2003) with their best-fitting logarithmic spiral model.

interams of their best fit.

The works of Kolpak et al. (2003), Fish et al. (2003), Sewilo et al. (2004) Watson et al. (2003) and Paladini et al. (2004) measured the distances to several H II regions. The distance measurements of the three latter studies agree reasonably well with the 4 spiral arms of TC93. Yang et al. (2002) measure distances to a large number of CO sources, many of which correlate well with the nearby Sagittarius arm. Despite their large number of sources, few can be attributed to any other arm features, and their sample selection is biased against targets less than 5 kpc from the Galactic centre. The spatial distribution of high and low mass X-ray binaries studied by Grimm et al. (2002) shows while low mass binaries show no real preference towards any spiral pattern, the high mass binaries trace a 4-armed spiral pattern (be it that of TC93 or a simple symmetric 4-armed, 12°spiral).

Nakanishi & Sofue (2006) measure the H I distribution (in column density) throughout the galactic disc. They find that the distribution is in fact best described by a 3-armed logarithmic spiral, with pitch angles ranging from 7-18°. They find no evidence for the existence of the Scutum-Crux arm, or any strong H I emission 5 kpc from the Galactic centre. Using numerous H II complexes, Russeil (2003) perform a full fit to spiral arm parameters, and their data is shown in the right of Figure 1.20 with their best fitting model. A spiral pattern is clearly visible by-eye, and they find that a 2-armed model is insufficient to fit their complex distances. Their data seems to fit a 3 and 4-armed spiral reasonably well, with pitch angles around 11°. The main difference between their 3 and 4-armed fits is whether the Norma arm joins to the Cygnus or Perseus arm (see Fig.1.24). An important aside when viewing Figure 1.20 is that the spiral pattern is becoming less clear the more recent the study, and the more detail that becomes available. Specifically the distribution of sources < 3kpc from the Earth displays no clear structure, which explains the uncertainty in the Carina arm as $l \rightarrow 0°$ and the nature of the Local arm.

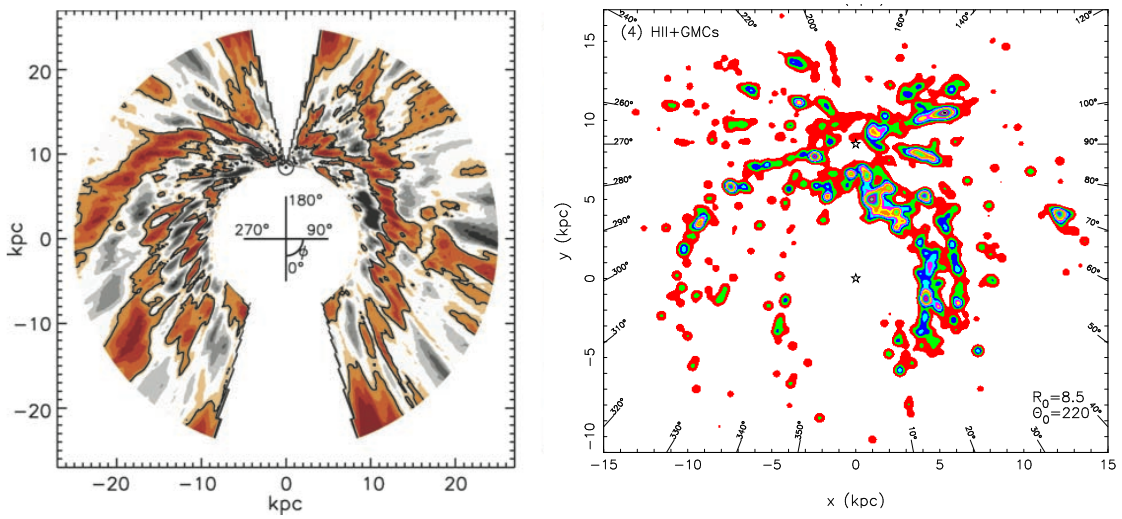

Figure 1.21: Two studies of Galactic kinematic distance determinations. Left: H I normalised surface density in the outer Galactic disc from Levine et al. (2006). Right: H II region and GMC distribution from Hou et al. (2009).

Levine et al. (2006) fit an asymmetric 4-armed spiral with $\alpha \approx 23°$ in their analysis of H I in the outer ($6 < R < 40$ kpc) Milky Way. A symmetric spiral model is investigated, but the H I in the fourth quadrant requires three arms of small separation. Their map is reproduced in the left of Fig. 1.21. The authors note the pitch angles are rather large compared to previous studies, and that this may indicate the arms are unwinding in the outer disc. Larger pitch angles in the outer galaxy compared to the inner galaxy have been suggested in previous studies (e.g. Simonson 1976). In more recent work by Hou et al. (2009) the authors fit different spiral arm models to H II and GMC literature data (right, Fig. 1.21). They find best-fitting values for α of approximately 5, 8, and 10° for 2, 3 and 4 armed models respectively, finding that the 2-armed model is a much poorer fit to the data. The distribution of CS mapped by Lépine et al. (2011) also provides a strong indication of spiral structure. They attempt to fit the actual orbital resonances that drive density waves, and fit a 4:1 box-like resonance to the inner 7kpc, which can produce a 4-armed spiral structure.

1.6.2 Structure: tangency profiles

Some of the most conclusive evidence of spiral structure comes from longitude maps with the use of the *COBE* and *Spitzer* satellites. Drimmel (2000) uses data from the DIRBE instrument aboard *COBE* to construct K-band and 240μm (dust) emission profiles for $|l| \leq 90°$, shown in the left of Figure 1.22 left (K: top, 240μm: bottom). The central peak is from the galactic bulge/bar and the global emission profile drops off in accordance to the Milky Ways exponential disc. The K-band emission shows weaker structure compared to dust emission but what structure is there is mirrored between the two. The authors indicate 5 prominent features labelled S_1, C_1, T, S_2 and C_2, with the S tangent points belonging to the Scutum-Crux arm, C belonging to the Sagittarius-Carina arm and the T point to the 3-kpc arm. The minor Orion arm can be seen at $l = 80°$ in the emission but it's strength is over-exaggerated due to it's close proximity. The K-band and 240μm emission have distinct differences. The most striking being the lack of any conclusive tangency features

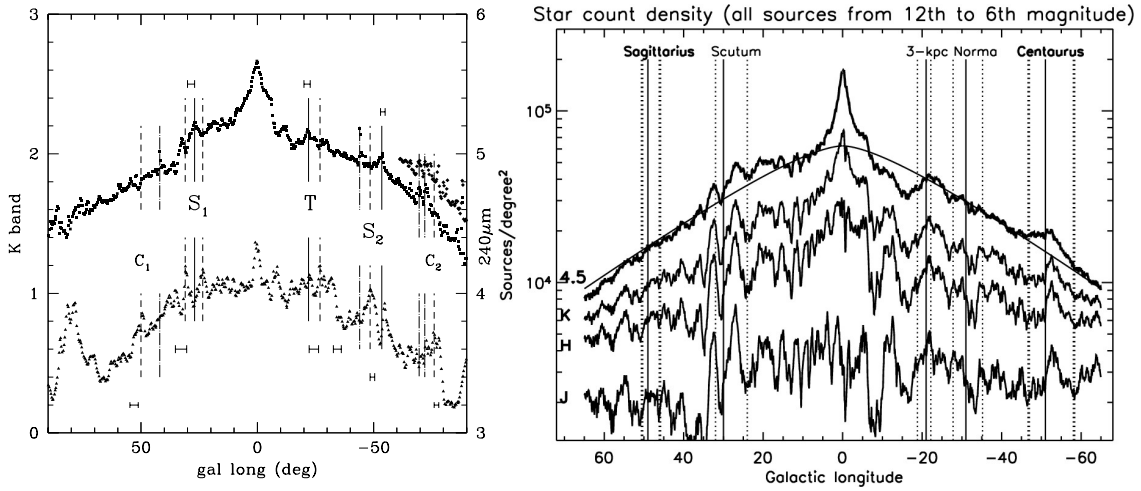

Figure 1.22: Two examples of Galactic arm tangency profiles. Left: *COBE*/DIRBE emission from old stellar population (K-band, top) and dust (240μm, bottom) from Drimmel (2000). Right: *Spitzer*/GLIMPSE source counts in the J, H, K and 4.5μm bands from Churchwell et al. (2009). Arm tangencies are indicated by vertical lines.

at 50° or −35° in K-band compared to 240μm. They infer from this that there exists only a two armed structure in the stars (seen in the K-band emission) joining with the bar. The gas/dust then forms a four-armed pattern in response to the two armed stellar potential. This interpretation has been suggested by numerous observations (e.g Drimmel & Spergel 2001; Benjamin 2008) and has been seen in hydrodynamical simulations (e.g. Englmaier & Gerhard 1999; Fux 1999; Martos et al. 2004). This also goes some way to explain the large ensemble of different arm combinations found in the literature; there could be two or four armed perturbations depending on the observation. A later study using *COBE*/DIRBE data by the same authors find similar conclusions (Drimmel & Spergel 2001). Their best fits to the emission in dust is a four-armed spiral, while the stars (K-J band) best suits a two armed fit.

The *Spitzer* GLIMPSE Legacy program is analysed by Benjamin et al. (2005) where the authors present similar maps to Fig. 1.18 of IR sources within $10° < l < 65°$ and $295° < l < 350°$ at 4.5μm. There are tentative signs of the Centaurus and Scutum arms but no sign of other arm tangencies. The real find however is signs of the galactic bar in their source counts. There is a strong asymmetry in counts around the Galactic centre, with 25% more stars in the first quadrant compared to the fourth inside of $l < 30°$ (Churchwell et al. 2009). This agrees with the general consensus that the Milky Way's bar is orientated between $15° - 30°$ which would show up in the count maps around $0 < l < 45°$ (Gerhard 2002). They then fit to the bar's orientation and length, finding a value of 44° and a length of around 4.5kpc. Churchwell et al. (2009) also use the GLIMPSE survey to highlight spiral arm tangents in 4.5μm, K, J and H bands (shown in the right of Figure 1.22). The Scutum, 3kpc, and Centaurus arm tangents can be seen clearly in all bands but there is no clear sign of the expected Sagittarius tangency.

Steiman-Cameron et al. (2010) analyse the C II (158 μm) and N II (205 μm) lines from the FIRAS instrument onboard *COBE*, which are known to trace spiral structure to greater densities and pressures. They find strong tangent signatures of the Scutum, 3kpc, Centaurus, Carina, Sagit-

tarius and Orion arm features. By fitting logarithmic spiral models they find a four-arm pattern fits the data well. As N II and C II should trace gaseous and young stellar/star forming regions they conclude that the Milky Way is four armed in the gas, and agree with Drimmel (2000) and Churchwell et al. (2009) that the older, evolved, stellar population (i.e. K and M stars) exist in a two armed pattern. This is supported by evidence that over the many arm models over the past decades almost all tracers of young stellar populations and gas are best fit with four armed models (e.g. H II, CO, OB stars, molecular clouds, Cephids, C II and N II). On the contrary the majority of two armed models from the literature stem from observations of the older stellar population, i.e. K and M stars (Steiman-Cameron et al. 2010).

1.6.3 Structure: longitude-velocity maps

There have been numerous *l*-*v* maps constructed in the literature, predominantly using CO and H I emission (e.g. Dame et al. 1987; Hartmann & Burton 1997; Strasser et al. 2007; McClure-Griffiths et al. 2012). Two modern maps of ISM emission over the entire Galactic plane are shown in Figure 1.23. These are the H I 21-cm emission from Kalberla et al. (2005) and the CO $J = 0 \rightarrow 1$ emission from Dame et al. (2001). While higher resolution data is available for both tracers, these are the most up-to-date maps available of the *entire* plane. Spiral arm features can clearly be seen in each map, with the Perseus, Outer and Carina arms being the clearest. The Sagittarius and Local arms are less clear, the former due to the mixing with the large amount of emission towards the Galactic centre, and the latter due to the ambiguous nature of local structure ($v_{los} \approx 0\,\mathrm{km\,s^{-1}}$). There are some key differences between the two. The CO is much patchier than the H I, while the H I appears less confined to spiral arms and extends much further radially than CO. The CO displays a strong inner feature, dubbed the central molecular zone (CMZ). Asymmetric in nature, it is believed to be product of the ILR of the bar (Lee et al. 1999; Rodriguez-Fernandez & Combes 2008). There is a strong feature approximately diagonal in the CO emission in Fig. 1.23 in the inner Galaxy, that is not as distinct in the atomic emission. This has been attributed to a molecular ring of material around 4kpc in radius (Marshall et al. 2009). While rings are not uncommon in external galaxies, no substantial evidence exists that shows the feature can be better fit by a combination of arms rather than a ring (Dobbs & Burkert 2012). We will refer to this feature as the Inner Ridge of emission, as to not imply its structure as a ring or arm.

One of the more difficult tasks when determining the spiral structure of our Galaxy is detecting spiral arms beyond the Galactic centre, due to the large amounts intervening ISM dust and the strong emission towards the galactic bulge. Dame & Thaddeus (2011) find a Galactic arm beyond the galactic bulge in CO and H I *l*-*v* maps, its existence unnoticed due to it's location 3°above the galactic plane. They suggest that this new arm is an extension of the Scutum-Centaurus arm beyond the Galactic centre, an analogue to the Perseus arm, which the authors suggest supports the 2-armed picture proposed by Drimmel (2000) and Churchwell et al. (2009). Similar earlier work by the same authors (Dame & Thaddeus 2008) discovered a far counterpart to the nearby 3kpc arm in CO *l*-*v* data, further supporting a symmetric Milky Way model.

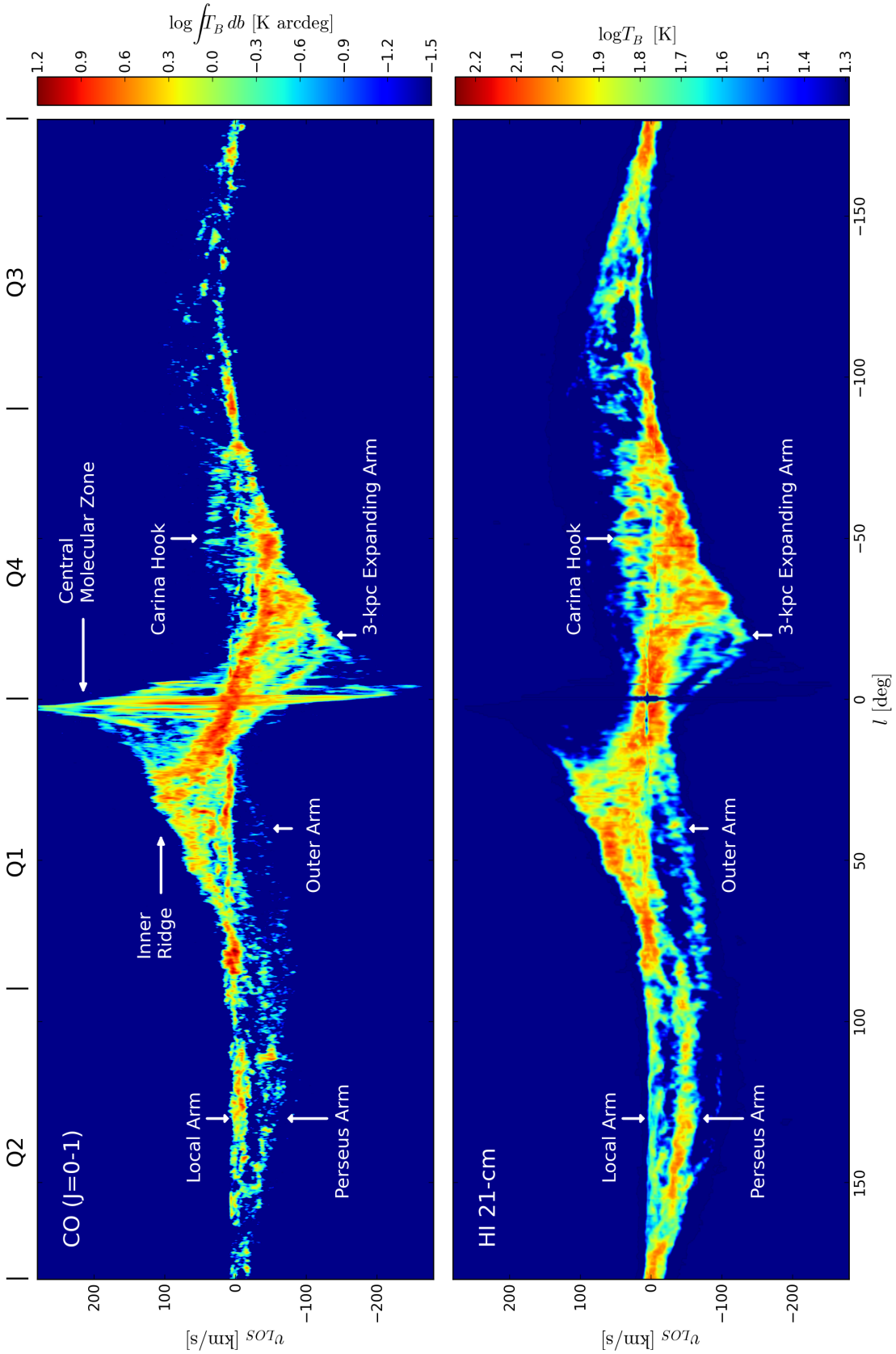

Figure 1.23: Brightness temperature emission maps of the Galactic plane in CO ($J = 0 \rightarrow 1$ transition, top) and H I (21-cm transition, bottom). H I data taken from Kalberla et al. (2005) and CO from Dame et al. (2001). Also labelled are a selection of morphological features. Due to the significantly weaker emission of the CO line, we have integrated through $b \pm 2°$.

1.6.4 Structure: the bar(s)

Specifically regarding the bar, evidence of its morphology is perhaps even less convergent than the arms. The bar appears either short and spheroidal or long and thin. The former bar is the classical bar, in that evidence for which has existed for many decades. This bar is angled at roughly 20° to the Sun-Galactic centre line and is approximately 3kpc long. This bar is commonly referred to as the *COBE*/DIRBE bar due to the most convincing evidence coming from *COBE* source counts (Blitz & Spergel 1991; Dwek et al. 1995). It is also believed to be the cause of asymmetries seen in the velocity distribution of ISM gas. The bar is also referred to as the triaxial bulge or the boxy/bulgey/peanut bar due to the shape of the best fitting mass models. See Blitz & Spergel (1991); Weiland et al. (1994); Binney et al. (1997) and the review by Gerhard (2002) for more information.

The other, "Long", bar was originally proposed by Hammersley et al. (2000) and additional evidence for which was seen in GLIMPSE data (Benjamin et al. 2005; Churchwell et al. 2009). This bar is believed to be longer ($\approx$ 4kpc) and thinner than the DIRBE bar, and much less vertically extended. The GLIMPSE data suggests the bar is angled at approximately 45°, though studies are still in their infancy in discerning whether these bars are indeed separate entities (the orientations agree within errors reported by respective studies). Regardless of which shape the bar takes, it is still unclear whether the arms join exactly to the ends of the bar, or whether there is some contact region, perhaps indicated by a ring (both cases are seen in external galaxies). There is evidence, however, that the bar does drive some spiral structures in the disc. The near 3kpc expanding arm, so named for the velocities that significantly deviate from circular rotation, has been reproduced by Englmaier & Gerhard (1999) by the inclusion of a bar, where the arm is seen to directly trail from the bar end.

1.6.5 Pattern speeds

As with external Galaxies, determining the arm and bar pattern speeds (Ω_{sp} and Ω_b) of the Milky Way is somewhat more difficult than determining the structure due to observations only probing a very small time window with respect to Galactic rotation periods. Determining the pattern speed also usually relies on some assumed morphology. For example, if the method uses the location of resonances to determine the pattern speed, these are dependant on the arm number adopted. The rotation speed of the arms is of specific interest for its creation of a co-rotation radius. Many models place the Solar position at the CR, which could in theory be a site for steady star formation due to material co-rotating with the high densities arms found in arms, though it could lessen its importance due to the lack of shocks experienced by the traversal of gas into the arms initially. An important aside is that for many of these pattern speeds the value is coupled to the local radius and circular velocity. This in itself is subject to uncertainty, with values of the Earth's Galacto-centric distance ranging from 7.0-8.5kpc and velocity from 200-230 $\mathrm{km\,s^{-1}}$(Binney & Tremaine 1987; Reid 1993).

A common method is that of Tremaine & Weinberg (1984), where the pattern speed is calculated from integrating specific velocity components across the disc. This method is designed

for external galaxies, but can be applied to the Milky Way. By applying this method to stars in our own Galaxy, Debattista et al. (2002) find a pattern speed[12] of 60km s^{-1} kpc^{-1}. However, this is simply attributed to a non-axisymmetric feature, which while seemingly reasonable for the bar, could be from the arms themselves.

By measuring the ages of open clusters, which are assumed to have been created in spiral arms, and rotating them backwards in time it is possible that they trace out spiral arms at their birthplaces. Dias & Lépine (2005) use this method give a constant value of 25km s^{-1} kpc^{-1}, though this is only for clusters near the Solar position and has additional errors associated with the age determinations of the clusters. Another method is to model the kinematics of OB and Cepheid stars, which can be constructed to contain a spiral perturbation with numerous free parameters, including the spiral pattern speed. Applications of this method suggest the arms are rotating with a speed of 22-30km s^{-1} kpc^{-1}(Avedisova & Palous 1989; Amaral & Lepine 1997; Mishurov & Zenina 1999; Fernández et al. 2001; Lépine et al. 2001).

The bar pattern speed can be estimated by use of Equation 1.10 and measuring the bar length though distance determinations. This method requires the bar length to be well measured, and that the CR lies exactly at the bar end, which is somewhat of an approximation. This method can give a wide range of bar pattern speeds from 35-60km s^{-1} kpc^{-1}(see Gerhard 2011).

Pattern speeds can also be measured by use of a stellar steaming method (Dehnen 2000; Quillen & Minchev 2005; Minchev et al. 2007). By measuring the tangental and perpendicular velocity components to a circular orbit in the Solar vicinity ($u - v$), and creating so-called velocity ellipsoids, models can be constructed to replicate the features. The pattern speed directly impacts the features seen in these ellipsoids, though it is not clear how to differentiate between the effect of the bar or the arms. Dehnen (1999) and Minchev et al. (2007) find approximate pattern speeds of 50km s^{-1} kpc^{-1} by inferring the position of the OLR.

One interesting method is to use ice age epochs here on Earth to determine the time of spiral arm passage. Ice ages correlate with cosmic ray strength. As the Earth passes into and out of a spiral arm, it experiences a differing amount of Galactic cosmic rays due to the greater net supernovae flux in the arm regions. Therefore peaks in cosmic ray fluxes are inferred as corresponding to Earth's passage through spiral arms, which allows for an estimate of arm pattern speed. Shaviv (2003) and Gies & Helsel (2005) use this method to infer an arm pattern speed of 14-17km s^{-1} kpc^{-1}.

It is somewhat more straightforward, if more time-consuming, to simply tailor numerical simulations to observations and thus infer the corresponding pattern speed (e.g. Rautiainen et al. 2008). This is simple to do for external galaxies, where the radial extent of features is expected to enclosed by the ILR/OLR which are in turn a direct result of the pattern speed. However, for the Milky Way this is again more complicated, and simulations must be tailored to some other observational constraint such as Oort constants, rotation curve, or l-v data. Modelling of velocity field by Chakrabarty (2007) suggest 58km s^{-1} kpc^{-1} for the bar, and find the arm speed is less well constrained. Modelling of the spiral and bar component and constraining to the l-v plot,

[12]The pattern speed is often in units of km s^{-1} kpc^{-1}, despite it being an angular frequency. 1km s^{-1} kpc^{-1} is equivalent to 0.001rad Myr^{-1}.

Bissantz et al. (2003) find a best fit bar speed of 60km s^{-1} kpc^{-1} and arm speed of 20km s^{-1} kpc^{-1}, though this is only done so for the inner disc ($R < 7$kpc). Simulations of gas flow inside a 2-armed potential by Martos et al. (2004) using a fine grid of pattern speeds find that 20km s^{-1} kpc^{-1} provides good dynamical consistency. Englmaier & Gerhard (1999) perform hydrodynamical simulations looking into the effect of different bar pattern speeds. They tend to favour values from 50-60km s^{-1} kpc^{-1}, corresponding to a bar co-rotation radius near 3.5kpc. They also include an armed potential, but assume it rotates with the bar. Fux (1999), Weiner & Sellwood (1999) and Rodriguez-Fernandez & Combes (2008) perform hydrodynamical simulations in the presence of a bar perturbation and attempt to match features in *l*-*v* observations. Collected together their best-fitting values span a wide range, with orientations of 20-40°and pattern speeds ranging from 30-50km s^{-1} kpc^{-1}.

In most of studies the arms and bars have been found to be rotating at very different pattern speeds, with the bar rotating up to three times as fast as the arms. This brings into question just how the two are related. If there are two distinctly different pattern speeds, then the arms need not necessarily be attached to the end of the bar. Indeed, this is not always the case in external galaxies also (e.g. NGC 1073, NGC 4548, NGC 5383). While there is some evidence for distinct pattern speeds in simulations (Sellwood & Sparke 1988) and external galaxies (e.g. Rautiainen et al. 2008; Gabbasov et al. 2009), if the pattern speed is measured as a function of radius it has been seen to be decreasing towards the outer disc (i.e. behaving as material arms) in some external galaxies (e.g. Speights & Westpfahl 2012; Meidt et al. 2008) and simulations (Grand et al. 2012; Baba et al. 2013). Needless to say, the true nature of arm and bar structures, including their origin, longevity and rotation rate, is still somewhat of an unknown.

1.7 Summary of Galactic structure

As can be seen by the previous sections, there is beginning to emerge some consensus on the spiral/bar structure, though there is still plenty of room for interpretation. With recent works there has emerged the idea that a 2-armed in stellar distribution could be driving 4-armed features in the gas, which goes some way of explaining the 2/4-armed dichotomy in the literature. The values of the arm pitch angles seem to lie between 10° and 25°, with the standard value approximately 13°. To put this into a galactic perspective, the pitch in external galaxies range from 4°to 20°, with Sa galaxies having a mean pitch angle of 6°whereas the Sc galaxies have a mean pitch angle of 18°(Russeil 2003). Studies of local material however tends to be highly dispersive, with a large amount of material lying away from spirals arms in the models. This could be because the Local arm is a separate entity to a grand design structure, or it could be that the Galaxy is better represented by a flocculent disc. Spirality appears to extend from $3 < R < 15$kpc, with the pitch angle potentially increasing in the outer disc. At least one bar appears present in the inner disc, but the already uncertain length, orientation, and rotation speed are only complicated by the suggestion of a second bar.

The pattern speeds of the arms and bar are also uncertain, though rough consensus tends to be that each rotates with a different speed. Past studies suggest arms in the outer disc appear to

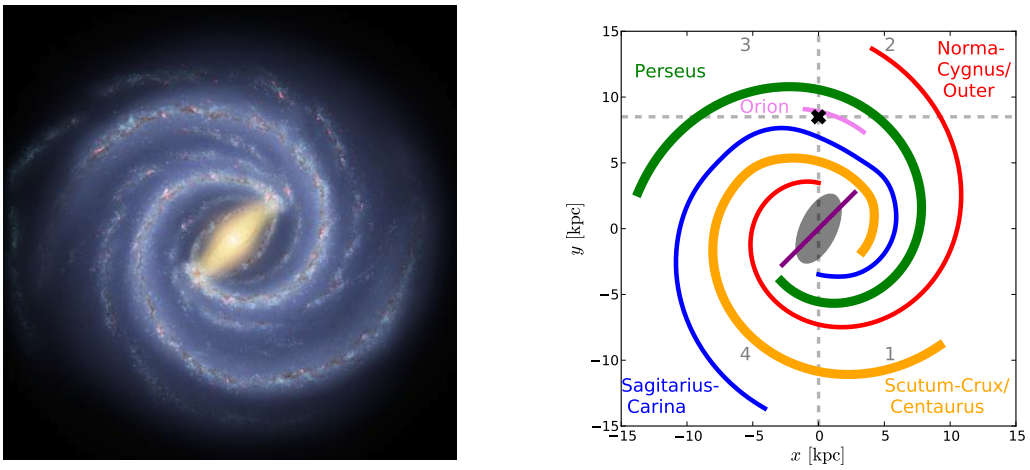

Figure 1.24: The current "standard" Milky Way morphology. The left panel shows an artist impression presented in Churchwell et al. (2009). The right panel is a schematic representation, showing locations of the primary spiral arm and bar features. The thick arms are stellar arms in 2:4, star:gas arm models and the thinner arms those primarily seen in gas. Two inner bars are shown, the spheroidal "boxy/peanut" bar ($\theta_b \approx 20°$) and the "Long" bar ($\theta_b \approx 45°$).

rotate about a third of the rate of the inner bar, though these values have large uncertainties.

The current "standard" artist interpretation of the Milky Way is shown in the left panel of Figure 1.24 taken from Churchwell et al. (2009). Beside which is a simple schematic of the arm and bar structures, modelled after a similar diagram in Benjamin (2008). The approximate locations of the four primary spiral arms are shown, with the density higher in the Scutum-Crux-Centaurus and Perseus arms compared to the others. In the centre the two possible bars are shown with differing orientation and lengths. Collating all of this together, the Milky Way is likely a SAB galaxy, similar in nature to NGC 1232, NGC 2336 and M61, which are each shown in Figure 1.25 for comparison. However, the reader must keep in mind that the evidence of the previous sections is effectively all that stands behind the illustration in Figure 1.24. It still seems like somewhat of a leap from the data in Figures 1.20, 1.21 and 1.22 to Figure 1.24.

1.8 Thesis aims

We propose to lift the veil on some of this confusion by performing a study to reproduce the *l*-*v* features of our Galaxy using numerical simulations of the Galactic ISM. The *l*-*v* distribution is unique in that it enables the tracing of spiral features separately without having to perform difficult distance determinations. A simulation is ideal as it contains all the spatial information, enabling for the simple reconstruction of a top-down distribution. We choose to primarily concentrate our efforts on reproducing the CO distribution, rather than H I, as it is a stronger tracer of spiral features, appearing in much denser regions of the ISM. While a similar approach has been attempted by some studies in the past, none has attempted to fully model all arm and bar parameters in depth, instead usually concentrating on constraining one or two values (e.g. bar pattern speed and orientation). We also utilise a radiative transfer scheme and chemical network to more closely model

Figure 1.25: A collection of Milky Way analogues from various sources. Note the multi-armed structure and short inner bar. UGC 12158 in Fig. 1.4 is also such a galaxy. Images are, from left, NGC 1232 (credit: ESO/IDA/Danish 1.5 m/R.Gendler & A. Hornstrup), M61 (credit: R. Gendler & R. Hannahoe) and NGC 2336 (credit: A. Block/Mount Lemmon SkyCenter/University of Arizona) inclined at approximately 60°.

the ISM emission.

There have been a number of previous numerical works aiming to reproduce *l*-*v* features. Lee et al. (1999) and Weiner & Sellwood (1999) observe the effect of a barred potential on a gas disc in the inner Galaxy, and projecting the gas particles into *l*-*v* space to match the observations. Similarly Rodriguez-Fernandez & Combes (2008) compare the *l*-*v* features of a number of bar models to observations, instead concentrating on matching the terminal velocity curves in the inner Galaxy. Bissantz et al. (2003) use arm and bar potentials to match *l*-*v* data, specifically investigating pattern speeds of each component. Baba et al. (2010) instead use the effect of an *N*-body model on a gas disc to match *l*-*v* features, varying the location of the observer somewhat in a single model. A key difference to our approach is to take into account the optical depth effects of the ISM by the use of a radiative transfer code. The aforementioned attempts at reproducing *l*-*v* structures simply re-project the positions and velocity of the gas into *l*-*v* space, taking no account of the relative strength of these features. The addition of a chemical network also allows for a direct tracing of CO gas, rather than simply assuming that high gas density corresponds to emission features in *l*-*v* space as done by the above studies. Previous studies also tend to focus on a single aspect of the Galaxy, such as pattern speed, or bar orientation. We instead aim to match all primary morphological features of the Milky Way; arm number, patterns speeds, pitch angles, bar orientations and allow for a variable observer position within the disc to thoroughly investigate the possible models. This requires a large number of models compared to the studies mentioned above, and at a reasonable resolution to allow for the sufficient formation of molecular gas.

Some key questions we intend on answering with this approach are:

- Can we create synthetic molecular emission maps of our own Galaxy sufficient for the purpose of constraining morphology?
- Can a grand design spiral perturbation sufficiently reproduce the observed features in *l*-*v* space (using a fixed potential)?
- Is a 2-armed structure sufficient to reproduce all the features, or is a 4-armed model needed?

- Does a 2-armed stellar distribution produce a 4-armed gas morphology sufficient to match *l*-*v* features?
- Can instead a transient spiral structure better fit the observations (using an *N*-body stellar system)?

While a full reproduction of all of the features seems unlikely due to the simplifications needed in any such treatment of a galactic-scale system, this thesis aims at narrowing the parameter space describing the morphology of the Milky Way, and eliminate some of the confusion in the many different, seemingly conflicting, paradigms.

The following chapters will be as follows. Chapter 2 will discuss the simulation technique and ISM specific physics required to model the molecular component of the Milky Way. Chapter 3 presents the results of simulations using fixed potentials for the arms and bar, and a simple method of addressing the uncertainty in the Earth's position and velocity. Chapter 4 describes the method of creating synthetic observations and the application to the calculations in the previous chapter, and the resulting best fit barred-spiral model of the Galaxy. Chapter 5 presents a similar study to that of the previous two chapters, but instead using an *N*-body prescription to model the stellar component of the Milky Way, rather than using fixed analytic potentials. We finish in Chapter 6 with a discussion of future work and conclusions to the work presented in this thesis.

2

Numerical methods: simulations with smoothed particle hydrodynamics

"...and one has to resort to the indignity of numerical simulations to settle even the simplest questions... "
– Philip Anderson, Nobel Lecture, 1977

2.1 Introduction

In order to construct synthetic Galactic observations we first need to generate the physical conditions from which to build them. Numerical simulations presented in this thesis are performed using the *smoothed particle hydrodynamical* technique, or SPH, where the fluid is decomposed into discretised packets, or *particles*. This chapter presents an overview of the SPH method and codes used throughout this thesis. We begin with a discussion of the basic principles, including some simple tests of the codes, in Section 2.2. We then discuss the additions to allow for the study of ISM scale physics in Section 2.3. This includes additions to the standard energy evolution to allow for ISM heating and cooling, and the various chemical processes needed to track the Galactic molecular content. Two existing SPH codes are used in this study, the structure of each and the developments made for the work in this thesis are discussed in Section 2.2.12.

These codes and techniques will be utilised in simulations using both fixed analytic stellar potentials and live stellar systems, presented in Chapters 3, 4 and 5.

2.2 Smoothed Particle Hydrodynamics

The problem of simulating fluid motion is by no means a new one. Clearly the fluid cannot be simulated on a point mass level, molecule-by-molecule, so some large scale discretisation must be used. The two main techniques are to either evolve the flow of packets of the fluid in a Lagrangian prescription, or to measure the flow of fluid though a static or adaptive grid in a Eulerian sense. These methods include Eulerian grid based method such as adaptive mesh refinement, or AMR, codes (e.g. FLASH, Fryxell et al. 2000; RAMSES, Teyssier 2002; ENZO, Bryan et al. 2014), Lagrangian particle based methods such as smoothed particle hydrodynamics, or SPH, codes (e.g. GADGET, Springel et al. 2001; GASOLINE, Wadsley et al. 2004; SEREN, Hubber et al. 2011) or some intermix of the two such as moving mesh codes (e.g. AREPO: Springel 2010a). While each has its own merits, no clear consensus has been reached as to whether there is a single method that outstrips the others in every regard, though numerous studies have focused on comparing the different techniques (e.g. Agertz et al. 2007, Tasker et al. 2008, Price & Federrath 2010), with a large number specifically focussing on comparisons in a cosmological context (e.g. Frenk et al. 1999, Thacker et al. 2000, O'Shea et al. 2005).

In this thesis simulations are performed using the SPH method, specifically using the codes PHANTOM (Price & Federrath 2010) and SPHNG (Bate et al. 1995) the details of which will be discussed in greater detail later in this chapter. The SPH method was first formulated by Lucy (1977) and Gingold & Monaghan (1977). The crux of the method is to discretise a fluid into a finite number of mass elements with variable density, i.e. volume. The density of a particle is calculated by interpolation between neighbouring particles, normalised by some smoothing function known as the smoothing kernel function, $W(r)$, that decreases in magnitude with increasing distance from the particle of interest.

In the 40 years since its conception the SPH method has evolved considerably. While today it is arguably most well know for its application in the field of cosmology it has been applied to numerous media both in and out of astrophysics (e.g. the study of accretion discs, planet and star formation). As such there are numerous additional physics that have been added to study different problems, including magnetic fields, radiative transfer and relativity. Further information on these improvements, as well as the basics of SPH can be found in the reviews of Price (2012a), Rosswog (2009), Monaghan (1992, 2005) and (Springel 2010b). As with any numerical method, there are key benefits and detriments of SPH. Some, but certainly not all, of these are highlighted below in particular in comparison to grid-based methods.

Advantages

- SPH is usually boundless, so no matter is lost or forced back into the simulation at domain boundaries thereby inherently conserving the mass of the system.
- The code spends its time evolving only the regions with a non-zero density field, so no time is wasted modelling empty space as in grid codes.
- The adaptive resolution (both spatially and temporally) are relatively easy to implement, i.e.

no need to re-create/adapt meshes as in grid-based codes.

- The fluid evolution history is intrinsically simple to trace due to the particle-like nature. This would require the inclusion of tracer particles in grid-based codes to follow the fluid flow.
- SPH is comparatively simple and easy to model complex physics and geometries in 3D, due to free/moving material boundaries.
- Particle nature makes coupling to N-body or self-gravity physics relatively straight-forward.
- The distribution of mass between particles ensures exact conservation of mass, as the mass of each particle is constant throughout time.

Disadvantages

- Need to build and constantly update neighbour lists (by link-lists or binary trees) in order to evaluate particle summations.
- The initial conditions can be influential on the eventual outcome. Need to decide on whether to set particles on a cubic, hexagonal or random lattice arrangement initially.
- Resolution is limited by particle number, which is fixed at the start of the simulation, whereas in theory a grid can be sub-divided indefinitely.
- Radiative transfer and magnetohydrodynamics can be more difficult to implement than the cell structured nature of grid-based codes.

2.2.1 Equations of fluid dynamics

Throughout this chapter we will be referring to numerous standard formulae to derive and explain the SPH equations. We include these here briefly for reference before continuing. SPH is a Lagrangian fluid formulation by design, where the Lagrangian itself takes the classical form

$$L = T - V = \int \left(\frac{1}{2}\rho v^2 - \rho u \right) d\vec{r}, \tag{2.1}$$

which is simply the difference between the kinetic and thermal potential energy, T and V respectfully (neglecting gravity for now), where ρ, u, v and $\vec{r}$ are the density, internal energy, velocity and position of a fluid element. We can minimise the action of the Lagrangian to give the Euler-Lagrange equations of fluid dynamics

$$\frac{\partial L}{\partial \vec{r}} - \frac{d}{dt}\frac{\partial L}{\partial \vec{v}} = 0, \tag{2.2}$$

which can be used with an appropriate Lagrangian to obtain the equations of motion (EoM) of the fluid system. We will also be making use of the material, or Lagrangian, derivative which is given by

$$\frac{D}{Dt} = \frac{\partial}{\partial t} + \vec{v} \cdot \vec{\nabla}, \tag{2.3}$$

where the first derivative is the local rate of change (i.e. the Eulerian derivative), and the second the convective derivative. We will also utilise the Navier-Stokes equations for fluid flow (a.k.a. the Euler equations) given by

$$\frac{D\vec{v}}{Dt} + \frac{\vec{\nabla}P}{\rho} + \vec{f_{visc}} + \vec{f_{ext}} = 0, \tag{2.4}$$

where $\vec{f_{visc}}$ contains all the physical viscosity information and may also contain extra magneto-hydrodynamical (MHD) terms. For gravitational external forces $\vec{f_{ext}} = -\vec{\nabla}\Phi$, where Φ is the external potential. In the work presented here Φ comes from galactic potentials we impose, which are related to the density distribution by Poisson's equation, $\nabla^2\Phi = \rho_{ext}(\vec{r})4\pi G$. The material derivative is effectively Newton's second law for a fluid. Built into any numerical fluid simulation should be the continuity equation, which ensures mass conservation in the system

$$\frac{\partial\rho}{\partial t} + \vec{\nabla} \cdot (\rho\vec{v}) = \frac{\partial\rho}{\partial t} + \vec{v} \cdot \vec{\nabla}\rho + \rho\vec{\nabla} \cdot \vec{v} = \frac{D\rho}{Dt} + \rho\vec{\nabla} \cdot \vec{v} = 0. \tag{2.5}$$

And finally we will also use the first law of thermodynamics. For an adiabatic ($dQ = 0$) equation of state (EoS) we have $dU = dQ - PdV = Pd\rho/\rho^2$, giving the rate of change of internal energy as

$$\frac{Du}{Dt} = \frac{P}{\rho^2}\frac{D\rho}{Dt}. \tag{2.6}$$

where specific internal energy is $u = U/m$. Between these formulae we have a framework to evolve a fluid system over time, tracing changes in velocity, internal energy and position ($d\vec{r}/dt = \vec{v}$) while maintaining mass conservation by satisfying Equation 2.5. We can also calculate the total energy simply by the addition of the internal to the kinetic energy, $e = u + v^2/2$.

2.2.2 The SPH kernel

The kernel function is a key parameter of SPH, and defines how much we care about particle neighbours when calculating fluid properties, akin to a window function. It effectively puts the "smooth" in SPH, and makes sure particle properties are smoothly interpolated from neighbouring particles. The kernel is defined by some scale length/smoothing length/kernel support radius, h, which determines the rate of radial decay. Two basic properties of an appropriate kernel are that it is correctly normalised

$$\int W(|\vec{r} - \vec{r}'|, h)d^3\vec{r}' = 1, \tag{2.7}$$

and that it tends to a delta function as the kernel support radius tends to 0

$$\lim_{h\to 0} W(|\vec{r} - \vec{r}'|, h) = \delta(\vec{r} - \vec{r}'). \tag{2.8}$$

The kernel is chosen to be spherically symmetric so that the system is independent of rotation, and to be only a function of separation, rather than actual particle position. We can first define a property of the system, $A(\vec{r})$, using the delta function by

$$A(\vec{r}) = \int A\delta(\vec{r} - \vec{r}')d^3\vec{r}'. \tag{2.9}$$

We can then approximate this expression with our kernel function to give the integral interpolation approximation

$$A(\vec{r}) = \int A(\vec{r}\,')W(|\vec{r} - \vec{r}\,'|, h)d^3\vec{r}\,', \tag{2.10}$$

where the parameter A is integrated over all other fluid elements at positions $\vec{r}\,'$. This would produce $A(\vec{r})$ exactly when the kernel is the delta function. For practical purposes the above integral is formulated into a summation over a set of interpolation points throughout the medium, the SPH particles. This then means we can estimate A for some particle at $\vec{r}$ by a weighted sum of that same A evaluated at every other particle at $\vec{r}\,'$. We can replace the volume integral for a mass integral, as in the usual construction of SPH we know the mass of each particle, so that Equation 2.10 becomes

$$A(\vec{r}) = \int \frac{A(\vec{r}\,')}{\rho(\vec{r}\,')}W(\vec{r} - \vec{r}\,', h)\rho(\vec{r}\,')d^3r' = \int \frac{A(\vec{r}\,')}{\rho(\vec{r}\,')}W(\vec{r} - \vec{r}\,', h)dm \tag{2.11}$$

we can then form a discretised version, by a summation interpolation using particles as our interpolation points. This gives a sum over b particles at positions $\vec{r}\,'$

$$A(\vec{r}) = \sum_b m_b \frac{A_b}{\rho_b} W(\vec{r} - \vec{r_b}, h) \tag{2.12}$$

where m, ρ are the particles' mass and density respectively. These leads to a way of calculating some property of the system, A, at any given point by summation over discretised fluid elements. For instance, we can find the density simply by substituting $A(\vec{r}) \rightarrow \rho(\vec{r})$ to give the standard SPH density summation equation

$$\rho(\vec{r}) = \sum_b m_b W(\vec{r} - \vec{r_b}, h). \tag{2.13}$$

In replacing the integral with summation expressions (Equations 2.10 and 2.12) with have introduced some discretisation/sampling error of the order h^2 (Monaghan 1992, 2005), which depends on particle disorder and is reduced by increasing the number of particles (Price 2005). There is also an error associated with the initial introduction of the integral interpolation Equation 2.10 (Monaghan 2005; Liu & Liu 2010) which is also of order h^2, which is reduced by decreasing the smoothing length (evident by Equation 2.8). This would lead to the conclusion of using a high number of particles that are well ordered and a kernel with a small smoothing length to reduce errors. However this would increase computational time-scales, requiring a give-and-take approach between reducing errors and optimising calculation times (Cossins 2010).

By using Equation 2.13 we have the capability to calculate the density of the fluid at any arbitrary point by summing over the kernels of the neighbouring particles. This is illustrated by the cartoon in Figure 2.1. We shall show later in this chapter that this approach can be used to calculate other properties of the system, specifically the forces and internal energies of the particles. But first we turn our attention to the actual form of the kernel function.

Ideally an appropriate kernel must have several properties, in addition to those of Equations 2.7 and 2.8. The kernel should be "bell-shaped" (Lucy 1977) so that the kernel smoothly decreases with distance but also flattens near the centre to avoid steep gradients for particles in close proxim-

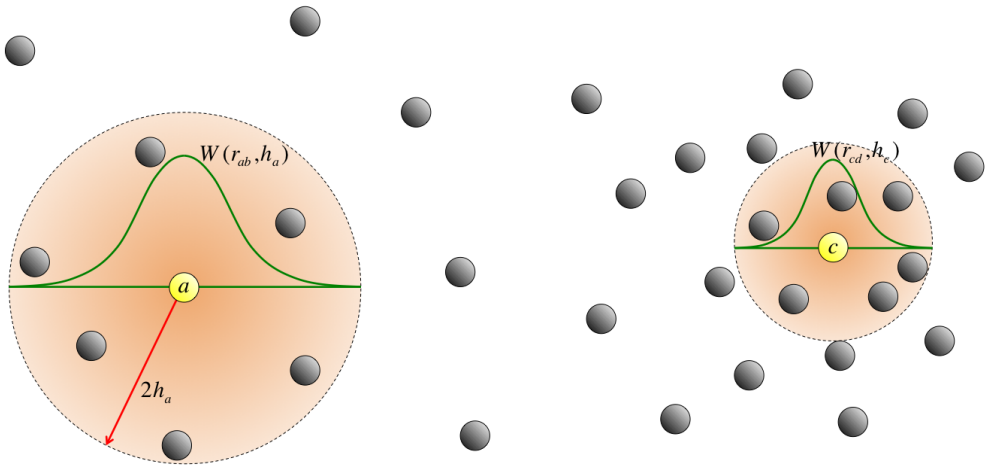

Figure 2.1: Simple schematic of how to visualise SPH particles. Density is calculated by summing over neighbours, with masses weighted by some smoothing kernel, $W(r,h)$, that decays with distance from the particle of interest. The compact support shown here is $2h$, specifically that of the cubic spline kernel. This cartoon shows particles with individual smoothing lengths so that each particle has approximately equal neighbours.

ity. The kernel should also be smoothly differentiable (at least singularly) and be an odd function and ≥ 0 in all space. Given these pre-requisites the simplest choice is a Gaussian kernel function which has the advantage of being smooth for any order of differentiation (employed by Gingold & Monaghan 1977). However as it is non-zero at all radii we would require the summation over all neighbours. Instead we can choose to limit our summation to a kernel of "compact support", i.e. one that drops to 0 outside some radius, limiting ourselves to a finite number of particles and the kernel to a finite volume (e.g. a sphere of radius $2h$ in Fig. 2.1). A common choice is the cubic spline (Monaghan & Lattanzio 1985) with compact support inside $2h$, used by default in both PHANTOM and SPHNG. This kernel takes the form

$$W(\vec{r},h) = \frac{\sigma(\nu_D)}{h^{\nu_D}} \begin{cases} 1 - 1.5q^2 + 0.75q^3 & 0 \leq q < 1 \\ 0.25(2-q)^3 & 1 \leq q < 2 \\ 0 & 2 < q \end{cases} \tag{2.14}$$

where $q = |r|/h$, ν_D is the number of spatial dimensions and $\sigma = (2/3, 10/7\pi, 1/\pi)$ for 1, 2 and 3D, ensuring the correct normalisation (Equation 2.8). The number of terms can be increased to form quartic, $O(q^4)$ or quintic splines, $O(q^5)$, though at the expense of increased computation time. Plots of a selection of kernels and their derivatives are shown in Figure 2.2. Here we can see the commonly used cubic spline and its derivative has the same overall shape as other kernels, but the second derivative is discontinuous. Note that the second derivative is not used in this study, and comes into play when using velocity dependent forces (e.g. MHD). Now we have a suitable kernel we must find some appropriate value for the smoothing length, which we will address next.

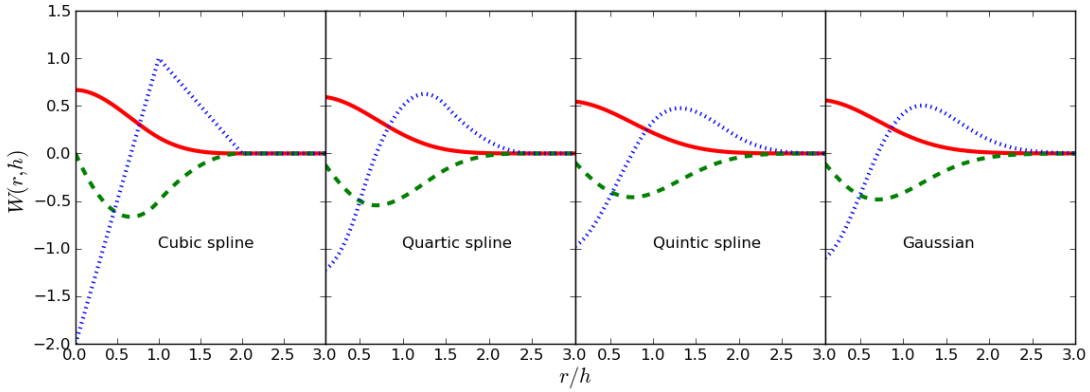

Figure 2.2: Various SPH kernels in red, their first and second spatial derivatives (dashed and dotted lines). The cubic spline is the simplest, but experiences discontinuities at higher derivatives, while the Gaussian is the most robust it has the undesirable feature of being non-zero in all space.

2.2.3 Mass equation of SPH

As we have shown above the a^{th} particle density is calculated in SPH formalism by setting $A_a = \rho_a$ in the interpolation summation to give a density equation of the form

$$\rho_a = \sum_b m_b W_{ab} \tag{2.15}$$

where we will be using the shorthand notation of $\vec{r}_{ab} = \vec{r}_a - \vec{r}_b$ and $W_{ab} = W(|\vec{r}_{ab}|, h)$ throughout the remainder of this chapter. The density summation shows that the dimensions of the kernel are [1/distance^3] in 3D, hence the h^{ν_D} factor in Equation 2.14. The density of each particle is not constant, but rather the mass is (i.e. the "size" of the particles the variable).

Any density formulation we construct should inherently satisfy the continuity equation (Equation 2.5), ensuring that the rate of change of material in a system is equal to the rate it flows out of the surface. First addressing the left hand side of the continuity equation, in material derivative form, we obtain

$$\begin{aligned} \frac{D\rho_a}{Dt} &= \sum_b m_b \frac{D}{Dt} W_{ab} = \sum_b m_b \frac{\partial W_{ab}}{\partial r_{ab}} \frac{Dr_{ab}}{Dt} \\ &= \sum_b m_b \frac{\partial W_{ab}}{r_{ab}} \hat{e}_{ab} \cdot \vec{v}_{ab} = \sum_b m_b \vec{v}_{ab} \cdot \vec{\nabla}_a W_{ab} \end{aligned} \tag{2.16}$$

where we have substituted for the particle velocity, $\vec{v}_{ab} = D\vec{r}_{ab}/Dt$. This could be used to evolve the density of the particles in the system, rather than evolving the integration of an additional quantity (as we will with v, and u). However we would be introducing additional errors from the adopted integration scheme and it is more practical to calculate the density via direct summation. This can be done in the same loop over particles as all the other summation formulae (discussed in the following subsections) at little additional cost. Now evaluating the right hand side of the

continuity equation we find that

$$\begin{aligned}\rho_a \vec{\nabla}_a \cdot \vec{v}_a &= \vec{\nabla}_a \cdot (\rho_a \vec{v}_a) - \vec{v}_a \cdot \vec{\nabla}_a \rho_a \\ &= \vec{\nabla}_a \cdot \left(\sum_b \frac{m_b}{\rho_b} (\rho_b \vec{v}_b) W_{ab} \right) - \vec{v}_a \cdot \vec{\nabla}_a \left(\sum_b \frac{m_b}{\rho_b} (\rho_b) W_{ab} \right).\end{aligned} \tag{2.17}$$

Where we have used the SPH summation equation with the variables $\vec{A}_a = \rho_a \vec{v}_a$ and $A_a = \rho_a$. We can move the gradients inside the summations as they act only upon the properties of a. This gives (recalling that $a \cdot b = b \cdot a$)

$$\begin{aligned}\rho_a \vec{\nabla}_a \cdot \vec{v}_a &= \sum_b m_b \vec{v}_b \cdot \vec{\nabla}_a W_{ab} - \sum_b m_b \vec{v}_a \cdot \vec{\nabla}_a W_{ab} \\ &= -\sum_b m_b (\vec{v}_a - \vec{v}_b) \cdot \vec{\nabla}_a W_{ab} \equiv -\sum_b m_b \vec{v}_{ab} \cdot \vec{\nabla}_a W_{ab}.\end{aligned} \tag{2.18}$$

The SPH continuity equation is then simply the sum of equations 2.16 and 2.18

$$\frac{D\rho_a}{Dt} + \rho_a \vec{\nabla}_a \cdot \vec{v}_a = \sum_b m_b \vec{v}_{ab} \cdot \vec{\nabla}_a W_{ab} - \sum_b m_b \vec{v}_{ab} \cdot \vec{\nabla}_a W_{ab} = 0 \tag{2.19}$$

thus satisfying the continuity equation. This is somewhat of a mute point however, as by construction SPH *should* conserve mass due to each particle having a fixed mass. The process of re-working the format of the SPH equation, i.e. "putting the density inside the operator", is a good way of ensuring symmetric functions (Monaghan 1992 refers to this as the second golden rule of SPH).

So far we have limited our discussion to particles with fixed smoothing lengths. If we were to give each particle its own individual smoothing length then we allow for an additional adaptability. This does however negate some approximations in the derivations above as we can no longer neglect the gradients in the smoothing lengths. An additional normalisation factor must be added, Ω_a, to the Equation 2.16 above

$$\frac{D\rho_a}{Dt} = \frac{1}{\Omega_a} \sum_b m_b \vec{v}_{ab} \cdot \vec{\nabla}_a W_{ab}(h_a). \tag{2.20}$$

the origin of which, and its affect on the standard SPH rate equations is the subject of Appendix A. For the purpose of this chapter we simply quote the resulting rate equation with the additional "grad-h" term where W_{ab} has been replaced by $W_{ab}(h_a)$. The smoothing gradient factor can be shown to be

$$\Omega_a = 1 - \frac{\partial h_a}{\partial \rho_a} \sum_b m_b \frac{\partial W_{ab}(h_a)}{\partial h_a} \tag{2.21}$$

which is also shown in Appendix A.

2.2.4 Momentum equation of SPH

The fluid mechanics momentum equation is summarised by the Navier-Stokes equations (or Euler equations with no viscous forces) given by Equation 2.4. Ignoring the viscosity and the external forces for now, the EoM of the system becomes[1]

$$\frac{D\vec{v}}{Dt} = -\frac{\vec{\nabla}P}{\rho}. \tag{2.22}$$

In order to find the rate of change of momentum we need find an expression for $\vec{\nabla}P/\rho$, the force for a purely inviscid fluid under no external forces. We will use the second golden rule of SPH again and put the density inside the operators. First we will re-arrange the pressure gradient to give

$$\frac{\vec{\nabla}_a P_a}{\rho_a} = \vec{\nabla}_a\left(\frac{P_a}{\rho_a}\right) + \frac{P_a}{\rho_a^2}\vec{\nabla}_a\rho_a \tag{2.23}$$

and substituting in the relevant SPH summation equations

$$\frac{\vec{\nabla}_a P_a}{\rho_a} = \vec{\nabla}_a\left(\sum_b \frac{m_b}{\rho_b}\left(\frac{P_b}{\rho_b}\right)W_{ab}\right) + \frac{P_a}{\rho_a^2}\vec{\nabla}_a\left(\sum_b \frac{m_b}{\rho_b}(\rho_b)W_{ab}\right) \tag{2.24}$$

which re-arranges to give:

$$\frac{\vec{\nabla}_a P_a}{\rho_a} = \sum_b m_b \frac{P_b}{\rho_b^2}\vec{\nabla}_a W_{ab} + \sum_b m_b \frac{P_a}{\rho_a^2}\vec{\nabla}_a W_{ab}. \tag{2.25}$$

The basic momentum equation is then simply

$$\frac{D\vec{v}_a}{Dt} = -\sum_b m_b\left(\frac{P_a}{\rho_a^2} + \frac{P_b}{\rho_b^2}\right)\vec{\nabla}_a W_{ab}. \tag{2.26}$$

If we had not placed the density inside the operator then we would not have this antisymmetric form (noting that $\nabla_a W_{ab} = -\nabla_b W_{ba}$). This momentum equation fulfils the conservation of momentum, and Newton's third law, seen upon the swapping of indexes a and b and checking the forces between them are antisymmetric ($F_{ab} = -F_{ba}$). For individual smoothing lengths ("grad-h" formalism) we again just quote the solution here

$$\frac{D\vec{v}_a}{Dt} = -\sum_b m_b\left(\frac{P_a}{\Omega_a\rho_a^2}\vec{\nabla}_a W_{ab}(h_a) + \frac{P_b}{\Omega_b\rho_b^2}\vec{\nabla}_a W_{ab}(h_b)\right), \tag{2.27}$$

and direct the reader to Appendix A for a brief derivation of this form, and also evidence that the momentum equation can also be derived from the Lagrangian and the Euler-Lagrange equations rather than the Navier-Stokes equation.

[1] While we could simply use the discretisation equation and set $A_b = P_b$ to give $\rho_a D\vec{v}_a/Dt = -\sum_b m_b(P_b/\rho_b)\vec{\nabla}_a W_{ab}$, this does not conserve momentum. This is seen by calculating the forces from a on b, using the anti-symmetric identity $\nabla_a W_{ab} = -\nabla_b W_{ba}$ and seeing that $F_{ab} \neq -F_{ba}$, i.e. conflicting with Newton's third law (see Rosswog 2009).

2.2.5 Energy equation of SPH

The final basic SPH equation required for the evolution of a fluid system is the energy equation. We start from the first law of thermodynamics, $dU_a = P_a dV_a$. Working in per-unit-mass units we can substitute $dV_a = d(1/\rho_a) = 1/\rho_a^2 \times d\rho_a$. Taking these rates as a function of time and using D/Dt for Lagrangain dynamics we have

$$\frac{DU_a}{Dt} = \frac{P_a}{\rho_a^2}\frac{D\rho_a}{Dt}. \tag{2.28}$$

We then use the continuity equation to substitute the change in density, giving the energy equation

$$\frac{DU_a}{Dt} = \frac{P_a}{\rho_a^2}\sum_b m_b \vec{v}_{ab} \cdot \vec{\nabla}_a W_{ab}. \tag{2.29}$$

Monaghan (1992) uses the same method as for the above formulations to derive a similar expression instead involving P_b and ρ_b,

$$\frac{DU_a}{Dt} = \frac{1}{2}\sum_b m_b \left(\frac{P_a}{\rho_a^2} + \frac{P_b}{\rho_b^2}\right) \vec{v}_{ab} \cdot \vec{\nabla}_a W_{ab}. \tag{2.30}$$

which conserves energy exactly. This form is less often used in practice however (e.g. Hubber et al. 2011, Rosswog & Price 2007) as it has the unfortunate side effect of producing negative energies if there are significant local pressure variations, caused by the P_b term in the energy calculation of a (Benz 1990; Wadsley et al. 2004). We can also include the effect of individual smoothing lengths (see Appendix A),

$$\frac{DU_a}{Dt} = \frac{1}{\Omega_a}\frac{P_a}{\rho_a^2}\sum_b m_b \vec{v}_{ab} \cdot \vec{\nabla}_a W_{ab}(h_a) \tag{2.31}$$

which is equivalent to $P_a/\Omega_a\rho_a^2 \times D\rho_a/Dt$

2.2.6 The equation of state

In order to evaluate the SPH rate equations we need to set an equation of state to provide the pressure of the ISM particles as a function of density. Our primary interest is the abundance of molecular material which, as will become clear in the following sections, is a strong function of temperature. As such we must evolve the thermal energy of the particles alongside the kinematic quantities. We utilise an adiabatic equation of state, which gives the pressure as a function of internal energy and density of the particles

$$P = (\gamma - 1)\rho u \tag{2.32}$$

where γ is the adiabatic index, given by the ratio of specific heats at constant pressure and volume, which for a monatomic gas is $5/3 \approx 1.67$, which is the case for the majority of the ISM (but is 5/7 for diatomic molecules such as CO and H_2). If we were not storing thermal energy we could use a

general polytropic form without thermal energy, $P = K\rho^{\gamma}$, where K is some constant, though this would result in a phase diagram that is a poor representation of the ISM[2], where complex heating and cooling mechanisms determine the evolution of u (see Section 2.3.1 and Figure 2.12). We also use an isothermal EoS for testing purposes, where $P = K\rho$.

When we are discussing artificial dissipation in a later section we will be referring to the adiabatic sound speed of the gas. This is calculated as

$$c_s = \sqrt{\frac{\partial P}{\partial \rho}} = \sqrt{\frac{\gamma P}{\rho}} = \sqrt{\frac{k_B T}{m_p \mu}} \tag{2.33}$$

where μ is the mean molecular weight of the material in question (see Section 2.3 for a brief description in relation to the ISM). We can then also calculate the thermal temperature from $T = P\mu/R\rho$, i.e. $T = \mu u(\gamma - 1)/R$, where R is the gas constant.

2.2.7 The density and smoothing length in "grad-h" SPH

As a rule of thumb we want the kernel to contract in regions of high density and keep the number of neighbours per particle approximately constant, making sure the resolution is consistent between dense and diffuse regions of particles. The particles in the denser regions require smaller smoothing lengths compared to those in the more diffuse medium, maintaining the same number of neighbours (6 in the case of Fig. 2.1). If fixed smoothing lengths are used then some sacrifice would need to be made between either over-resolving the very diffuse media, which are usually of minimal importance, or under-resolving the high density regions which is often the location of the more complex and interesting physics.

A natural choice would be to choose a smoothing length that is analogous to the length scale which defines the density of a SPH particle, $\rho \propto m/h^{\nu_D}$, where ν_D is the number of spatial dimensions (Gingold & Monaghan 1982; Price 2012a). This gives a simple equation relating the density and smoothing length of each individual particle

$$h_a = \eta \left(\frac{m_a}{\rho_a}\right)^{1/\nu_D}. \tag{2.34}$$

The η factor is chosen to roughly give a number of neighbours, and specifies the smoothing length scale, which can be calculated by

$$N_{neigh} = \frac{4}{3}\pi (\zeta\eta)^3 \tag{2.35}$$

in 3D[3] where ζ is the compact support of the kernel, which is $2h$ for the cubic spline (i.e. the finite radius of the smoothing sphere). We could define the number of neighbours explicitly rather than η, but there are numerous pit-falls when constraining the N_{neigh} factor throughout a simulation (see Price 2012a for a discussion). Good values of η have found to be between 1.2-1.5 (Rosswog & Price 2007), and we adopt $\eta = 1.2$ in all simulations presented here corresponding to $N_{neigh} = 58$

[2]This would correspond to an isentropic flow, applicable in the absence of shocks or external energy sources (Springel 2010b).

[3]2D and 1D forms are similarly given by $\pi(\zeta\eta)^2$ and $2\zeta\eta$ respectively (Price 2012a) .

in 3D.

As we have now defined h in terms of ρ, and ρ in terms of h we can use these relations to iteratively solve for the smoothing lengths by ensuring that Equation 2.15 and Equation 2.34 are equivalent, i.e. $\rho_{\rm sum} = \rho(h_a)$ to some tolerance. To do so it is common to use some solver to find solutions (i.e. minimising the function) of the non-linear equation

$$f(h_a) = \rho(h_a) - \rho_{\rm sum} \tag{2.36}$$

which can be done by the Newton-Raphson method (Gingold & Monaghan 1982; Price 2012a), which requires the derivative of the density difference function, $f'(h_a)$,

$$\begin{aligned}\frac{\partial f(h_a)}{\partial h_a} =& \frac{\partial \rho(h_a)}{\partial h_a} - \sum_b m_b \frac{\partial W_{ab}(h_a)}{\partial h_a} \\ =& \frac{\partial \rho_a}{\partial h_a}\left[1 - \frac{\partial h_a}{\partial \rho_a}\sum_b m_b \frac{\partial W_{ab}(h_a)}{\partial h_a}\right] = \frac{\partial \rho_a}{\partial h_a}\Omega_a\end{aligned} \tag{2.37}$$

where $\partial\rho_a/\partial h_a$ can be easily computed from the analytic expression for ρ_a. This results in the iteration equation

$$h_{a,n+1} = h_{a,n}\left(1 + \frac{\rho(h_{a,n}) - \rho_{sum}}{3\Omega_a \rho(h_{a,n})}\right) \tag{2.38}$$

which can be iterated until some convergence is reached. We have used the definition of the smoothing gradient parameter from Equation 2.21, the calculation of which is already done in the force and energy rate equations, reducing the overall computational cost of the density calculation. The cost can be reduced further by making a sensible initial estimate for the smoothing length iterations using a predictor step for h and $dh_i/dt = dh_i/d\rho_i \times d\rho_i/dt = -h_i/3\rho_i \times d\rho_i/dt$ (Price & Monaghan 2007).

2.2.8 Evolving the system

Once the forces have been calculated from the SPH summation equations, giving $\dot{v}_{x,y,z}(t)$, $\dot{u}(t)$, they are used to evaluate new positions (x, y, z), velocities (x, y, z), and energies, as well as updating h if required. We effectively now need to solve a set of ordinary differential equations in order to find the change in position and velocity from $\dot{v}$ and $\dot{u}$.

Each of the codes we utilise uses a different integrator. In PHANTOM a second order "leapfrog" is used, with a specific "kick-drift-kick" formulation (Springel 2005; Monaghan 2005). The initial force "kick" is the applied to the velocity for half the initial timestep, and the particle is allowed to "drift" at this speed for the full timestep. The force is then re-evaluated at the post-drift position and is used to provide an additional velocity kick to update the velocity to the full timestep. This integrator has been shown to be stable considering its low order, displaying greater integration stability and conservation properties over its "drift-kick-drift" and even higher order Runge-Kutta contemporaries (Springel 2005; Rosswog 2009).

SPHNG uses the Runge-Kutta-Fehlberg integrator, specifically the RKF1(2) integrator, which is in essence a second order method imbedded within a first order method (Fehlberg 1985, see

Cossins 2010 for a discussion). The construction of a first and second order estimate for the updated variables means we can control the error in the integration explicitly, though we would have to use the first order estimate in the actual integration. This issue can be mitigated by simply enforcing a very small tolerance on the first-second order difference, effectively making RKF1(2) a second order method with controllable accuracy.

2.2.9 Timestepping

Regardless of the actual integration scheme, we need some way of sensibly deciding the timestep on which to advance the properties of the system. In the most basic case a timestep can be imposed that is the time between the creation of dump files, Δt_0 (e.g. every 1/100th of the total simulation run-time). However, this can easily be much larger than the dynamical time-scale of changes in system variables, resulting in integration steps that do not correctly encompass the physics of the system. The size of a timestep can then be chosen by use of the Courant condition which relates the ratio of the spatial resolution Δx to the time resolution Δt and the velocity of the simulated particles by $C_{CFL} = v\Delta t/\Delta x$, which ensures information speed does not exceed the physical speed of material in the simulation (Courant et al. 1928). C_{CFL} is the dimensionless Courant number, and has been constrained from numerical studies to be from 0.25-1 in order to satisfy convergence of the time integration. We take a minimum of this timing criteria over all particles in the simulation to obtain the global Courant timestep as

$$\Delta t_{CFL} = C_{CFL} \min\left(\frac{h}{|v_{sig}|}\right) \tag{2.39}$$

where v_{sig} is the same signal velocity as that defined in Section 2.2.11. We use $C_{CFL} = 0.3$ in the simulations in this thesis. We also include a forcing timestep, which is calculated from the ratio of the magnitude of the forces to the smoothing length

$$\Delta t_f = C_f \min \sqrt{\frac{h}{|\vec{f}|}} \tag{2.40}$$

where we use $C_f = 0.25$. Finally there is a time scale for astrophysical cooling, which will be discussed later,

$$\Delta t_{cool} = C_{cool} \min\left|\frac{U}{\dot{U}_{ISM}}\right| \tag{2.41}$$

where $C_{cool} = 0.3$ as in Glover & Mac Low (2007). This is normally grouped with the forcing timestep condition. The hydrodynamical time is dictated by the Courant timestep, whereas the forcing and cooling times are used to advance the timestep with the same initial SPH force, i.e. external and cooling forces are subcycled inside the main steps which is where neighbour calculations are required.

Individual timesteps

In astrophysical simulations time scales of importance can be very large when assessing gravitational effects, or small when resolving molecular/shock effects. It then becomes prudent to allow each particle its own individual timestep to avoid evolving all particles in the calculation on integration times of the slowest particles. In these cases particles are binned up into groups of $2^n \Delta t_{min}$ and each time bin is evolved separately (Rosswog 2009; Hubber et al. 2011). For example these timesteps can be of similar form to those above, but the actual evolution of the particles is done in bins of particles with similar magnitude timesteps, making sure the timesteps of all particles in the simulation coincide at some point, i.e. they should all be synchronisable at any given point in the calculation (Hernquist & Katz 1989). Care must obviously be take to ensure that a particle is correctly aligned with the others in the simulation before it is moved to a different timestepping bin as the individual timestep increases or decreases (Hubber et al. 2011).

2.2.10 Neighbour finding

Now we have a good grounding in the numerical recipes behind SPH, and a method of advancing the particle properties, all that remains is some way of knowing the relevant particles in the SPH summation equations, the "nearest neighbours" (i.e. the relevant b's for which to calculate the properties of a). The most obvious way to do so would be to simply loop over all particles, but this would be a $O(N^2)$ process, a very computationally expensive scaling. By using a kernel of compact support we have limited ourselves to a small number of neighbours (usually in the range 50-100) but as the particles move around the identity of these neighbours will change, so some method of re-populating these neighbour-lists is required. Two such options that are used frequently in SPH codes are "Link lists" and "Tree codes", both offering an improvement on the basic $O(N^2)$ neighbour search (Liu & Liu 2003).

Link lists

A simple neighbour searching scheme is to use a link list method. All SPH particles are binned into a grid that covers the entire computational domain, where grid cells have a size of $2h$ when using the cubic spline. Particles in a cell only then search their own and adjacent cells for neighbours, resulting in a much smaller search domain, only 27 cells in 3D (Domínguez et al. 2011). Particles are also chained to each other via some link array allowing for fast looping through all particles in each cell (Liu & Liu 2003).

This method can be of order $O(N)$ in some cases, but can be less efficient if there are large fluctuations in smoothing lengths, as it could result in large numbers of particles in each of the grid cells increasing the time required to walk through the neighbouring cells (Hernquist & Katz 1989). Link lists are used in PHANTOM where the cell width is set to $2\sum_a h_a/N$ and we utilise a cylindrical cell structure for our galactic disc simulations.

Trees

The other common neighbour finding method is to use a hierarchical tree-like structure, such as that of Barnes & Hut (1986). The basic method involves building up an octree of the simulation domain (i.e. first splitting the simulation into a 2x2x2 octal) which is then subdivided into further cells if they contain any particles. This is done until the child cells at the bottom of the tree contain 1 or 0 particles (the "leaves" of the tree, where the tree is actually an inverted tree). For nearest neighbour calculations, such as finding which particles are required for the SPH summations, a search is done by moving back up the tree from the particle of interest to find which particle nodes (a point where branches separate) are within the region of interest. For instance, whether a neighbouring particle is within the kernels compact support radius, $r \leq 2h$ when using a cubic spline. The neighbour search then descends down the branches of that node, checking whether the leaf particles are within the compact support region, thus building a neighbour list for a specific particle while retaining the tree for use with the other particles.

The use of a tree has the added advantage of being able to be used for the neighbour finding and gravitational force calculation (Hernquist & Katz 1989), and is used for calculation of N-body gravitational forces in SPHNG. When the calculating the gravitational forces the tree is walked through, instead of only using the nearest neighbours the gravitational calculation must also take into effect the material outside the kernel support radius. As the tree is traversed a distance criterion is calculated on each node. If ratio of the size of the node to the distance from the particle of interest is greater than some tolerance then the branches of the node are then traversed. However, if less than this tolerance then the material encompassed by the node is lumped together to form a single larger body from which the gravitational attraction is calculated using the appropriate centre of mass and node mass which is stored when the tree is created (Hernquist & Katz 1989). The gravitational forces must also be softened to avoid extreme accelerations of particles during close-encounters; this is soften on a scale of the smoothing kernel (Bate & Burkert 1997). The tree in SPHNG is described in greater detail in Benz (1988) and Benz et al. (1990), which was implemented using the version from Press (1986). Tree based neighbour finding is usually an order $O(N \log N)$ process and can be pushed down to $O(N)$ by clever symmetrising and storing of cell-cell forces (Hernquist & Katz 1989; Dehnen 2002).

2.2.11 Artificial dissipation

Artificial viscosity

One of the major advantages of SPH is that it is completely dissipation free by construction. This can have adverse properties when attempting to model shock-based problems. On large scales the rapid change in system properties (be it density, velocity, pressure, internal energy etc.) appear as discontinuities in the fluid flow. While in reality this discontinuity is in fact smooth it would require a simulation resolution on macroscopically small scales to correctly capture. The smooth gradients inherent in the SPH formulation do a poor job in such regions where steep gradients are effectively discontinuities on macroscopic scales.

Von Neumann & Richtmyer (1950) suggested that this problem could be over-come by the addition of some artificial dissipation, or viscosity. The addition of an artificial viscosity (AV) smoothes out gradients near these discontinuities, acting similarly to physical viscosities. Such an artificial viscosity will dissipate kinetic energy into heat, generating the required entropy increase, and will broaden the shock to a resolvable scale rather than a discontinuous one, allowing for shock capturing. The AV does not in essence reproduce a physical process but rather smooth out a shock front that would otherwise be discontinuous on the length scales relevant to the calculation.

Von Neumann & Richtmyer (1950) formulate this viscosity into a pressure of the form $P_v = -A\rho c_s l(\vec{\nabla}.\vec{v}) + B\rho l^2(\vec{\nabla}.\vec{v})^2$ for some constants A and B over some resolvable length scale l (h in SPH Rosswog 2009). The A term is analogous to a classical bulk viscosity (as is α described shortly) and B the Neumann-Richtmyer quadratic term (as is β), and both only activate in converging flows ($\nabla \cdot v < 0$). Using AV's of this form had drawbacks however, resulting in either over-dissipation or post-shock oscillations (Monaghan & Gingold 1983). This approach was refined by Monaghan & Gingold (1983) who suggested additional pressure term (actually of dimensions P/ρ^2) to be included in the standard momentum equation, Equation 2.26, of the form

$$\Pi_{ab} = \frac{-\alpha \bar{c}_{ab}\mu_{ab} + \beta\mu_{ab}^2}{\bar{\rho}_{ab}} \tag{2.42}$$

where

$$\mu_{ab} = \frac{h_{ab}\vec{v}_{ab} \cdot \vec{r}_{ab}}{r_{ab}^2 + \epsilon\bar{h}_{ab}^2} \tag{2.43}$$

where α, β, ϵ are constants to be set. The over-lined terms indicate averaged quantities between two particles; $\overline{\rho}_{ab} = [\rho_a + \rho_b]/2$ and $\overline{h}_{ab} = [h_a + h_b]/2$ where the velocity term is simply $\vec{v}_{ab} = \vec{v}_a - \vec{v}_b$. Then $\vec{r}_{ab} \cdot \vec{v}_{ab}$ will be < 0 if particles are approaching, i.e. when a shock may occur, and is used as a criterion for activating the viscosity (i.e. $\Pi_{ab} = 0$ if $\vec{r}_{ab} \cdot \vec{v}_{ab} > 0$). This form is effectively a combination of Neumann-Richtmyer (β) and bulk (α) viscous terms. The β term was not originally present in the Monaghan & Gingold (1983) formalism but was added to prevent particle penetration and correctly model strong shocks (Monaghan 1992). The standard values adopted are $\alpha = 1, \beta = 2\alpha$ (Monaghan 1992), usually providing adequate dissipation at a shock while $\epsilon = 0.01$ protects against small separation singularities (as $r_{ab} \to 0$). There is also the capacity to set individual values of α to the particles, to avoid dissipation where it may not be needed such as converging flows in the absence of shocks.

This results in a full momentum equation of the form

$$\frac{D\vec{v}_a}{Dt} = -\sum_b m_b \left(\frac{P_a}{\rho_a^2} + \frac{P_b}{\rho_b^2} + \Pi_{ab} \right) \vec{\nabla}_a W_{ab}, \tag{2.44}$$

where the artificial viscous force produces a repulsive force when particles move towards each other. The dissipated kinetic energy must be re-assigned as thermal energy to satisfy energy conservation. To this end the standard SPH energy equation gains the contribution

$$\frac{DU_{a,AV}}{Dt} = \frac{1}{2}\sum_b m_b \Pi_{ab} \vec{v}_{ab} \cdot \vec{\nabla}_a W_{ab} \tag{2.45}$$

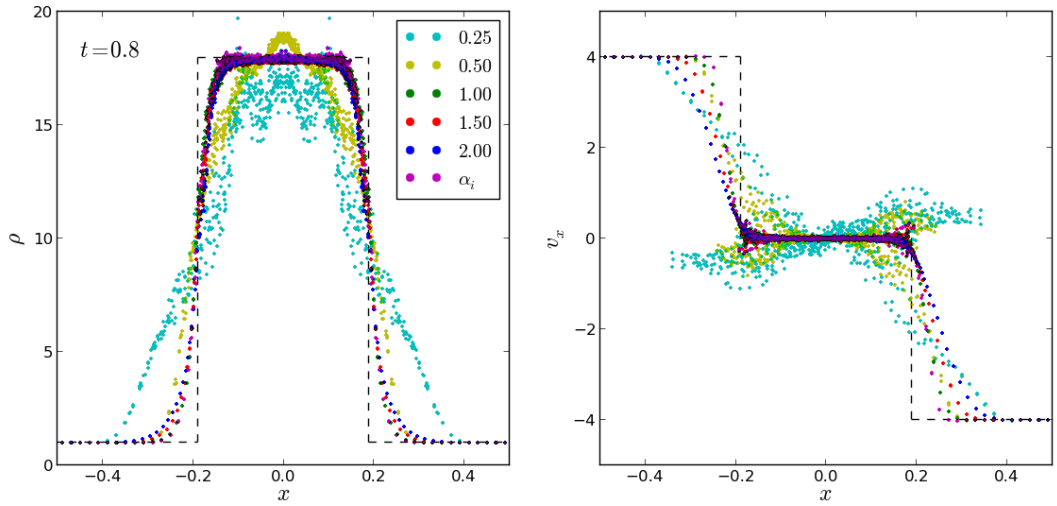

Figure 2.3: An isothermal colliding flows test using PHANTOM in 3D where gas flows are moving at $v = \pm 4$ initially. The density and velocity profiles are shown after 0.8 dimensionless time units. Differences in shock capturing can be with different AV parameters, shown in different colours. The β term is fixed to 2α when α is fixed, and 2 when variable (pink points). The analytical solutions are shown by dashed lines.

giving a full energy equation

$$\frac{DU_a}{Dt} = \sum_b m_b \left(\frac{P_a}{\rho_a^2} + \frac{\Pi_{ab}}{2} \right) \vec{v}_{ab} \cdot \vec{\nabla}_a W_{ab}. \tag{2.46}$$

This is the "classical" AV formulation, and is the standard in the SPHNG code (with additional "grad-h" terms). The α term can actually be related directly to the coefficients of physical viscosity[4]. The shear viscosity parameter can be shown to be equivalent to $\eta = \alpha h c_s/10$ and bulk parameter to $\zeta = 5\eta/3$ (Monaghan 2005; Lodato & Price 2010; Price 2012b).

The addition of AV is illustrated by the colliding flows test shown in Fig. 2.3. Here we have set up an isothermal shock tube test in 3D in a box of dimensions $8 \times 1 \times 1$ using approximately 160000 particles initially arranged on a hexagonal lattice with velocities $v = \pm 4$ with flows directed towards each other either side of $x = 0$. While better analysis of AV forces is seen in 1D, neither of the codes we use in this thesis have the capacity for anything but 3D. This results in a strong shock propagating from $x = 0$ manifesting as a plateau in ρ and v_x, shown by the analytic solution (dashed line). The different coloured points refer to different values for the AV coefficients and $\beta = 2\alpha$ for all tests apart from the pink points where α is variable and we have fixed $\beta = 2$. It is clear that $\alpha = 1$ to 2 do a good job at capturing the shock in ρ and v_x whereas lower values do a poorer job. The $\alpha = 2$ case applies slightly too much dissipation, which can be clearly seen in the pre-shock regions of the v_x panel. A test was also performed where individual values of α are assigned to each particle which allow for dissipation only where necessary utilising the switch of Morris & Monaghan (1997) that is a function of sound speed and smoothing length of the particles

[4]The shear viscosity develops when a fluid flow when it passes some boundary moving at a different velocity, know as a shear flow. Bulk viscosity on the other hand is the manifest as the viscous friction experienced by a fluid expansion or compression in the absence of shear flow. The η and ζ terms enter into the viscous Euler equations, quantifying shear and bulk viscosity respectively.

(Lodato & Price 2010). This differs little compared to the fixed case, though it does apply the least dissipation in the region not yet experiencing a shock (v_x panel). This highlights that a variable α can be useful in that it applies less dissipation where it is not needed.

An alternative formulation of AV was proposed by Monaghan (1997), where the authors use solutions analogous to Riemann solvers[5]. The original purpose of which was to enable the capture of relativistic shocks. We present this form of AV in a similar form to the classical $\alpha - \beta$ version using the parameter Q_{ab} with the same dimensions as Π_{ab} such that the AV contribution to the momentum equation is given by

$$\frac{D\vec{v}_{a,AV}}{Dt} = -\sum_b m_b Q_{ab} \nabla_a \overline{W}_{ab} \tag{2.47}$$

where Q_{ab} is given by

$$Q_{ab} = \frac{\alpha^{AV} v_{sig} |\vec{v}_{ab} \cdot \hat{r}_{ab}|}{\overline{\rho}_{ab}} \tag{2.48}$$

when $\vec{v}_{ab} \cdot \hat{r}_{ab} \leq 0$ and 0 otherwise to ensure converging flows. We use the shorthand notation of $\overline{W}_{ab} = [W(r_{ab}, h_a) + W(r_{ab}, h_b)]/2$ to average kernel weights, and can include additional Ω denominators for the kernels to correct for variable smoothing lengths. This formulation contains a signal velocity term, v_{sig}, which is the averaged signal speed between two particles. The exact choice of signal velocity differs between users, but a general form is given in Price (2012a) as

$$v_{sig} = \frac{1}{2}\left[c_{s,a} + c_{s,b} - \beta^{AV} \vec{v}_{ab} \cdot \hat{r}_{ab}\right] \tag{2.49}$$

for $\vec{v}_{ab} \cdot \hat{r}_{ab} \leq 0$, and is 0 otherwise, where c_s is sound speed of a given particle. While some forms in the literature fix $\beta^{AV} = 1$ (Rosswog & Price 2007; Hubber et al. 2011) or some other value (Springel 2010b) the general form is that of a sound speed term in combination with a velocity term. The formalism is similar to the previous notation, with linear and quadratic terms in velocity projection ($\vec{v}_{ab} \cdot \hat{r}_{ab}$) scaled by α^{AV} and β^{AV} terms respectively. This can then be similarly applied to the thermal energy equation to give

$$\frac{DU_{a,AV}}{Dt} = \frac{1}{2}\sum_b m_b Q_{ab} \vec{v}_{ab} \cdot \vec{\nabla}_a \overline{W}_{ab} \tag{2.50}$$

which can be added to the standard energy equation.

Artificial thermal conductivity

It has been shown that in some cases the AV alone is not enough to resolve certain physical phenomena. There is a need to add additional dissipation terms for each variable of the system. In adding AV we have corrected for discontinuities in the velocity distribution, but it is also necessary to add additional dissipative energy terms. This problem was noted by Agertz et al. (2007) whose calculations of Kelvin-Helmholtz instabilities showed a lack of characteristic rolling fea-

[5] A Riemann solver is (unsurprisingly) designed to solve Riemann problems which include shock dynamics and other discontinuities coupled to the Euler equations (e.g. Toro 1992).

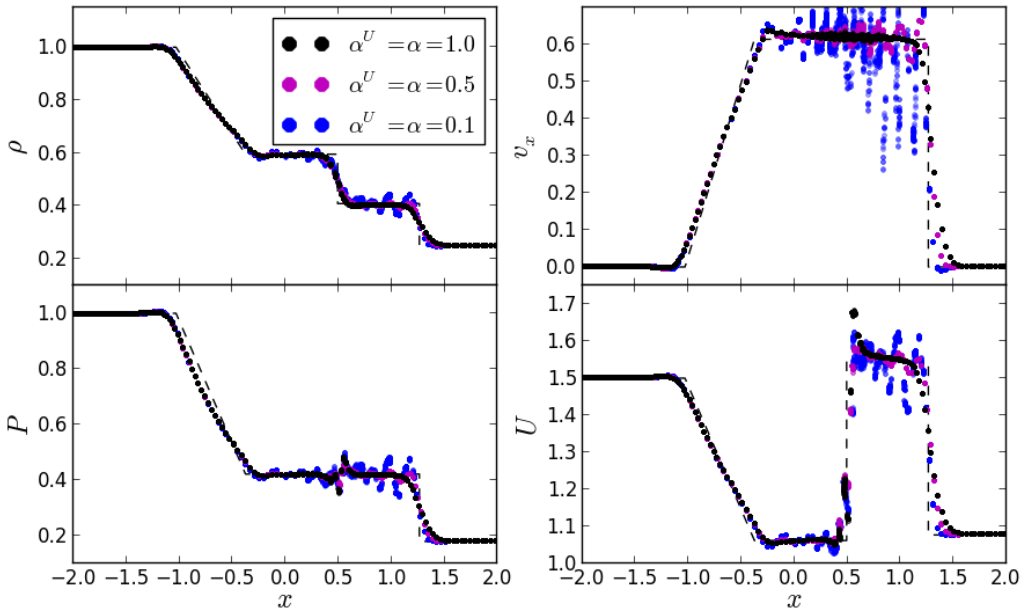

Figure 2.4: Adiabatic "sod" shock tube problem test in 3D using PHANTOM with differing values of α, β and α^u, indicated by different colours. The fiducial values are shown in black. Analytical solutions to the density, velocity, energy and pressure over-plotted as dashed lines. Low values of α and β result in a failure to capture many aspects of the shock structure and sinusoidal oscillations

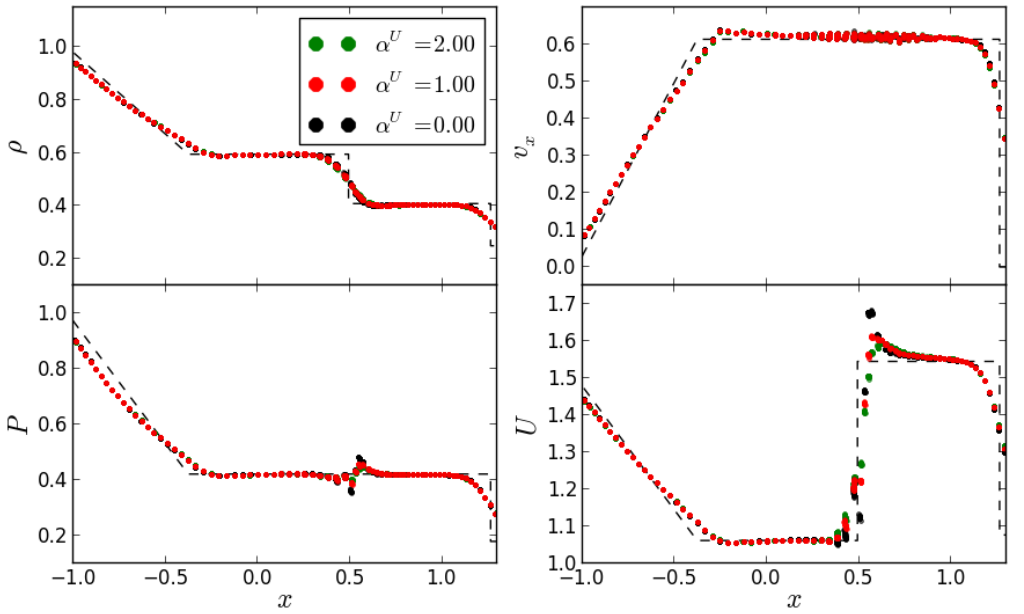

Figure 2.5: Same as Fig. 2.4 but keeping α and β fixed to 1.0 and 2.0 respectively while only varying α^U. The main effect of α^U is to reduce the energy (and consequentially P) spike at $x = 0.5$ in the figure. α^U is fixed to 1 when used. The x-axis shows a narrower range than Fig. 2.4 as the points are indistinguishable outside of the range shown.

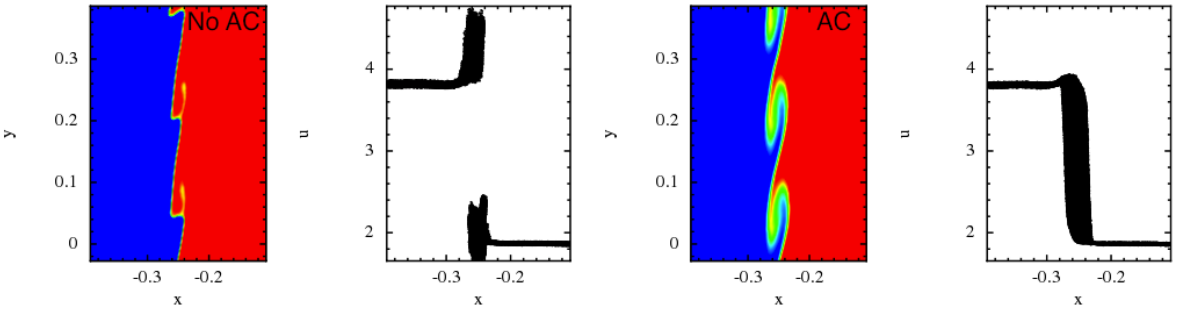

Figure 2.6: Kelvin-Helmholtz instability test without and with artificial thermal dissipation (left and right panel pairs respectively). The lack of heat dissipation across the density boundary is clearly seen in the run without artificial conductivity, which also manifests as a strong discontinuity in internal energy of the particles. With the addition of artificial thermal conductivity the fluid dissipates energy smoothly across the contact region, and displays a smooth energy transition. The test was set up using an initial 2:1 density contrast and 3.8 million particles in 3D using PHANTOMwith α^u fixed to 1 when used.

tures at the high-low density contact region. Price (2008) proposed an additional artificial thermal conductivity, AC, to address this problem, where the energy equation is augmented by

$$\frac{DU_{a,AC}}{Dt} = -\sum_b m_b \frac{\alpha^U v^U_{sig} u_{ab}}{\overline{\rho}_{ab}} \hat{r}_{ab} \cdot \vec{\nabla}_a \overline{W}_{ab} \tag{2.51}$$

where α^U is the dimensionless artificial thermal conductivity parameter that smoothes out gradients in internal energy between particles, and $u_{ab} = u_a - u_b$ (see also Valcke et al. 2010). There is an additional signal velocity which can be different to that used in standard artificial viscosity. Two suggestions in the literature are either a pressure difference, $v^U_{sig} = \sqrt{|P_a - P_b|/\hat{\rho}_{ab}}$ from Price (2008) or velocity projection, $v^U_{sig} = |\vec{v}_{ab} \cdot \hat{r}_{ab}|$ from Wadsley et al. (2008). The velocity projection form is used in PHANTOM.

Illustrations of the importance of AC are shown in Figures 2.4, 2.5 and 2.6. In Figures 2.4 and 2.5 we show an adiabatic/Sod shock tube test, where gas is initially stationary but with large discontinuities in the density and energy distributions on either side of $x = 0$. The gas is then allowed to expand, causing a shock wave to propagate through the tube. Once again this test is in 3D, and the analytic solutions for ρ, v_x, P and U are shown by the dashed lines. β=2α for all the tests shown. Figure 2.4 shows that the change in the standard α and β viscosity parameters result in poor capturing of the shock, magenta and blue points, as in Figure 2.3.

In Figure 2.5 the effect of AC is included, where the black points are the same as those in the previous figure and represent $\alpha^U = 0$. Increasing α^U to 1 or 2 has a much more subtle effect than α, but can be seen to reduce the "blip" in U and P at the contact discontinuity. The points for $\alpha^U = 2$ are beginning to over-smooth the shock, and if increased further will severely dissipate the shock front discontinuity.

The importance of AC is much more evident from the Kelvin-Helmholtz test shown in Figure 2.6, where the gas is set in two parallel streams of material with a 2:1 density contrast. The left panels show the test with no AC, and the right with AC added and $\alpha^U = 1$. In the test with

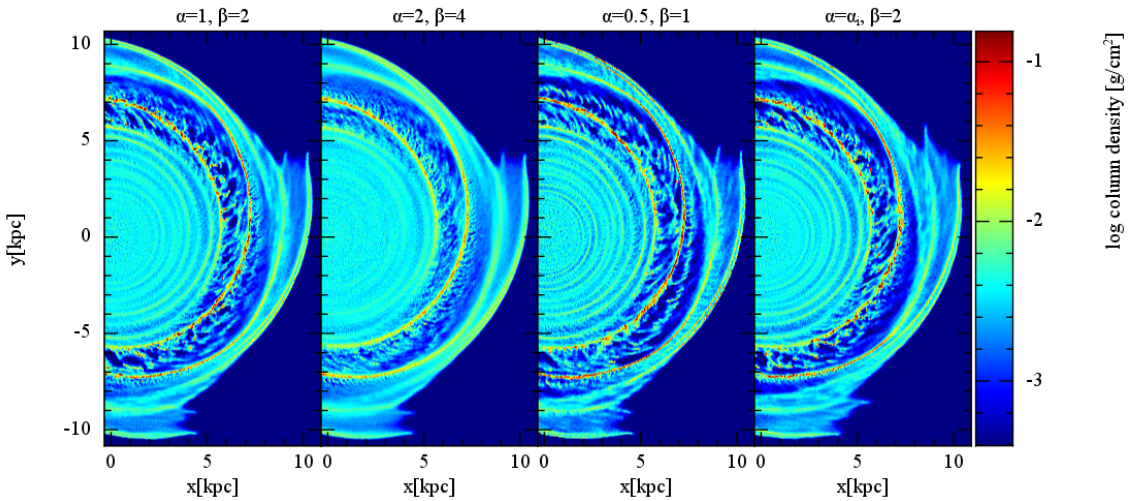

Figure 2.7: Top-down column densities of disc galaxies after 330Myrs of evolution with different AV parameters. A simulation with the fiducial values of $\alpha = 1$ and $\beta = 2$ is shown in the first panel, with double and half these values in the second and third panels. The fourth panel shows a simulation with $\beta = 2$ and individual α parameters for each particle in the range $0 < \alpha_i < 1$.

active AC the thermal energy smoothly traverses the contact discontinuity. The run with no AC keeps the different flows segregated throughout the test, with a clear discontinuity in the thermal energy.

The impact of different artificial viscosity parameters in our simulations is shown in Figures 2.7 and 2.8. Here we show a simple galactic disc simulation with a four armed spiral pattern (details of which will be discussed in Chapter 3) after 330Myrs of evolution. The four different simulations show our standard parameters, $\alpha = 1$, $\beta = 2$, double and half these values, and a simulation where each particle has its own individual α_i. The top-down column density plot in Fig. 2.7 shows some differences with AV parameters. It appears that increasing the strength of the AV causes the dilution of inter-arm structures, and decreasing the AV enhances them. The calculation with variable viscosity appears similar to the standard values. Figure 2.8 clarifies this difference somewhat by showing the temperature profile of the gas as a function of density. Here we see that the calculations with higher or lower than the standard AV strength do not produce the coldest regions present when using the fiducial values. The variable viscosity calculation has a temperature distribution near identical to that of the standard values, though this could be a result of both having $\beta = 2$. The main conclusion to draw from these figures is that there is not a large difference in morphology and thermal properties when using the standard, weaker, or adaptive AV parameters but using stronger than average values can cause artificial smoothing of morphological features and a less populated cold phase ISM.

Similar tests to those shown for AV were performed for the α^U parameter, with values 0, 0.5, 1 and 2. Both the top-down density distributions and the thermal properties of the gas were effectively the same for the different values of α^U. The only minor difference was a reduced population of the hottest ISM gas with the highest strength AC, $\alpha^U = 2$. The gas in the simulations presented here is unlikely to have strong thermal discontinuities as present in the Kelvin-Helmoltz

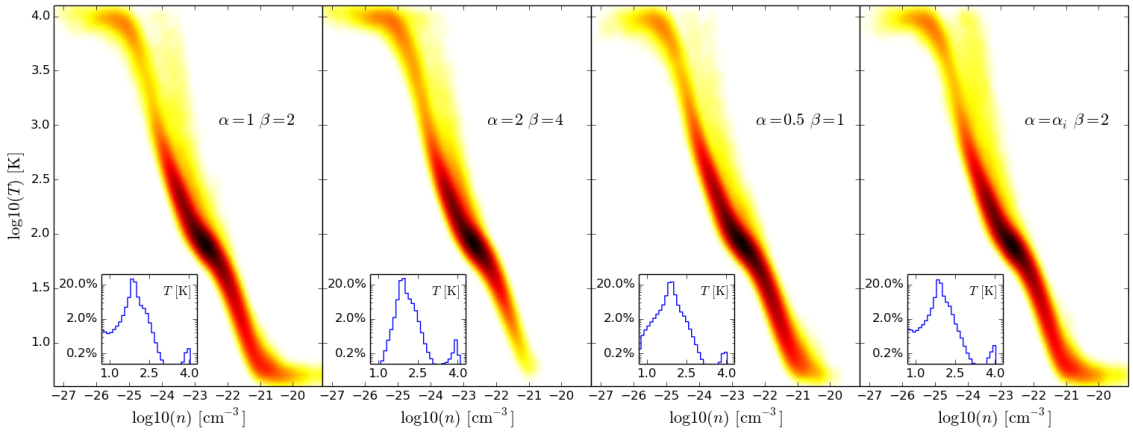

Figure 2.8: Temperature-density distribution from the same four simulations shown in Figure 2.7. The small insert shows a histogram of T for each case. The standard AV parameters allow for the development of cold ISM component, where CO is easily maintained. The impact of individual α coefficients is marginal.

test, as any dramatic thermal change should be smoothed out by astrophysical cooling and strongly coupled to density gradients which should be smoothed by standard AV. If there were some strong thermal source that caused large temperature gradients in the gas then the choice of α^U could become more important. This could play a role in calculations including supernovae feedback, where the resulting instantaneous thermal shockwave could produce strong thermal discontinuities.

The standard literature values of $\alpha = 1, \beta = 2$ and $\alpha^U = 1$ appear suitable for capturing the shock fronts in the tests shown here, to the capabilities of SPH. Lower values of α and β result in a dramatic inability to reproduce shock features in thermodynamical quantities, as shown by the colliding flows and sod tube tests ins Figures 2.3 and 2.4. Stronger values can be seen to be beginning to add too much dissipation to the shocked front, evident from Figures 2.7 and 2.8. α^U had a much weaker effect, but is seen to reduce artefacts at the contact region in the sod tube test (Fig. 2.5). We therefore adopt $\alpha = 1, \beta = 2$ and $\alpha^U = 1$ throughout the remainder of this thesis. Some improvement can be found in using individual values of α to avoid unwanted dissipation, but the results shown in Figures 2.7 and 2.8 shows the effect of this is unnoticeable for the scales investigated here.

2.2.12 SPH code specifics

Here we provide a brief description of the SPH codes used in this thesis. The main differences/similarities between the two codes are summarised in Table 2.1.

PHANTOM

The PHANTOM code is built specifically for non-gravitating problems, at high resolutions with a low-memory footprint, and has been extensively adapted for MHD computations (Price & Federrath 2010; Lodato & Price 2010; Tricco & Price 2012). The particles have individual smoothing lengths and timesteps, the system is evolved using a leapfrog integrator, and neighbours found

Characteristic	PHANTOM	SPHNG
Neighbour finding	Link list	Binary tree
Time-step integrator	2^{nd} order leapfrog	2^{nd} order Runge-Kutta-Fehlberg
Gravity	N/A	Binary tree (or Grape board)
Dissipation	Adapted Monaghan 97 + Conductivity	Standard α-β
Kernel	Cubic spline	Cubic spline
N_{neigh} (3D)	58	58
Density evolution	Newton-Raphson iteration	Newton-Raphson iteration

Table 2.1: Summary of the main aspects of the two SPH codes used in this thesis.

using linked-lists for reducing computational effort with OpenMP and MPI parallelisation. Due to a unique arrangement of the SPH equations, and separation of the average density terms in Equation 2.47, the density sums need only be calculated once on each timestep. This speed comes at a cost, with no current implementation of particle self-gravity (which would require a much slower tree-like neighbour finding algorithm).

ISM chemistry, cooling and simple galactic potentials were only recently incorporated into PHANTOM (Dobbs 2011a), but have not been well tested. Here we extensively tested the code, leading to corrections in the particle timestepping. The main improvement was the inclusion of a suite of gravitational potentials for use with galactic disc simulations, and are discussed in Chapter 3.

SPHNG

The second SPH code utilised in this thesis is SPHNG ("SPH-Next-Generation"). An older code than PHANTOM, SPHNG is based on the original version of Benz et al. (1990) and has been substantially modified since its creation. Notable improvements include the addition of accreting sink particles (Bate et al. 1995), magnetic fields (Price & Monaghan 2004) and radiative transfer (Whitehouse et al. 2005), as well as the standard variable smoothing lengths, individual timesteps and parallelisation using both OpenMP and MPI. Most importantly is that SPHNG allows for the calculation of gravitational forces. This allows for inclusion of point mass gravitating particles that are used to represent the Galactic stellar component, the subject of Chapter 5.

The code has already been used extensively for galactic scale ISM modelling. These studies include the effect of ISM cooling and chemistry (Dobbs et al. 2008), self-gravity (Dobbs 2008) and stellar feedback (Dobbs et al. 2011).

Brief comparison between codes

Figure 2.9 shows simulations of simple, low-resolution galactic discs using the SPHNG (top: blue) and PHANTOM (bottom: red) codes. These snapshots are at 472 Myrs of evolution[6] and show the top down particle distribution, the temperature-density profile and the CO abundance (the calculation

[6]The evolution times frequently used in this thesis of 236, 354 and 472 Myrs correspond to 5, 7.5 and 10 code units, determined from the gravitational constant, the distance and mass code units adopted; $u_m = 1 \times 10^5 M_\odot$ and $u_d = 100$ pc, giving a time unit of $u_t = \sqrt{u_d^3/G u_m} = 47.2$ Myrs.

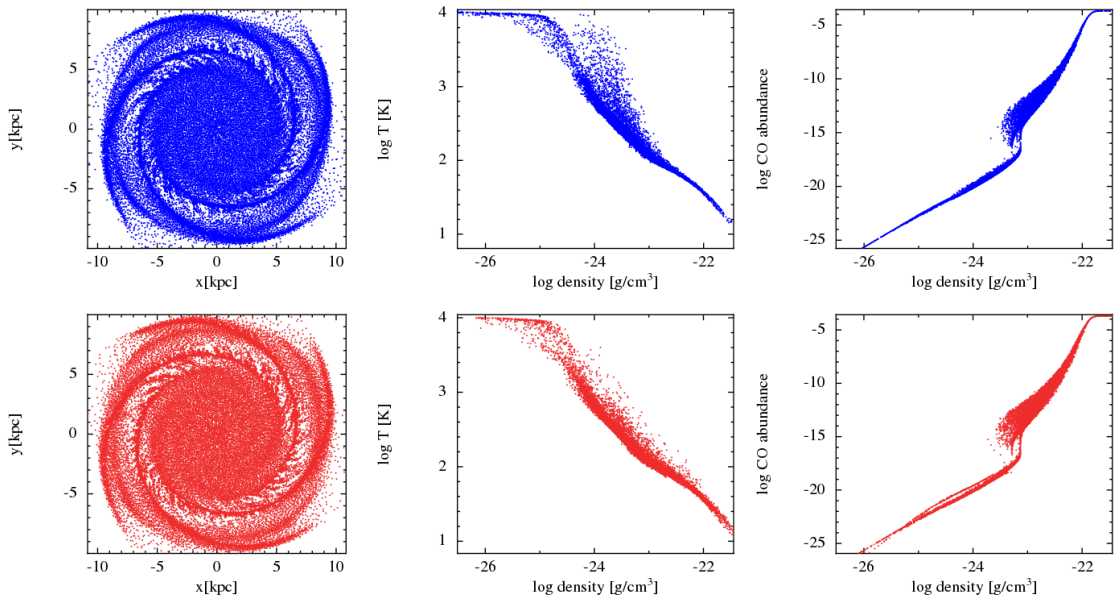

Figure 2.9: Simulations of gas in a disc galaxy constituting of 40000 particles with a total mass of $4 \times 10^9 M_\odot$. The top row is from a simulation in PHANTOM, and the bottom in SPHNG, both after 472 Myrs of evolution. The position, T and CO abundance of the SPH particles trace the same global flow in codes, with minor differences resulting from inherent code differences listed in Section 2.2.12. The chemical network are described in detail in Section 2.3.

of which is discussed in the next section). The simulation is of only 40000 particles, embedded in a simple disc potential constructed to reproduce the flat Galactic rotation curve including a a four armed spiral potential.

Comparing global quantities of the simulations from each code we see that they agree reasonably well considering the different architecture. The position of the gas traces that of the spiral arms, with small scale spurs peeling away at around R=5kpc. The temperature of the particles behaves the same with density for both codes. There is a small population of particles that reach higher temperatures in the range $-24 < \log_{10}\rho < -23$ in the PHANTOM run, though this only amounts to 1% of the particles. The associated phase diagram shows that the gas has followed the warm ISM track into the unstable region (left, Fig. 2.12), implying the PHANTOM calculations allow gas to maintain its warm nature longer in the thermally unstable region before rapidly cooling into the cold ISM region compared to SPHNG. This could easily be the result of the different AV formalism, or the different formulation of the SPH energy equation. The chemical evolution is similar for both codes, showing only minor differences. The median values[7] of the thermal energy, CO, H_2 and H I fractions agree between 0.5-10%, with CO giving the greatest discrepancy between the codes. This CO is sub-cycled numerous times, and is an extremely sensitive function of density, making slight differences in density evolution between the codes lead to moderate differences in the CO abundance of individual particles.

[7] As the abundances vary on log scales their means are extremely sensitive to single particles having a slightly increased density, which can differ easily between codes due to the different architecture.

2.3 ISM specific physics

The physics so far discussed only covers hydrodynamical and gravitational forces. For the use of SPH on galactic scales we must include additional physical effects, predominantly ISM heating and cooling mechanisms. The various heating and cooling mechanisms have been adapted for Galactic scale use in Dobbs et al. (2008), and will only briefly be discussed in Section 2.3.1. Of paramount importance to the work presented here is the molecular content of the ISM. Rather than assuming some constant molecular gas fraction that would linearly scale with gas density, we evolve the gas content of each SPH particle individually. This is discussed in full in Section 2.3.2.

The various heating, cooling and chemical processes require a measurement of temperature, determined by the equation $T = \mu u(\gamma - 1)/R$. This requires some value of the mean molecular weight, defined by the ratio of mass density to number density (M/n) of all species of interest, j. We can use the atomic weight, A_j, of each species to make the calculation simply a sum of number ratios of each species, χ, a.k.a. the abundance of each species[8] with respect to H I, given by $n_j/n_{\rm HI}$. The mean molecular weight is then

$$\mu = \frac{\sum_j M_j}{\sum_j n_j} = \frac{\sum_j n_j A_j}{\sum_j n_j} = \frac{\sum_j \chi_j A_j}{\sum_j \chi_j} = \frac{\sum_j q_j}{\sum_j \chi_j} \tag{2.52}$$

where we have divided through by the number density, and refer to the ratio by mass of each species as $q_j = \chi_j A_j$. In the ISM there are a wealth of different species, but only a handful are of significant abundance to contribute to the calculation above, specifically H I, He and H_2 where each has weights of $A_{\rm HI} = 1$, $A_{\rm H_2} = 2$ and $A_{\rm He} = 4$. The abundance of H_2 is evolved in our calculations, so we know this at any point in the simulation, and as it is composed of hydrogen we can formulate the H I abundance simply as $\chi_{\rm HI} = 1 - 2\chi_{\rm H_2}$. Helium is of little importance to the simulations presented in this thesis, so we have fixed the abundance at $\chi_{\rm He} = 0.1$ (Glover & Mac Low 2007). This gives the following equation for the mean molecular weight

$$\mu_{ISM} \approx \frac{q_{\rm HI} + q_{\rm H_2} + q_{\rm He}}{\chi_{\rm HI} + \chi_{\rm H_2} + \chi_{\rm He}} = \frac{\chi_{\rm HI} + 2\chi_{\rm H_2} + 4\chi_{\rm He}}{\chi_{\rm HI} + \chi_{\rm H_2} + \chi_{\rm He}}. \tag{2.53}$$

In the case where the gas is entirely atomic we find $\mu_{ISM} = 1.27$ and if the hydrogen is entirely in a molecular state then $\mu_{ISM} = 2.33$.

Several processes involved in the chemistry and cooling involve the heating/destructive effects of the local radiation field. Here we need to take into account the attenuation/extinction effects from the column density of the surrounding material that effectively shield the target atom/molecule from the incident photons. This manifests as an additional multiplicity factor that reduces the reaction rate as a function of the optical depth of the surrounding medium, simply of the form[9] $f = e^{-\tau_\lambda}$. This can be through individual line absorption by certain species, such as in H_2 self shielding, or through continuous absorption by ISM dust grains. We can relate the opacity

[8] The number ratios and mass ratios are χ and q respectively, where for the species of interest we have $q_{H2} = 2\chi_{H2}$ and $q_{He} = 4\chi_{He}$.

[9] This is solution of the radiative transfer equation in the absorbing only case, i.e. Beer's Law, and will the subject of further discussion in Chapter 5

to a parameter called the "visual extinction", A_v, by $\tau = \gamma A_v$, which is the difference in magnitudes between the shielded and unshielded cases. The ratio of visual extinction has been seen to be a constant ratio of the colour excess, $E(B-V) = A_B - A_V$, (Draine & Bertoldi 1996; Bergin et al. 2004), by amounts of either

$$R_V = \frac{A_V}{E(B-V)} \approx \begin{cases} 3.1 & \text{In diffuse ISM} \\ 5.0 & \text{In dense clouds} \end{cases} \tag{2.54}$$

Calculating the visual extinction is no easy task, but there exists a simple conversion between the column density of the gas and the extinction using a visual extinction conversion factor, A_V^{CF}, via

$$A_V^{CF} = A_V / N_{col} = 5.348 \times 10^{-22} \mathrm{cm}^{-2} \tag{2.55}$$

where A_V^{CF} is the extinction per unit column density (N_{col}) for which we will use a constant value throughout the work presented in this thesis unless stated otherwise. This relation was found by measuring the colour excess as a function of column density in various Galactic sources and noticing the ratio between them was roughly constant, with a slope $E(B-V)/N_{tot} = A_V^{CF} R_v$ (Bohlin et al. 1978). The value above is the standard value from the work of Bohlin et al. (1978) but there are several values in the literature. A statistical analysis by Güver & Özel (2009) find a value 20% greater than this standard, however, as we will show later in this section, A_V^{CF} must change by orders of magnitude to have a noticeable effect in our calculations. This extinction will come into play in dust shielding factors in photon based reactions in dense regions. In several rates the UV radiation field will be attenuated by a dust shielding factor, e.g. $G_{dust} = f_{dust} G_0$ where $f_{dust} = e^{-\gamma_X A_v^{CF} N_{HI}}$. The values of γ_X adapt this relation slightly for specific target species (Glover et al. 2010), and take values of 2.5 for cooling, H I and CO chemistry and 3.74 for H_2 dust shielding (which has additional self shielding attenuation).

In order to utilise Equation 2.55 we require a measurement of column density, which is the density of material integrated spatially along the line of sight between two points. The column density is somewhat difficult to compute while keeping the code relatively simple and streamlined. A full treatment of column densities would require large neighbour calculations, scaling as $O(N^{5/3})$ compared to the $O(N \log N)$ for gravity or $O(N)$ for nearest neighbour finding (Glover & Mac Low 2007). Instead we assume the column density is simply the local density times by some distance measurement, l_i

$$N = \int n \mathrm{d}s \approx n l_i \tag{2.56}$$

where we have approximated the distance of integration by a distance relevant to that of the chemistry in question. The smallest is the general distance scale used for cooling and heating rates, specifically PAH and photoelectric effects, where we adopt $l_{cool} = 10$pc. The H I ionisation is shielded on much larger scale, a value of $l_{\mathrm{HI}} = 100$pc, due to its chemistry mostly evolving in sparser regions. Finally there is the length scale used in the evolution of H_2 and CO, which evolves in much denser regions than H I, hence has a smaller column density scale length $l_{ph} = 35$pc. The latter of these comes from the typical distance to a B0 star, due to their large luminosity and higher abundance than the more luminous O stars. This is the same method as adopted by Dobbs (2008),

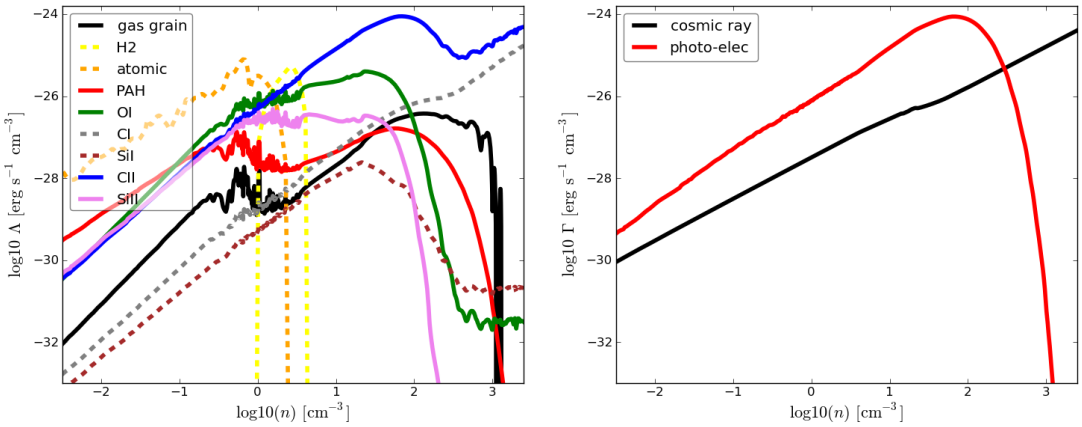

Figure 2.10: Cooling (left) and heating (right) functions discussed in the main text and utilised in our calculations. We have included CI and SiI for comparison using abundances of 1% of their ionised counterparts, but these are absent in our simulations. The pressure-density profile used is similar to that shown in Fig. 2.12.

who investigate values of l_{ph} from 15-100pc, finding the amount of molecular gas is only weakly coupled to this distance measurement.

2.3.1 Cooling and heating functions

The thermal evolution of the ISM can be separated into two distinct components,

$$\dot{U}_{ISM} = \Gamma_{ISM} + \Lambda_{ISM}, \tag{2.57}$$

which are added into the standard SPH energy equation. We use the convention that Λ is energy loss (cooling) and Γ is energy gain (heating). The various heating and cooling processes contributing to Λ and Γ are taken from the work of Glover & Mac Low (2007). In order for an energy scheme to be relevant to the calculation there are numerous criteria that must be satisfied. The species involved in the process must be abundant enough to ensure frequent collisions. The energy required for the reaction must be of the order of the kinetic energy of the gas, and the probability of the reaction (e.g. the Einstein coefficients) must be large enough for the process to be sufficiently frequent. The various heating and cooling effects relevant to our calculations are shown as a function of density in Figure 2.10, and are described individually briefly below. Due to the complex nature of many of these rates, the cooling and heating is tabulated into numerous arrays as a function of temperature at the beginning of the calculation. Rates that are collisional in origin have a density dependance of n^2, whereas those caused by direct photon interaction scale as n.

The various heating and cooling processes are listed in Table 2.2, along with their corresponding references. We refer the reader to these references for details and formulation of the heating and cooling processes, and will only briefly discuss them here. ISM cooling comes from a variety of mechanisms including H I collisional excitation, H_2 vibro-rotational collisional excitation, fine structure excitation of C II, Si II and O I, heat transfer between gas and dust grains, and

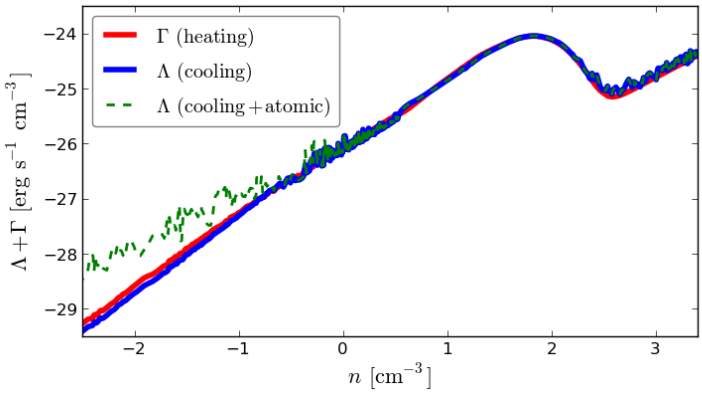

Figure 2.11: Combination of the heating and cooling functions shown in Fig. 2.10. The atomic (H I) cooling is shown for comparison but only dominates for a small number of particles in each simulation. Si I and C I are not included in these total rates. The resulting heating and cooling functions are of the same order of magnitude as a function of density.

the recombination of free electrons with PAH and dust grain surfaces. The dominant of these processes are the fine-structure cooling lines in the mid to high density regime, with recombination cooling becoming more important at lower densities (Fig. 2.10). Atomic and molecular hydrogen cooling, while strong, only becomes significant in a small fraction of the ISM. These are shown as the dashed lines in Fig. 2.10. We neglect the cooling effects of CO, but this is compensated for by maintaining a constant fraction of C II for cooling purposes, and the fact that the C II and CO cooling functions are similar (Glover & Jappsen 2007).

ISM heating is provided by two mechanisms; photo-electric heating on dust grains, large molecules and PAH's, and heating by cosmic-rays (right panel of Fig. 2.10). The photo-electric heating is the stronger of the two, except in the densest regions where dust becomes significantly shielded by the high column density ISM (Bergin et al. 2004). Cosmic-ray heating provides 20eV per reaction and takes into account heating of all ISM species, though is predominantly the ionisation of H I.

Process	Description	Reference
H I (atomic) cooling	Electron collisional excitation/ resonance line emission	Sutherland & Dopita (1993)
H_2 (molecular) cooling	Vibrational/rotational excitation cooling by collisions with H I, He and H_2	Le Bourlot et al. (1999)
Fine structure cooling	C II, Si II and O I collisions with H I, H_2, free e^- and H II	Glover & Jappsen (2007)
Recombination cooling	Free e^- recombining with ionised gas on PAH and dust grain surfaces	Wolfire et al. (2003)
Gas-grain cooling	Dust-gas collisional heat transfer	Hollenbach & McKee (1989)
Cosmic-ray heating	Temperature independent 20eV cosmic-ray photons	Goldsmith & Langer (1978)
Photo-electric heating	UV e^- excitation from dust and PAH	Wolfire et al. (2003)

Table 2.2: Heating and cooling processes present in our ISM calculations.

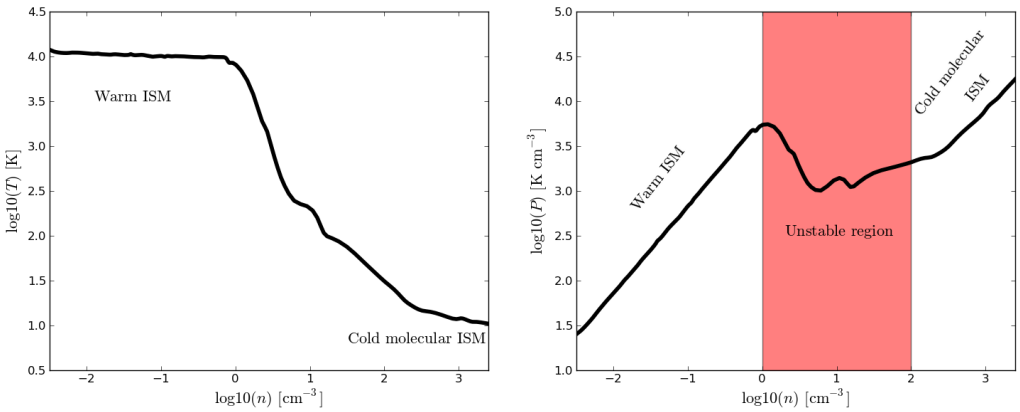

Figure 2.12: Thermodynamical properties in a simple disc galaxy simulation. Particle properties have been averaged in density space over the 1 million particles to clarify features. The temperature of the gas plateaus around 10,000K, corresponding to the warm neutral/ionised ISM component. A two-phase ISM is clearly seen in the P-ρ diagram, separated by an unstable region. A small fraction of the gas follows the warm track higher with increasing density and drops down further later in the unstable region.

The total heating and cooling rates are shown in Figure 2.11. We also show the effect of the atomic cooling function, which dominates the hot medium, but this is only a small fraction of the simulation particles (green dashed line). The heating and cooling is of comparable strength in most places (as can be seen by eye). In the region of thermal instability near 1 atom cm^{-3} there is a lot of variation in the cooling rates (this has been smoothed over in Figure 2.11 for clarity). This is due to the splitting of the population between gas that falls into the pressure well and gas that continues to travel up the warm branch of the phase-diagram before falling in, continuing to cool.

The resulting thermodynamic properties of the ISM gas in a "standard" simulation are shown in Figure 2.12. The temperature and pressure profiles as a function of number density are shown for gas in a disc subject to the multitude of heating and cooling effects outlined above. Properties have been binned in density space for clarity, as there is a large variation in the mid-density range. The temperature profile in the left panel shows a clear plateau around 10000K, where the gas condenses almost isothermally up to a density of 1 atom cm^{-3}. Here the gas begins to cool and experiences a drop in pressure, entering the thermally unstable region (the shaded area in the right panel of Fig. 2.12). The gas can continue to cool and contract, becoming molecular in the process. These phase curves are a direct result of the heating and cooling functions, and show a good match to others in the literature (e.g. Field et al. 1969, Wolfire et al. 1995, Liszt 2002) showing a clear distinction between warm and cool phases (see Section 1.4).

2.3.2 Chemistry

One of the most important aspects of the calculations is the tracing the chemical evolution of the gas. As hydrogen is the most abundant gas in the ISM, the first order chemical processes of this gas are some of the most important in the ISM. Hydrogen is allowed to dissociate over time (and to recombine), and to become molecular at higher densities. In order to create molecular

emission maps we must also include a prescription for creating CO. This process is much more complex than the other reactions as it is dependent on numerous intermediate species between the atomic stage and the creation of CO. The ionisation processes alone for the species relevant to CO formation encompass a staggering amount of different processes (Glover & Jappsen 2007; De Becker 2013). If we were to attempt to include only molecular hydrogen and carbon monoxide, then the data in the UMIST database (McElroy et al. 2013) suggests you would need to encompass approximately 800 and 400 reactions respectively (assuming that database is complete!). This is clearly not computationally feasible, especially in the case of a galactic scale simulation where our time and spatial dimensions far exceed those important chemically. Instead it is prudent to limit ourselves to only those reactions deemed most important in each case, sacrificing some of the accuracy for computational simplicity.

The chemical evolution of each species (i.e. the evolution of the number density, n_X) is encompassed by a single ordinary differential equation of the form

$$\frac{dn_X}{dt} = C_X - D_X n_X, \tag{2.58}$$

so that the density of species X at the next timestep, $t + \Delta t$, is

$$n_X(t + \Delta t) = n_X(t) + \frac{dn_X}{dt}\Delta t \tag{2.59}$$

including a creation coefficient, C_X, and a destruction coefficient, D_X, unique to the species and often a complex function of density, temperature, and the abundance of other species. For example, the rate of H_2 formation will depend heavily of the abundance of atomic hydrogen. The exact form of our H I, H_2 and CO rate equations are discussed in the following sub-sections. Each particle in our calculations carries with it a chemistry array of the form $\vec{\chi}_a = (\chi_{\rm HI}, \chi_{\rm H_2}, \chi_{\rm CO})|_a$, which is $(1, 0, 0)$ initially. The chemistry arrays keep track of 3 distinct parameters, the H I ionisation fraction, the H_2 ratio and CO abundance which have the values of $(0, 0, 0)$ and $(1, 0.5, \chi_{\rm CII})$ in the low and high density extremes respectively. The electron and proton abundances are also tracked, but χ_{pr} is simply $\chi_{\rm pr} = 1 - \chi_{\rm HI}$ and $\chi_{\rm el} = 1 - \chi_{\rm HI} + \chi_{\rm c}$ where $\chi_{\rm c}$ is the constant free electron abundance, a result of the ionisation of species other than H I.

The regime of negative abundances should be avoided at all times, i.e. the right hand side of Equation 2.59 should always be > 0. To ensure this we must include some chemical timestepping criteria (Glover & Mac Low 2007; Dobbs et al. 2008). This can be calculated from $dt_{dest} = -n_X/(C_X - D_X n_X)$. The sub-stepping time frame is then taken to be 10% of the time taken to completely destroy the species of interest ($dt_{chem} = 0.1 dt_{dest}$), ensuring negative abundances are avoided. If creation is occurring, then the chemistry is sub-cycled on some fixed scale ($dt_{chem} = dt_{hydro}/200$). The sub-stepping used to avoid negative abundances is not applied to the H I chemistry, as the abundance never reaches into this range in our simulations. Some sub-stepping is still applied however, as the chemistry is at least evolved on the cooling time-scale (Equation 2.41). The CO evolution is done inside of the H_2 evolution, as the two are intrinsically linked, and the CO evolution is also allowed to sub-step further if required.

As the chemistry is evolved as in Equation 2.58 there is expected to be some loss of accuracy

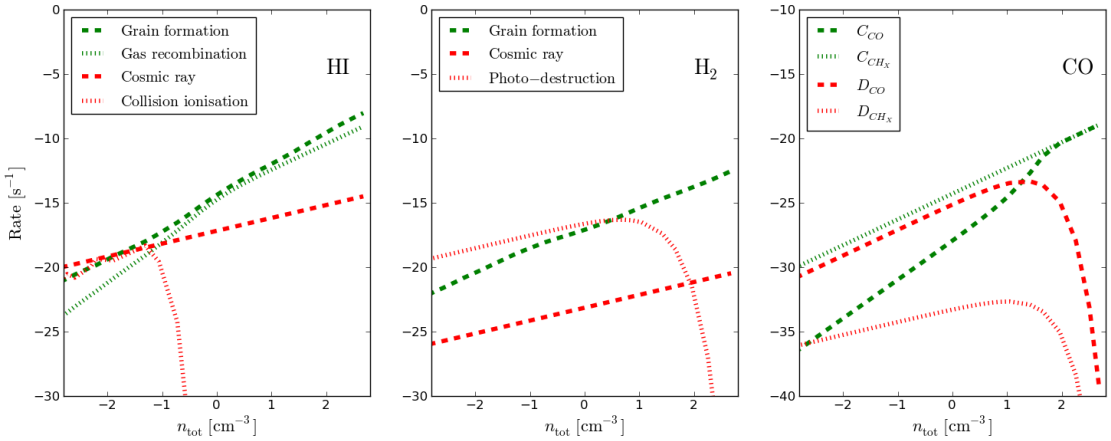

Figure 2.13: The individual components in the creation and destruction terms for H I (left), H_2 (middle) and CO chemistry (right). The density-temperature profile is that used in Figure 2.12 where the rates are calculated at fixed abundances of $\vec{\chi} = (0.94, 1 \times 10^{-6}, 1 \times 10^{-15})$.

over large integration time-scales (as opposed to the 2nd order integrations used to evolve the SPH quantities). However, by evolving the chemistry on the cooling time-scale, as well as including additional chemistry sub-stepping if required, we hope to minimise this. Any sources of error involved in the order of integration are also considered to be minimal compared to the simplistic nature of the chemistry itself.

Three figures will be referenced when referring to the chemical evolution. Figure 2.13 shows the various components contributing to the various creation and destruction rates of each species and Figure 2.14 shows the resulting evolution tracks for each species. The latter was created using a simple 1D code used to test the chemistry, that evolves abundances alone without various thermodynamical properties, but with a fixed P-T profile representing the general behaviour of the ISM cooling function (as in Fig. 2.12). Figure 2.15 is similar to Figure 2.14 but shows the effect of changing various parameters important for the chemistry of H_2 and CO. All the various chemical reactions are listed in Table 2.3 and the multitude of required parameters are included in Table 2.4.

HI chemistry

At the most basic chemical level we must include the effect of the ionisation of neutral hydrogen gas, creating an abundance of H II and free electrons. The various atomic hydrogen processes have been coded by Glover & Mac Low (2007) and included in our codes (see Table 1 of their paper). The H I chemistry coefficients included are

$$C_{\rm HI} = k_{rec} n_e n_p + k_{gr} n_p n \tag{2.60}$$

and

$$D_{\rm HI} = \zeta_{CR} + k_{ci} n_e \tag{2.61}$$

where we include the effects of gas-phase recombination, k_{rec}, formation on grain surfaces, k_{gr}, cosmic ray ionisation, ζ_{CR} and free electron collisional ionisation, k_{ci}. The gas-phase recombina-

tion rate of hydrogen, $\mathrm{H\,II} + \mathrm{e}^- \rightarrow \mathrm{H\,I} + \gamma$, is that of Ferland et al. (1992) who produce a grid of temperature based recombination rates and approximate temperature dependent functions. The exact form is from Glover & Jappsen (2007), given as

$$k_{rec} = 2.753 \times 10^{-14}(315614/T)^{3/2}(1 + (115188/T)^{0.407})^{-2.242} \tag{2.62}$$

which is purely temperature dependent, but the actual recombination rate is a function of n_e and n_{HII} which are heavily density dependent. The gas phase reaction is often an order of magnitude lower than the grain phase, though will exceed the grain phase in the highest density regions. The grain phase recombination, $\mathrm{H\,II} + \mathrm{e}^- + \mathrm{grain} \rightarrow \mathrm{H\,I} + \mathrm{grain}$, is given in Weingartner & Draine (2001) as;

$$k_{gr} = \frac{1.22 \times 10^{-13}}{1 + 8.074 \times 10^{-6}\psi^{1.378}(1 + 508.7T^{0.01586}\psi^{-0.4723-1.102\times10^{-5}\ln T})} \tag{2.63}$$

with the effect of grain charging is characterised by ψ parameter, given by $\psi = G_{dust}\sqrt{T}/n_e$. The ionisation of H I comes from a combination of cosmic ray ionisation and ionisation by collisions with free electrons, $\mathrm{H\,I} + e^- \rightarrow \mathrm{H\,II} + 2e^-$, from Abel et al. (1997) at a rate

$$k_{ci} = \exp\left(\sum_{i=1}^{8} c_i(\ln T)^i\right) \tag{2.64}$$

where the c_i parameters were fit to experimental data. This rate decays extremely fast with increasing density (and decreasing temperature), as seen in Fig. 2.13, and so will only add to additional ionisation already caused by cosmic rays. The evolution track of H I ionisation is shown in Fig. 2.14 (left panels). The figure shows that the ionisation is of little importance in the cold phase of the ISM ($n >$ cm^{-3}) and has a near linear dependance on density in the warm phase. The maximum ionisation fractions seen in our calculations are approximately 15%. While seemingly low, it is not surprising considering we are not effectively modelling the hot ISM component.

An important note is that we are talking about the hydrogen ionisation fraction above. The actual abundance of atomic hydrogen is the amount of unionised hydrogen that is not locked in molecular form, $\chi_{\mathrm{HI}}(1 - \chi_{\mathrm{H_2}})$.

H_2 chemistry

The chemistry of H_2 used here is taken from Bergin et al. (2004) and Draine & Bertoldi (1996) based on the work of Hollenbach et al. (1971), and used by Glover & Mac Low (2007) and Dobbs et al. (2008). The creation and destruction terms are given by

$$C_{\mathrm{H_2}} = R_{gr}(T)n_{tot}n_{\mathrm{HI}} \tag{2.65}$$

and

$$D_{\mathrm{H_2}} = \zeta_{CR} + \zeta_{\mathrm{H_2}}(N_{\mathrm{H_2}}, N_{\mathrm{tot}}). \tag{2.66}$$

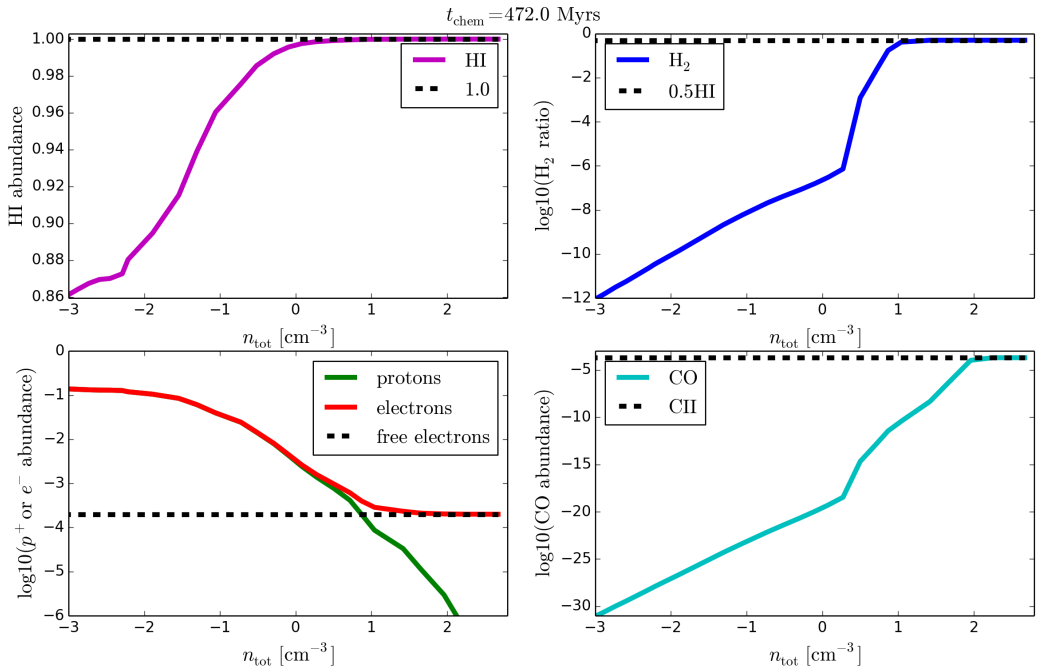

Figure 2.14: Chemical evolution for a simple 1D code with a fixed *P-T* profile (Figure 2.12). Moelcular processes are a strong function of total gas density, with abundances displaying a sharp increase in the region of thermal instability of the ISM phase diagram. The ionisation fraction of H I also scales with density, reaching a maximum ionisation fraction of 15% in our calculations. The high density limits for the H I, H_2 and CO abundances of 1, 0.5 and $\chi_{\rm CII}$ are shown as dashed lines.

where H_2 is formed on grain surfaces and is destroyed by photo-dissociation and cosmic rays. The formation of H_2 on grain surfaces occurs at a rate of

$$R_{gr}(T) = R_{gr}(T_\circ) S \sqrt{T} \ {\rm cm^3 s^{-1} K^{-0.5}}, \tag{2.67}$$

where $R_{gr}(T_\circ) = 2.2 \times 10^{-18} {\rm cm^3 s^{-1}}$ and the grain formation efficiency is $S \approx 0.3$. The efficiency factor should be a function of gas and grain temperatures, but we use a fixed value for simplicity (Dobbs et al. 2008). The destruction of H_2 is a result of cosmic ray photo-ionisation, ζ_{CR}, and a local photo-destruction term, $\zeta_{\rm H_2}$, which is a function of the column density and the visual extinction, A_v. The term takes the form as given in Draine & Bertoldi (1996)

$$\zeta_{\rm H_2}(N_{\rm H_2}, N_{\rm tot}, A_v) = f_{\rm shield}(N_{\rm H_2}) f_{\rm dust}(N_{tot}) \zeta_{\rm H_2}(0) \tag{2.68}$$

where the constant raw/unshielded photo-dissociation rate is $\zeta_{\rm H_2}(0)$ (with a UV field strength of $G_\circ$ built in). The additional terms are the dust shielding/attenuation, $f_{\rm dust}$ and the self-shielding, f_{shield} (i.e. shielding by absorption of other H_2 molecules). The dust shielding factor is similar to that used in the cooling, specifically given by

$$f_{\rm dust} = e^{-\tau_{d,1000}} \tag{2.69}$$

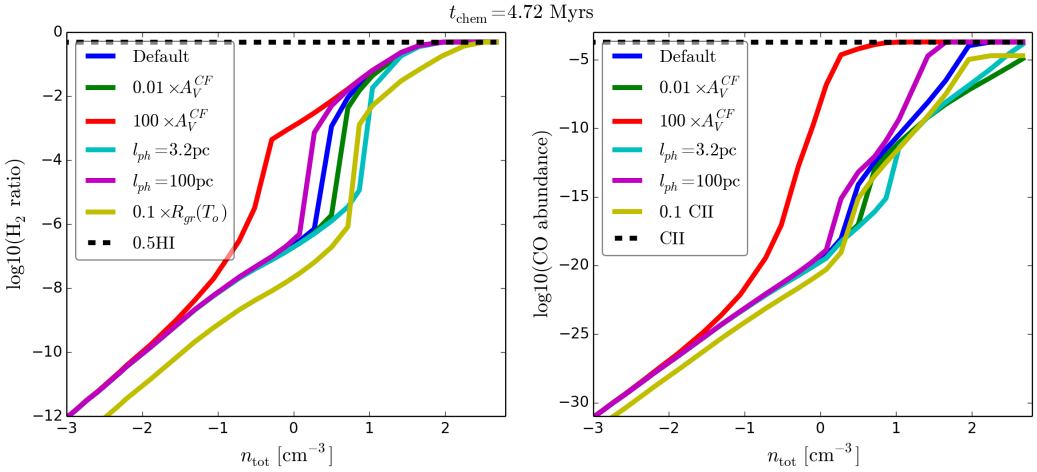

Figure 2.15: Similar evolution tracks as Figure 2.14 but showing the effect of different values of A_V^{CF}, l_{ph}, $R_{gr}(T_\circ)$ and C II on the formation of H_2 and CO.

where the optical depth for shielding is taken at 1000Å. This is given by the $\tau_{d,1000} = \gamma_{H_2} A_V$ where the visual extinction can be calculated from the column density of the gas and $\gamma_{H_2} = 3.74$ (Glover et al. 2010) for the diffuse ISM where $R_V \approx 3.1$, but could grow much greater in the dense, $R_V \approx 5$, ISM. The self shielding factor is given by

$$f_{\rm shield} = \frac{0.965}{(1 + x/b_5)^2} + \frac{0.035}{\sqrt{1+x}} \exp\left[-8.5 \times 10^{-4} \sqrt{1+x}\right] \tag{2.70}$$

where $x = N_{H_2}/5 \times 10^{14}$ cm^{-2} and b_5 is the Doppler broadening width of the line absorption in units of 10^5cms^{-1}, where we adopt 3km s^{-1} (Lee et al. 1996), and approximate column densities by $N_X = n_X l$.

The cosmic ray rate is only significant in regions of high column density gas where H_2 is well shielded against the surrounding UV field (middle, Fig. 2.13). The grain formation rate is predominantly a linear function of density, with the $\sqrt{T}$ dependance only having a marginal effect. The majority of parameters included in the above equations do not have a very strong effect on the global H_2 production, illustrated by Figure 2.15. The impact of varying l_{ph} and A_V^{CF} is only noticeable in the mid-density regime. Changes in the extinction conversion factor, A_V^{CF}, need to be of around two orders of magnitude to see a noticeable difference H_2 production. Fortunately the parameter with the greatest uncertainty, the distance for column density calculations, shows to only impact the density range of 1cm^{-3} < n < 10cm^{-3}. Even then the change is only minor considering the distance is changed from 3.2-100pc.

CO chemistry

The chemistry underlying the production of CO is somewhat more complicated than that of H_2 due to the wealth of intermediate species between the atomic and final molecular stage of CO. Previous studies rarely attempt to model all the species involved in CO formation/destruction due to the cripplingly slow speed it which it would take to evolve all these species, and their ions.

Instead works in the literature focus on what they deem to be the most important rates for the problem at hand. In Glover et al. (2010) the authors compare some of these different approaches including (ordered by complexity) Glover et al. (2010), Keto & Caselli (2008), Nelson & Langer (1999) and Nelson & Langer (1997), ranging from modelling 218 to 4 reactions. The authors find that more reactants doesn't necessarily imply better accuracy, and that if the primary concern is the distribution of galactic CO then even the simplest model does a good job compared to the those with much greater complexity. In light of this we utilise the simple model of Nelson & Langer (1997)[10]. In this model C II is converted to CO through the production of some intermediate hydrocarbon step, denoted CH_X, resulting from an initial reaction of C II with H_2 (at a rate k_0). An intermediate stage of the neutralisation of CH_2^+ to CH_X (encompassing CH_2 and CH) is not modelled, and is assumed to occur on timescales much smaller than anything else in the CO formation process. The CO and CH_X are subjected to photodestruction which is several orders of magnitude stronger than cosmic ray ionisation in most regions. The creation and destruction rates of CO are

$$C_{\rm CO} = k_0 n_{\rm H_2} n_{\rm CII} \beta \tag{2.71}$$

and

$$D_{\rm CO} = \zeta_{\rm CO}(N_{tot}), \tag{2.72}$$

where β quantifies the efficiency of the reaction $CH_X + O\,I \rightarrow CO + H_X$ (at a rate k_1) over the photodestruction of CH_X. This is represented by

$$\beta = \frac{k_1 n_{\rm OI}}{k_1 n_{\rm OI} + \zeta_{\rm CH_X}(N_{tot})}. \tag{2.73}$$

The abundances of O I and C II are needed to quantify the production of CO, however as we have already mentioned these are not species we follow in our calculations. We make the basic assumption that O I and C II are either in their original forms or locked into CO, i.e. $n_{\rm CII}(t) = n_{\rm CII}(0) - n_{\rm CO}(t)$ and $n_{\rm OI}(t) = n_{\rm OI}(0) - n_{\rm CO}(t)$. The two separate photo-destruction rates are given by

$$\zeta_{\rm CH_X}(N_{tot}) = G_{dust}\, \zeta_{\rm CH_X}(0) \tag{2.74}$$

and

$$\zeta_{\rm CO}(N_{tot}) = G_{dust}\, \zeta_{\rm CO}(0) \tag{2.75}$$

where $\zeta_{\rm CH_X}(0) = 5{\times}10^{-10}{\rm s}^{-1}$ and $\zeta_{\rm CO}(0) = 1{\times}10^{-10}{\rm s}^{-1}$ and the UV field coupled to the dust attenuation is similar to previous sections, $G_{dust} = G_\circ f_{dust} = G_\circ e^{-\tau_{UV}}$. The visual extinction is grouped together for both processes and calculated using the total column density as $\tau_{UV} = \gamma_{\rm CO,CH_X} A_V$ where $\gamma_{\rm CO,CH_X} = 2.5$ (Nelson & Langer 1997). There have been a few simplifications in this model, not including the simplification of a limited number of tracked species and reactions. No self-shielding of CO, or shielding by H_2 is included (f_{H_2},f_{CO}), which will inhibit the destruction of CO in high density regions. Tabulated forms of these shielding factors are given by (Lee et al.

[10]We actually use the formulation from Glover & Clark (2012) as it appears there are a couple of minor typos in the equations of Nelson & Langer (1997) that allow CO formation in the complete absence of H_2. Though this change made only very minor difference to the CO abundance, and only at the highest densities.

1996), but we maintain standard form from Nelson & Langer (1997) as above. We also do not include cosmic ray ionisation in the CO chemistry as the photodissociation rate is many orders of magnitude greater. Even when using 1000 times our fiducial value of ζ_{CR} there was no visible effect on the evolution track of CO in shown in Fig. 2.15. There is also the assumption that the dust shielding factors ($\gamma_{\rm X}$) are the same for all reactions in the CO chemistry. In the substantially more complicated chemical network of Nelson & Langer (1999) the authors use separate factors of $\gamma_{\rm CO} = 3$ and $\gamma_{\rm CH_X} = 1.5$. Individual coefficients for the $\rm CH_X$ components are given in Glover et al. (2010) as $\gamma_{\rm CH}$ =1.2-2.8 and $\gamma_{\rm CH_2}$ =1.7-2.3 depending on whether the reaction is dissociative (former) or ionising (later), though the incorporation of these would require a much more sophisticated network. This additional shielding is of little importance in the simulations shown here, as once present in the coldest regions it is very stable, there is no efficient heating mechanism to break it apart once there. Thus any additional shielding to the photo-dissociation is not needed, as the CO is already saturated. If we were to include additional feedback mechanisms then additional shielding may be required.

The behaviour of CO with varying A_V^{CF} or l_{ph} is similar to $\rm H_2$ in Figure 2.15. The broad evolution is insensitive to small variations in either parameter. However, with either l_{ph} as low as 3.2pc or an extinction factor two orders of magnitude lower than fiducial value then C II is no longer fully saturated into CO in the range of densities modelled in our calculations.

Reaction	Description	Reference
$\rm H\,II + e^- + grain \rightarrow H\,I + grain$	Grain surface formation	Weingartner & Draine (2001)
$\rm H\,II + e^- \rightarrow H\,I + \gamma$	Gas-phase recombination	Ferland et al. (1992)
$\rm H\,I + e^- \rightarrow H\,II + 2e^-$	$\rm e^-$ collisional ionisation	Abel et al. (1997)
$\rm H\,I + c.r. \rightarrow +H\,II + e^-$	Cosmic ray ionisation	Glover & Mac Low (2007)
$\rm H\,I + H\,I + grain \rightarrow H_2 + grain$	Grain surface formation	Bergin et al. (2004)
$\rm H_2 + \gamma \rightarrow 2H\,I$	UV photodissociation	Draine & Bertoldi (1996)
$\rm H_2 + c.r. \rightarrow H_2^+ + e^-$	Cosmic ray ionisation	Bergin et al. (2004)
$\rm C\,II + H_2 \rightarrow CH_2^+ + \gamma$	Radiative association	Nelson & Langer (1997)
$\rm CH_2^+ + various \rightarrow CH_X + various$	Rapid neutralisation*	-
$\rm CH_X + O\,I \rightarrow CO + H_X$	Gas phase formation	-
$\rm CH_X + \gamma \rightarrow C + H_X$	UV photodissociation	-
$\rm CO + \gamma \rightarrow C\,I + O\,I$	UV photodissociation†	-

Table 2.3: Processes present in our chemical model focussed on tracing the evolution of H I, $\rm H_2$ and CO with their relevant references.

* Process is intermediate and is assumed rather than fully represented.

† C I is not present in our chemistry, but is assumed to very rapidly photoionise to C II.

Term	Description	Value
l_{cool}	Distance measurement for cooling	10 pc
$l_{\rm HI}$	Distance measurement H I chemistry	100 pc
l_{ph}	Distance measurement for H_2 and CO chemistry (B star)	35 pc
$R_{gr}(T_o)$	H_2 grain formation rate at T_o = 100K	6×10^{-18}cm^{3}s^{-1}
k_0	CH_X intermediate species formation rate from C II	5×10^{-16} cm^{3}s^{-1}
k_1	CO formation rate from O I + CH_X	5×10^{-10} cm^{3}s^{-1}
$\zeta_{\rm H_2}(0)$	Unshielded H_2 photodissociation rate	4.17×10^{-11} s^{-1}
$\zeta_{\rm CH_X}(0)$	Unshielded CH_X photodissociation rate	5.00×10^{-10} s^{-1}
$\zeta_{\rm CO}(0)$	Unshielded CO photodissociation rate	1.00×10^{-10} s^{-1}
ζ_{CR}	Cosmic ray ionisation rate	1.00×10^{-17} s^{-1}
$\gamma_{\rm H_2}$	Dust shielding factor of H_2 photodissociation	3.74
$\gamma_{\rm CO,CH_X}$	Dust shielding factor of CO & CH_X photodissociation	2.50
b_5	Doppler broadening factor for H_2	3 km s^{-1}
T_{dust}	Dust temperature for heating/cooling	10 K
A_V^{CF}	Visual extinction conversion factor (A_V/N_{tot})	5.348×10^{-22} cm^{-2}
G_o	Strength of the UV radiation field in Habing units	1.56
$\chi_{\rm He}$	He abundance	1.0×10^{-1}
$\chi_{\rm el}$	free e$^-$ abundance	2.0×10^{-4}
$\chi_{\rm CII}$	CII abundance	2.0×10^{-4}
$\chi_{\rm SiII}$	SiII abundance	3.0×10^{-5}
$\chi_{\rm OI}$	OI abundance	4.5×10^{-4}
$\chi_{\rm CI}$	CI abundance	0.0
$\chi_{\rm SiI}$	SiI abundance	0.0

Table 2.4: Various parameters and their adopted values for the various chemistry and cooling routines used in this thesis, unless otherwise specified.

2.4 Chapter summary

In this chapter the we have outlined the main computational details of our calculations presented in the remainder of this thesis. In Section 2.2 we discussed the primary workhorse of our investigation, smoothed particle hydrodynamics, used to simulate the evolution of the ISM on a galactic scale. The SPH density formulation was constructed, and momentum and energy rate equations we derived. These including the effect of hydrodynamical and artificially dissipative forces, taking the general forms

$$Dv/Dt = f_{hydro} + f_{AV} + f_{ext}, \tag{2.76}$$

$$DU/Dt = \dot{U}_{hydro} + \dot{U}_{AV} + \dot{U}_{AC} + \dot{U}_{ISM} \tag{2.77}$$

where f_{ext} will be discussed further Chapters 3 and 5. In the former case this is due to purely analytical, smooth potentials, while in the later this is a combination of analytical potentials and the evolution of an N-body stellar component. The importance of artificial dissipation was also discussed (f_{AV}, $\dot{U}_{AV}$, $\dot{U}_{AC}$), required to correctly capture shocks in the converging flows and contact discontinuities, illustrated with a few well known test cases. The two SPH codes utilised in this work were briefly discussed, and a few test calculations were presented to illustrate correct behaviour of the codes in a galactic context.

Section 2.3 presents the main adaptations to required to track the molecular content of the ISM. The thermal profile is reproduced by the inclusion of the $\dot{U}_{ISM}$ term. This includes the various heating and cooling mechanisms of importance to galactic scales, and is discussed briefly in Section 2.3.1. A simple chemical network is also included that allows the tracing of the abundances of H I, H_2 and most importantly CO. The chemical processes are outlined in Section 2.3.2 including the effects of grain formation, gas phase formation, cosmic ray ionisation and photodestruction. While seemingly rudimentary, the chemistry includes the basic processes required to track the global distribution of molecular gas. If smaller scale structures such as individual clouds were the subject of investigation then the chemical network, and possibly cooling processes, would need to be substantially more complex.

To actually construct our synthetic observations we must use another numerical technique to calculate the emission from the ISM gas. A brief discussion of the theory of radiative transfer, and the TORUS code used is included in Chapter 4.

3

Simulations with fixed analytic potentials I: armed and barred simulations

"In the beginning the universe was created. This made a lot of people very angry and has been widely regarded as a bad move."
– Douglas Adams, The Hitchhikers Guide to the Galaxy, 1978

3.1 Introduction

In order to construct synthetic emission maps, numerical simulations are needed to generate the kinetic, thermodynamical and chemical properties of the ISM gas. The simplest way to do so is to subject the gas to a number of gravitational fields that represent the various mass components of our Galaxy. This includes the central bulge, the disc in which the Earth resides, and the dark matter halo, required to reproduce the observed flat rotation curve. With these three components we can simulate a basic disc galaxy structure. The arms and bar are second order mass components that, while being weak in comparison to the bulge-disc-halo system, define the characteristic morphology of any disc galaxy. These are added through the addition of further gravitational fields, and are altered to investigate the effect of the morphology on the emission features seen in observations. The arm parameters under investigation are the rotation speed, the arm number and the pitch angle while for the bar we focus on the pattern speed and orientation. We also test different formulations of arm and bar structures, and the effect of the mass of each component.

Before including both arm and bar components together in the same simulation, the effects of each individually are studied. When creating synthetic observations it became clear that there is a significant parameter space that also needed exploring, the position and velocity of the observer.

A simple fitting routine was developed to narrow down the parameter space for each component and find the best fitting observer coordinates. This was done by the use of simple *l*-*v* maps not built using radiative transfer, and is discussed later in this chapter.

The combined arm and bar simulations, and the process of creating full radiative transfer synthetic observations, is the subject of Chapter 4.

3.2 Galatic potentials

The most important ingredient when simulating galactic scales is the inclusion of the gravitational force. For ISM gas this is dominated by the gravitational attraction of the stellar and dark matter distribution. The computation of the gravitational forces from the many billions of stars upon each SPH gas particle would be cripplingly slow for the calculation. Instead the large scale matter distribution is approximated by a continuous density distribution, significantly reducing the computational effort. This density distribution is related to the gravitational potential, Φ, by Poisson's equation, $\nabla^2\Phi = \rho_{ext}(r)4\pi G$. The force on each particle is then simply calculated from the derivative of the potential

$$\vec{f}_{ext,a} = m\frac{D\vec{v}_a}{Dt} = -\vec{\nabla}_a\Phi(\vec{r}_a) \tag{3.1}$$

which can easily be included in the SPH momentum equation (Equation 2.76). The actual form of the full galactic potential must take into account the density distribution of the Galaxy in all components. The potential is decomposed morphologically into a halo, a disc, a bulge, numerous arms, and at least one bar component

$$\Phi(\varpi, z, \phi, t) = \Phi_d(\varpi, z) + \Phi_b(\varpi, z) + \Phi_h(r) + \Phi_{bar}(\varpi, z, \phi, t) + \Phi_{sp}(\varpi, z, \phi, t) \tag{3.2}$$

where we will primarily working in cylindrical polar co-ordinates from here onwards ($\varpi^2 = x^2+y^2$ and $r^2 = \varpi^2 + z^2$).

3.2.1 Axisymmetric potentials

While some previous studies have used potentials to produce completely flat rotation curves (e.g. Binney & Tremaine 1987), this fails to capture peak velocities near the galactic centre. This is shown in the rotation curve in Figure 3.1, using rotation curve data from Sofue (2012). Early tests with simple single component rotation curves produced *l*-*v* diagrams that were too-shallow in velocity towards the Galactic centre, because by construction these flat rotation curves are decaying in velocity rather than increasing at $R = 1$kpc.

A true Milky Way model must reproduce a semi-flat rotation curve with a magnitude of around 220kms^{-1} near the Solar position ($\approx$ 8kpc). We use an axisymmetric disc, bulge and halo based on that of Pichardo et al. (2003) and Allen & Santillan (1991). The disc component is the standard Miyamoto-Nagai form (Miyamoto & Nagai 1975) with a potential of

$$\Phi_d(\varpi, z) = \frac{GM_d}{(\varpi^2 + [a_d + (z^2 + b_d^2)^{1/2}]^2)^{1/2}}, \tag{3.3}$$

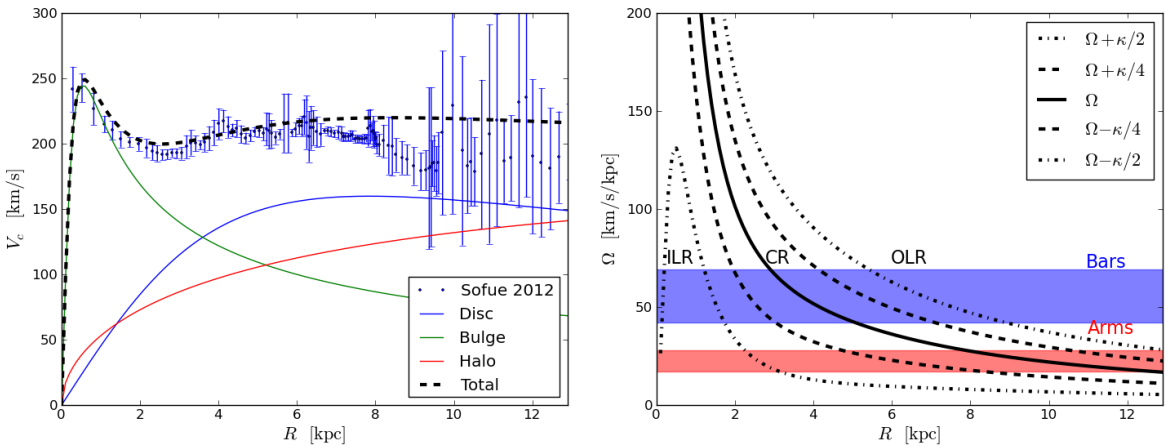

(a) Galactic rotation curve

(b) Galactic resonance features

Figure 3.1: Left: rotation curve used in our simulations resulting from axisymmetric galactic potentials with observed rotation curve data from Sofue (2012). The dashed line is the combined bulge-disc-halo model from Allen & Santillan (1991) shown individually in green-blue-red respectively. Right: rotation speeds from our adopted Milky Way rotation curve. The dashed and dot-dashed lines show the 4:1 and 2:1 resonances calculated from the epicycle frequency, κ. Upper and lower shaded regions show the possible region encompassed by the arm and bar pattern speeds, with maxima and minima from Gerhard (2011).

where a_d controls the radial scaling and b_d the vertical. The bulge is described by a spherical Plummer potential (Plummer 1911),

$$\Phi_b(r) = -\frac{GM_b}{\sqrt{r^2 + r_b^2}}, \tag{3.4}$$

with r_b controlling the radial scaling, and $r^2 = x^2 + y^2 + z^2$. The spherical dark matter halo is taken from Allen & Santillan (1991),

$$\Phi_h(r) = -\frac{GM_h(r)}{r} - \frac{GM_{h,0}}{\gamma r_h}\left[-\frac{\gamma}{1+(r/r_h)^\gamma} + \ln\left(1+(r/r_h)^\gamma\right)\right]_r^{r_{h,max}},$$

where $r_{h,max} = 100$ kpc is the halo truncation distance and $\gamma = 1.02$. The mass inside the radius r of the halo is given by

$$M_h(r) = \frac{M_{h,0}(r/r_h)^{\gamma+1}}{1+(r/r_h)^\gamma}. \tag{3.5}$$

The various axisymmetric potential parameters are fixed throughout all simulations to best match the rotation curve of the Milky Way and are given in Table 3.1, taken from Allen & Santillan (1991). This same bulge-disc-halo model was found to also provide a good match with more recent rotation curve measurements in Irrgang et al. (2013) but with slightly different values than those in Table 3.1. We choose to retain our values in Table 3.1 however, as they provide a better match to the inner Galaxy while keeping the rotation curve high in the outer disc. There are numerous other potential sets in the literature we could have chosen to represent the axisymmetric component, and we will in fact use a slightly different model in Chapter 5.

This is a very idealised and simplified perception of the gravitational field of our Galaxy.

Term	Description	Value
M_d	Disc mass	$8.56 \times 10^{10}\,\mathrm{M}_\odot$
M_b	Bulge mass	$1.40 \times 10^{10}\,\mathrm{M}_\odot$
$M_{h,0}$	Halo mass	$10.7 \times 10^{10}\,\mathrm{M}_\odot$
a_d	Disc radial scale length	5.30 kpc
b_d	Disc vertical scale length	0.25 kpc
r_b	Bulge radial scale length	0.39 kpc
r_h	Halo radial scale length	12.0 kpc

Table 3.1: Fixed Galactic axisymmetric potential parameters used to reproduce the observed rotation curve.

The gravitational attraction of the gas disc has been neglected, which is assumed to be negligible compared to that of the stellar disc. The stellar disc is a single component system, though there has been some evidence that the stellar disc is composed of two distinct populations (Gilmore & Reid 1983; Bovy et al. 2012). The bulge is assumed to be spherical, though there is evidence that the bulge is flattened, and non-axisymmetric (e.g. Dwek et al. 1995, McWilliam & Zoccali 2010). For simplicity we assume all asymmetry towards the Galactic centre is reproduced by the bar, and that the spherical bulge is sufficient to reproduce the features of the rotation curve. As little is known about the dark matter structure of our Galaxy, a spherically symmetric model that provides a good fit to the rotation curve is assumed sufficient. Another feature of minor importance to the work presented here is the warp of the Galactic disc (e.g. Kalberla et al. 2007), though as the warping is minor within $R < 20$ kpc it is assumed to be of little importance.

3.2.2 Spiral arm potentials

The spiral and bar features are produced by subjecting the gas to further stellar potentials. When using fixed analytic potentials the structure of the Milky Way is assumed to be that of a grand design galaxy, driven by some stable stellar density wave. The potentials used here have a constant strength throughout the simulation. The radial extent of structures is determined by the location of the inner and outer Linblad resonances, ILR and OLR, which are in turn determined by the pattern speed of the density wave, Ω_{bar} or Ω_{sp}. The frequencies resulting from our rotation curve are shown in the right panel of Fig. 3.1. For example, a 4-armed spiral perturbation with a pattern speed of $20\,\mathrm{km\,s^{-1}\,kpc^{-1}}$ has ILR, OLR and CR located at a radius 7.0, 14.4 and 10.9 kpc respectively, shown by where the $\Omega \pm \kappa/4$ and Ω lines cross $20\mathrm{km\,s^{-1}\,kpc^{-1}}$ in Fig. 3.1.

Bar and spiral potential parameters we choose to vary are summarised in Table 3.2. These include the pitch angle of spiral arms (α), the number of spiral arms (N), and the pattern speed of the bar and arms (Ω_b, Ω_{sp}). We also investigate the effects on altering the strength of the potential perturbations, though we only use two separate values for the arm and bar components. The orientation of the bar/arm features to the observer (l_{obs}), and the observer's velocity and Galactocentric distance ($V_{\mathrm{obs}}, R_{\mathrm{obs}}$) are also investigated but these are varied during the construction of l-v maps. Our choice of parameters is broad and numerous to allow for an unbiased study, with as little recourse as possible to previous findings. There is both observational and numerical evidence for different pattern speeds for the arm and bar components in our Galaxy (e.g. Gerhard 2011 and

Term	Description	Values
Ω_b	Bar pattern speed	20, 40, **50**, **60**, 70km s^{-1} kpc^{-1}
θ_b	Bar orientation	0°, 10°, ..., 50°, 60°
Ω_{sp}	Arm pattern speed	10, **15**, **20**, 25, 30km s^{-1} kpc^{-1}
α	Arm pitch angle	5°, **10°**, **12.5°**, **15°**, 20°
N	Number of arms	**2**, **4**
$\lvert\Phi_{sp}\rvert$	Relative arm potential strength	×**1**, ×2
$R_{\rm obs}$	Radial position of the observer	7, 7.5, 8, 8.5, 9 kpc
$V_{\rm obs}$	Circular velocity of the observer	200, 205, ..., 225, 230 km s^{-1}
$l_{\rm obs}$	Azimuthal position of the observer	0°, 10°, ..., 350°, 360°

Table 3.2: Variable parameters of the simulations, including those of the arm/bar potentials and those used in defining the observer co-ordinates. Parameters in bold define the refined parameter space used in calculations with both bar and arm potentials in Chapter 4.

Sellwood & Sparke 1988), though some simulations are performed with equal speeds for both components.

In Dobbs et al. (2006) a logarithmic spiral potential from Cox & Gómez (2002) was used, hereafter referred to as CG arms. This is our primary arm model, and takes the form

$$\Phi_{sp}(r,\phi,z) = 4\pi G h_z \rho_\circ \exp\left(-\frac{r-r_o}{R_s}\right)\sum_n^3 \frac{C_n}{K_n D_n}\left[\mathrm{sech}\left(\frac{K_n z}{\beta_n}\right)\right]^{\beta_n}\cos\left(N\left[\phi - t\Omega_{sp} - \frac{\ln(r/r_o)}{\tan(\alpha)}\right]\right) \tag{3.6}$$

where

$$K_n = nN/r\sin(\alpha), \tag{3.7}$$

$$D_n = \frac{1 + K_n h_z + 0.3(K_n h_z)^2}{1 + 0.3K_n h_z}, \tag{3.8}$$

$$\beta_n = K_n h_z(1 + 0.4K_n h_z), \tag{3.9}$$

and the constants are the same as those used in Dobbs et al. (2006), namely $h_z = 0.18$kpc, $R_s = 7$kpc, $r_0 = 8$kpc, $C = (8/3\pi, 1/2, 8/15\pi)$ and a fiducial spiral density of $\rho_0 = 1$ atom cm^{-3}. These spiral arms take the form of a three part sinusoidal perturbation that exponentially decays with increasing radius. The three component sum nature of the potential makes the potential relatively flat in the inter-arm region compared to a purely sinusoidal case, and more strongly peaked (Cox & Gómez 2002).

The logarithmic spiral perturbation of Pichardo et al. (2003) is also included in our calculations due to its apparent effectiveness at creating four armed spiral patterns in the ISM gas from only a two armed stellar potential (Martos et al. 2004), which has been proposed by some to be the reason behind the 4/2 armed model dichotomy in the literature (Churchwell et al. 2009). This potential is substantially more complicated and represents the spiral arms as a superposition of oblate spheroids (Schmidt 1956; Ollongren 1967) whose loci are placed along a modified

logarithmic spiral arm function of the form

$$f(r) = \frac{1}{N} \ln\left(1 + (r/r_o)^N\right) \cot(\alpha) \tag{3.10}$$

instead of the standard shape function of

$$f(r) = \ln(r/r_o) \cot(\alpha) \tag{3.11}$$

stemming from the $r = r_o e^{\tan(\alpha)\phi}$ logarithmic nature. This allows for a smooth turn off from a spiral to bar-like structure at some small radius. Each of the spheroids themselves have an linear internal density profile of $\rho_{ss}(a, r) = p_0(a, r) + ap_1(a, r)$ where a is the distance to the spheroids centre. The authors suggest the density parameters $p_0(r)$ and $p_1(r)$ themselves follow either a linear or logarithmic decay with increasing distance, r, from the Galactic centre. They find the logarithmic decrease and lower arm mass is most effective at creating secondary arm structures in the gas, so we adopt the same here. This potential had to be constructed using the work of Ollongren (1967) and Schmidt (1956) as it was not given in Pichardo et al. (2003). As this was a discrete analytic function, a derivative could easily be computed for force calculations. The full solution for the forces in the radial and azimuthal directions is given in Appendix B.1. This potential is referred to as the PM model for the remainder of this thesis.

Upon integration into the SPH code it became clear that this potential was creating a bottleneck in the run-time of the simulation. This is a result of the sum of forces over each individual spheroid in the arms, which proved to be very time-consuming at high resolutions. To combat this a 3-dimensional grid of the potential was written to a file to be read in at the start of the simulation and used throughout for all ensuing force calculations. Forces were then computed by finite differences between the potential in neighbouring grid-cells, and linear interpolation inside each cell. Sufficient resolution of the grid was determined by comparison to the analytic form of the forces. The rotation of the arms was produced by simply rotating the particles to the frame of the arms, evaluating the forces, rotating the force field back to the position of the particle and applying it (also detailed briefly in Appendix B.2).

All of our arm models are assumed to be logarithmic, with constant pitch angles and are evenly spaced azimuthally. However, as mentioned in Chapter 1, there is evidence of the individual arms of the Milky Way being best fit by different pitch angles.

3.2.3 Bar potentials

The dynamics in the inner Galaxy ($R < 4$kpc) is believed to be dominated by a bar structure, in essence a spheroid elongated along one axis parallel with the Galactic disc. Models for the bar vary greatly in complexity. These range from those tuned to match a specific density profile constrained by observations, to ones that simply give a trough of gravitational potential every π radians. Several separate bar potentials have been tested to see which functional representation best matches the l-v features of our Galaxy. The first is a commonly used sinusoidal perturbation

of the Galactic disc. We employ the specific form of Wada & Koda (2001);

$$\Phi_{bar}(r,\phi) = \Phi_0 \cos\left(2\left[\phi + \Omega_b t\right]\right) \frac{(r/r_c)^2}{\left((r/r_c)^2 + 1\right)^2}, \tag{3.12}$$

where $\Phi_0 = \epsilon V_0^2 \sqrt{27/4}$, $\epsilon = 0.05$ and $V_0 = 220\,\mathrm{km\,s^{-1}}$. We employ two different values of the bar core radius, r_c, either 2 kpc or $\sqrt{2}$ kpc (used in Wada et al. 1994 and Wada & Koda 2001 respectively). We will refer to these as the WK and WKr2 bars respectively throughout this manuscript. A measurement of the inner drop off radius of the bar potential, r_c here also determines the strength of the potential, and so these values enable us to investigate the effect of the strength of the bar. The models of Dehnen (2000) and Minchev et al. (2007) were also investigated, but showed little difference to the bar above so were not used beyond initial testing.

Another bar we employ is that of Long & Murali (1992), referred to hereafter as the LM bar. The authors provide a bar model that is simply a softened line of gravitational potential. While not physically a bar, i.e. not the result of some density profile, the effect on the gas is still that of a non-axisymmetric perturbation. This potential is aligned with the x-axis by definition so we apply co-ordinate transforms to the positions and accelerations to simulate the rotation of the bar. The potential is given by

$$\Phi_{bar}(x,y,z) = \frac{GM_{bar}}{2a} \ln\left(\frac{x - a + T_-}{x + a + T_+}\right), \tag{3.13}$$

where $T_\pm = [(a \pm x)^2 + y^2 + (b + \sqrt{c^2 + z^2})^2)]^{1/2}$, with a, b and c roughly corresponding to the bar semi-major and minor axes respectively. We adopt a bar mass of $6.25 \times 10^{10}\mathrm{M}_\odot$ as used by Lee et al. (1999) for the same potential. This bar has the advantage of a controllable minor-axis length while maintaining a simple analytical form.

Both of these models are simplistic in design, and there have been several studies that have managed to fix specific density distributions to the bar. These include the "Dwek" (Dwek et al. 1995; Zhao et al. 1996), "Ferrers" (Ferrers 1887; Kim et al. 2012) and "Freeman" (Freeman 1966) bar models, though many different prescriptions exist in the literature (e.g. Pichardo et al. 2004). A significantly more complex bar model was included in our investigated based on a peanut/boxy morphology from Wang et al. (2012). As this density profile is so complex the authors expand the potential and density into a set orthogonal basis pairs (Hernquist & Ostriker 1992; Zhao et al. 1996), of the form

$$\Phi_{bar}(r,\phi,\theta) = -\frac{GM_{bar}}{r_{bar}} \sum_{n,m,l} A_{nlm}(\rho_{bar})\Phi_{nlm}(r,\phi,\theta) \tag{3.14}$$

where Φ_{nlm} is composed of spherical associated Legendre and Gegenbauer polynomials and is independent of the actual density profile (see Wang et al. 2012 for specific formulation). The A_{nlm} coefficients contain the density information, and are constants independent of position. The coefficients provided by (Wang et al. 2012) have a built-in bulge. To keep the rotation curve consistent with the rest of our calculations the coefficients are re-computed just using the bar component. As this potential is an extremely complex function the forces are evaluated using finite differences in a pre-made potential grid (as in the PM arm model).

The final bar model used is that of Vogt & Letelier (2011). This model is similar to the

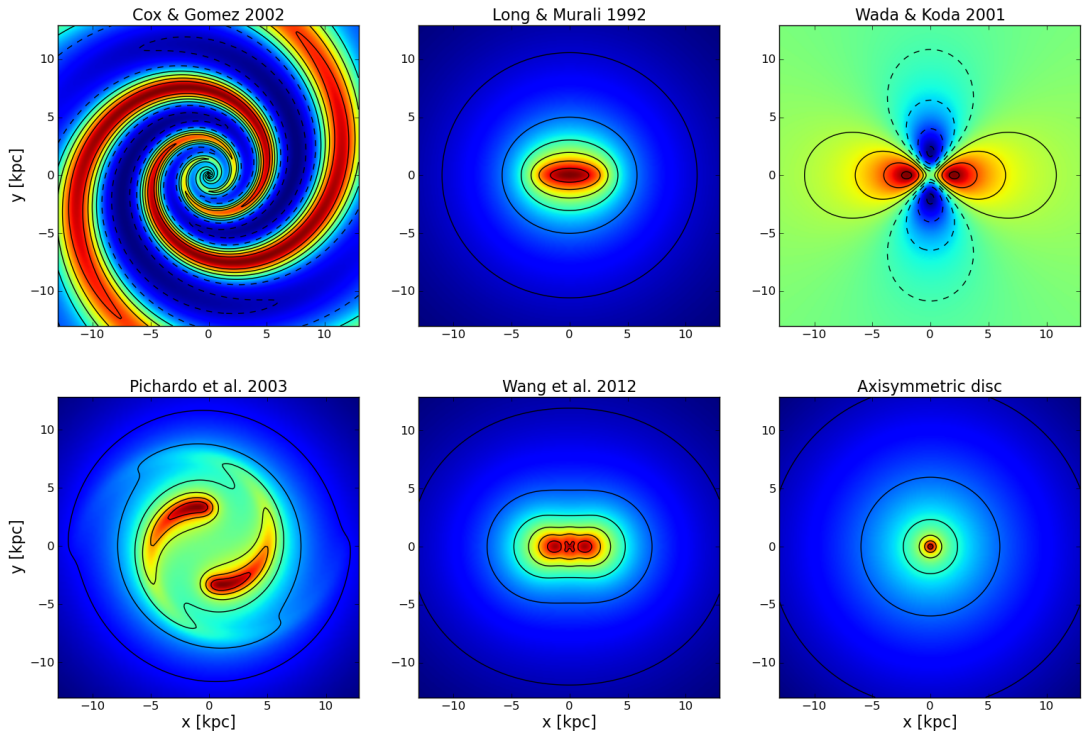

Figure 3.2: Various potentials used in our simulations. From top left to bottom right; Cox & Gómez (2002), Long & Murali (1992), Wada & Koda (2001), Pichardo et al. (2003), Wang et al. (2012) and our axisymmetric model adapted from Allen & Santillan (1991). Relative potential strength (normalised for each model) is indicated by colour scheme, with equipotential contours shown as solid (troughs) and dashed (peaks) lines.

LM bar but is adapted to allow to subtle bending into an "S" shape. This allows a bar that could smoothly tail off as it rotates, rather than abruptly cut-off at the end of the bar. The authors also provide a prescription for a "C" shape, but it is not used in this study.

Early tests were performed with the combined bar-arm model of Khoperskov et al. (2013) where a strong 2 arm, weak 4 arm, and inner bar structures are all combined into a single potential that rotates at some global pattern speed. While a reasonable approximation for the global structure of the Galaxy, this model was quickly abandoned due to its simplicity and built in assumptions of the Galactic morphology.

The gravitational fields of each of our primary potentials, including the full axisymmetric component, are shown in Figure 3.2. Here the differences between the arm potentials becomes clear. The CG arms are persistent throughout the entire disc, while the PM arms are strongest around $R = 5$kpc and decay rapidly towards the edge of the disc. The bar structures also show some striking differences. The peanut/boxy nature of the Wang et al. (2012) is only slightly visible, but is clearer if the vertical direction. The odd appearance of the WK bar is due to it being a sinusoidal perturbation to the Galactic disc with peaks/troughs every $\pi/2$ radians, with no corresponding physical density profile[1].

[1]The potentials used can be split into two distinct categories; those that perturb the gravitational field of an existing

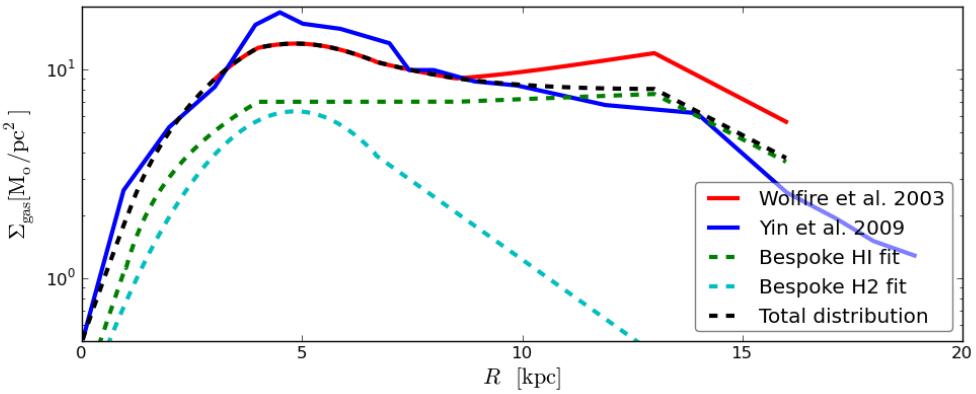

Figure 3.3: Initial surface density profile used in our simulations, shown as the black dashed line. The red line is the model of Wolfire et al. (1995) and the blue line is the data from Yin et al. (2009), taken from Boissier & Prantzos (1999), which extends to the Galactic centre. Note that we only set gas out to a radius of 13 kpc.

3.3 Setting the initial conditions

The ISM gas is initially distributed in the Galactic plane, with a disc height of 0.4 kpc. The initial vertical distribution is of little importance, as all the gas falls into a disc of height 0.1 kpc after only 50Myrs of evolution. The initial surface density profile is chosen to match observational data. This is based on the functional form of Wolfire et al. (2003). We impose a flat distribution instead of the slightly increasing density profile in the 8.5-13.0 kpc region so that our surface density is not increasing near the edge of the disc. Some observations suggest the distribution is effectively flat from 5-15 kpc (see Kalberla & Kerp 2009 and references therein). We also extrapolate the density profile to the Galactic centre, using the data from Yin et al. (2009). Our adapted surface density function is thus for H I

$$\Sigma_{\rm HI}(R) = 1 M_\odot\,{\rm pc}^{-2} \times \begin{cases} 0.2\exp\left(R_k/0.7\right) & 0 \le R_k < 1 \\ 1.4R_k - 0.6 & 1 \le R_k < 4 \\ 5 & 4 \le R_k < 8.5 \\ 4.15 + 0.1R_k & 8.5 \le R_k < 13 \end{cases} \tag{3.15}$$

and for H_2

$$\Sigma_{\rm H_2}(R) = 1 M_\odot\,{\rm pc}^{-2} \times \begin{cases} 4.5\exp\left(-\left[\frac{R_k-4.845}{2.6545}\right]^2\right) & 0 \le R_k < 6.67 \\ 2.5\exp\left(\frac{6.97-R_k}{2.89}\right) & 6.67 \le R_k < 24 \end{cases} \tag{3.16}$$

where $R_k = R/1{\rm kpc}$. Both are added together to give the distribution in Figure 3.3. Gas in our simulations is set between 0 and 13 kpc. To actually place the gas the surface density profile is used as a PDF (probability density function), which is then integrated to create a CDF (cumulative distribution function), which is then tabulated and inverted to allow the drawing of semi-random particle positions according to the surface density shown in Fig. 3.3. The azimuthal position is

Galactic disc (WK and CG models), or those that add an extra mass component to the system (LM and PM models). While this implies the latter category will cause an overall increase in the rotation curve, the effect of this was seen to be marginal due to the weak nature of all the potentials used here.

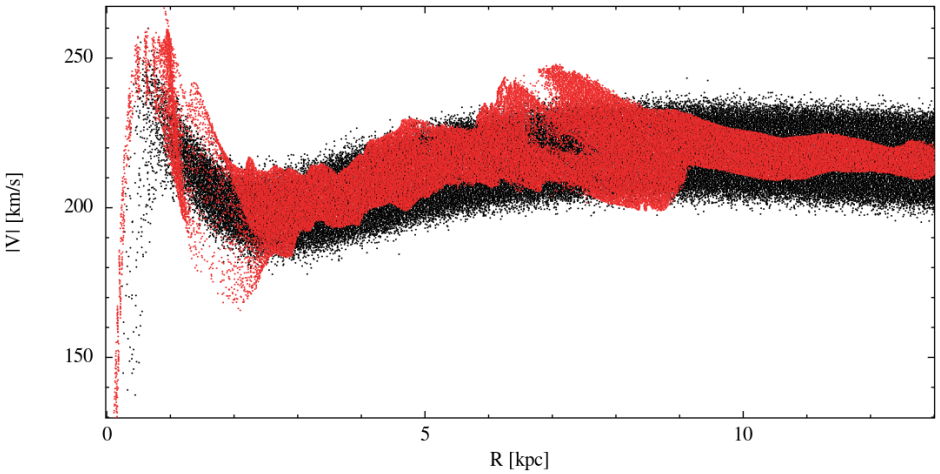

Figure 3.4: Initial rotation curve from an ISM simulation of 1 million SPH particles (black points) and after 300Myrs embedded in a barred-spiral potential (red points). Regions of higher dispersion coincide with arm and bar resonance regions.

drawn from a uniform random distribution from 0-2π. Our choice of limiting our disc to 13 kpc ensures the major spiral features recorded in the literature are included as far out as the Outer and Perseus arms. Though there is some evidence for weak spiral structure extending to 20 kpc (Levine et al. 2006), this would have required a large increase in particle number to achieve the same resolution, whilst any features at such large radius would have little influence on our results due to the low gas density in the far outer disc. Integration of this surface mass distribution gives a total gas mass of approximately 8×10^9 M$_\odot$, corresponding to an average ISM density of approximately 1 g cm^{-3} or 15M$_\odot$ pc^{-2}. This is used as our fiducial disc mass, though simulations are also performed with lower values to test the effect of the gas mass.

Initial velocities are seeded from the axisymmetric potentials directly via

$$v_c^2(R) = R\frac{d}{dR}\left[\Phi_d + \Phi_h + \Phi_b\right] \tag{3.17}$$

which is then split between v_x and v_y to ensure a purely circular orbit at t = 0Myrs. A random velocity perturbation is added to each component drawn from a Gaussian distribution of width 5 km s^{-1}, so that $\vec{v}(t = 0\text{Myrs}) = (v_c \sin\phi + \delta v_x, -v_c \cos\phi + \delta v_y, +\delta v_z)$. An example of a rotation curve from a barred-spiral model is shown in Figure 3.4 where the black points show the rotation at t = 0Myrs and red points after 300Myrs of evolution in a barred-spiral potential. The rotation curve at later times does not deviate strongly from that initially, but there is considerable dispersion at the resonance radii of the bar and spiral features (R = 2kpc and R = 8kpc).

The remaining value needed to set up the SPH particles is the initial gas temperature (which determines the internal energies). Obviously this will have a large effect on isothermal simulations, where the internal energy will not change and will dictate the efficiency of gas mixing. In adiabatic+cooling simulations it is less obvious how this would effect the evolution of the system. Tests were performed with gas initially at 10000K and 200K with active ISM chemistry and cooling. Gas is seen to cool very fast in the hotter simulation, and after 15Myrs has reached the same magnitudes as the colder simulation. After 100Myrs there is only minimal differences between

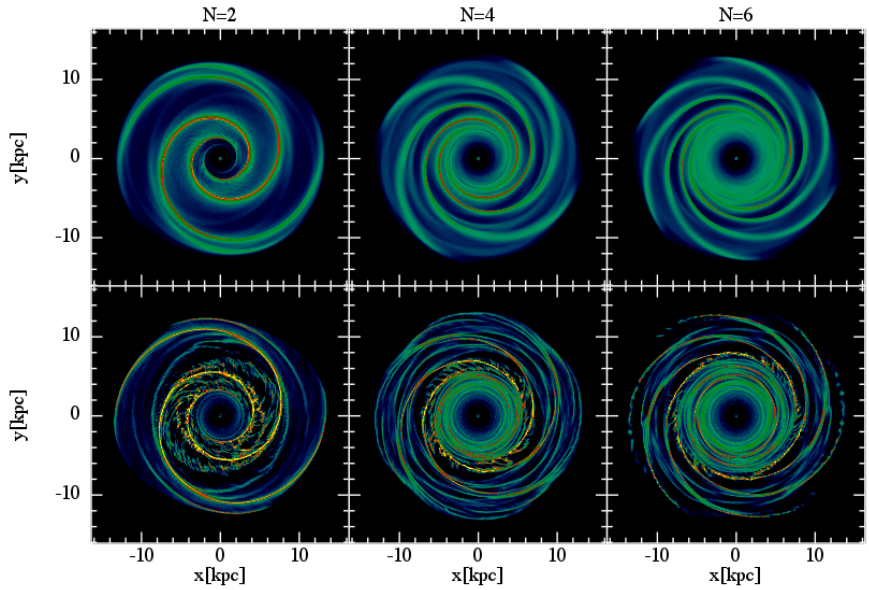

Figure 3.5: Isothermal calculations with $T = 10000$K (top) and $T = 200$K (bottom) for $N = 2, 4, 6$ armed models using the CG potential.

the initially hot and cold disc. As the simulations are normally ran for at least 200Myrs (to ensure all particles and potentials have conducted at least one full rotation) the initial temperature of the gas is assumed unimportant. To avoid spurious side-effects of the rapid cooling of an initially hot disc the initial temperature of the gas particles is set to $T = 200$K.

Our fiducial simulation resolution is 5 million SPH particles. Tests were made with 1-10 million particles. Morphological differences were minor between the different resolutions, but the amount of CO created was considerably reduced with lower resolutions. 5 million particles was found to be a good trade off between CO production and run-time. This was further supported by tests with *l*-*v* maps, where the additional emission from the increase to 10 million particles was marginal compared to the increase from 1-5 million. See Section 4.4.1 for a more in-depth analysis of the effect of simulation resolution.

3.4 Isothermal simulations: testing the potentials

In this section the general features of the potentials in isothermal calculations are shown. The cooling and chemically active calculations take considerably longer to run, so isothermal calculations provide a good test-bed for the various potentials before full production calculations are made. Simulations presented here are at a resolution of 1 million SPH particles. The effect of varying temperature in simple isothermal calculations is shown in Figure 3.5, where the top row shows calculations at $T = 10000$K and the bottom at $T = 200$K for various numbers of arms using the CG model at $\Omega_{sp} = 20\mathrm{km\,s^{-1}\,kpc^{-1}}$. The hotter calculations are much "cleaner", in that the gas is clearly smoothly tracing out the spiral potential, producing regions of high density in the bottom of the potential wells. The colder simulations reach much higher densities but also have a large amount of supplementary structure. The $N = 4$ model in particular has a large amount of arm

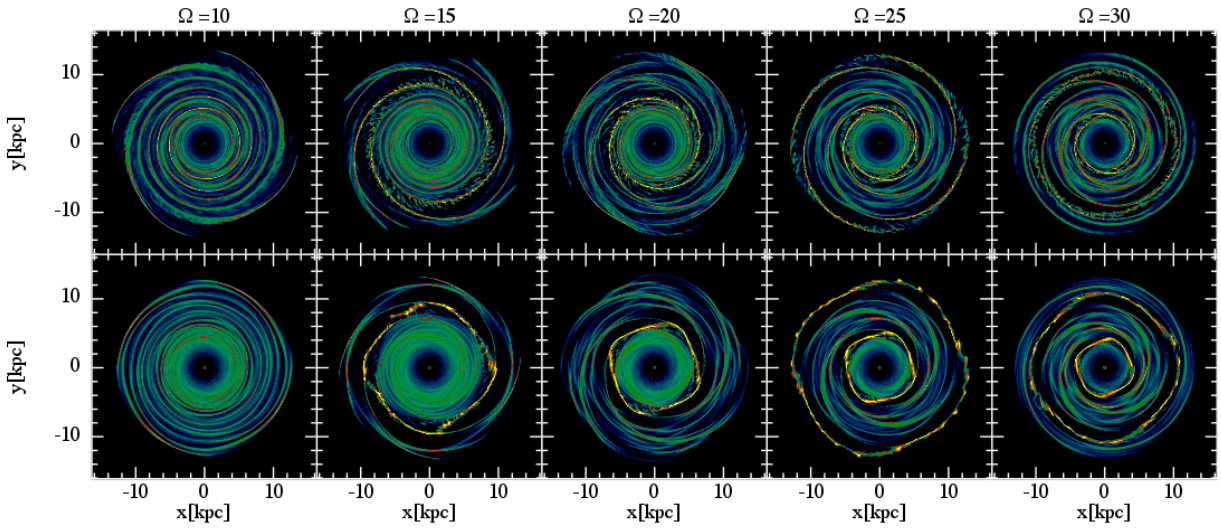

Figure 3.6: Isothermal simulations with $T = 200$K and varying spiral arm pattern speed (10-30km s^{-1} kpc^{-1}, increasing to right) for a four-armed potential at two different times (400Myrs top and 1Gyr bottom).

branches that are not associated with the bottom of the potential well. The increased temperature of the simulations with warm gas makes the gas much more diffuse, and disperses these features. Traces of these branches can still be seen, but are much less defined than the cooler simulations (seen by comparing the hot and cold $N = 4$ models). Shocks experienced upon the passage into arms are also much weaker. Another feature exclusive to the cold models is the onset of spurs (small scale features peeling away from the arms at a large pitch angle, see Dobbs & Bonnell 2006) in the mid-disc. These are clearest in the $N = 2$ case and occur near to the location of the ILR (see Fig. 3.1b).

To investigate the effect of the ILR and OLR on the gaseous structures further calculations were ran with differing arm numbers and pattern speeds, values of which determine the radial positions of the resonances. Figure 3.6 shows simulations with differing arm pattern speeds after 400Myrs and 1Gyr of evolution. As pattern speed increases to the right the location of the ILR can clearly be seen to radially contract, initially lying beyond the disc edge in the 10km s^{-1} kpc^{-1}case. The OLR is then seen the appear as the pattern speed is increased, becoming apparent only in the model with the fastest rotation. The spurring appears predominantly at the ILR and OLR. At the later time stamp of 1Gyr the gas at the ILR and OLR creates closed orbits that match the orbits proposed by density wave theory, the same as those shown in Figure 1.9. The spiral structure is then seen only to exist between the ILR and OLR. The timescales needed to see these enclosed orbits is well beyond the timescale required for chemistry to settle to a steady state (see Section 3.5). The location of these features can be used to infer some information about Galactic spiral structure. For instance, a $N = 6$, $\Omega_{sp} = 25$km s^{-1} kpc^{-1} model has an ILR inside of 10kpc and therefore it is unlikely that such a model would produce spiral features beyond this radius, such as seen in the Outer arm, and so is a poor choice for our Galaxy.

There appears a lot of branching structure between the arms in the colder models, and this

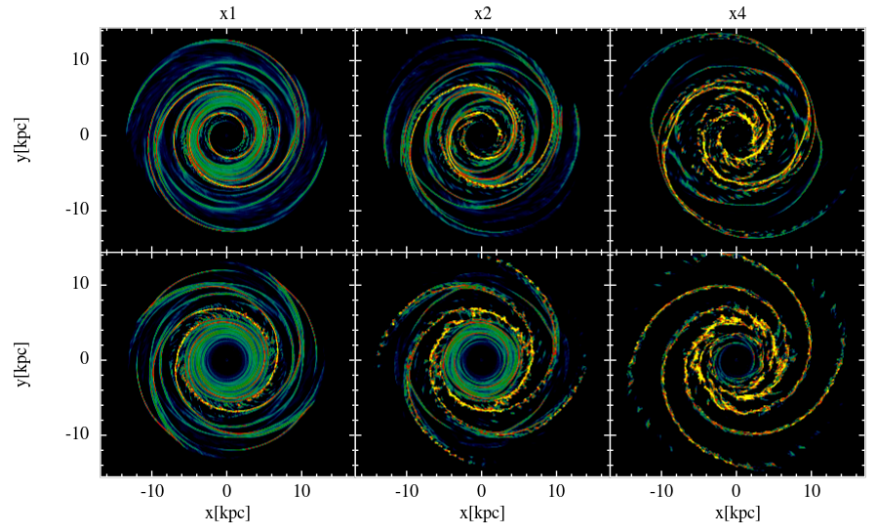

Figure 3.7: Isothermal simulations of with $T = 200$K with varying potential strength (1, 2, 4×$\rho_\circ$) after 400Myrs of evolution. The top and bottom rows show $N = 2$ and $N = 4$ models respectively.

is especially so in the case of $N = 2$. The superposition of arm features in the CG model could be a cause of this, due to the triple minima nature of a superimposed three component spiral pattern. To check this was not the case, calculations were performed with only certain components of the spiral summation in Equation 3.6 active. The resulting spiral structures were much weaker than in the three component case, and less pronounced at larger radii. Furthermore, the inter-arm branches were still present, implying they are not a result of the superposition nature of the CG model.

Some of the arm features are quite weak in the plots shown above, even between the ILR and OLR. To try and improve the tracing of the spiral potential in these models, calculations were performed with ×2 and ×4 the standard spiral arm density ($\rho_\circ$ in Equation 3.6). The results of 2 and 4 armed calculations with different strengths are shown in Figure 3.7. The higher the strength, the higher the densities in the arms become, and the clearer the spiral structure in the gas appears. The highest strength calculation has little gas in the inter-arm region, not merely just low density gas, but very few actual gas particles. There is also a significant amount of dispersion in the rotation curve in the highest strength calculation. There appears to be a sort of buckling effect near the ILR, where the highest density regions are not tracing the logarithmic spiral structure well. Due to these reasons the ×4 strength model seems inappropriate for further use. However the ×2 model still has a large amount of inter-arm gas and only moderate dispersion of the rotation curve, so this model is deemed as appropriate for further calculations with chemistry and cooling along with the fiducial value.

The bar models show a similar behaviour with pattern speed as the arm models. However, as they are believed to be rotating much faster than the arms, the OLR will usually lie within the inner Galactic disc. All bars have the same general features, and we will be using the WK and LM bars for further chemical and cooling calculations (we will discuss the morphology of these in greater detail later in this chapter).

The LM bar has been included to specifically allow the alteration semi-major and minor

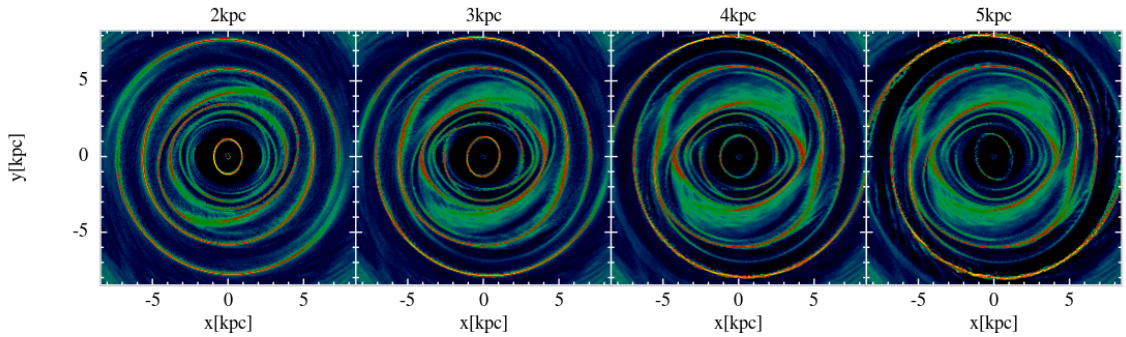

Figure 3.8: Isothermal disc simulations at $T = 200$K with an LM rotating at $\Omega_{bar} = 50\text{km s}^{-1}\,\text{kpc}^{-1}$ with different bar lengths of 2, 3, 4, 5kpc increasing to right and an axis ratio of 4:1.

axes. Calculations with bar lengths of 2, 3, 4 and 5kpc are shown in Figure 3.8. It can be seen that the increase in major axis has a minimal effect on the gas morphology. The shortest bar has reduced arm-like features compared to the other arms, presumably simply because the bar does not span as large a radial distance of the Galactic disc. Likewise the bar driven arms appear slightly stronger the longer the bar becomes. The longer the bar becomes the greater the shearing off these structures becomes, similar to that seen in the arm potentials. Tests were conducted with different semi-major to semi-minor axis ratios, ranging from values of 2:1 to 6:1. As the semi-minor axis is decreased with respect to the major axis (i.e. the bar becomes narrower) the inner structures such as those seen in the 3kpc case in Figure 3.8 become more defined, but in doing so causes a larger dispersion in the rotation curve. Similar effects are seen in the study of Lee et al. (1999) who find that the gas infall to the Galactic centre increases as the bar axis ratio increases. Inner bar structures are weak when using a ratio of 2:1, whereas Rodriguez-Fernandez & Combes (2008) and López-Corredoira et al. (2005) find this as the nominal value, though they use a much more complex potential than that of LM. Changes are only minor when using sensible values such as 3:1-5:1 (Dwek et al. 1995; Freudenreich 1998) so 3:1 is adopted as our fiducial axis ratio for the LM bar.

Tests of the complex bar of Wang et al. (2012) showed there was in fact very little difference morphologically between this and the other bar models. The minor differences showed features were more in common with the WK than the LM model, which is somewhat surprising given differences in the potential fields shown in Fig. 3.2. Though in models where we included the bulge of Wang et al. (2012) rather than fiducial Plummer bulge there was a suppression of the inner elliptical structures. These structures are seen in other studies with complex bars also (Kim et al. 2012) and are also reproduced in our simulations with live stellar systems where bars are formed (see Chapter 5). Overall, a lack of difference in the global morphology lead to the excluding of this bar from further analysis in an attempt to narrow down our already considerably large parameter space.

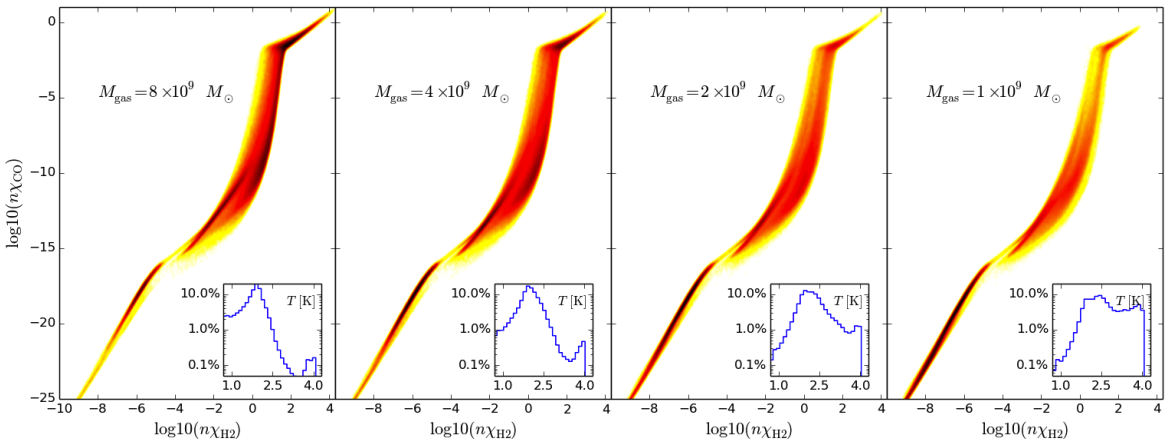

Figure 3.9: Abundance of molecular gases, weighted by density, in simulations with various surface densities (decreasing right to left). The temperature distribution for each surface density is shown in the insert in each panel. The higher the surface density runs have a greater mass of molecular gas.

3.5 General results of chemistry and cooling

Once a selection of appropriate potentials and parameters to be investigated had been narrowed down they can be used in simulations with active ISM chemistry and cooling to track the model the evolution of molecular gas for the construction of CO *l-v* emission maps. These simulations take considerably longer to perform than say isothermal simulations at $T = 200$K, mostly due to the cooling time-step criterion controlled by Equation 2.41. Computational time is also increased due to the additional chemical sub-stepping that acts inside the cooling time-stepping, but as this does not involve updating the positions or velocities of the SPH particles it is relatively inexpensive.

The abundance of H_2 and CO as a function of particle density is shown in Figure 3.9 for a simple barred-spiral disc galaxy simulation of 1 million particles after 200 Myrs of evolution. The figure shows the abundances weighted by number density of the particle to disperse the region in the upper right where the carbon and hydrogen is nearly saturated into CO and H_2. The particles perform move in molecular abundance-density space as they pass into and out of high density regions. The molecular fraction of each particle increases as it passes into the high density potential well of the arms/bar, and drops when it leaves (for an in-depth discussion see Dobbs et al. 2008). The higher the surface density (i.e. total gas mass) in the simulation then the more efficient it is at producing and maintaining molecular gas. The lowest surface density shown here has a very small amount of molecular gas, and also a very small cold ISM population, seen in the small histogram insert. Our fiducial surface density (far left panel) has a well populated cold ISM component where molecular gas is maintained ($T \approx 10$K), while also displaying a moderate warm component ($T \approx 100$K). The effect of surface density on the actual emission will be discussed in the next Chapter.

In Figure 3.10 the evolution of the molecular gas content over time is shown for the same simulations as in Fig. 3.9. The figure shows the H_2 ratio and CO abundance summed over all 1 million particles with different colours illustrating different surface densities. There is a rapid

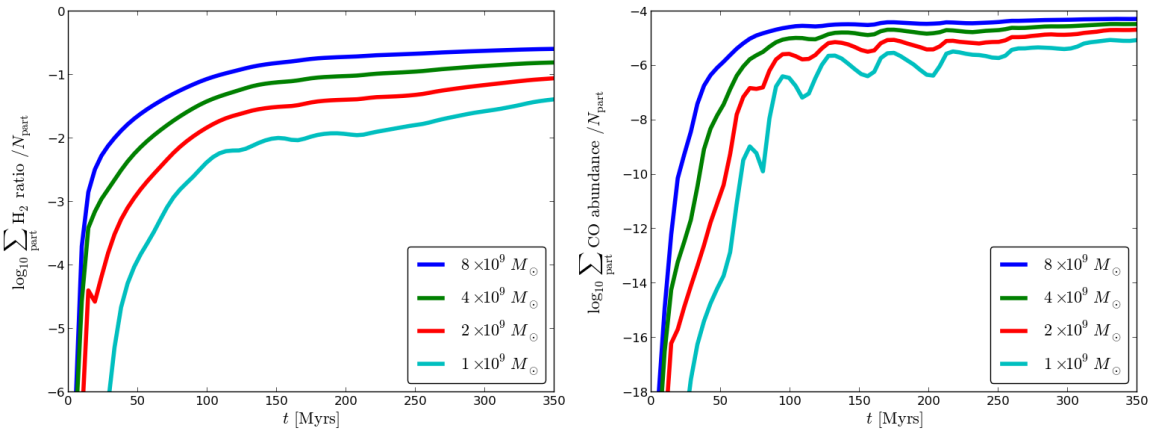

Figure 3.10: The time evolution of the molecular gas abundances averaged over all particles in a barred-spiral simulation with 1 millions SPH particles and various surface densities. H_2 and CO are shown to the right and left respectively. Large scale changes in the amount of molecular gas appears to cease after approximately 100Myrs.

increase in molecular content in the first 50 Myrs, which coincides with the time-scale for the spiral and bar patterns to become clearly visible in the gas density. The CO and H_2 evolution reaches a steady state plateau after approximately 100 Myrs, where changes of the order of magnitude no longer occur. Simulations with cooling and chemistry are chosen to run until at least 300 Myrs and until a maximum of 472 Myrs. This is the timescale needed for arm and bar structures to become well developed, but they will continue to slowly evolve on the order of Gyrs (Fig. 3.6). Despite the abundance sums being independent of gas mass/density there is a clear separation between runs with surface densities, showing that the higher surface density calculations are inherently more efficient at producing molecular gas, as expected. The evolution of CO abundance in the lowest mass calculation displays oscillations of an order of magnitude on a timescale of 40Myrs. This is assumed to be the result of gas in the lowest mass simulations being very susceptible to destruction, falling into the lower tracks in Fig. 3.9. The oscillation occurs as gas that was in the bottom of the potential well at t = 0Myrs leaves at later times and experiences an abrupt loss of molecular gas. The peak is then reached by gas that is rising in density as it flows into the arms, but again drops abruptly as it leaves. This is less pronounced in higher mass calculations where the gas mass is higher and higher density gas is well shielded against abrupt molecular destruction due to the higher column densities.

The gas properties in our simulations as a result of the cooling and chemical effects are similar to those seen in the phase diagrams of Figure 2.12. We find that there is a significant amount of gas found within the thermally "unstable" regime, with temperatures of the order of 100K to 1000K. The amount of this unstable gas is a strong function of surface density (i.e. total gas mass) used in the simulation, seen in the temperature histogram inserts in Figure 3.9. These histograms also clearly show a two-peaked distribution at temperatures of 10^2K and 10^4K, which correspond to the warm and cold ISM components. The lower the surface density, the larger the warm gas fraction, and lower the cold gas fraction. For example, in the highest and lowest surface density calculations the warm component ($6000K < T < 10000K$, as defined in Table 1.1)

constitutes 1% and 10% of the gas mass respectively, while the cold component ($50 < T < 100K$) takes up approximately 45% and 17% respectively. These values are similar to those of Dobbs et al. (2008) but with slightly different definitions of warm and cold components. The rest of the gas is composed of gas transitioning between the phases in the unstable region, or is locked in a a very cold molecular component, especially so in the heaviest gas disc. Having a large amount of supposedly unstable gas which has been seen in observations (Heiles & Troland 2003) and previous numerical simulations (Kritsuk & Norman 2002; Piontek & Ostriker 2005; de Avillez & Breitschwerdt 2004). The amount of molecular gas produced is also a strong function of surface density, as it is well shielded in the high density regions found in cold pockets of the ISM. The molecular mass fraction is dominated by the H_2, with CO being 3 or 4 orders of magnitude lower. The highest mass disc has a molecular mass fraction of approximately 4.0% (out of a total mass of $8 \times 10^9 M_\odot$), while the lowest surface density disc has a value of 0.5% (out of $1 \times 10^9 M_\odot$). While our standard surface density may seem appear too high, in that it produces a low amount of warm atomic gas, we show in Section 4.4 that the higher surface densities are required to create sufficient CO emission to be on on the same scale as those seen in observations.

3.6 Simple kinematic *l-v* maps

When building synthetic *l-v* maps to constrain Galactic structure there is another substantial parameter space that needs to be explored in addition to that parameterising the morphology of the potentials. The co-ordinates of the observer, i.e. the velocity, radial and azimuthal position ($V_{\rm obs}$, $R_{\rm obs}$ and $l_{\rm obs}$), adopted have a direct impact on the features seen in *l-v* space. A shift in an observers position of only 0.5 kpc could make the difference between a spiral arm lying in the inner or outer galaxy, completely altering its position in *l-v* space. The azimuthal position of the Earth in the Galactic disc has a similar effect, with changes in this value shifting structures in longitude, an effect that is more pronounced the closer these structures are to the Solar position.

The International Astronomical Union (IAU) recommends values for $V_{\rm obs}$ and $R_{\rm obs}$ of 220 km s^{-1} and 8.5 kpc respectively, but there are a wealth of other values used in the literature (see Reid 1993 and Majewski 2008 and references therein). $l_{\rm obs}$ is less well defined, as it encompasses both the distance from the Earth to arms and the orientation of the bar, while in our calculations it is simply a co-ordinate to be defined. Rather than simply assuming some standard value, each simulated CO *l-v* map was fitted to the observed CO map to find a best fit $V_{\rm obs}$, $l_{\rm obs}$ and $R_{\rm obs}$ for the calculation in question. In order to fully explore the observer parameter space we would need to construct numerous *l-v* maps. If we were to construct full radiative transfer maps (as done in Chapter 4) for each point in the observer parameter space then the computational cost would be extremely high as this would have to be done for each model, at each time step of interest. We instead use approximate *l-v* maps to fit to the observers position, rather than performing radiative transfer calculations for each case. By doing so the computational time is reduced from the order of a day to seconds to build a single CO *l-v* plot, allowing a fast sweep though observer co-ordinates. Once the best-fit observer position is known for a specific galactic simulation we then perform a full radiative transfer calculation with TORUS to construct a map that is used for

comparing different spiral/bar models.

These purely chemo-kinematically derived maps are a simplification compared to those constructed with TORUS, but give a good idea of the position of the emission in *l*-*v* space, and a rough idea of its intensity. The maps are constructed as follows. First we choose the observer co-ordinates from the grid of observer parameter space ($V_{\rm obs}$, $l_{\rm obs}$ and $R_{\rm obs}$, with ranges given in Table 3.2). Then we calculate a synthetic CO brightness temperature, $T_{B,\rm synth}$, from each SPH particle in the simulation using the particle's velocity, position and CO abundance. As the CO is heavily density dependent, this contains density information for each particle. To create a quantity analogous to emission we use a simple radiative scaling law of the form

$$I_{i,\rm synth} \propto \chi_{i,\rm CO}/d_i^m \tag{3.18}$$

where $\chi_{i,\rm CO}$ is the abundance of CO for the i^{th} SPH particle and d_i is the distance from the observer to the particle. This is similar to the approach of Dobbs & Burkert (2012), except we do not need to assume the density profile of the ISM gas as it is provided by the SPH particles in the abundance of CO. While the brightness temperature does not technically follow an inverse square law, the column density (and therefore opacity) of material the emission passes through does increase with distance. The $I_{\rm synth}$ factor is then scaled for each particle to match the range of emission in the observed CO map, giving a value of $T_{B,\rm synth}$ for each particle.

A longitude velocity map is then constructed using the SPH particle coordinates and assuming the observer is on a purely circular orbit. The particles are all first rotated by $l_{\rm obs}$ and then their line-of-sight velocity is calculated as given in Binney & Tremaine (1987);

$$v_{{\rm los},i} = \sqrt{v_{x,i}^2 + v_{y,i}^2}\,\sin\left(l_i - \theta_{v,i}\right) - V_{\rm obs}\sin(l_i), \tag{3.19}$$

where simple geometry gives the longitude of the particles, $l_i = \arctan(y_i - y_{R_o}/x_i - x_{R_o})$ and the velocity vector is at an angle of $\theta_{v,i} = \arctan(v_{y,i}/v_{x,i})$. An extra b factor for latitude dependence can also be included but it made no difference to the quality of the fit, likely because our simulations vary little in the vertical direction. There is evidence that the Sun exhibits peculiar motion relative to the local standard of rest of the order $10\,{\rm km\,s^{-1}}$(Dehnen & Binney 1998). We investigated adding peculiar motion (up to $20\,{\rm km\,s^{-1}}$) for a single model and the resulting best fitting map showed little difference to the case of a circular orbit. For the remainder of this thesis we assume circular orbits to reduce our parameter space.

The emission (in log-brightness temperature) of the particles is then binned into a grid of *l*-*v* space of the same resolution as the Dame et al. (2001) CO map (0.125° by $1\,{\rm km\,s^{-1}}$). Particles act as a point source, with emission occupying a single pixel of *l*-*v* space. To better represent the structure of ISM observations the emission from each particle is broadened and smoothed out into neighbouring *l*-*v* bins. The value of this smoothing, and the exponent in Equation 3.18, are parameters that must be set to build an *l*-*v* map. To do so the maps cannot be fit against the observed *l*-*v* map, as this would assume the model is a correct representation of Galactic structure. Instead these kinematic *l*-*v* maps were compared to ones created using the TORUS radiative transfer code, which will be used to create full synthetic observations and is the subject of the following Chapter.

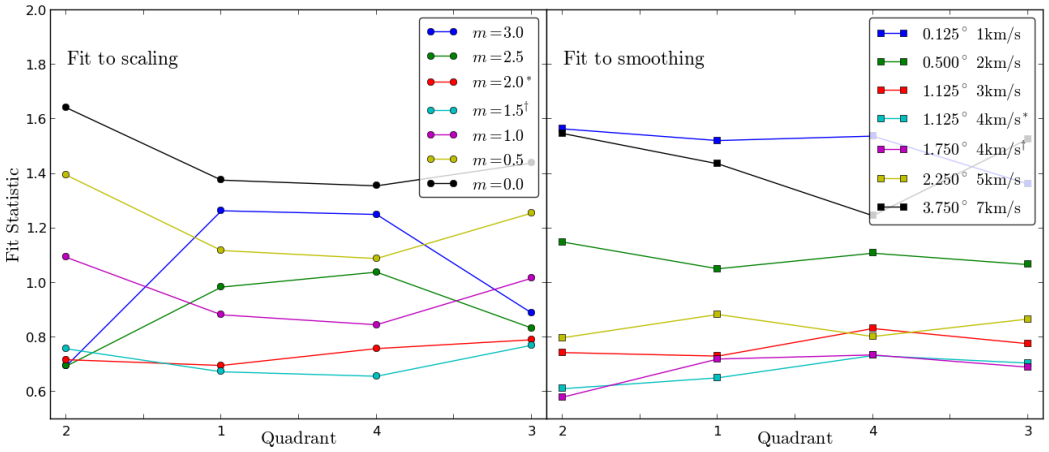

Figure 3.11: Fit statistic as a function of differing powers in distance drop-off (m in Equation 3.18) in the left panel and as a function of smoothing in longitude in the right, across the four Galactic quadrants.

Best fit values of the smoothing and scaling were found by minimising the difference between the kinematic and TORUS maps, using a simple mean-absolute-error statistic. The behaviour of the fit as a function of these parameters is shown in Figure 3.11, across all four Galactic quadrants. In the left panel the fit to m is shown, and on the right the fit to the longitudinal smoothing, with the two best fitting values given a $*$ and † in the legends. The figure shows the best fitting values lie in the range m = 1.5-2 and dl = 1.125°-1.725°, surprisingly showing the emission can indeed be approximated by a inverse square law. This longitudinal smoothing is somewhat larger than that of the binning of the Dame map, but is required to smooth out the point-like SPH particles into a finite size (a further improvement to this method would be to use the SPH smoothing kernel to give each particle a physical size). The adopted values for smoothing are a half width of 1.125° in longitude and 4 km s^{-1} in velocity using a Gaussian profile, with a m = 2 decay. The 4 km s^{-1} velocity smoothing matches the turbulent velocity width we add to the TORUS maps (discussed in Chapter 4). The smaller of the smoothing scales was chosen as the maps made using dl = 1.725° seemed to be over-smoothed when viewed by-eye.

Figure 3.12 shows l-v maps constructed within a barred galaxy simulation. The upper panel shows a map made using the method described above, and the lower panel shows a map made using the radiative transfer technique. Both are constructed using the same values for $V_{\rm obs}$, $R_{\rm obs}$ and $l_{\rm obs}$. Both maps trace the same regions of l-v space, with roughly the same intensities. The simple map underestimates the emission in some regions, and overestimates in others. This is expected; if the simple map reproduced the TORUS map there would be no need to perform the radiative transfer calculation.

These simple maps enable us to find a best-fitting map for each individual Galactic simulation, removing the uncertainty in placing the observer at some arbitrary position. The range of observer co-ordinates investigated in this fit are given in Table 3.2. Once a best fit is known, TORUS is then used to build a full map using the best-fitting observer co-ordinates, which can then be used to compare the different galactic potentials.

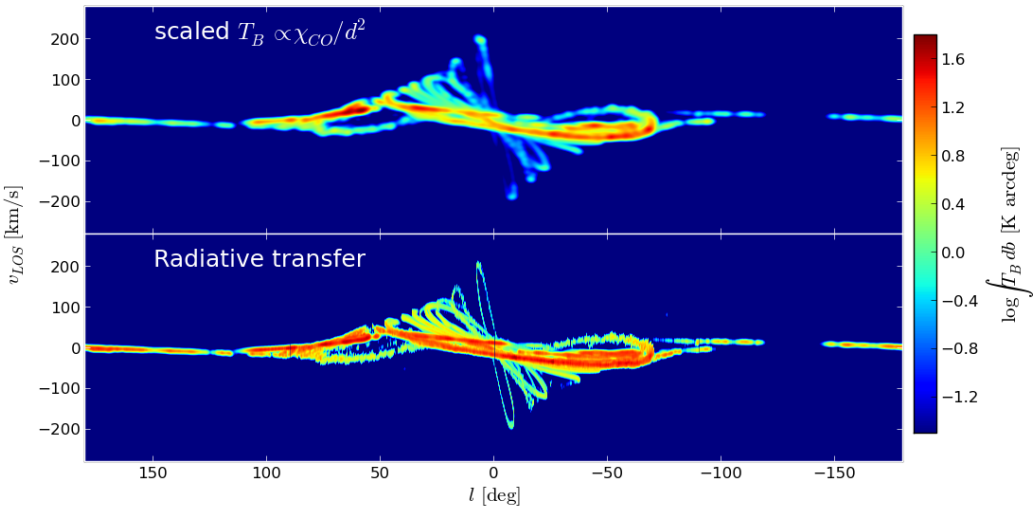

Figure 3.12: Two emission maps of a barred Milky Way simulation, of WK type. Top: synthetic CO l-v map constructed using Equation 3.18. Bottom: l-v map created at the same observer coordinates but with the radiative transfer code TORUS, with the same values of $R_{\rm obs}$, $V_{\rm obs}$ and $l_{\rm obs}$.

To quantify the goodness of fit for each model we use a simple fit statistic. We calculate a mean absolute error (MAE) to gauge the goodness of fit. Our choice of MAE over RMS is to ensure that single pixels far from the observed value do not cause severe deterioration in the fit statistic, as we are interested in a global match, rather than whether individual features can be exactly reproduced. The emission is first integrated in latitude and then the logarithmic difference, $\log T_B db$, is compared between the synthetic map and the CO map of Dame et al. (2001). This is then normalised by the number of pixels with non-negligible emission in the observed l-v map, $n_{\rm pixels}$, simply to obtain a fit statistic close to unity (this is the same value for all maps). The form of our fit statistic is thus,

$$\text{Fit} = \frac{\sum_{\rm pixels} |\log T_{B,\rm synth} db - \log T_{B,\rm Dame} db|}{n_{\rm pixels,\,Dame}}, \tag{3.20}$$

where $T_B db$ is the brightness temperature integrated over latitude. This is therefore the sum of the logarithmic ratio of the integrated synthetic brightness temperature to the observed brightness temperature for a specific longitude-velocity bin. Initially a linear summation was used, but the fit had a great tendency to be swayed by a single pocket of strongly emitting dense gas that did not agree with observations. We effectively calculate the linear deviation from the emission features shown in maps such as Fig. 3.12, where the intensity is shown on a log scale to highlight low lying features. Note that due to the non-zero nature of the background emission in the observations (which is also added to the synthetic map) there is never a case when a divide by zero occurs in the logarithm, or where $\log 0$ occurs. This statistic was tested using a simple model 4-armed model against the Dame map and varying the azimuthal position of the observer. The fit statistic was then measured in individual quadrants to check the desired behaviour; that the minimum was seen when arm features aligned with those seen in observations. This was easiest done in the second

and third quadrants where the Perseus and Carina arms are clearly visible. The use of this fit statistic blindly however is somewhat dangerous, as a model that is a seemingly good fit but has arm features that are only slightly misplaced in velocity space will have a poor fit statistic, despite having the arms in a near perfect position. The variation of the observers position rectifies this somewhat, allowing for the movement of *l*-*v* features for each model. However, as in fitting we still must produce *l*-*v* maps to compare to observations, we double check by-eye that no seemingly good model has been discarded for having a poor fit despite it showing a relatively good match. In actuality this only occurred on a few cases, once for a barred simulation, which was not better than those of other potentials anyway, and one for a live-disc calculation (which is discussed in Chapter 5). Because our simple approximate *l*-*v* maps and those made using radiative transfer are calculated using two very different methods the fit statistic should not be quantitively compared between these two different types of map. However, the relative strength of emission features, and the general morphology, can be.

Now a parameter space, model prescription, mapping methodology and quantitive fit statistic has been established we can now move on to exploring the morphological parameters with high resolution calculations. Sections 3.7 and 3.8 describe simulations with bar and arm potentials respectively, where the effect of pattern speed and morphological parameters upon *l*-*v* features is investigated. This is used to narrow down the parameter space for the next Chapter, where we will conduct simulations with both arm and bar potentials, and produce *l*-*v* maps using full radiative transfer rather than the simple prescription outlined above. A key caveat to this approach is the assumption that a bar/arm model that provides an good fit in isolation will do so when combined with another potential. While this may not be necessarily correct, it allows for an approach with a realistic amount of free-parameters. This is not an entirely unfounded assumption, as the bar and arms will dominate the gas morphology in the inner and outer galaxy respectively, with only the region of $4 < R < 7$kpc being influenced by both (seen from inspection of the isothermal simulations in the previous section).

3.7 Barred simulations with cooling and chemistry

3.7.1 Simulations

An example of the evolution of a barred galaxy simulation with active chemistry and cooling is shown in Figure 3.13, using the bar model of Wada & Koda (2001) with a core radius of 2 kpc rotating at $50\,\mathrm{km\,s^{-1}\,kpc^{-1}}$. When using different bar potentials the overall evolution is similar. The bar potential is active throughout the entire simulation, and gas within the bar establishes elliptical orbits along the major axis of the bar from 100 Myrs onwards. After 150 Myrs the gas in the outer disc displays a two armed spiral structure inside the OLR, the strength of which is related to the core radius and strength of the potential. These arms are not in a steady state, and their pitch angle is decreasing over time. After about 4 rotations of the bar (the last panel in Fig. 3.13) the arms are wound up enough that they begin to join to create elliptical/ring-like structures at the OLR, with the orbits set as being either perpendicular to the bar inside the OLR or parallel to outside the OLR (Combes et al. 1995; Buta & Combes 1996; Mel'Nik & Rautiainen 2009). Any

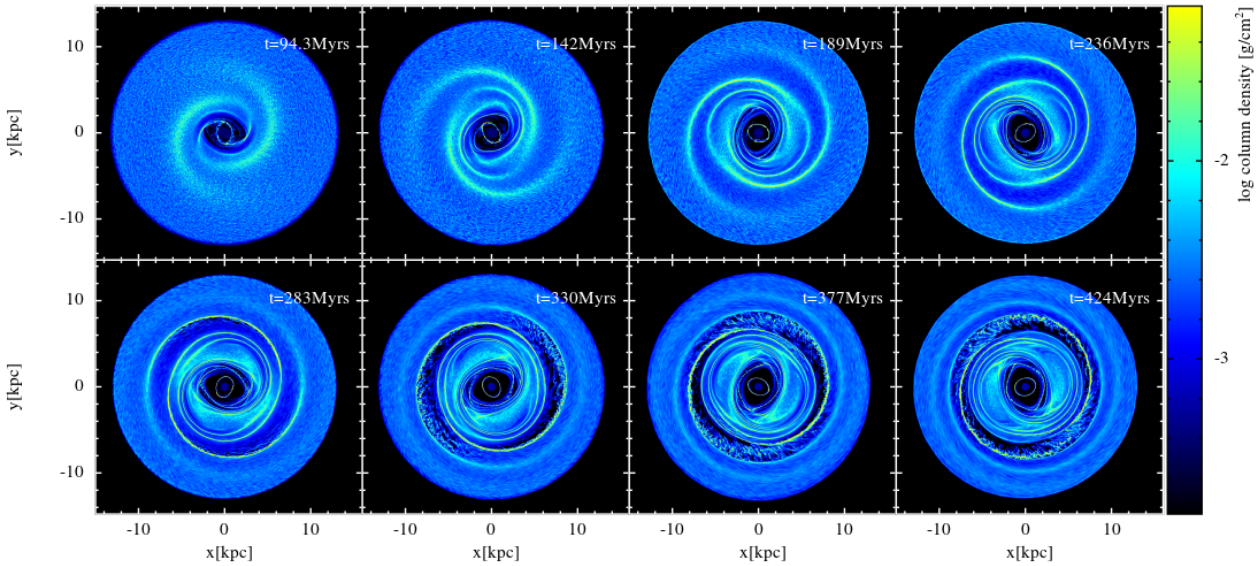

Figure 3.13: The evolution of the bar model of Wada & Koda (2001) with a core radius of 2 kpc rotating at 50 km s^{-1} kpc^{-1}. Both the bar and the gas are rotating clockwise. Note that the morphology is effectively the same from 350-470 Myrs and the arms will eventually wind up to form a ring-like structures with elliptical orbits parallel and perpendicular to the bar major-axis. The orientation of the features in this and other top-down figures is determined by the initial alignment of the non-axismmetric potential with the x-axis at t = 0Myrs, orientation does not correspond with any of the l-v maps shown in other figures.

arm potential we combine with these bars would be substantially subdued in this region, which is near to the Solar radius. At early times there is a distinct sweeping up of gas inside the ILR, seen in the earliest three panels. In the low density region around R = 2kpc at later times there are very few SPH particles, as most are now associated with the inner ring or the outer region. In the case of Figure 3.13 there is significant infall of gas onto the central, bar dominated, region but this seems to cease after approximately 150Myrs. This may indicate the end of the bar infall phase, or merely be a resolution effect and there are simply no more free particles within the capture distance of the inner bar. In Figure 3.14 the surface density for several models is shown as a function of radius. The left panel shows the initial profile, and that of an armed, barred, and barred-spiral calculation after 236Myrs of evolution. The surface density is effectively unchanged in the armed model, but there is a significant infall of gas into R < 2kpc in models with a barred potential, at the expense of gas inside R < 3kpc. In the right panel the evolution of a barred model is shown, which indicates the infall phase ceases after approximately 170Myrs. Over this time gas from 1 < R < 3kpc falls into the rings around R = 1kpc.

In test calculations where we use an isothermal equation of state to model the ISM the arms driven by the bar are maintained when the temperature is high (10000K). However, in low temperature isothermal cases and adiabatic+cooling cases the arms enclose on the aforementioned set of orbits around the OLR. There also exists a set of orbits perpendicular to the bar in the inner galaxy. These orbits (commonly referred to as x_2 orbits) only exist when there is a region between two separate ILR's (Contopoulos & Papayannopoulos 1980). In calculations where we used a

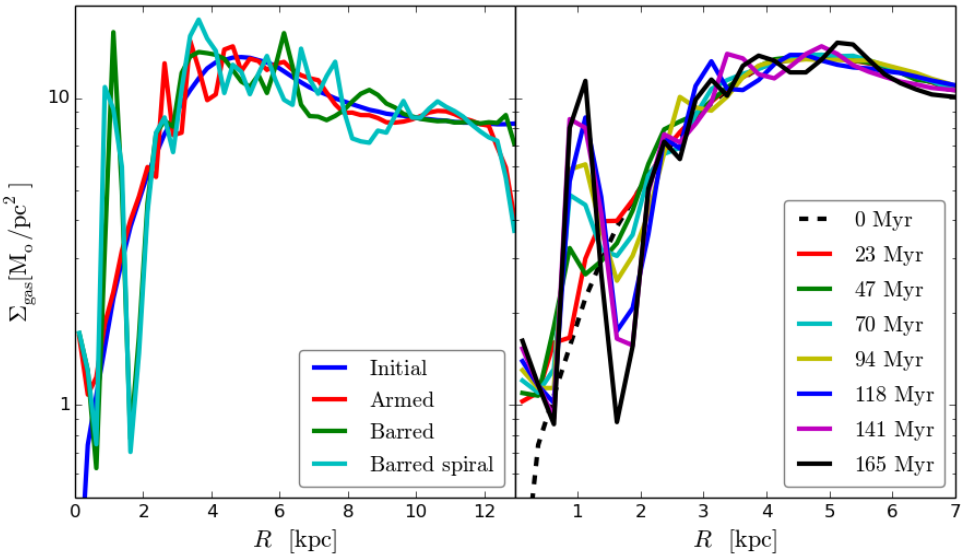

Figure 3.14: The gas surface density profile as a function of R for three different models after 236Myrs of evolution (left) and time evolution for a barred calculation (right) showing gas infall occurs in barred models within $R < 3$kpc up to 170Myrs.

more simplified axisymmetric potential (a bulge-less flat logarithmic potential) there were no such inner orbits as there was only a single ILR. However the rotation curve we use here has an inner bulge (see Fig. 3.1b), providing a second ILR and so setting up a family of inner perpendicular orbits. These orbits are seen in other works using analytic barred potentials (e.g. Lee et al. 1999; Mel'Nik & Rautiainen 2009). When using the LM bar model these inner orbits contract radially as the semi-major or semi-minor axis is decreased (Fig. 3.8).

The pattern speed of the bar is key in determining the structures that develop in the inner Galaxy. Plots of the WK bar model are shown at various pattern speeds in Fig. 3.15. All the bar potentials used in this study display similar behaviour as a function of pattern speed. As the pattern speed increases, the ILR and OLR contract, reducing the radial extent of features driven by the bar. There is also an inability of the slower bars to drive any strong arm-like features compared to the faster pattern speeds, owing to the fact that the OLR is beyond the edge of the Galactic disc. The slower bars also have a greater impact on the dispersion in the rotation curve compared to the faster bars. The $20\,\mathrm{km\,s^{-1}\,kpc^{-1}}$ bar in Fig. 3.15 has a dispersion of around $\pm 50\,\mathrm{km\,s^{-1}}$ at $R = 2$kpc. Conversely the faster bars have a greater variation in the rotation curve in the outer regions of the disc corresponding to the location of the driven arms, but of a much smaller scale than that of the inner region of the slow bar.

Figure 3.16 shows a comparison between our three different bar models. All have a pattern speed of $50\mathrm{km\,s^{-1}\,kpc^{-1}}$ and are shown after 236 Myrs of evolution angled at 45°with respect to the Sun-Galactic centre line. The inner x_2 orbital structure is similar for all models. Immediately outside this there are other thin orbital structures, more so in the case of the LM bar. The arm structures generated in the outer disc are different in each model. The LM bar has formed very tightly wound arms compared to the others, a result of the different radial drop-off compared to the other models. The LM bar potential is thinner along the semi-minor axis than the others, which

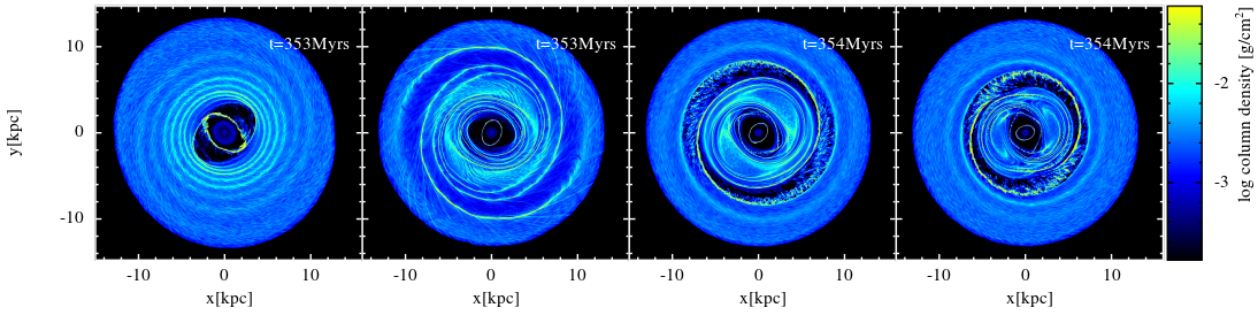

Figure 3.15: The bar model of Wada & Koda (2001) with a core radius of 2 kpc rotating at pattern speeds of 20, 40, 50 and 60 km s^{-1} kpc^{-1} , increasing from left to right, at a time of 354 Myrs. The gas and potentials are rotating clockwise viewed from above. These top-down maps correspond to the central row of Fig. 3.18. The contraction of the outer Linblad resonance is clearly as Ω_b = 50 $\rightarrow$ 60km s^{-1} kpc^{-1}. The 70km s^{-1} kpc^{-1}model is not shown but is similar to the 60km s^{-1} kpc^{-1} model but with bar/arm features confined to R < 6kpc.

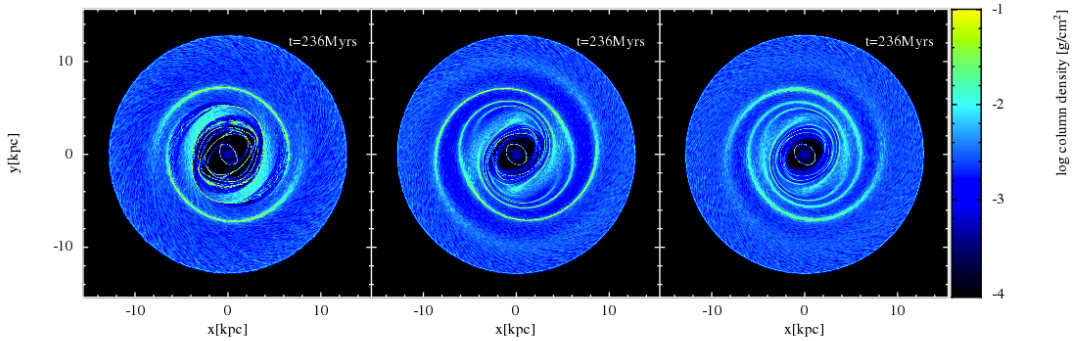

Figure 3.16: Different bar models angled at 45°to the Sun-Galactic centre line with a pattern speed of 50km s^{-1} kpc^{-1}after 236 Myrs of evolution. The models (left to right); WK, WKr2 and LM are described in the main text.

could also contribute to the tighter arm structures. The WK and WKr2 bars differ in the extent of their central core radius, the effect of which can be seen in Fig. 3.16. The bar with the smaller core radius has weaker arms compared to the bar with a larger core.

3.7.2 Simple kinematic maps

Results for a single bar model

Fitting to the observers co-ordinates was then performed on the chemically/cooling active simulations described above, using the WK, WKr2 and LM models, with the fit statistic of Equation 3.20 used to quantify how well each model reproduced the observed emission features. An example of the results of fitting to the observer's co-ordinates is shown in Figure 3.17. The Galaxy model used in this example is a WK barred potential with a bar pattern speed of 50 km s^{-1} kpc^{-1}. The parameter sweep is performed at a timestamp of 470 Myrs and the bar major-axis lies along the y-axis by default. The left panel of Fig. 3.17 shows that a best fit orientation of θ_b = 40° is preferred, broadly in keeping within the accepted range for the "Long bar". The fit as a function of velocity gives the IAU standard value of 220 km s^{-1}, but it is clear the velocity fit is not as well constrained

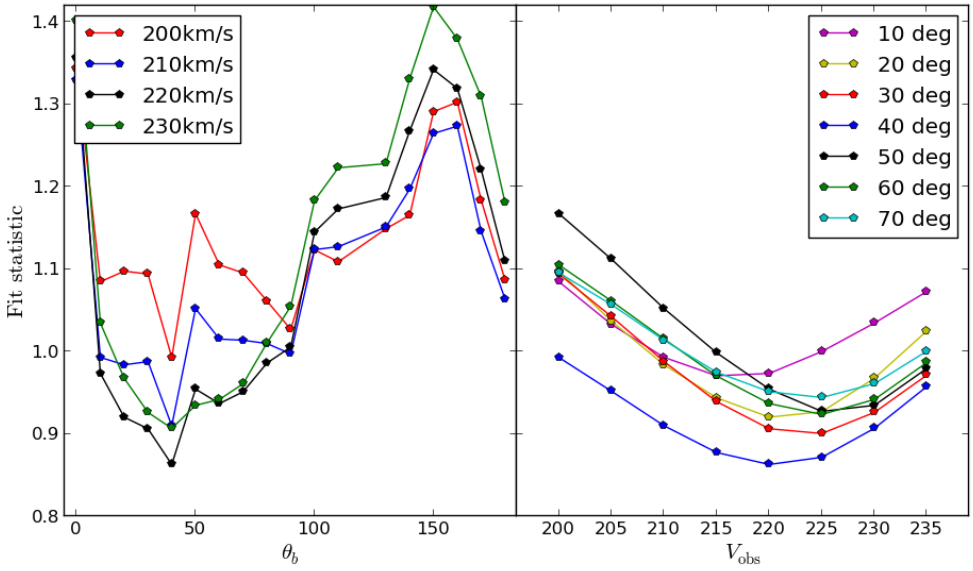

Figure 3.17: An example of fitting to the observer's co-ordinates using simplified l-v maps as described in Section 3.6. Here we show the fit statistic for a barred Milky Way after 470 Myrs of evolution. The fits to the observers azimuthal position and circular velocity are shown in the left and right panels respectively at $R_{\rm obs} = 8.5$ kpc (the fit as a function of $R_{\rm obs}$ is not shown for clarity). The different coloured lines show the fit for a certain value of $V_{\rm obs}$ (left) or θ_b (right).

as the bar orientation. While not shown here, $R_{\rm obs}$ is similar to $V_{\rm obs}$ in that it shows a shallow global minimum. This is the case with most potential models, with the $l_{\rm obs}$ parameter showing the clearest troughs/peaks of the fit statistic. The l_{obs} parameter is only shown between 0-180°, as the potentials, and fit statistic, are symmetric. While the azimuthal position of arm models in the literature seems poorly constrained, there if effectively no observational evidence for the bar major axis to not be pointing towards the second quadrant. That is to say, the bar orientation is always found to be $0° < \theta_b < 90°$, seen both in numerical (Weiner & Sellwood 1999; Yang et al. 2002; Minchev et al. 2007; Rodriguez-Fernandez & Combes 2008; Mel'Nik & Rautiainen 2009) and observational studies (Dwek et al. 1995; Binney et al. 1997; Hammersley et al. 2000; López-Corredoira et al. 2007) regardless of whether with respect to the *COBE* or "Long" bar. In some instances the best fitting bar orientation is found to be outside of this range. This occurs for about 10% of the models, across different potentials, strengths, pattern speeds, and time-stamps. In these instances there is a second minima that does place the end of the bar in the second quadrant. Here we allow for the slight influence of observational evidence and choose to only to accept best fits that place the bar end in the quadrant heavily suggested by observations, choosing to orientation minima only in the range $0° < \theta_b < 90°$.

The resulting best fit l-v maps, from the fit to all bar parameters (Ω_b, θ_b, $R_{\rm obs}$ and $V_{\rm obs}$) for the simulations in Fig. 3.15 are shown in Figure 3.18. Fig. 3.18 shows the best fitting l-v plots for pattern speeds of 20, 40, 50, 60 and 70km s^{-1} kpc^{-1} after 236, 354 and 472 Myrs of evolution. The parameters for each of the best fitting maps (θ_b, $R_{\rm obs}$ and $V_{\rm obs}$) are over-plotted onto each individual map, along with the corresponding fit statistic. We do not show the maps of the WKr2 and LM bars but will include their quantitive results across all parameters later in this section. Inspection of

Figure 3.18 shows that bars moving at 50-70km s^{-1} kpc^{-1} tend to favour an orientation of around 50°, while the lower pattern speeds favour lower values. This is a result of the shift in the OLR from the external Galaxy to the internal Galaxy as we increase pattern speeds, and the resulting location of the arms driven by the bar. For lower pattern speeds the arms extend to outside the Solar radius, up to the OLR. This means these arms fit the outer quadrants, while the central bar structure fits the inner quadrants. For the higher pattern speeds the driven arm structures lie inside the Solar radius, and so the bar and arm structure is contained within the inner Galactic quadrants alone, leaving the outer quadrants empty. The resulting two different bar pattern speed domains cause the different bar orientation ranges. Our grid of values for the θ_b parameter is fairly coarse, incrementing in steps of 10° from the bar's position at times of 236, 354 and 472 Myrs after being initially aligned with the x-axis at t = 0Myrs. As such there is an uncertainty up to 10° in the values given here. This means that the frequently used value suggested for the "Long bar" by Churchwell et al. 2009 of θ_b = 45°, is within the bounds of the values found here by our best fitting bars with Ω_b =50-60km s^{-1} kpc^{-1}.

The l-v maps shown in Figure 3.18 rarely generate considerable structure in the outer quadrants. The exception is the 40km s^{-1} kpc^{-1} model at later times, where the arm structures driven by the bar persist into the outer disc due to the OLR's position beyond the Solar radius. At later times the arm structures driven by the bar join to create closed orbits, that are clearly visible in the l-v diagram (especially for the Ω_b = 70km s^{-1} kpc^{-1} cases). This process can occurs on the Gyr time-scale, and could be a plausible progenitor of Galactic ring structures (Mel'Nik & Rautiainen 2009). While not shown here, the l-v maps of the WKr2 bar are very similar morphologically.

The best fitting structures fit one of two regions well. The first category of good fitting maps are those that simply fill out more structure in l-v space, such as the 50km s^{-1} kpc^{-1} WK bar at 472 Myrs (bottom central panel of Fig. 3.18). In these cases the arms driven by the bar extend to relatively large radii, spreading the emission into a larger range of $|l|$. The other category of good fits are those where the strength of the emission in the inner Galaxy follows a pattern similar to the observed CO map. This ridge of CO emission not present in HI is often attributed to a molecular ring-like structure, but could also be explained by arm or bar features of the correct geometry (Dame et al. 2001, Dobbs & Burkert 2012). In Fig. 3.18 at early times, the 60km s^{-1} kpc^{-1} bar is a good fit for central emission due to arm-like structures extending to a radius of about 5 kpc, with a fairly wide pitch angle. By 472 Myrs the arms have closed upon each other, creating an elliptical structure where the arms once were. Both early and late times fill out the same area of l-v space, but the advantages of an arm structure over that from a ring is that it can curve in the correct direction in l-v space. A elliptical or ring like structure would show 2-fold rationally symmetry about l = 0°, v_{los} = 0 km s^{-1}, not seen in the observed CO l-v map. The strong central ridge in seen in the 20km s^{-1} kpc^{-1} l-v maps in Fig. 3.18 seems to provide a reasonable match for the central ridge in the CO data. This structure actually results from the concentric rings surrounding the bar, as seen in Fig. 3.15. The addition of an arm potential disrupts these relatively weak structures easily, and are needed to drive outer arm features absent in the 20km s^{-1} kpc^{-1} bar. The emission for this bar is also relatively confined to this ridge, in comparison to the early time 60 or 70km s^{-1} kpc^{-1} maps.

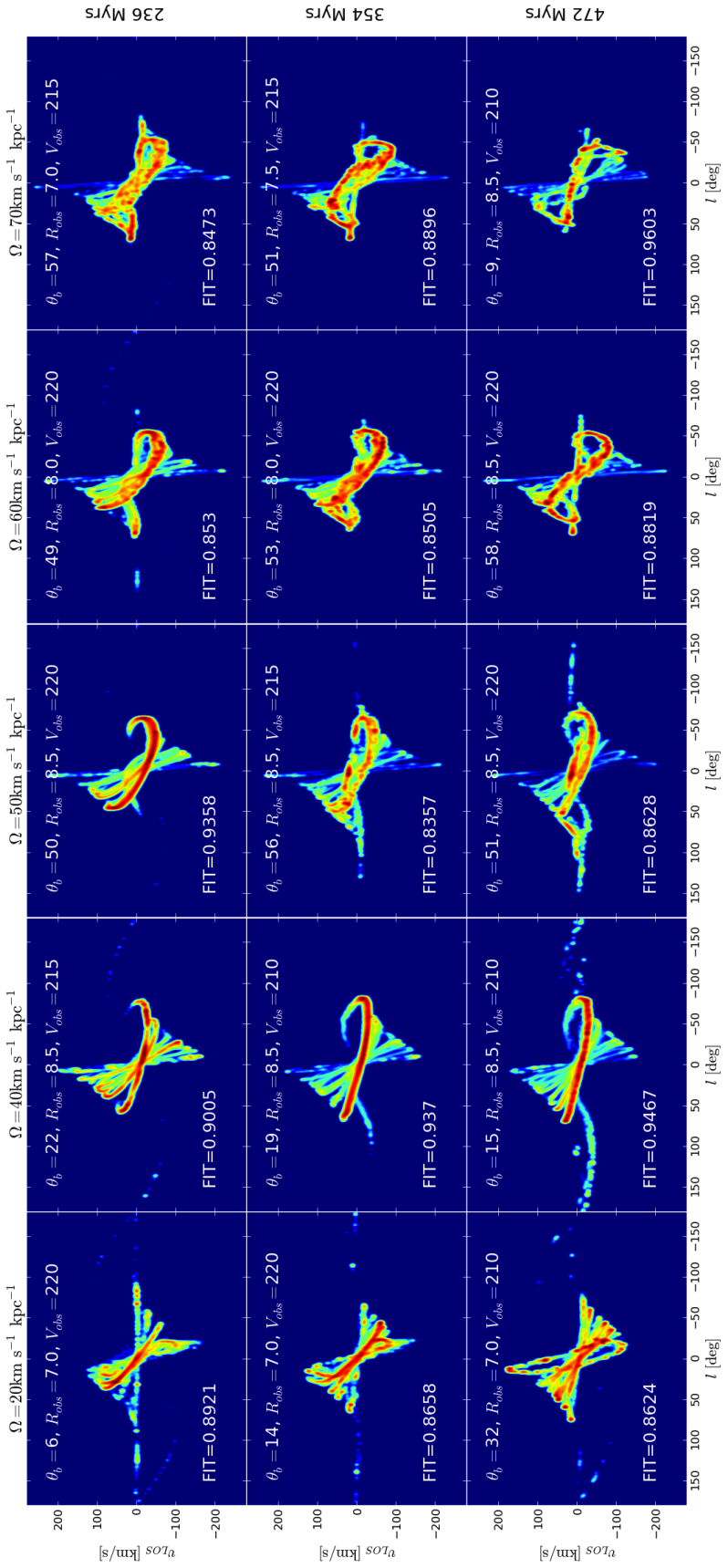

Figure 3.18: The bar model of Wada & Koda (2001) with a core radius of 2 kpc rotating at pattern speeds of 20, 40, 50, 60 and 70 km s^{-1} kpc^{-1} increasing from left to right with time increasing from top to bottom (236, 354, 472 Myrs). The values for the bar orientation, observer distance and circular velocity, and fit statistic are over-plotted on each Ω_b-t pair (in degrees, kpc and km s^{-1} respectively).

	Bar model		
Best fit paramater	WK	WKr2	LM
Ω_b [km s^{-1} kpc^{-1}]	50	60	70
$V_{\rm obs}$ [km s^{-1}]	215	220	235
$R_{\rm obs}$ [kpc]	8.5	8.5	7.0
θ_b [°]	56	51	41

Table 3.3: Best fitting values for the bar only simulations. A systematic uncertainty for each value is present due to the coarseness of the parameter space; $\Delta\Omega_b$ = 10km s^{-1} kpc^{-1}, $\Delta V_{\rm obs}$ = 5 km s^{-1}, $\Delta R_{\rm obs}$ = 0.5kpc and $\Delta\theta_b$ = 10°.

The *l*-*v* maps in Fig. 3.18 seem to be heavily time-dependent. Over a 200 Myr time frame the emission structures can change considerably. The 60km s^{-1} kpc^{-1} model in particular changes from having an emission ridge comparable to observations to a looped structure that is a poor by-eye match to the CO data. Maps of the WKr2 bar (a smaller core radius) evolve slower than the WK bar, maintaining their features due to the relatively weaker potential. For example the 60km s^{-1} kpc^{-1} map at 472 Myrs does not display the strong figure-of-eight like structure seen in the equivalent map of the WK bar (Fig. 3.18).

Results across all bar models

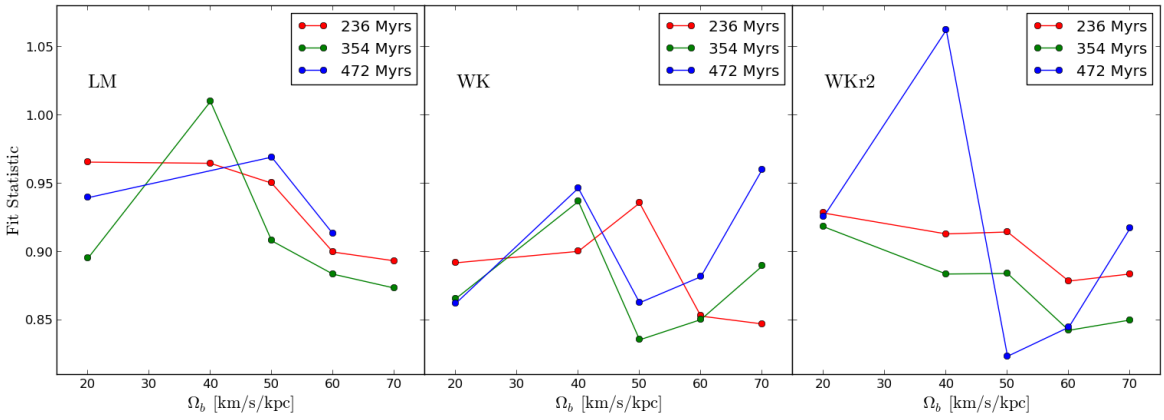

Figure 3.19: The fit to pattern speed across all bar models. There is a slight preference towards 50-60 km s^{-1} kpc^{-1}. Note that the LM bar has a poorer fit statistic overall, and that the simulations of this bar were halted before it reached the final timestamp for Ω_b = 40 and 70 km s^{-1} kpc^{-1}.

A comparison of the fit statistic as a function of Ω_b for all our bar models at the three different time-stamps is shown in Fig. 3.19, and the best-fitting values are explicitly shown in Table 3.3. At first glance there seems to be no strong relation between the goodness of fit and Ω_b. There are however some common features between the different models. The 40km s^{-1} kpc^{-1} models tend to have some of the worse fits, for reasons discussed above relating to the position of arms in the outer Galaxy. The best fitting speeds tend to be in the $\Omega_b > 40$km s^{-1} kpc^{-1} range. The best fitting pattern speed for the WK and WKr2 bars is 50km s^{-1} kpc^{-1}, though the 60km s^{-1} kpc^{-1} is better fit for 2 of the 3 timestamps for the WKr2 bar, hence its inclusion as the best fitting value in

Table 3.3. While the 70km s^{-1} kpc^{-1} and 20km s^{-1} kpc^{-1} pattern speeds are numerically a good fit in some instances, we choose to not include these in our models with arm and bar potentials. This is because of the relatively short time-scale on which the l-v emission structure appears a good match to the CO data compared to the 50 and 60km s^{-1} kpc^{-1} models. Figure 3.19 also indicates that overall the LM bar is a poorer fit than the model of Wada & Koda (2001), so we choose not to follow these up for further analysis in combination with arm potentials. Morphologically speaking this bar is somewhat thinner than the bar of Wada & Koda (2001) due to our choice of axis ratios. The quality of the fit could be a result of the chosen axis ratios but we do not consider this further.

Our best fitting bar models suggest a bar orientation of $\approx 45°$, in accordance with observations of the "Long bar". In Fig. 3.20 we show the fit statistic as a function of Ω_b for the WK bar with θ_b fixed at 45° while keeping $V_{\rm obs}$ and $R_{\rm obs}$ free. The lowest fit statistics over all times considered are for the 50 and 60km s^{-1} kpc^{-1} models, which is consistent with the fits where θ_b is left free, and the general trend with Ω_b is similar to the WK and WKr2 bars in Fig. 3.19.

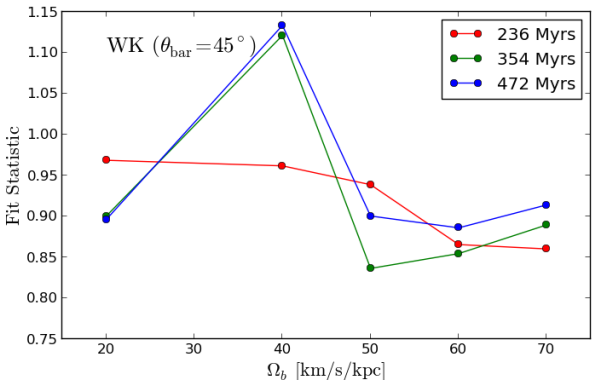

Figure 3.20: The fit statistic for the Wada & Koda (2001) bar when fixed at $\theta_b = 45°$ with $V_{\rm obs}$ and $R_{\rm obs}$ left free. The simulations data is identical to that used in Fig. 3.19.

Summary of bar models

From the evidence shown above bar pattern speeds of 50 and 60km s^{-1} kpc^{-1} are chosen to be used further in our arm-bar mixture models. We chose to run WK bars (which appear stronger in the outer disc) at 50km s^{-1} kpc^{-1} and WKr2 bars at 60km s^{-1} kpc^{-1}, the best fitting values as given in Table 3.3 for respective bars. This choice is also supported by the fit statistic shown in Fig. 3.19, which shows that 2/3 of the timestamps investigated have their minima at 50km s^{-1} kpc^{-1} for the WK bar and 60km s^{-1} kpc^{-1} for the WKr2 bar. These values are also promising as they give best-fitting values of $V_{\rm obs}$ and $R_{\rm obs}$ close to accepted literature values (Table 3.3). We do not follow up the 70km s^{-1} kpc^{-1} models because they lose their arm structure relatively fast compared to other models, resulting in ellipses in l-v space. Their speed is also fast enough to sweep up a large quantity of gas inside of 4 kpc. This would make it impossible for arm structures to exist in the inner Galaxy, making it difficult to see emission not associated with the elliptical bar orbits within $|l| < 45°$. We exclude 20km s^{-1} kpc^{-1} due to their lack of any arm feature and strong inner resonance features that fail to match the morphology of the inner l-v structure seen in the data.

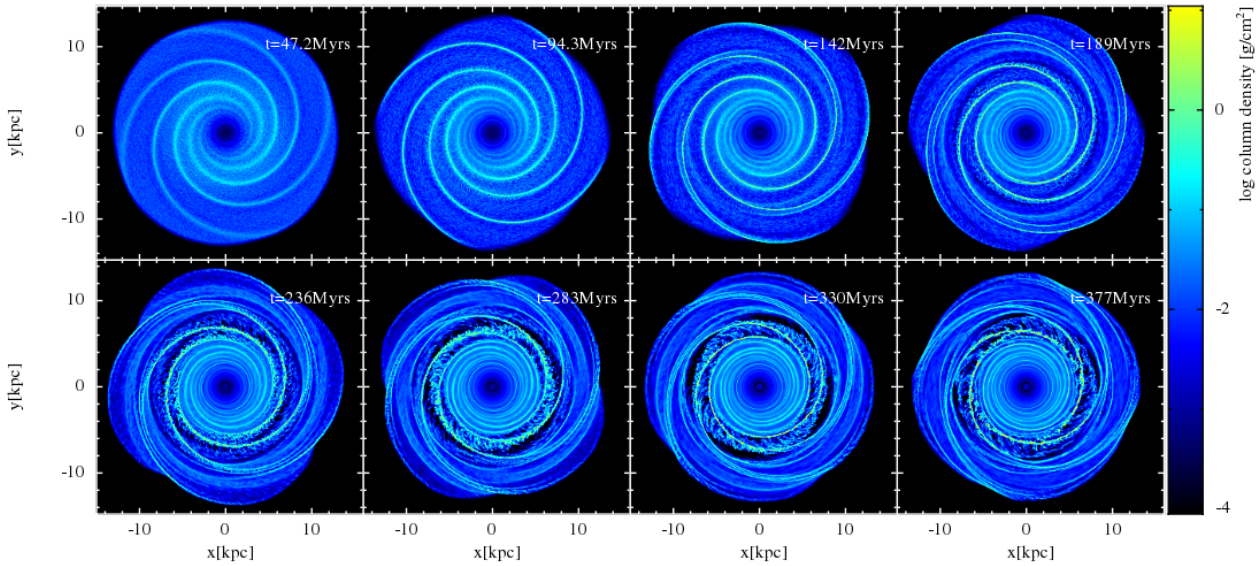

Figure 3.21: The evolution of the 4-armed model of Cox & Gómez (2002) moving at a pattern speed of 20km s^{-1} kpc^{-1} with a pitch angle of 15°. Arm spurs are clearly seen near the ILR ($R \approx$ 7kpc) after 200 Myrs. The outer Linblad resonance is beyond the simulation radius.

They also lack any inner features that can match the peak velocities seen in the observed CO data. The 40km s^{-1} kpc^{-1} models are excluded due to their poorer fit statistics in the case of each model (see Fig. 3.19).

3.8 Armed simulations with cooling and chemistry

3.8.1 Simulations

An example of the evolution of an isolated CG-type arm model is shown in Figure 3.21, with the parameters; $N = 4$, $\alpha = 15°$, $\Omega_{sp} = 20$km s^{-1} kpc^{-1}. The spiral structure in the gas tends to survive only between the ILR and OLR region, even though the potential is present throughout the disc. For the 20km s^{-1} kpc^{-1} case shown in Fig. 3.21 the OLR is beyond our simulation radius, but the ILR is clearly seen at later times at $R \approx 7$ kpc. Around this radius there exists strong spur features as seen in Dobbs & Bonnell (2006). After approximately a Gyr of evolution the gas becomes aligned on 4:1 orbits at the OLR and ILR with spiral arms persisting in between. This is similar to the ring-like structures seen in the fastest bars in the previous section.

A comparison of the ISM gas response to different arm pattern speeds is shown in Figure 3.22 for our CG 2 and 4-armed models after 354 Myrs of evolution with a pitch angle of $\alpha = 12.5°$. The variation with Ω_{sp} behaves in a similar fashion for different values of α. Each model has a region where spurs exist, the radial position of this decreases with increasing pattern speed and roughly corresponds with the location of the ILR. Even by-eye it is clear that some of the models in Fig. 3.22 do not display the desired morphological features. The 10km s^{-1} kpc^{-1} $N = 4$ models all lacked spiral features that represented the underlying potential, regardless of pitch angle. While these models do show spiral structure, the gas is rotating too fast with respect

to the potential inside the ILR, resulting in a winding up of spiral features. Structure in the inner galaxy would need to be produced by the inclusion of a bar potential in this case. The fastest $N = 4$ model has the opposite problem, with a pattern speed high enough that the ILR and OLR are well inside the simulation radius (similar to bar simulations in the previous section) and there are no spiral arms in the outer disc. The slowest $N = 2$ models display very strong spur features inside of $R = 7$ kpc, with some pockets of gas maintaining a high density as it exits the arm potential. Over long time-scales this turbulent structure will form elliptical 2:1 orbital structures, similar to those seen in bar potentials.

The $N = 2$ spirals with moderate pattern speeds (15-20km s^{-1} kpc^{-1}) show evidence of supplementary spiral structure branching off the main arms. The 15km s^{-1} kpc^{-1} model in particular has a pair of branches of comparable density to those driven by the spiral potential, but of a much shallower pitch angle (second panel, top, in Fig. 3.22). These additional arm features are seen in other numerical studies of logarithmic spirals such as Patsis et al. (1994), where the bifurcation of 2 to 4 armed spirals occurs at the inner 4:1 (ultraharmonic) resonance (Patsis et al. 1997; Chakrabarti et al. 2003). The additional branching arm features seem to peak in strength around 200 Myrs, and become less defined as evolution passes 500 Myrs though are still present at much later times.

3.8.2 Simple kinematic maps

Results for a selection of arm models

A selection of *l*-*v* maps made using the method described in section 3.6 are shown in Figure 3.23. We show maps for $\alpha = 5°$, 12.5° and 20° and omit those for 10° and 15° due their similarity to the 12.5° models. The upper rows show $N = 2$ models and the lower $N = 4$ models. The maps are the results of the fit to $R_{\rm obs}$, $V_{\rm obs}$ and $l_{\rm obs}$ similar to the previous section for the isolated bar models. Best fit parameters for the observer position and velocity are over-plotted on each map. We include no bias towards certain values of $l_{\rm obs}$ as we did for fitting to the bar to constrain θ_b.

l-*v* features are allowed to be fit by any part of the gas disc, rather than make assumptions about which *l*-*v* features should be fit by certain structures in *x*-*y* space. For instance, the local arm material was allowed to be fit to small arm branches or large primary arm structures. If the latter were the case the fit statistic should penalise the additional emission that would be present in the third quadrant but not seen in observations. As some features of the *l*-*v* maps are believed to be due to local structures, rather than a global spiral arm, it is unlikely that any single model would perfectly fit the local emission and outer arm features exactly. To investigate this, tests were made where pockets of local emission were masked out when fitting the arm models. This includes the Local arm emission ($104° < l < 150°$, $-25 < v_{los} < 15$ km s^{-1}), the Cyg X complex ($68° < l < 105°$, $-16 < v_{los} < 30$ km s^{-1}) and Vela region ($-106° < l < -81°$, $-14 < v_{los} < 23$ km s^{-1}). The results of this test were somewhat inconclusive. While some models favoured a different parameter minima, the results for most were unchanged, indicating the emission for the inner quadrants was driving the fit statistic. Masking out material is not a very prudent approach, as the ability of some models to produce off-arm local material would be muted by this, which could penalise a model

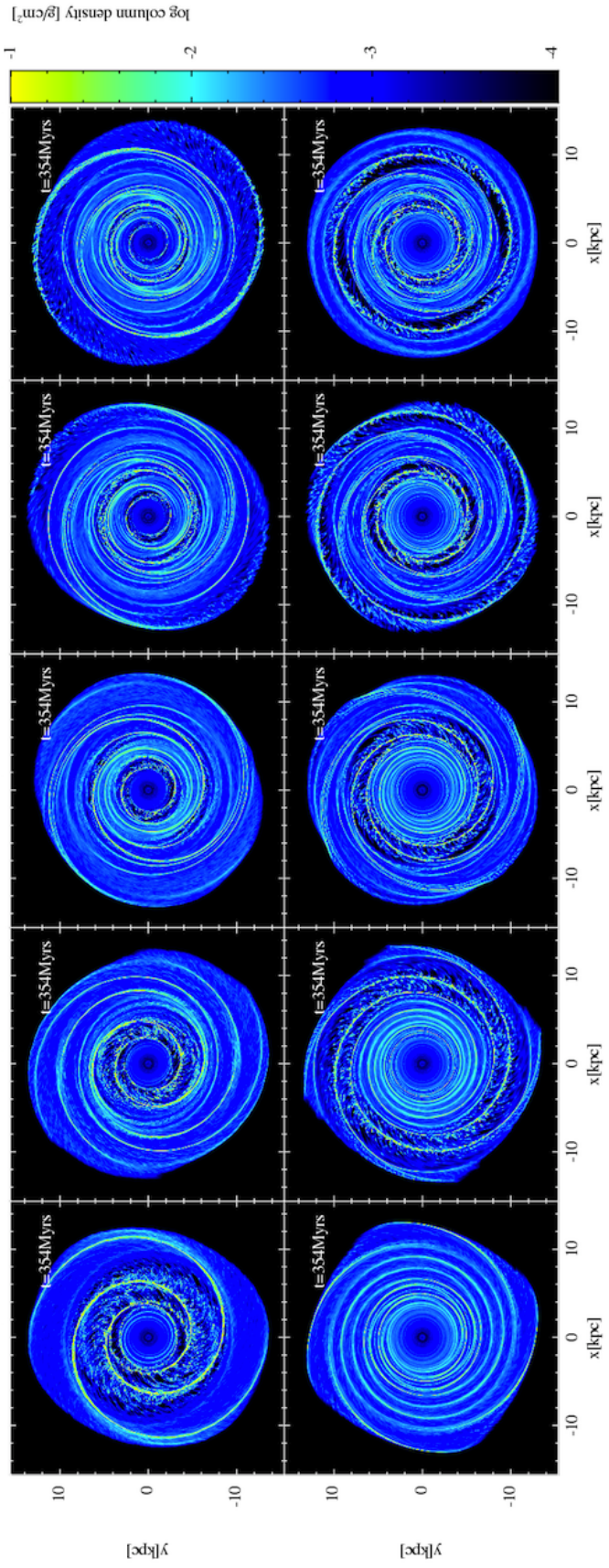

Figure 3.22: Response of the gaseous disc to arm potentials of different pattern speeds. 2-armed and 4-armed models are on the top and bottom rows respectively with increasing pattern speed along the x-axis (10, 15, 20, 25, 30km s^{-1} kpc^{-1}). All models are of that of Cox & Gómez (2002) after 354 Myrs of evolution with a pitch angle of 12.5°.

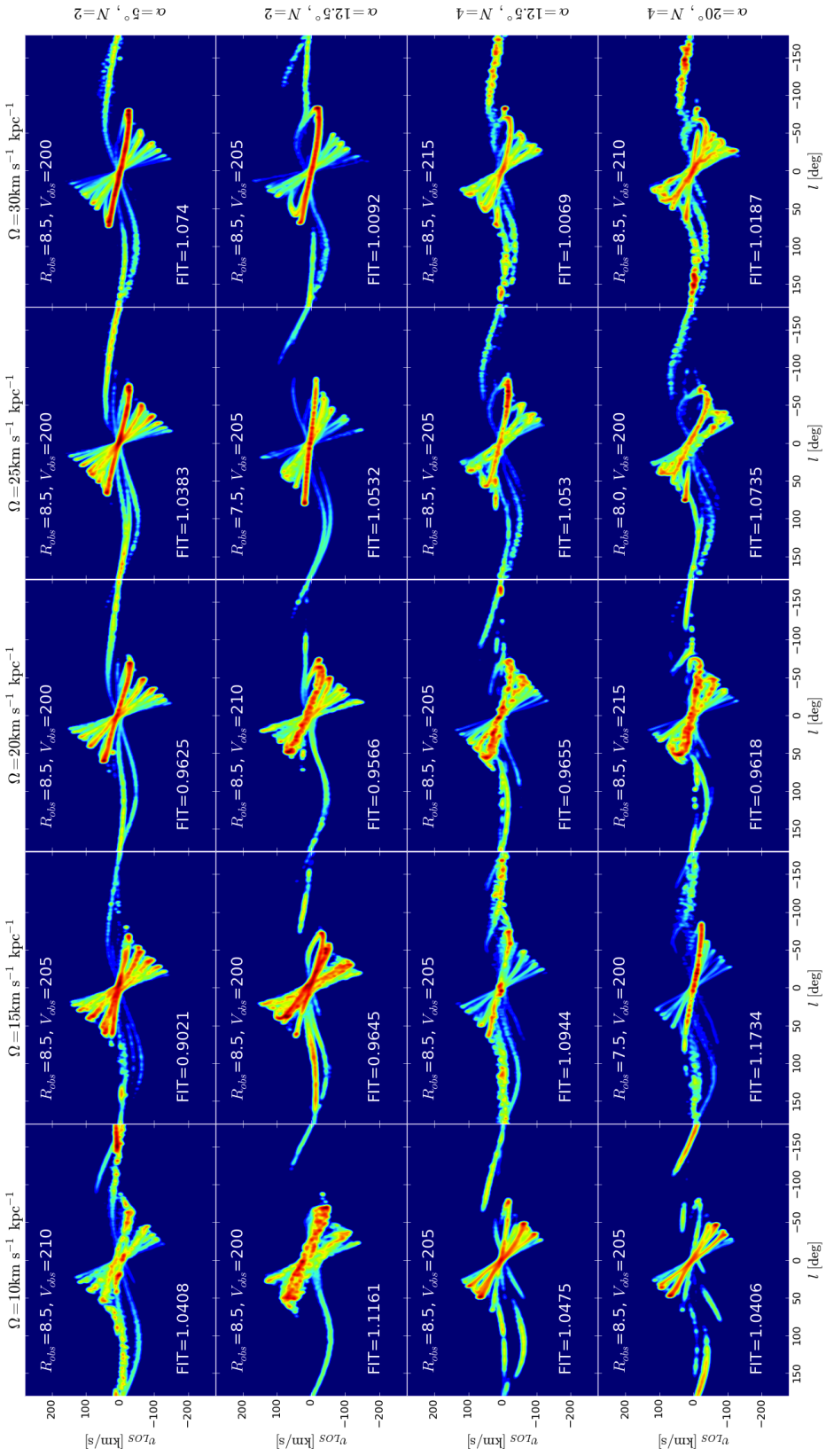

Figure 3.23: The best fit *l*-*v* maps for the arm model of Cox & Gómez (2002) rotating at pattern speeds of 10, 15, 20, 25 and 30 km s^{-1} kpc^{-1} increasing from left to right with pitch angle increasing from top to bottom (5°, 12.5° and 20°). The values for the observer distance, circular velocity, and fit statistic are overplotted on each Ω_{sp}-α pair (in kpc and km s^{-1} respectively). The maps are created after the simulation has evolved for 354 Myrs. The $\alpha = 12.5°$ models include both $N = 2$ and $N = 4$ morphologies. The 10° and 15° models are not shown but differ only marginally compared to the 12.5° maps.

	Arm model	
Best fit paramater	CG(N=2)	CG(N=4)
Ω_{sp} [km s^{-1} kpc^{-1}]	20	20
$V_{\rm obs}$ [km s^{-1}]	210	205
$R_{\rm obs}$ [kpc]	8.0	8.5
α [°]	12.5	10.0

Table 3.4: Best fitting values for the arm only simulations.

that provided a good fit to all features of the *l*-*v* diagram. As such no features are masked out for any of the results shown.

General trends in the fitting are seen for all arm models. The strong local emission in the second quadrant is often fit by a major arm in the gas. The Local arm material appears significantly stronger than that of Perseus and Outer arms in the CO *l*-*v* data, giving the fit a preference to fitting to local material over the Outer arm, despite the physical size of the Outer arm being considerably greater. Fitting to the Local arm feature in *l*-*v* space causes the fit to miss the Outer arm in the second quadrant for $N = 2$ models as there is simply not enough arm structure to produce 3 distinct arms in the first and second quadrants.

Results across all arm models

The full results of our fitting to the observer's position using simple kinematic *l*-*v* maps are shown in Figure 3.24 as a function of arm pattern speed, with the best fitting values for individual parameters given in Table 3.4. The top panel shows the fit statistic for $N = 2$ models with $\alpha = 5°, 10°, 12.5°$ and $15°$ and the bottom panel the fit to $N = 4$ models with $\alpha = 10°, 12.5°, 15°$ and $20°$. Only the results for the 236 and 354 Myr time-stamps are shown for clarity. We also looked at the 472 Myr time-stamp and the trends with the fit were similar. Our overall interpretation is that the 20km s^{-1} kpc^{-1} models offer the best fit to the CO *l*-*v* data for both the $N = 2$ and $N = 4$ models. This is well within the observational bounds and is an often used value in other numerical investigations (Gerhard 2011). While Ω_b =20km s^{-1} kpc^{-1} produces the lowest fit statistic for the all models (Table 3.4) this is not as consistent over time in the $N = 2$ models compared to $N = 4$. While the best fitting values for $R_{\rm obs}$ are consistent with literature values, $V_{\rm obs}$ is slightly lower (205 and 210 km s^{-1}). This could be because the central bar is required in the central disc to better match peak inner velocity structures, forcing outer emission features to move to greater velocities and fitting to higher values of $V_{\rm obs}$, nearer to 220 km s^{-1}.

The $N = 2$ arms favour a minimum of 15km s^{-1} kpc^{-1} for the later time-stamp. Upon inspection of the individual *l*-*v* and *x*-*y* maps for this model (Fig. 3.22 and 3.23), it is apparent that the supplementary arm branches mentioned previously are the cause of this minimum. The branches are approximately 90° out-of-phase with the spiral potential and are much more apparent at 354 Myrs than 236 Myrs. These branches have a much shallower pitch angle than those being directly driven by the potential and decay before reaching the outer disc. This increase in arm features in the $N = 2$, $\Omega = 15$km s^{-1} kpc^{-1} models at later times allows for the reproduction of Perseus, Outer and Local arm features, but does not produce as strong emission in the third

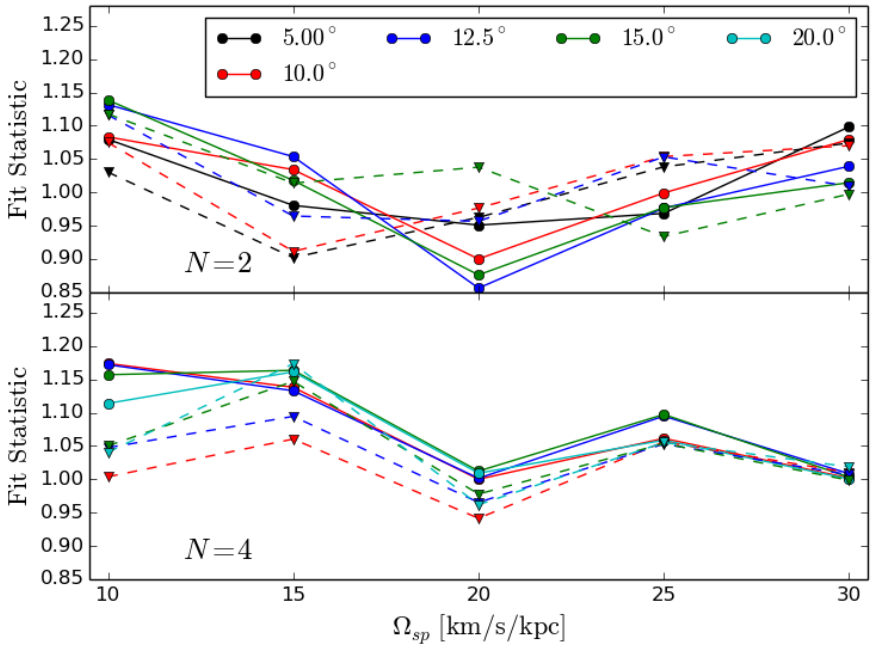

Figure 3.24: Fit statistic found by varying observer co-ordinates as a function of pattern speed of all Cox & Gómez (2002) type arm models, with various values for the pitch angle. Two different time-stamps are shown as solid (236 Myrs) and dashed (354 Myrs) lines. $N = 2$ and $N = 4$ models are shown in the upper and lower panels respectively.

quadrant as that of the $N = 4$ models (seen by comparing the $N = 2$ and $N = 4$, $\alpha = 12.5$ models). This lowers the fit statistic compared to the $N = 2$, $\Omega \neq 15 \mathrm{km\,s^{-1}\,kpc^{-1}}$ models in the top panel of Fig. 3.24 at the later time stamp.

The additional arm features in the $N = 4$ models allow the reproduction of the 3 arm features seen in the observed CO data in the 1st and 2nd quadrants (Local, Perseus and Outer arms). They are also able to reproduce the characteristic "hook" in l-v space from the Carina arm in the 4th quadrant while also placing material along the Perseus and Local arms. This is seen in the $N = 4$, $\alpha = 12.5$, $\Omega_{sp} = 20 \mathrm{km\,s^{-1}\,kpc^{-1}}$ model in Fig. 3.23. In order to fit to the Carina arm, there must be an arm structure placed very close to the observer's position. For pure logarithmic spirals with constant pitch angles this will result in very bright horizontal structures in l-v space, as seen in Fig. 3.23. This is clearly at odds with the observed emission in CO (and HI), which contains no strong emission at local velocities in the inner Galaxy. There was no single arm model that could place local emission, the Carina arm and the Perseus arm in their correct places, as well as producing a strong ridge of emission angled correctly in the inner Galaxy. From Fig. 3.23 it can be seen that for any model that has a central ridge that is similar to that seen in CO observations, the Carina arm-like structure is pulled into the $|v_{los}| < 20 \mathrm{\,km\,s^{-1}}$ range. The resulting arm emission from the $N = 4$ models in the 3rd quadrant is detrimental to the goodness of fit, due to the lack of molecular emission in the observations. This excess emission makes the $N = 4$ models systematically worse compared to those with $N = 2$ in Figure 3.24.

Out of all parameters the pitch angle of the arms is the poorest constrained in our arm-only

models. Figure 3.24 shows no strong preference towards any given pitch angle, in the 2-armed case especially. The minima of all arm models are at 12.5° and 10°, both of which have pattern speeds of $20\mathrm{km\,s^{-1}\,kpc^{-1}}$. At this stage there may simply be too many variables to establish a best fitting pitch angle, especially when the orientation of the arms is still a completely free parameter (determined by the best-fitting l_{obs}). The pitch angle produces fairly subtle differences in morphology compared to the arm number and pattern speed, which could explain the relatively loose correlations seen in Fig. 3.24. To try to find a stronger fit to α we attempted to fit to only the outer quadrants, where the arms should dominate the l-v structure, and negate the dominance of the central ridge in the fit statistic. The results were still inconclusive, and the fit behaved similarly as it did to the entire Galactic plane.

Summary of arm models

To further narrow down our parameter space for simulations with both arm and bar potentials we reject our $\alpha = 5°$ and 20° models. By-eye inspection shows that while these models do cover a similar area of l-v space as observations, they do not trace the features correctly. The 5° models appear similar to concentric rings in l-v space, with many bright tangencies along the terminal velocity curve. The 20° models appear too wide to match features in l-v space, and stray from the potential structure at $R > 9$kpc. As there is no clear preference towards a 2 or 4 armed model seen for isolated arm simulations, we continue to use both 2 and 4-armed models in conjunction with the best bar models from the previous section. We choose to primarily use the minimum from Fig. 3.24 of $\Omega_{sp} = 20\mathrm{km\,s^{-1}\,kpc^{-1}}$ for further arm simulations. We also include 2-armed, $\Omega_{sp} = 15\mathrm{km\,s^{-1}\,kpc^{-1}}$potentials due to the secondary minimum in Fig. 3.24.

It is clear from the results shown here that the pattern speed is an extremely important parameter for any arm/bar model of the Milky Way, perhaps as important as arm number or bar orientation. Especially in the case of the bar, where it dictates the radial extent of the bar, more so that the actual bar length incorporated into the potential. Regardless of the presence of a stellar potential, the pattern speed dictates whether the gas will trace the potential, due to the radial placement of resonance features. Figure 3.25 shows the position of a stellar potential and the gaseous response (top), along with the potential's projection in l-v space and the synthetic l-v map of the gas. While the outer arms trace the potential well (both in x-y and l-v space) the inner disc is devoid of structure, and the pitch angle is increasingly wound up as you approach the galactic centre. The arms have been orientated to reproduce the Carina tangency in the 4^{th} quadrant. For cases such as these where the arms seem well represented in the outer disc there is little structure in the inner Galaxy. This means that in these cases emission in the inner Galaxy needs to be driven by the inclusion of a bar potential, leading to the conclusion that both arm and bar features are needed to fully represent Galactic emission. Having differing pattern speeds for each would especially help the $N = 2$ case, as it would allow molecular structures to exist throughout the disc (as two $m = 2$ potentials moving at the same pattern speed would span the same radial domain).

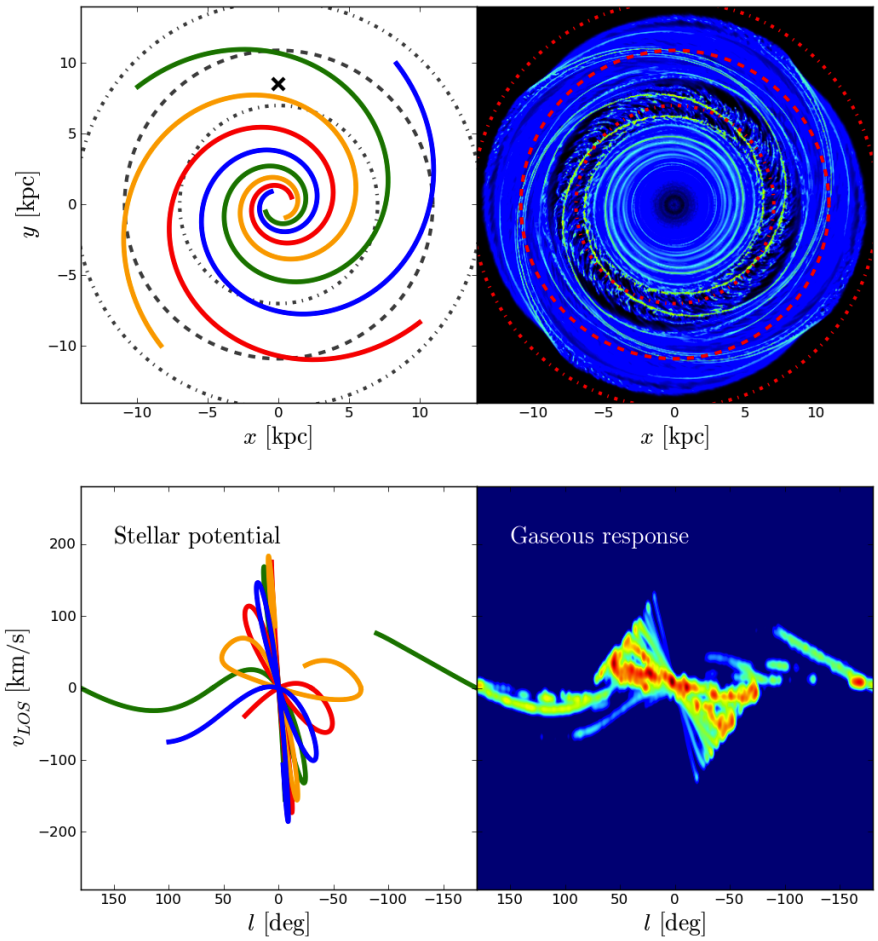

Figure 3.25: Illustration of the arm locations in simulations resulting from positions of resonances. Top: 4-armed spiral model moving at 20km s^{-1} kpc^{-1} with $\alpha = 12.5°$ after 354Myrs of evolution (left) and the position of the spiral stellar potential (left). Dashed circles show the locations of the ILR, CR and OLR in order form centre. Bottom: the location of the spiral potential in *l*-*v* space (right) and the gaseous response in the simulation (right). Note the lack of spiral structure inside the ILR and subsequent absence in *l*-*v* space.

3.8.3 Arm strength

In addition to the standard CG spiral arms we performed calculations with arm potentials with double the strength of our fiducial value. The purpose of which was to improve the gas tracing of the potential, as in some instances in the models shown in Figure 3.22 the gas only weakly traces the imposed arm structure. For example, the $N = 2$ models have significant branches at moderate pattern speeds, and the highest density gas is not exclusively associated with the bottom of the spiral potential, even within the ILR and OLR. Figure 3.26 shows stronger arm models with double the fiducial arm strength, with 2 or 4 arms (top and bottom rows) and pattern speeds of 15, 20 and 25km s^{-1} kpc^{-1}. The best fitting *l*-*v* maps are shown in Figure 3.27. These can be directly compared with the central six panels in Figure 3.23, which have the same pitch angle, pattern speed and arm number (though have evolved for slightly longer). Characteristic 4:1 and 2:1 resonant orbits become clear much earlier in this simulations with increased potential

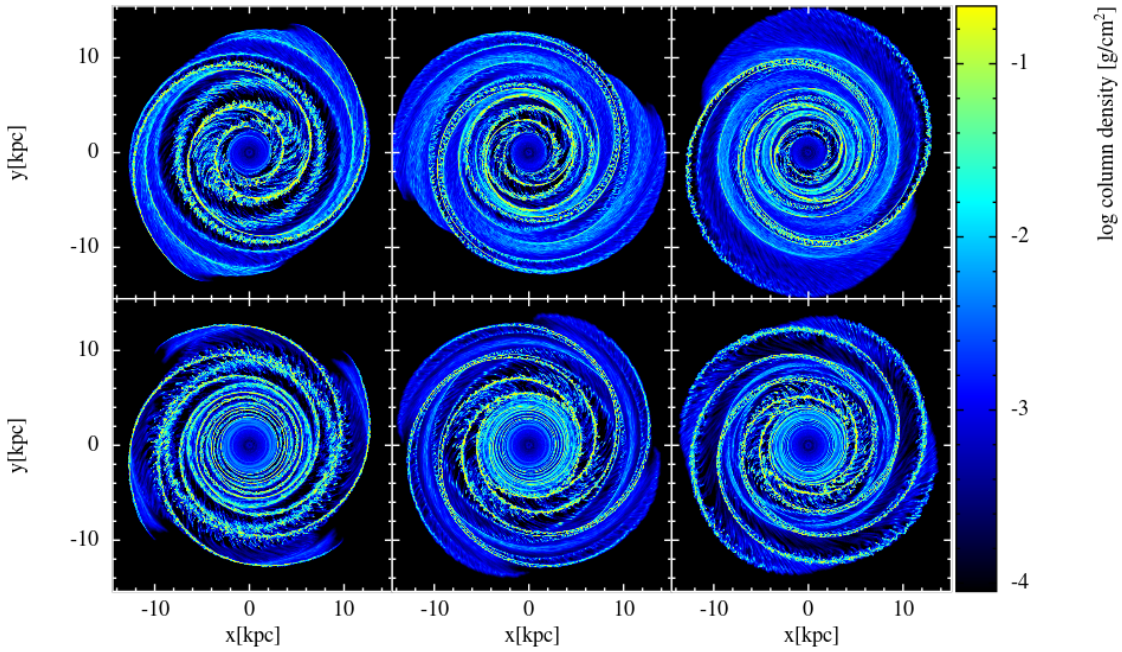

Figure 3.26: Calculations with double the normal arm potential strength with $N = 2$ (top) and $N = 4$ (bottom). The pattern speed varies from 15-25km s^{-1} kpc^{-1}from left to right. The calculations were performed up to 236Myrs. These can be compared to calculations with the standard potential strength shown in the central panels of Figure 3.22.

strength (even more so considering these have had less time to evolve). The 2:1 and 4:1 orbits can clearly be seen in the 15km s^{-1} kpc^{-1} calculations. Other than this difference the over-all morphology is the same. This can be seen by comparing between l-v plots. The 20km s^{-1} kpc^{-1} maps are extremely similar for both arm strengths, and still provide the best fit out of these models compared to the 15 and 25km s^{-1} kpc^{-1} models. These other speeds show slight differences. The $N = 2$, $\Omega_{sp} = 15$km s^{-1} kpc^{-1} model has lost some arm structure in l-v space, a result of the arm branches being wrapped up into 2:1 orbits much faster than the standard strength models. The $N = 2$, 25km s^{-1} kpc^{-1} model provides a better l-v map in the stronger case, due the additional potential strength sweeping up gas much more effectively in the outer disc.

These models with stronger arms do not show dramatic differences to our standard strength models, and provide the same best fitting pattern speed (though only the central 3 values were checked). A single arm strength was adopted for use for arm-bar mixed calculations, with some confidence that l-v features will not change greatly if a stronger potential were used.

3.8.4 Complex spiral arm model

Calculations using the PM arm model were made using a single pattern speed of 20km s^{-1} kpc^{-1} and pitch angle of 12°to investigate the plausibility of a four armed gas response to a two armed potential. This potential also decays away much faster with radius than the CG model. Figure 3.28 shows calculations with a spiral masses of 1.5×10^9 M$_\odot$ at 236 (top left), 354 (bottom left) and 472 (bottom right) Myrs. Also shown is a calculation with a larger spiral mass of 2.6×10^9 M$_\odot$

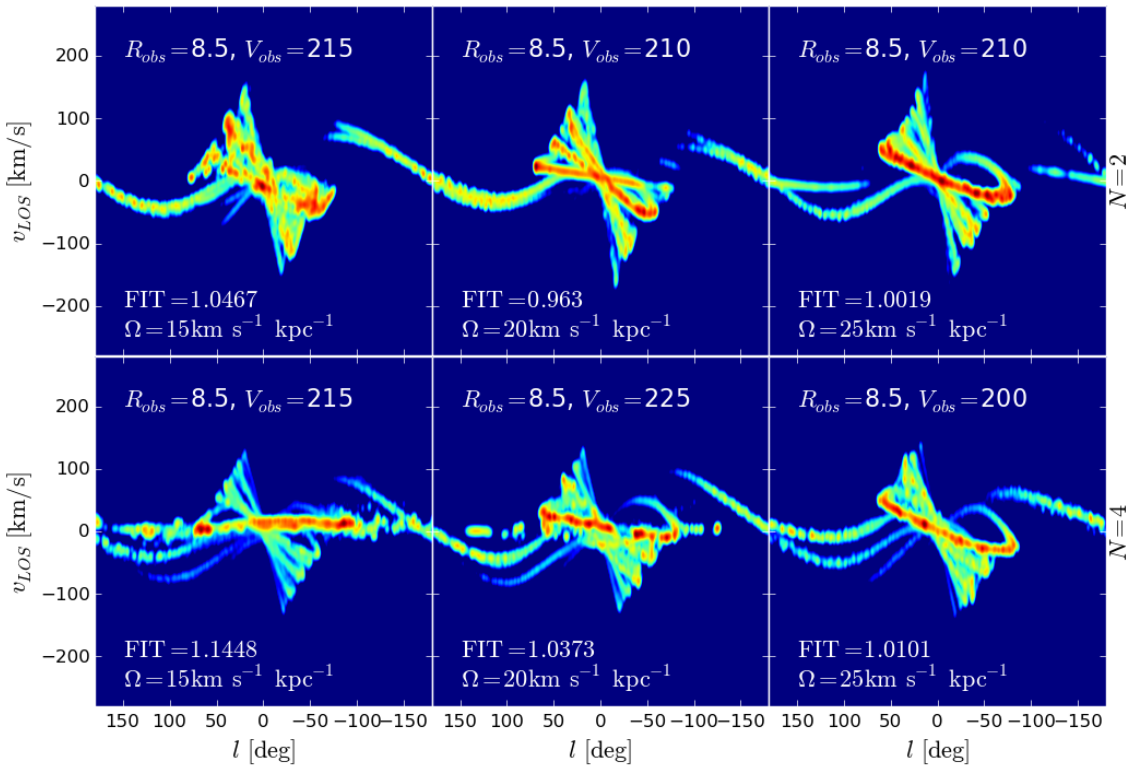

Figure 3.27: Best-fitting *l*-*v* maps of the calculations shown in Figure 3.26. These can be compared to calculations with the standard potential strength shown in the central panels of Figure 3.23.

(top right panel). In Pichardo et al. (2003) the authors state the supplementary arm features are stronger in the lower mass case. The figure shows that the PM arms do indeed drive additional arm structures, appearing strongest in the mid-Galactic disc in the top left panel. These supplementary arms seem to exist between the ILR and 4:1 resonance, located at approximately 8kpc. These additional spiral branches have shallower pitch angles than the arms driving their formation, and are nearly circular approaching the Solar radius. At later times the PM resonant arms become less pronounced, and the 4:1 resonance begins to dominate the flow of gas around R = 6kpc (the same position as the ILR of 4-armed models). Increasing the strength of the spiral potential makes little difference to the gas response, with the main effect being the additional spurring near the ILR (R <2kpc).

Arm branches are also present in the N = 2, CG models (upper panels in Fig. 3.22). The branches in the PM arms are slightly stronger than those seen in the CG potential, but the primary arms in the PM model are relatively weaker than those of the CG potential. In the CG arms these are more pronounced in the 15km s^{-1} kpc^{-1} calculations, though can still be faintly seen when Ω_{sp} = 20km s^{-1} kpc^{-1}. Calculations with this lower pattern speed were also performed for the PM model, and supplementary arm features are even stronger in the outer disc, but all arm structure is weaker at intermediate disc radii $R \approx$ 8kpc.

The main features of this model were also studied in Gómez et al. (2013), where the authors also found supplementary arm features with shallow pitch angles. However, in their study the supplementary arms maintain a form similar to that to the top left panel in Figure 3.28 for up to

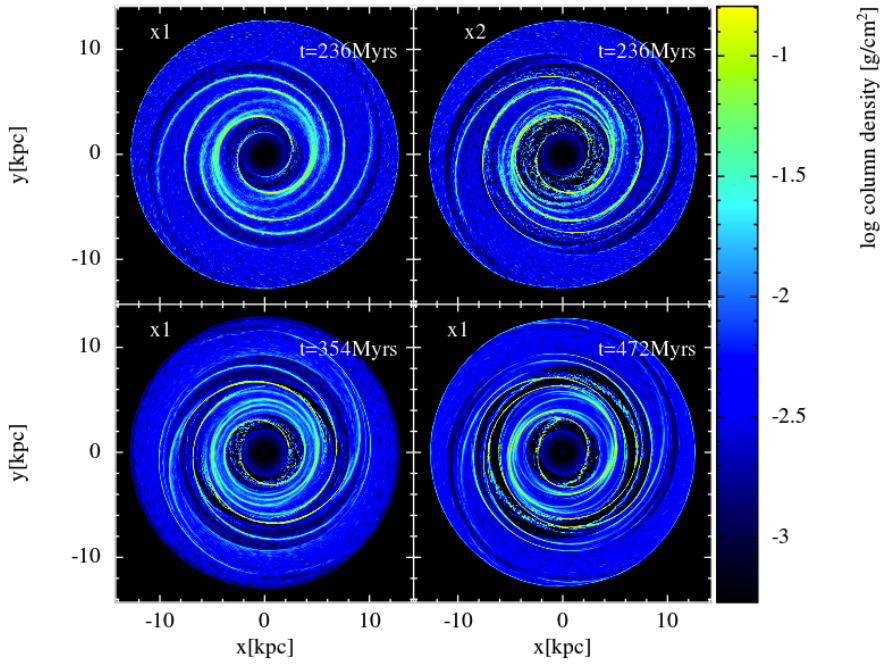

Figure 3.28: Two calculations with the PM spiral arm potential. A calculation with the fiducial arm strength is shown at three separate times in the top left, bottom right and bottom left panels. The top right shows a calculation with twice the fiducial arm strength at a time of 236Myrs.

4Gyrs, whereas we find these structures short lived. A possible explanation for this is that the calculations of Gómez et al. (2013) are isothermal at $T = 8000$K, which is considerably hotter than the gas in our calculations with active cooling. Figure 3.5 shows that isothermal calculations of the order $T = 10000$K produce a much smoother gaseous response, and trace the underlying potential much clearer than their 200K counterpart.

Figure 3.29 shows the best-fitting *l*-*v* maps of the models shown in Figure 3.28, where the disc is angled so that the observer is placed at $(0, R_{\rm obs})$. It is clear that although the arms display a 4 armed pattern in some cases, there is little arm structure in most of these maps, with the slight exception of the stronger arm case. The arms replicate the inner ridge of emission from the arm closest to the observer, but fail at reproducing the outer arm structures. This is due to the arm structures being confined to relatively small radii, while the Outer and Perseus emission comes from radii larger than the extent of the spiral structures shown in Figure 3.28. Using this potential with a pattern speed of $15\mathrm{km\,s^{-1}\,kpc^{-1}}$ it is possible to create arm features in the outer disc. However, at this speed the CG arms also provide strong secondary arm features, negating the benefit of using this complex potential. As this arm model provides no significant benefit to the CG arm model it is removed from our refined parameter space for use with bar potentials. Some preliminary calculations were made with this potential in combination with the WK bar model. Due to radially constrained nature of the PM arms they were heavily disrupted by the inclusion of a bar, making them even less suitable as a representation of the Milky Way's spiral structure.

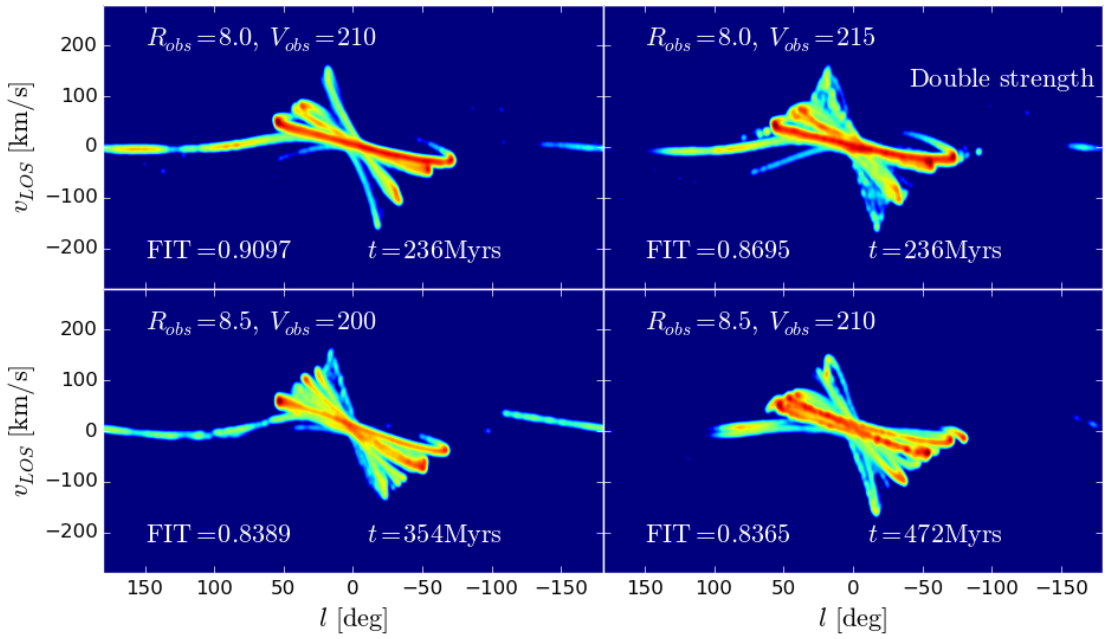

Figure 3.29: The best-fit l-v maps for the calculations shown in Figure 3.28, with best-fit parameters indicated in each corresponding panel. The discs in Figure 3.28 have been orientated such that the observer is located at $(0, R_{\rm obs})$ in the construction of these maps.

3.9 Chapter summary

In this chapter we have presented calculations of the evolution of ISM gas embedded in various stellar potentials representing the Galactic arms and bar. These include simple sinusoidal perturbations of the Galactic disc, and more complex models formulated from a density profile tailored to specific Milky Way mass components. The ISM embedded within these potentials has very diverse responses depending on pattern speed, which appears to be a key factor in determining the radial extent of the gaseous response.

In order to narrow down the hefty parameter space defining the exact morphology of these potentials we formulated a method of creating l-v maps that, while simplistic in nature, allowed for a very fast sweep through parameter defining the observers position and velocity. Using this technique allowed for the creation of a much narrower parameter space for use in calculations with active bar *and* spiral potentials. Best-fitting bar models favoured fast rotations, and orientation angles of approximately 45°, within agreement with values found for the "Long Bar". The best-fitting arm models seem only weakly dependent on pitch angle, but showed a clear minima for pattern speeds of 20km s^{-1} kpc^{-1}, also in agreement with values suggested in the literature. There is only a weak preference to a 2 over a 4 armed model regarding the values of the fit statistic, with each showing clear differences in l-v structures. The 4-armed models were however the only ones capable of reproducing all l-v features, the 2-armed models simply could not seem to produce enough emission structures in l-v space. The downside being that they produce too much emission where it is not needed.

The possibility of a 2 armed stellar spiral driving a 4 armed gas structure was also investigated. A slightly slower pattern speed of $15\mathrm{km\,s^{-1}\,kpc^{-1}}$ showed strong and long-lasting supplementary arm features. A complex arm model that is very efficient at creating supplementary arm features was investigated, but did not show a clear benefit to simpler arm models we have been using.

In the next chapter the refined arm/bar parameter space will be used in calculations with barred-spiral simulations, with the aim of producing an *l*-*v* map that produces all features observed in observations. As our parameter space is now much smaller, and we are approaching a global best-fit model, we will be employing a radiative transfer code to fully model the molecular emission of the ISM, as opposed to the simple maps used in this chapter.

4

Simulations with fixed analytic potentials II: barred-spiral simulations and synthetic observations

"Equipped with his five senses, man explores the universe around him and calls the adventure Science."
– Edwin Hubble (May 1929), Harper's Magazine 158: 732.

4.1 Introduction

In the previous chapter ISM gas was subjected to various arm and bar structures by the use of smooth analytic potentials. Alone, neither of these features provided a good match to all the observed *l*-*v* features of our Galaxy, though individual features could be reproduced. The current consensus is that the Milky Way has both bar and spiral components (Churchwell et al. 2009), and so it is not surprising that the all features cannot be reproduced with just arm or bar potentials. This leads to the next stage of our investigation; to perform calculations with both bar and spiral perturbations. In Section 4.6 we present the results of our investigation into the barred-spiral nature of the Milky Way, and our models that provide the best representation of Galactic structure.

The method to create *l*-*v* features in the previous section is simplistic in nature, and in no way takes into account the optical depth of the ISM, but instead simply approximates emission strength as decreasing with distance squared from the source gas particles. Now that a refined parameter space has been produced it is prudent to use a more sophisticated approach to creating *l*-*v* maps. A radiative transfer code is employed to create synthetic *l*-*v* maps of some of our best

Galactic models, so that emission can be directly compared with observations. In the first half of this chapter we briefly discuss the theory of radiative transfer relevant to our calculations. Tests of the method are shown before applying it to our SPH calculations from the previous chapter, and finally applying to the best-fitting barred-spiral calculations. The investigation using analytic potentials is then discussed in full in Section 4.7.

4.2 Theory of radiative transfer

The theory of radiative transfer is a way of describing the quantifiable amount of radiation received from some source, including effects of absorption and re-emission by any media in between the point of emission and observation. This is employed later in this Chapter to produce Galactic emission maps from the SPH calculations in the previous chapter, so we devote some time here to the discussion of the relevant fundamentals.

The simplest form of radiative transfer comes in the form of Beer's law, where an incident ray of intensity I_0 passes through some absorbing medium of thickness s resulting in an emergent intensity of $I = I_0 e^{-n\sigma s}$, where n is the number density and σ the cross section of absorption [cm^2]. The cross section is related to two other quantities, the absorption coefficient (α) and opacity (κ, or mass absorption coefficient) by $\alpha = n\sigma = \rho\kappa$. By differentiating Beer's law we can obtain the standard form for the attenuation of a ray passing though some absorbing media, i.e. radiative transfer equation for a non-emitting medium

$$\frac{dI_\nu}{ds} = -\alpha_\nu I_\nu \tag{4.1}$$

where intensity and absorption can be frequency dependant. This absorption can also incorporate scattering processes, as well as standard photon thermalisation. The optical depth can then be defined as[1]

$$\tau_\nu = \int_{s_0}^{s_1} \alpha_\nu ds \tag{4.2}$$

where significant absorption (of order e) will occur for optical depths of order 1, where the medium is referred to as *optically thick*. The medium can also be allowed to emit additional radiation as the incident ray passes through, contributing further to the total radiation intensity quantified by an emission co-efficient j_ν with units[2] [erg s^{-1} cm^{-3} Hz^{-1}ster^{-1}] which can similarly be related to a density independent emissivity, ϵ_ν, by $j_\nu = \rho\epsilon$. This changes Equation 4.1 to the full radiative transfer equation for an absorbing and emitting medium

$$\frac{dI_\nu}{ds} = j_\nu - \alpha_\nu I_\nu. \tag{4.3}$$

It is then prudent to define the source function, the ratio of emission to absorption processes,

[1] This is the same optical depth as used in the shielding processes incorporated in the cooling and chemistry in Chapter 2.

[2] These are the also the units of the ray intensity due to the definition of intensity as the energy emitted per unit area, per solid angle, per second, per unit frequency, i.e. $dE = I_\nu dA d\Omega d\nu dt$.

simply given by:

$$S_\nu = \frac{\epsilon_\nu}{\kappa_\nu} \equiv \frac{j_\nu}{\alpha_\nu} \tag{4.4}$$

which means we can re-cast Equation 4.3 as

$$\frac{dI_\nu}{d\tau_\nu} = S_\nu - I_\nu. \tag{4.5}$$

The solution to which can be found by multiplying through by e^{τ_ν}, grouping all I_ν terms into $d(I_\nu e^{\tau}_\nu)/d\tau$ and then integrating from $\tau_\nu = 0$ (the initial ray position) to τ_ν to give the full solution as:

$$I_\nu(\tau_\nu) = I_\nu(0)e^{-\tau_\nu} + \int_0^{\tau_\nu} S_\nu(\tau'_\nu)e^{-(\tau_\nu - \tau'_\nu)}d\tau'_\nu \tag{4.6}$$

where $I_\nu(0)$ is the incident intensity, and $I_\nu(\tau_\nu)$ the emerging intensity after attenuation through an optical depth τ_ν (Rybicki & Lightman 1979). If the source function is constant along the path of the ray (e.g. the temperature in the medium is constant) then the integral can easily be evaluated as

$$I_\nu(\tau_\nu) = I_\nu(0)e^{-\tau_\nu} + S_\nu(1 - e^{-\tau_\nu}) \tag{4.7}$$

in which the first term on the right hand side encompasses emission entering the medium and being attenuated by absorption, while the second term is the emission from within the medium, that is also being attenuated by the medium itself. In the optically thin limit ($\tau << 1$), this becomes $I_\nu(\tau_\nu) = I_\nu(0) + ds(j_\nu - \alpha I_\nu(0)) \approx I_\nu(0) + j_\nu ds$, and the incoming radiation only receives positive contributions from the medium. In the optically thick regime ($\tau >> 1$) this reduces to $I_\nu(\tau_\nu) = S_\nu$, with all the incident radiation being absorbed and the only contribution to the emerging ray coming from that emitted by the medium and not instantaneously absorbed.

The form of the source function depends on the physics of the medium in question. In complete thermal equilibrium there is no change in ray intensity, and so the source function is simply the radiation intensity, $S_\nu = I_\nu$. If thermal equilibrium is in effect then by Kirchoff's law the intensity is simply given by the Planck function, i.e. that of a black body, $I_\nu = S_\nu = B_\nu(T) = j_\nu/\alpha_\nu$. The relation between source and Planck functions not only holds in full thermodynamic equilibrium, but local thermodynamical equilibrium also (LTE) where $I_\nu \neq S_\nu = B_\nu(T)$. If intensity increases in passage through the medium then $dI_\nu/d\tau_\nu > 0$ and $B_\nu > I_\nu$, conversely if intensity decreases $dI_\nu/d\tau_\nu < 0$ and $B_\nu < I_\nu$ (Böhm-Vitense 1989). In LTE calculations the level populations required for transitions are purely a function of temperature, and collisional thermodynamical rates dominate the energy transport. In non-LTE the radiation field rates dominate the collisional rates, and the source function is no longer purely a result of black body emission.

We now turn to the determination of the emissivity and opacity for each of the two transitions of interest. These are the H I 21cm hyperfine transition, and the CO roto-vibrational $J = (0 \rightarrow 1)$ 2.6mm transition (see Sec. 1.4). The terms do not share the same formalism due to the different physical process underlying each transition. Beginning with the hydrogen line and the definition of emissivity as

$$j_\nu = \frac{h\nu_0}{4\pi} A_{ul} n_u \phi(\upsilon) \tag{4.8}$$

where the spin-flip hyperfine transition has an Einstein co-efficient of spontaneous emission of $A_{\mathrm{HI(21cm)}} = 2.9 \times 10^{-15}\mathrm{s}^{-1}$ and a wavelength ($\lambda_0 = c/\nu_0$) of 21cm, making the transition temperature between the upper and lower levels, u and l, $T_{ul} = 0.068$K (Binney & Merrifield 1998). $\phi(\nu)$ is the line profile function, discussed later in this section. The occupancy of states will determine the number density of the upper state; n_u. This can be determined from the Boltzmann equation

$$\frac{n_u}{\sum_i n_i} = \frac{g_u e^{-E_u/k_B T}}{Z(T)} \tag{4.9}$$

where the partition function is given by $Z = \sum_i g_i e^{-E_i/k_B T}$, a property of the system and solely a function of T, and g_i is the statistical weight of the i^{th} level. By equating partition functions and taking rates of the upper and lower levels of the transition we get the relation

$$\frac{n_u}{n_l} = \frac{g_u}{g_l} e^{-(E_u - E_l)/k_B T}. \tag{4.10}$$

The value $(E_u - E_l)/k_B$ is equivalent to T_{ul}. In every case the temperature of the medium will be greater than or equal to that of the CMB (2.73K), so $T >> T_{ul}$ and so reducing the exponential above to unity. As the 21cm line is a spin-flip transition the degeneracy of states is simply $g = 2S + 1$, where $S = 0$ or 1 and so $g_l = 1$ and $g_u = 3$. This makes the ratio of state number densities $n_u = 3n_l$, and $n_u = 3n_H/4$, where n_H is the total number density of hydrogen. This results in an emissivity that can be expressed from Equation 4.8 as (Acreman et al. 2010a):

$$j_\nu = \frac{3\nu_0 h A_{\mathrm{HI(21cm)}}}{16\pi} n_{\mathrm{H}} \phi(\upsilon). \tag{4.11}$$

By using the assumption of LTE and Kirchoff's law ($S_\nu = B_\nu = j_\nu/\alpha_\nu$) the opacity can easily be calculated. The Rayleigh-Jeans approximation reduces the Planck function to only the tail of the black body distribution, and is valid where thermal energy is much greater than that of the transition (such as radio astronomy) and $k_B T >> h\nu$. This reduces the Planck function to

$$B_\nu(T) = \frac{2h\nu^3}{c^2\left(\exp\left[\frac{h\nu}{k_B T}\right] - 1\right)} \approx \frac{2k_B T \nu^2}{c^2} \tag{4.12}$$

giving an opacity for the hydrogen line of

$$\alpha_\nu = \frac{3c^2 h A_0}{32\pi k_B \nu_0} \frac{n_{\mathrm{H}}}{T} \phi(\upsilon). \tag{4.13}$$

For the molecular CO transition the temperature of the transition is 5.53K, which is comparable to ISM temperatures so that the simplifications made above for H I no longer hold. The opacity is defined in full by the Einstein coefficients of stimulated emission (B_{ul}) and stimulated absorption (B_{lu}):

$$\alpha_\nu = \frac{h\nu_0}{4\pi}(n_l B_{lu} - n_u B_{ul})\phi(\nu) \tag{4.14}$$

for a transition from u to l, and the emissivity is again given by Equation 4.8. This reduces the source function to simply $A_{ul} n_u/(n_l B_{lu} - n_u B_{ul})$. To solve the radiative transfer equation the line

profile is still needed in the opacity, determined from Equation 4.14. The Einstein A co-efficient for this transition is $A_{CO(0\rightarrow1)} = 7.2 \times 10^{-8} s^{-1}$ (Schöier et al. 2005) from which the B coefficients can also be calculated[3]. The population of states is given by Equation 4.10 where the degeneracies of the upper and lower states are 1 and 3 respectively ($g = 2J + 1$), providing everything required to calculate the emissivity and opacity of the CO and H I transitions of interest. The above expressions are only valid in LTE where the level populations can be calculated by Boltzmann statistics. In LTE level populations are calculated from local temperature alone where the density is sufficiently high that thermal collisions dominate radiative effects. In non-LTE regions the level populations are calculated by assuming statistical equilibrium between states and must be iteratively solved for, including the effect of the global radiation field (i.e. n_u is a function of I_ν). This makes the calculation exceedingly more complicated and time-consuming. The calculations performed within this thesis assume LTE, which should hold in the dense cold regions of the ISM where CO emission originates. Non-LTE effects become important in diffuse regions where radiative effects dominate (e.g. stellar coronae, see Rundle et al. 2010 for an application).

The final ingredient of the radiative transfer equation is the profile function, ϕ_ν, which contains the velocity information of the medium. For the ISM thermal broadening is the dominant effect, for which the profile takes a Gaussian form

$$\phi_\nu = \frac{c}{\upsilon_b \nu_0 \sqrt{\pi}} \exp\left(-\Delta\upsilon^2/\upsilon_b^2\right) [\mathrm{cm}^{-1}] \tag{4.15}$$

where υ_b is the broadening width given by a combination of thermal (υ_T) and turbulent (υ_{turb}) effects as $\upsilon_b^2 = \upsilon_T^2 + \upsilon_{\mathrm{turb}}^2$ where $\upsilon_T = \sqrt{Tk_B/m}$. The turbulent velocity is a collection of any velocity structure not included in the global velocity field resolved by the calculation, e.g. supernovae feedback, stochastic gas motion, and MHD effects, which can be of the order of $\mathrm{km\,s^{-1}}$(Larson 1981). Other broadening processes include pressure and natural broadening which take the form of a Lorentzian profile but become important in extremely different environments such as planetary atmospheres. The velocity of the gas (υ) is incorporated in the Doppler shift of the rest frequency,

$$\Delta\upsilon = (\nu - \nu_0)\frac{c}{\nu_0} + \vec{\upsilon} \cdot \hat{n} \tag{4.16}$$

where ν is the frequency of the ray being traced. $\vec{\upsilon}$ is the velocity field of the gas causing the absorption/emission and $\hat{n}$ is the unit vector defining the direction of ray propagation (Rundle et al. 2010).

4.3 Creating *l-v* maps and quantifying the best fit

The 3D AMR Monte-Carlo radiative transfer code TORUS (Harries 2000) is used to create synthetic observations, using the formulae outlined above. TORUS is capable of creating synthetic brightness temperature, T_B, data cubes (data structures with dimensions l, b, υ and T_B) enabling us to compare our simulations directly with the map of Dame et al. (2001). TORUS has been employed in several studies already to create synthetic emission from SPH simulations including star formation regions

[3]The Einstein coefficients are related by the relations $B_{ul}g_u = B_{lu}g_l$ and $A_{ul} = B_{ul}2h\nu^3/c^2$.

(Rundle et al. 2010) and circumstellar discs (Acreman et al. 2010b). Synthetic H I maps of the spiral galaxies of M31 and M33 were created by Acreman et al. (2010a), finding good agreement with observed emission. Douglas et al. (2010) and Acreman et al. (2012) also used TORUS to create synthetic emission maps of the second quadrant of our Galaxy from SPH calculations in H I.

The procedure to create *l*-*b*-*v* data cubes, analogous to those created from observations, is described in detail in Acreman et al. (2010a) and we will give only a brief description here. Creation of synthetic observations is a two stage process. An AMR grid is first generated, containing all the data required for the radiative transfer calculation, through which the actual ray-trace can then be performed. The SPH data must first be converted to a grid for use by TORUS. This is done using the method of Rundle et al. (2010). A grid is constructed with SPH particles using an octree method, where the grid is initially a 2x2x2 cube. The grid is then subdivided according to a mass per unit cell criterion, thereby providing greater refinement in regions of high particle concentration. Our grid is somewhat larger than previous works of Douglas et al. (2010) and Acreman et al. (2012) that focused on the second quadrant alone. As such, to make the grid manageable in terms of memory and map construction time we use a higher mass per unit cell of $4 \times 10^4\,\mathrm{M}_\odot$ where each particle has a mass of $1.6 \times 10^3\,\mathrm{M}_\odot$, giving approximately 25 particles per cell. This results in approximately half a million splits by mass (around 4 million voxels) and a full galactic grid over 6GB in size. We find that higher mass thresholds (lower resolution) have very minimal effects on the resulting *l*-*v* maps, merely reducing the arm resolution slightly. The grid to SPH conversion is illustrated by Figure 4.1 where we show an SPH input file and the equivalent AMR grid, along with cell boundary and particle positions. The SPH particle properties including H I and CO number densities, temperature and velocities are mapped onto the grid using a summation of SPH kernels with a Gaussian form. The opacity and emissivity, assuming LTE, are then calculated and stored in the AMR grid for use in the radiative transfer ray-tracing.

The ray-trace is then performed with input values for the observer co-ordinates, requiring the distance from the Galactic centre, R_{obs}, the azimuthal position in the disc, l_{obs} and the circular velocity, V_{obs}. For a certain velocity channel rays are propagated from the observer throughout the disc in a range of $0^\circ < l < 360^\circ$ and $|b| < 6^\circ$. While out of plane emission is of minor importance for studying the Galactic disc, we pass rays out of the plane in a high enough latitude so we can produce an integrated emission map of comparable strength to that of Dame et al. (2001). As a ray enters a cell the intensity of emission is updated from I_ν to I'_ν using the opacity, emissivity and optical depth of the current cell at the frequency of interest ν (ϵ_ν, κ_ν and $d\tau$ respectively) via Equation 4.7 allowing for the optically thick or thin treatment of the transition. The actual quantities stored by the grid are independent of the velocity profile function, which is instead applied during the ray trace itself.

The intensity is transformed into brightness temperature by using the Rayleigh-Jeans approximation (Equation 4.12 with $I_\nu = B_\nu$). This process is then repeated for each velocity channel of interest, resulting in a cube of T_B as a function l, b and v_{los}. The resulting data cube is then integrated over the latitude dimension ($|b| < 2^\circ$) to produce an *l*-*v* map analogous to that in Dame et al. (2001). The number of velocity channels is considerably higher in the central galaxy in order to encompass emission up to a maximum of $280\,\mathrm{km\,s^{-1}}$ seen in the CO observations. To

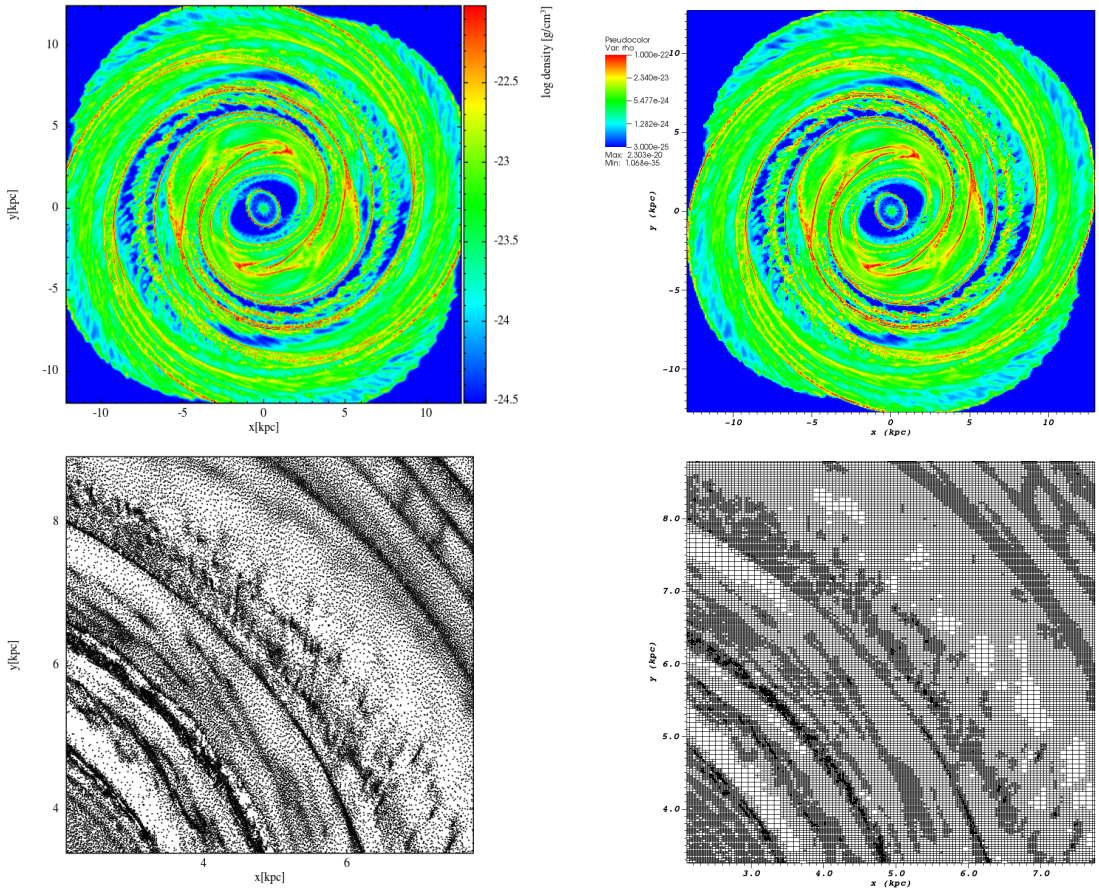

Figure 4.1: Illustration of the SPH to AMR grid conversion. Left column shows the SPH data (density render top, SPH particles bottom), and the right the ARM grid (density render top, grid cell boundaries bottom). The lower panels show a zoom in on the second quadrant and the upper panels the full barred-spiral galaxy density render.

avoid passing rays through empty regions of l-v space we use a number of channels that varies as a function of longitude, tailored to encompass the emission seen in Dame et al. (2001). As the H I emission spans a greater region of l-v space the datacube is simply cut-through at $b = 0°$ rather than integrated. The integration version of the observed H I emission adds little to the l-v structure, whereas the CO features show additional features upon integration. Though the CO integration usually does not introduce any new features in l-v space as our simulations are effectively confined to the Galactic plane.

A fit statistic is calculated for each resulting map to quantify similarity to observed emission. The statistic used is the same as Equation 3.20 for the simple kinematic l-v maps. The TORUS map tends to be of finer resolution than the relatively coarse Dame CO map, so is first rebinned to a lower resolution, after being smoothed in longitude slightly to provide a smoothness of the resolution of the Dame map. Our primary interest is whether emission features can be produced in the same location in l-v space, with comparable arm to inter-arm emission strengths. As such we are not so interested in the quantitive strength of the emission itself. As is discussed in greater detail below, the strength of the TORUS CO emission is somewhat higher than that in observations, with peak emission features approximately double the strength. To ensure the fit

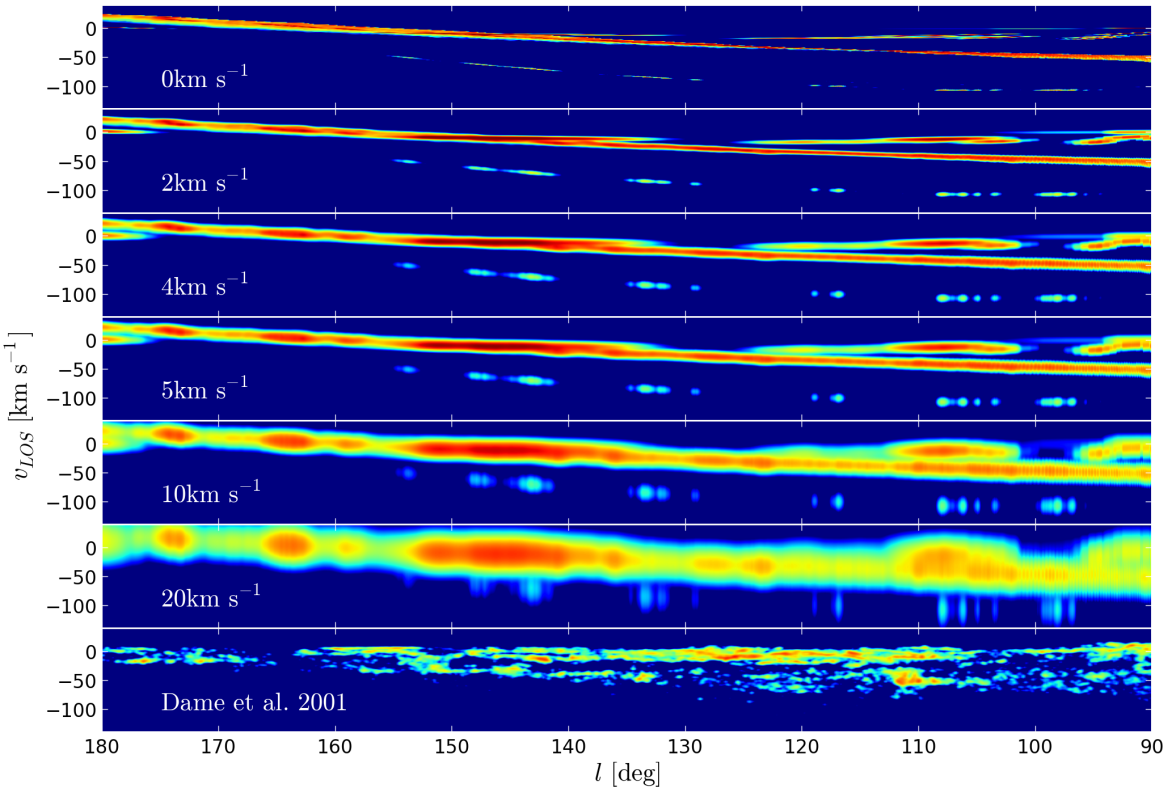

Figure 4.2: CO emission maps of the second quadrant in CO in a spiral galaxy with the galaxy aligned so arm features are located in the *l*-*v* space in a similar position to the Local and Perseus arms in observations (bottom panel). Each panel shows calculations with varying turbulent velocity contributions in Equation 4.15.

is not driven too much by this difference each map is scaled to have emission that matches that of the Dame map for the calculation of a fit statistic, which effectively halves the strength of CO emission. All plotted TORUS *l*-*v* maps retain their original strength.

4.4 General features of RT maps

Early tests using TORUS for CO *l*-*v* maps showed that the features created were far too narrow in velocity width compared to observations. Figure 4.2 shows CO emission from the second quadrant in an armed galaxy simulation with various turbulent velocity contributions ranging from 0-20 km s^{-1}. The map with no turbulent velocity has features much finer than those seen in observations (bottom panel). To resolve this we added a turbulent velocity to the width of the CO line emission profile of 4 km s^{-1}, a value high enough to smear out the fine emission features but not so strong as to blend features in *l*-*v* space. This is at the lower end of ranges suggested by CO observations of the outer regions of disc galaxies (see Dib et al. 2006 and references therein). The turbulent velocity could be scaled as a function of some cloud size determined by the clumpiness of SPH particles (Larson 1981; Dame et al. 1986; Brunt et al. 2003; Mac Low & Klessen 2004). However, we choose a constant factor to avoid introducing additional variables.

In Figure 4.3 we show full galactic plane *l*-*v* maps for H I and CO emission for calculations with varying surface density (i.e. total SPH particle gas mass), increasing from bottom to top. The CO emission is very strongly coupled to the disc mass, with emission features appearing

extremely weak in the lowest surface density case. With a low surface density the SPH particles are not massive enough to enter the upper region of the $n - \chi_{CO}$ diagram (Fig. 2.14), and stay relatively warm throughout the simulation. The two higher surface density calculations show CO emission that appears to trace arm and bar features, though still appear too weak in the $7.5 M_{\odot} pc^{-2}$ case compared to observations. The highest surface density calculation was deemed as having a high enough mass to have visible *l-v* emission features in CO, and so was the mass adopted in the highest resolution models used in this and the previous chapter.

While the structure of the H I emission is not the prime goal of this work, as it is not believed to trace high density structures as well as molecular gas, emission maps were also created of the entire Galactic plane with varying surface density, similar to those shown in Acreman et al. (2012). The features seen are quite different to those shown in the CO emission. The H I emission only seems to trace the high density regions associated with arms and bars in the lower surface density cases (lower two panels). In the calculations with higher surface densities there appears to an equal amount of emission coming from the inter-arm regions as the arms themselves, if not more. A possible explanation for this that the gas in simulations shown here is very confined to the *x-y* plane, as there is no mechanism to drive the gas off-plane and counteract the disc potential. This causes all the ISM material to be within a single latitude channel in the construction of the emission data cubes. This would cause the optical depth of the atomic gas to be very high in the $b \approx 0^{\circ}$ channels, especially in the highest surface density case. As such the high densities, and therefore high optical depths, of the H I in the arms can result in a net loss of emission, explaining why the arm features in the highest surface density H I map in Figure 4.3 seem to show dearth of emission compared to that with the lowest surface density. The reason this was not seen in the work of Acreman et al. (2012) is that their surface density was somewhat lower, corresponding with the lower panels of Figure 4.3, where the H I does trace arm structure. Stellar feedback was also included in those models, acting to drive material off-plane. The earlier calculations of Douglas et al. (2010) are similar to those shown here. There is a considerable amount of off-plane emission seen in observations (Grabelsky et al. 1987; Bloemen et al. 1990; Dame et al. 2001), so it may be that our axisymmetric model is too strong in the vertical direction, though this would lessen the amount of molecular gas due to the drop in density, and weaken the CO emission structures.

It may be the case that there is some careful balance required to having a high enough surface density to produce CO emission, but not too high to create adverse absorption in H I. There is also the possibility that the chemistry is too simplistic to allow the accurate modelling of H I and CO. To test the effects of the optical depth on the H I emission we performed calculations where the atomic and molecular gas was assumed to be optically thin. The calculation was performed by simply adjusting Equation 4.7 to instead read $I_{\nu}(\tau_{\nu}) = I_{\nu}(0) + j_{\nu} ds$ for both the atomic and molecular ray-trace. Figure 4.4 shows H I and CO emission for the optically thin case from the second quadrant alone, using the same SPH input as Figure 4.3. In this case both the atomic and molecular gas appears to trace the arm structures. The differences in CO emission are much less apparent than in H I, but there is a minor change in emission strength. The peak H I emission is much stronger than in the optically thick cases, reaching temperatures above 1000K, which far exceeds that of the optically thick calculation and temperatures seen in observations. This indicates

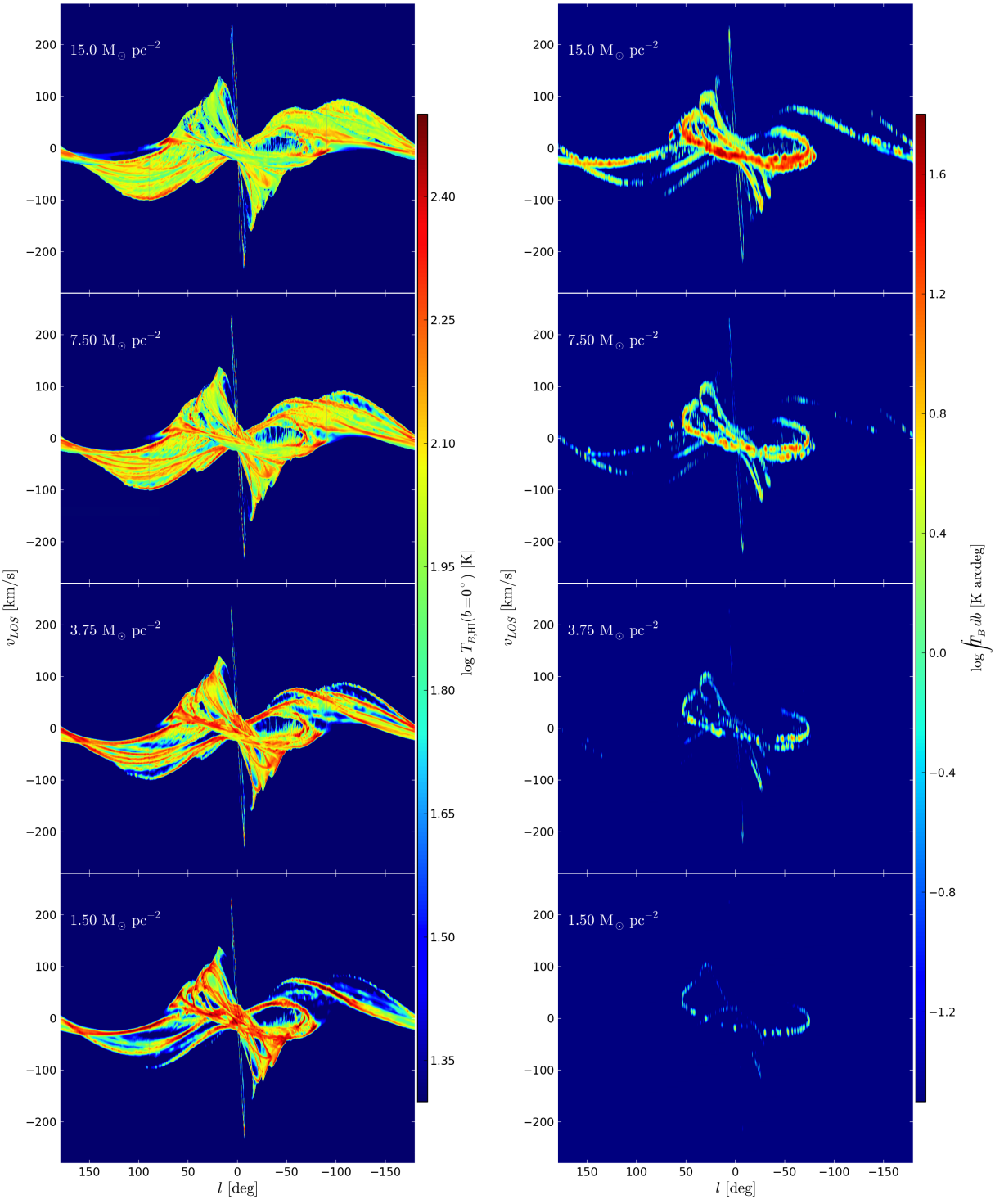

Figure 4.3: H I (left) and CO (right) emission maps of barred-spiral galaxies of similar morphologies to that in Fig. 4.1 with varying surface densities, increasing from bottom. The corresponding total gas mass is 8, 4, 2, and 0.8 $\times 10^9 M_\odot$ from top to bottom. The potentials and observer location are the same in all maps, with the observer placed at $R_{\mathrm{obs}} = 8$kpc.

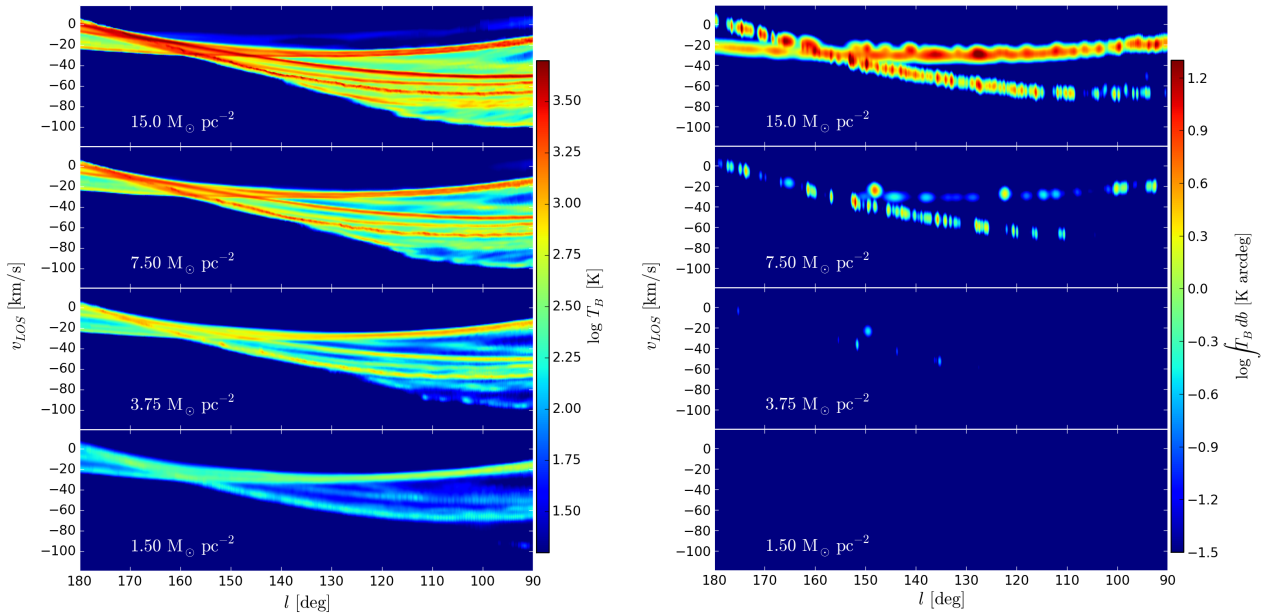

Figure 4.4: The same maps as Fig. 4.3 except in the optically thin regime with negligible optical depth, and only of the second quadrant. H I emission is shown in the left panel, and CO in the right in calculations with varying surface density.

that the H I does also trace arm structures, but that the absorption is too high in our standard calculations. Without such a high density however, CO production will be too low, and so we believe that correctly modelling the atomic and molecular emission simultaneously is not possible with the chemistry and potentials used here. Additional physics or more complex chemistry would be needed to break up the atomic gas and reduce its opacity while allowing for sufficient CO production to produce observable emission features.

The contrast between CO emission in our TORUS maps is comparable to that of the observations in the inner Galaxy when a 4 km s^{-1}turbulent velocity is added. The distribution of emission in general is smoother than that seen in observations. This is a result of the continuous nature of the potentials, which are idealised compared to the arm structures in observed spiral galaxies. Inclusion of other physical processes, such feedback as in Acreman et al. (2012) or a live stellar component as in the following chapter, will act to break up these smooth *l*-*v* features.

The strength of the CO emission in our TORUS maps is somewhat higher than that observed, peaking at approximately 40K compared to 20K seen in observations in the highest surface density case. The peak emission in the second highest density calculation is in closer agreement with observations, but arm features appear much weaker in comparison. There are several possible reasons for this difference. The first is that the strength of the CO emission is very sensitive to the surface density of the ISM disc. The disc mass found through integration of the disc surface density profile resulted in visible emission from the arm features, and so was used for the majority of the simulations presented here. Another consideration is that the production of CO has no limit other than the maximum amount of C allowed to be present in the ISM. All SPH particles tend to increase their molecular abundance (and density) up to this limit, as there is no strong process to break up and heat the gas. Additional heating mechanisms such as stellar feedback or magnetic

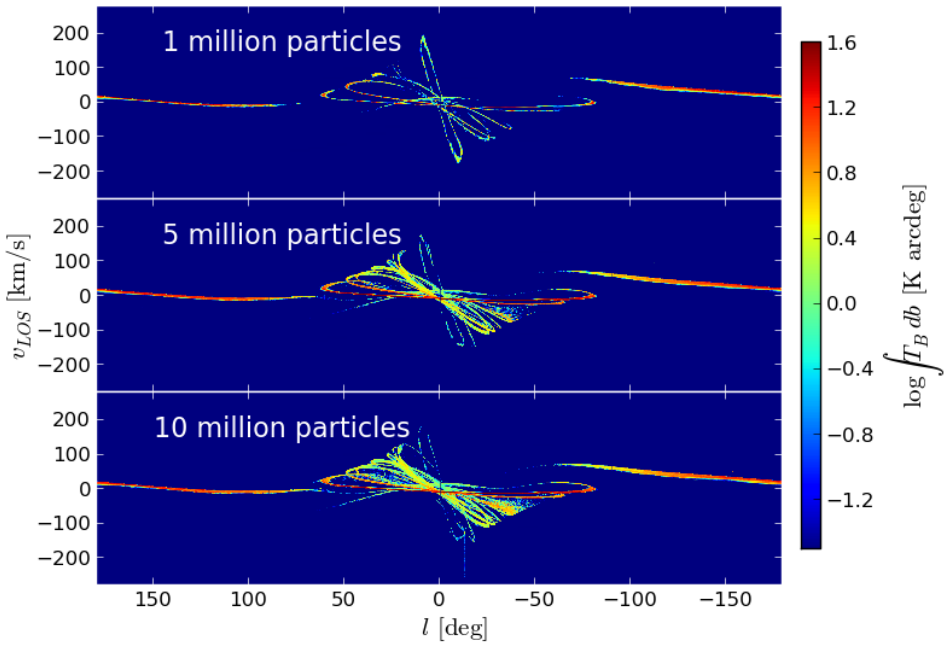

Figure 4.5: Radiative transfer CO *l*-*v* maps resulting from an SPH simulation with 1, 5 and 10 million particles (increasing from top). The gas is subject to a bar potential moving at 40km s^{-1} kpc^{-1}, shown after 280 Myrs of evolution. The observer is set to the IAU standard position and velocity. Turbulent velocity broadening is excluded to highlight differences between different resolutions.

fields would be required to break up the dense clumps of ISM gas and remove some of the excess CO build up. The addition of stellar feedback would also cause material to be more dispersed vertically compared to the no feedback case (Tasker & Bryan 2006; Dobbs et al. 2011; Acreman et al. 2012). The confinement of the gas to the *x*-*y* plane may also cause this over-emission. The molecular material will be located in a single latitude channel in the construction of the emission data cubes, increasing the strength of emission seen in *l*-*v* space, but the amount of the molecular material still being low enough to not have a large absorption effect.

4.4.1 Resolution study

To test our adopted simulation resolution of 5 million particles we ran a number of simulations with 1 and 10 million particles. Top down maps of 1 million particles displayed significantly less structure around the resonance regions of the potentials, while 5 and 10 million particle calculations showed little difference. Figure 4.5 shows CO *l*-*v* emission maps made using TORUS for simulations using 1, 5 and 10 million particles (increasing from top) inside a bar potential. No turbulent velocity term is added to the line profiles so as to highlight the resolution effects. The difference between 5 and 10 million particles appears to be minimal, but the 1 million run has considerably less emission in the inner Galaxy in comparison. We conclude the 5 million particle resolution is sufficient to capture the global Galactic CO emission.

The 1 million particle resolution calculations have a much lower CO formation efficiency, with a very low molecular gas fraction compared to the higher resolutions. They will cause weaker CO emission which, coupled with the weaker tracing of potentials in low resolution runs, causes

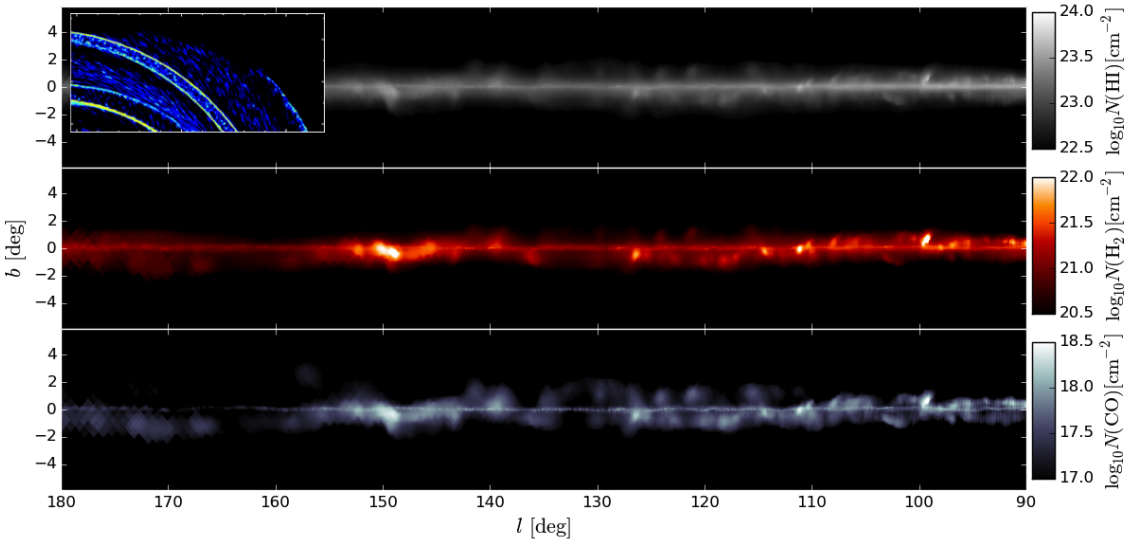

Figure 4.6: Column density of H I (top), H_2 (middle) and CO (bottom) of the second quadrant of a simulation with a spiral perturbation, shown in the insert.

the observable decrease in CO emission features seen in Figure 4.5.

4.4.2 ISM Column densities

The column density of the gas is an important quantity for both the radiative transfer and the ISM chemistry. Figure 4.6 shows the column density of the second quadrant of a spiral galaxy simulation (pictured in the top left corner). The column density of the atomic hydrogen, molecular hydrogen and CO gas is shown in the top, middle and bottom panels respectively, as a function of longitude and latitude. Firstly, it is clear that the column density (and therefore opacity) is decreasing with mass of the ISM species in question, due to the decreased abundance of each species in the simulation. There are two major arm segments in this quadrant seen in the insert, both of which can be seen in the column densities. The molecular gas (both H_2 and CO) is primarily confined to higher density regions associated with spiral arms. In the corresponding column densities a far and near arm structure can be seen. The far arm is confined to the $b \approx 0°$ plane due to its relatively large distance from the observer, while the near arm appears as the off plane clumps that span a wide range of latitudes due to their closer proximity. The atomic gas however has a weaker affinity to these arm features, especially compared to CO, seen throughout the plane.

In Figures 4.7 we show the column density of H I and CO for the entire Galactic plane of the same barred-spiral calculation as that used in Figure 4.1. Here an even clearer distinction between the atomic and molecular gas column density distribution can be seen. The H I column density is not only predominantly confined to the mid-plane, but also present at all longitudes. There is some off-plane emission in the inner disc where the bar is causing turbulent gas motions relatively close to the observer's location, but the column density is still relatively thinner than that in-plane. Conversely, the CO is much less uniformly distributed through longitude. The third quadrant in

particular has a very low column density compared to the inner quadrants. The off-plane density associated with arm/bar structure is also closer to that of the in-plane density than the H I.

Figure 4.7 shows some numerical artefacts of the SPH to grid conversion. The local material that has a relatively large angular size clearly shows cube-like features inherent to the grid based nature of the ray-trace. These features can be muted by decreasing the mass per units cell criterion, though this will further increase the already hefty memory requirements of the AMR grid. This will only help so much however, and in order to fully remove these artefacts the resolution of both the SPH calculation and the AMR grid must be increased. The effect of this numerical artefact is seemingly unimportant in the CO *l*-*v* maps, where the emission is integrated through latitude. This was tested by performing calculations with lower values of the mass per unit cell parameter, and the resulting *l*-*v* emission maps showed no visible change.

In Figure 4.8 the column density of H_2 and CO is shown for a Galactic simulations after 120Myrs and 340Myrs of evolution in the left and right panels. Column densities from several other works in the literature are also plotted as coloured circles, including data from Sheffer et al. (2008); Burgh et al. (2007); Ungerer et al. (1985); Baudry et al. (1981) and Federman et al. (1980). The figure also includes a line indicating the maximum CO column density allowed by formation from H_2 (Sheffer et al. 2008). The earlier time-frame shows column densities that agree with those of moderately diffuse molecular clouds, but not of the denser cores of Ungerer et al. (1985) and Baudry et al. (1981). The global trend does not match that seen in observations. The column densities in our calculations appear to drop away $N(H_2) < 10^{19}\mathrm{cm}^{-2}$, following an inverse exponential profile. Observations on the other hand appear to have a near constant $N(\mathrm{CO}) \approx 10^{12}\mathrm{cm}^{-2}$ when $N(H_2) < 10^{19}\mathrm{cm}^{-2}$, though there are much fewer data in this region, and the data appear to follow a quadratic profile. The densities at the later time agree much better with the higher density molecular clouds, but produces too high values of $N(\mathrm{CO})$ for the more diffuse clouds. This later time frame is much closer to that used for construction of *l*-*v* maps, thus at that time it is assumed that we are correctly reproducing the molecular column densities in the denser region of the ISM. We are however over-estimating the CO column densities for the more intermediate density clouds. This can result in excessive absorption of CO emission in some regions, but also reduced emission, as the column density is dependant of CO mass, which dictates the actual CO emission.

While we are not expecting to fully match the column densities of the ISM, the values in our calculations seem to agree well with those observed for the highest density regions. As these regions are the primary CO factories in our calculations it shows our chemical network underlying the CO emission maps matches some observed ISM properties. The lower column densities however likely need a better treatment of additional ISM physics. Our calculations are designed to resolve the colder ISM component rather than the warmer region where these lower column densities are seen. This region is also populated by very few data points compared to the well populated region that our calculations reproduce.

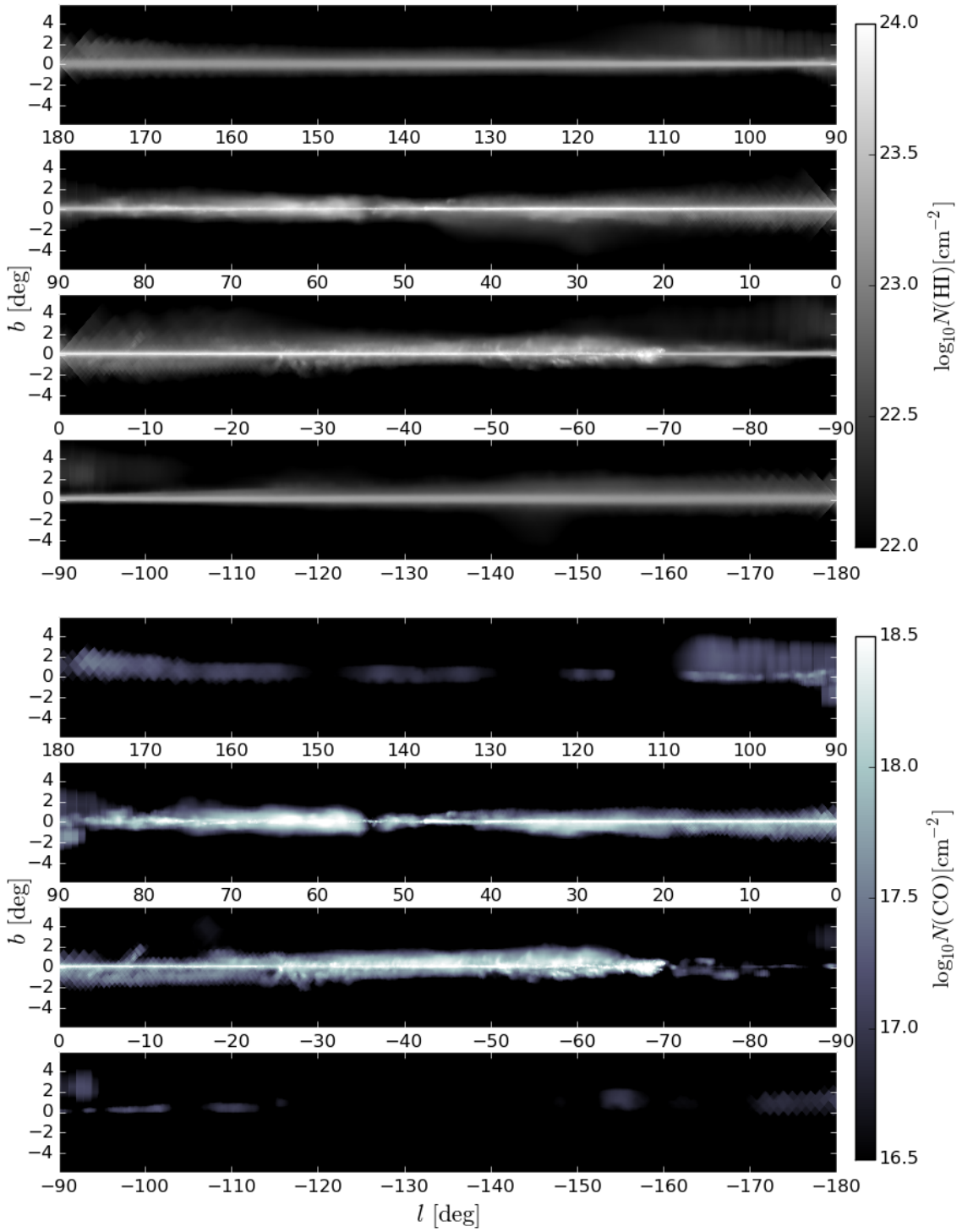

Figure 4.7: Column density of H I (top) and CO (bottom) of the entire Galactic plane for a barred-spiral calculation of similar morphology to that in Fig. 4.1. The four seperate panels show the column density in each of the four Galactic quadrants.

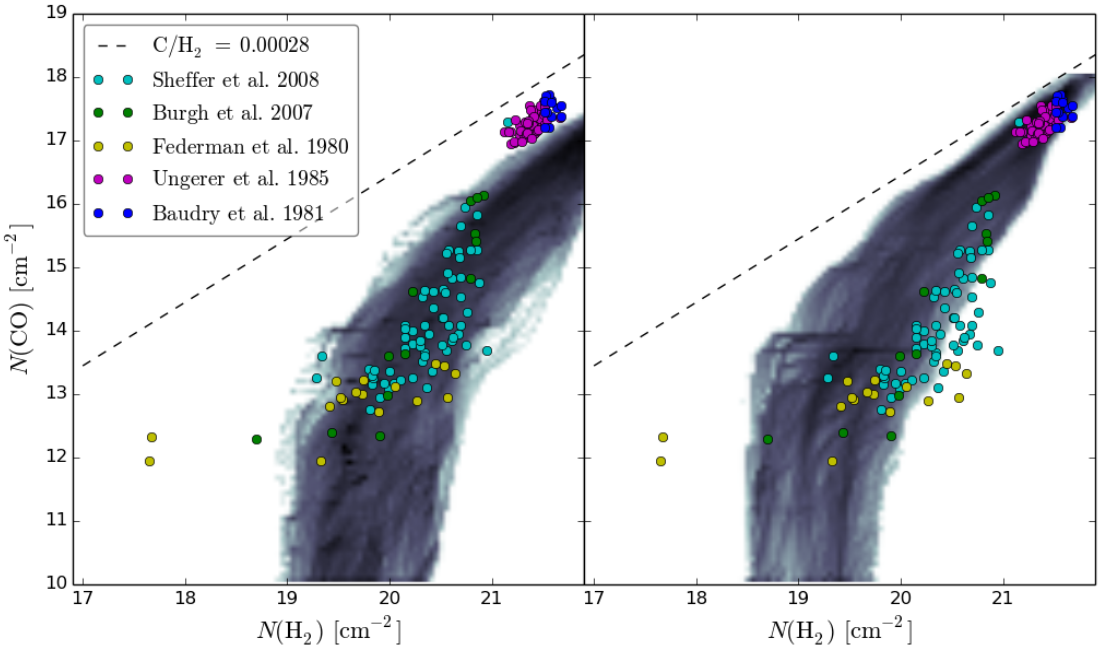

Figure 4.8: Column density of H_2 and CO for the second quadrant of a simulation with a spiral perturbation. The points show observational data from Sheffer et al. (2008); Burgh et al. (2007); Ungerer et al. (1985); Baudry et al. (1981) and Federman et al. (1980). The dashed line indicates the maximum CO column density allowed by formation from H_2 (Sheffer et al. 2008). Left and right panels show the calculation at 120Myrs and 340Myrs.

4.5 Radiative transfer maps of armed or barred simulations

Before considering barred-spiral models we first discuss a selection of maps made using TORUS of our models presented in Chapter 3. The SPH inputs to the TORUS calculations are the same as those for Figures 3.18 and 3.23 (5 million SPH particles, with a total gas mass of $8 \times 10^9 M_\odot$), using the same values for observer position and velocity. We show full radiative transfer maps for only a handful of these models due to the high computational cost of construction, and choose to use the radiative transfer to primarily differentiate between full models including bar and arm potentials.

In Figure 4.9 we show TORUS maps of the WK bar at pattern speeds of 40, 50 and 60km s^{-1} kpc^{-1} after 354 Myrs of evolution. These correspond to the simple maps shown in the centre of Fig. 3.18. The arm feature near the Solar position in the 40km s^{-1} kpc^{-1} model is visible as extremely bright emission in the top panel of Fig. 4.9. The strength of this emission far exceeds that seen in observations, and the arm appears uniformly bright, not just in a specific location. As the pattern speed increases, the emission covers a narrower range of longitudes, and increases the line-of-sight velocity of the central emission ridge. As with the simple maps from the previous chapter, there is little emission in the outer quadrants with these relatively fast rotating bars. The emission towards the Galactic centre ($|l| < 5$) with the greatest $|v_{los}|$ is a very clear feature in the observed CO emission; the CMZ. We find no such strong emission in our maps in Fig. 4.9. We do see some similar features to the peak velocity structures seen in observations in some of our maps in Fig. 3.18, but there is not enough CO produced to be seen in our TORUS maps. We discuss this further in Section 4.7.

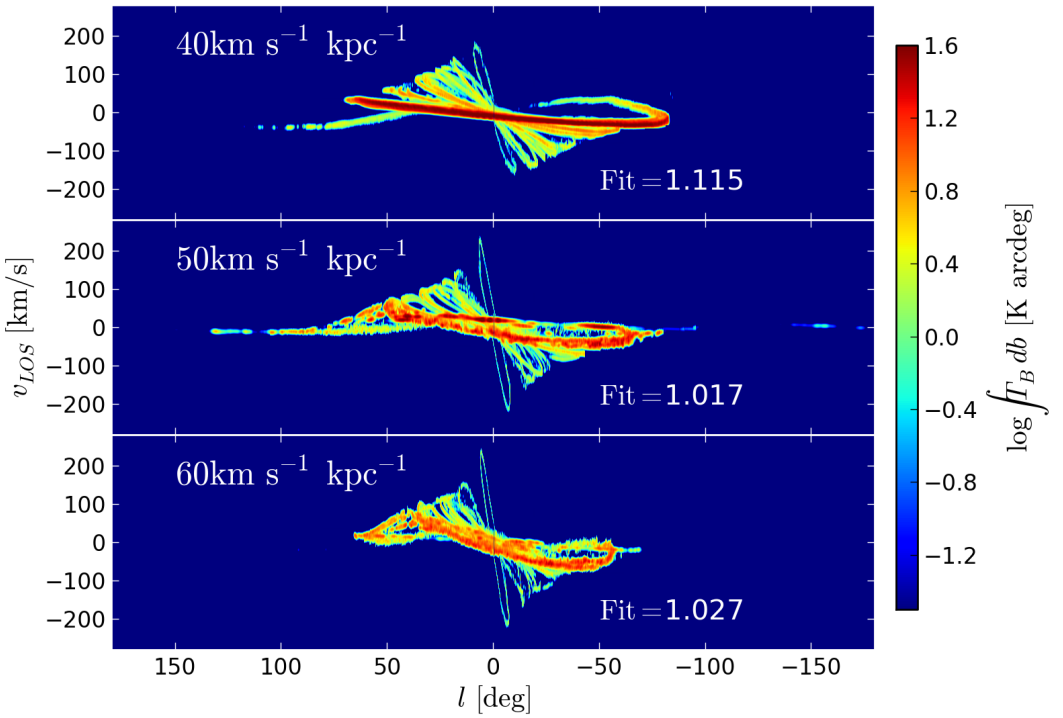

Figure 4.9: Radiative transfer *l*-*v* maps constructed using TORUS, rather than the simple chemo-kinematic re-mapping method used to create the maps in Fig. 3.18. The bar is that of Wada & Koda (2001) after 354 Myrs of evolution and pattern speeds of 40, 50, 60km s^{-1} kpc^{-1}(increasing from top to bottom). The brightness temperature scale is calculated exactly so the fit statistic is on a different scale to that for the previous maps.

Figure 4.10 shows a selection of 6 of the best fitting arm models made using TORUS, each with a different combination of N, α and Ω_{sp}. The $N = 2$ models cover a reduced area of *l*-*v* space compared to their $N = 4$ counterparts. This allows for $N = 2$ models to match emission in the 2$^{\text{nd}}$ quadrant while leaving the 3$^{\text{rd}}$ comparatively empty. This is seen in observations of CO, where possible arm features are much weaker in the in the 3$^{\text{rd}}$ quadrant compared to the 4$^{\text{th}}$. The $N = 2$ models tend to have the near arm aligned with the Perseus arm feature in the 2$^{\text{nd}}$ quadrant and this arm reaches the edge of the disc just as it enters the 3$^{\text{rd}}$ quadrant. The local emission in the 2$^{\text{nd}}$ quadrant is reproduced by branches, whereas in the 4-arm models this is reproduced by arms directly tracing the potential troughs (as seen in the top panels of Fig. 3.22).

In the maps shown in Figures 4.9 and 4.10 there is little difference morphologically to the maps constructed in the previous chapter. Emission strength is similar to values seen in observations, though peak strengths are higher. There also appears to be a lack of weakly emitting material on the order of tenths of kelvin that appears to be present in both arm and inter-arm regions of observations. A full reproduction of all features in *l*-*v* space still seems impossible with only an arm or bar potential. Arms without the inclusion of a strong bar to drive additional features in the inner disc cannot allow the arms to produce the Carina and Perseus features in the outer quadrant without trying to fit the central ridge simultaneously. The placement of the OLR of the bar at roughly the Solar position would impact upon the structures observed in the 1$^{\text{st}}$ and 4$^{\text{th}}$ quadrants formed

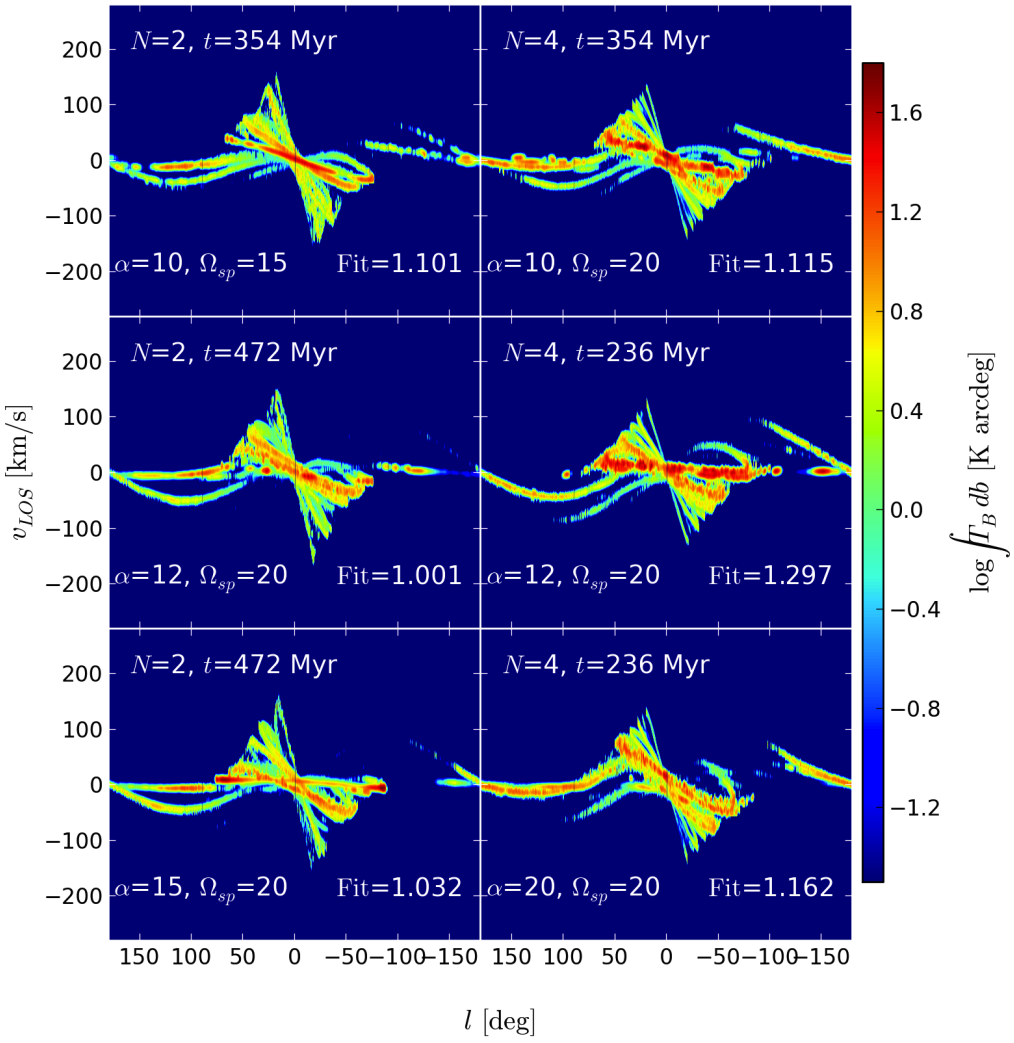

Figure 4.10: The best fitting maps from isolated arm potentials for a variety of pitch angles. *l*-*v* maps are made using the TORUS radiative transfer code, where the normalised fit to observed CO is shown in the bottom right of each panel. Ω_{sp} and α are in the units of km s^{-1} kpc^{-1} and degrees respectively shown in the bottom left.

by the arms.

We also constructed CO *l*-*v* maps using TORUS of different arm models, including that of Cox & Gómez (2002) with double the fiducial strength and the arm model of Pichardo et al. (2004). The resulting maps did not differ significantly from the "simple" versions made in the previous chapter (Figure 3.29), and so confirmed our decision to not include these models in the barred-spiral models.

4.6 Simulations including both arm and bar potentials

Using the refined parameter space found from calculations with arm and bar potentials we then performed calculations with both in various combinations. In the following section we show the results of our simulations, simple map fitting to place the observer, and full radiative transfer calculations to create *l*-*v* emission maps, and determine the best-fitting morphology.

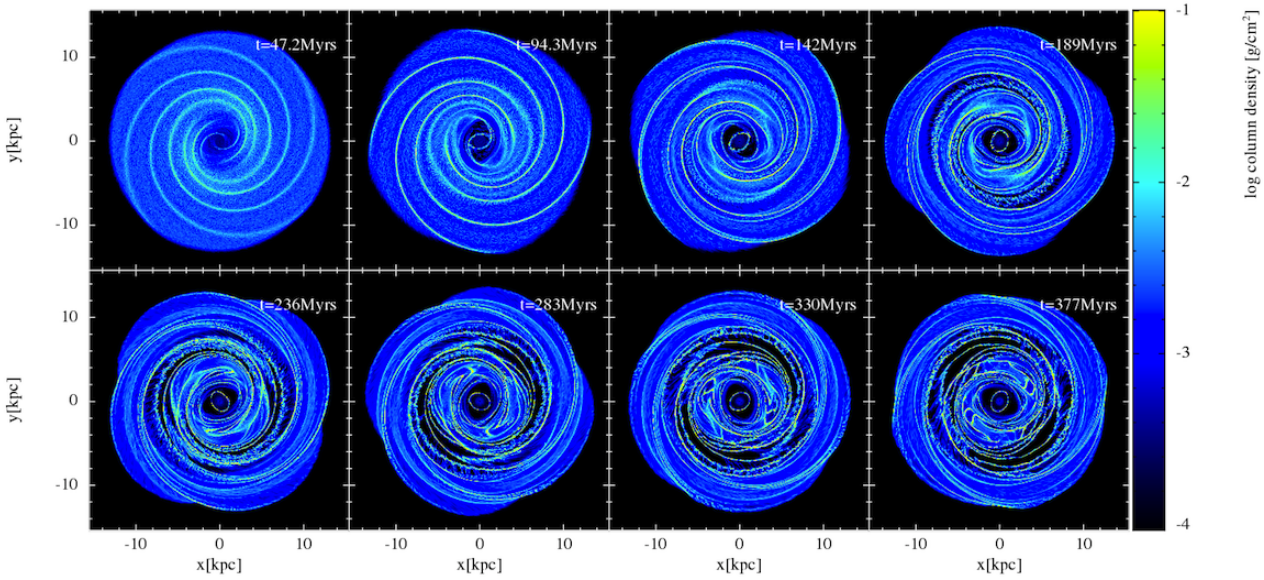

Figure 4.11: Example of the evolution of a barred-spiral Milky Way simulation. The central bar is of WK type with and the arms of CG type. The potential parameters are; $N = 4$, $\alpha = 12.5°$, $\Omega_{sp} = 20\text{km s}^{-1}\text{ kpc}^{-1}$ and $\Omega_b = 50\text{km s}^{-1}\text{ kpc}^{-1}$.

4.6.1 Simulations

Parameters in bold in Table 3.2 are those used in arm-bar simulations, chosen based on fits in previous sections. Note that we use $\Omega_b = 50\text{km s}^{-1}\text{ kpc}^{-1}$ for the WK and $\Omega_b = 60\text{km s}^{-1}\text{ kpc}^{-1}$ for the WKr2 potentials. We use $\Omega_{sp} = 15\text{km s}^{-1}\text{ kpc}^{-1}$, $N = 2$ arms only in conjunction with the $\Omega_b = 60\text{km s}^{-1}\text{ kpc}^{-1}$ bar potential as the OLR of the $\Omega_b = 50\text{km s}^{-1}\text{ kpc}^{-1}$ bar is close to the region of arm branching and this may result in a disruption of these features. In some models ressonances of arms and bars will overlap. For example, a $N = 4$ spiral at $\Omega_{sp} = 20\text{km s}^{-1}\text{ kpc}^{-1}$ and a bar with $\Omega_b = 50\text{km s}^{-1}\text{ kpc}^{-1}$ has the ILR of the arms at approximately the same radius as the OLR of the bar, so a clear distinction between arm and bar features should be seen in this model. This is not the case for the $N = 2$ models, where there will arm and bar features will overlap.

An example of the evolution of a barred-spiral simulation is shown in Figure 4.11, with the parameters; $N = 4$, $\alpha = 12.5°$, $\Omega_{sp} = 20\text{km s}^{-1}\text{ kpc}^{-1}$ and $\Omega_b = 50\text{km s}^{-1}\text{ kpc}^{-1}$ (with CG and WK type potentials). The addition of a bar distorts the arm features within a radius of 5 kpc, roughly corresponding with the bar's OLR. The bar-arm contact region has a large amount of complex structure where the gas in the arm potential strays from a logarithmic spiral structure to join those arms driven by the bar; which are much tighter wound. After 500 Myrs the gas around the bar establishes elliptical orbits similar to those seen in Fig. 3.15, though the addition of arm potentials inhibits the formation of parallel and perpendicular elliptical orbits seen at the OLR in bar-only simulations. We find that, as suggested by Sellwood & Sparke (1988), there is a clear inner region dominated by the bar potential and outer region dominated by the spiral potential, with only a small region where the two are intermixed.

The differences between the models as a function of Ω_b and N are shown in Figure 4.12.

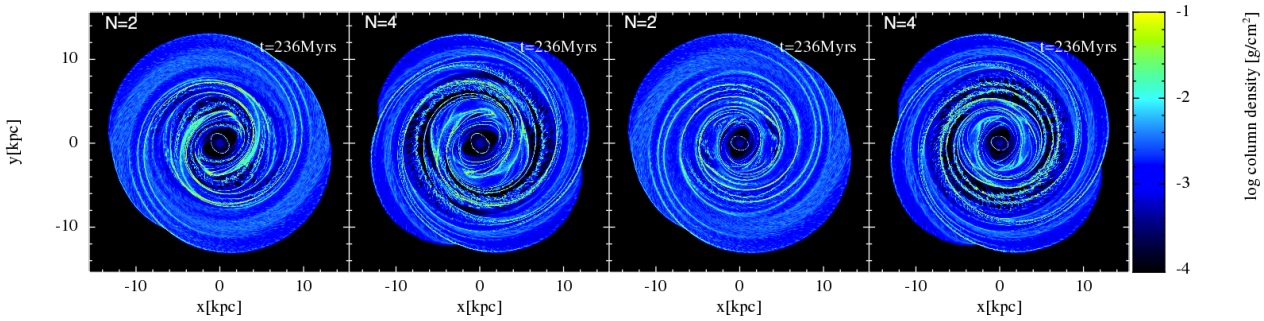

Figure 4.12: Top-down maps of the gaseous response to the different $N - \Omega_b$ potential pairs, all of which have $\alpha = 12°$, $\Omega_{sp} = 20\text{km s}^{-1}\,\text{kpc}^{-1}$ and evolved for 236 Myrs. The bar potential in the left panels has $\Omega_b = 50\text{km s}^{-1}\,\text{kpc}^{-1}$, and $\Omega_b = 60\text{km s}^{-1}\,\text{kpc}^{-1}$ in the right panels, shown in conjunction with 2 and 4 armed models.

The slower bars disrupt the arm features up to the Solar radius, while the faster bars are less radially extended, allowing arms to approach smaller radii. The 2-armed models still have a dearth of high density interarm material, though the arms in conjunction with the slower bar has additional inter-arm structure caused by the large radial extent of the features driven by the bar (though this is more evident at later times).

4.6.2 Simple kinematic maps

An additional complication to the barred-spiral models is the offset between the arm and bar potentials, which is time-dependent due to $\Omega_{sp} \neq \Omega_b$. By choosing to analyse the model at specific time-stamp, as in the arm and bar only simulations, we would have already selected the offset between the bar and arm features. Instead we analysed each barred-spiral model in the range of 280-370 Myrs, regardless of arm number and bar pattern speed. This range was the minimum required time between arm passages around a reference frame aligned with the bar for all models considered and includes the full possible range of arm-bar offsets.

To actually determine the best-fitting arm-bar offset we use the same fitting method to fit the observer's coordinates for the arm and bar calculations, leaving R_{obs} and V_{obs} free. We fixed the bar at $\theta_b = 45°$, effectively fixing l_{obs}, which is consistent with the best fitting value found in our bar-only simulations. This allows for a reference point for altering the arm-bar offset. This method has one major caveat, we must assume the morphological features do not change considerably in the time-frame used to perform the fit, approximately 100Myrs. Global arm and bar features tend to stay the same over this time frame, with the main difference seen in the gas around the OLR of the bar, effectively where the bar meets the arms. At this radius the material from the bar driven arms has altering substructure and begins to wrap around into a ring-like structure.

This process is illustrated by Figures 4.13 and 4.14, showing the fit statistic and corresponding l-v maps for a calculation with $N = 2$, $\Omega_b = 50\text{km s}^{-1}\,\text{kpc}^{-1}$ and $\alpha = 15°$. Figure 4.13 shows the behaviour of the fit statistic with varying observer position and velocity, and with varying time (which dictates the arm-bar offset). A clear broad minimum can be seen around 320Myrs, with corresponding values of $R_{\text{obs}} = 8.5\text{kpc}$ and $V_{\text{obs}} = 220\text{km s}^{-1}\,\text{kpc}^{-1}$. Figure 4.14 shows the l-v

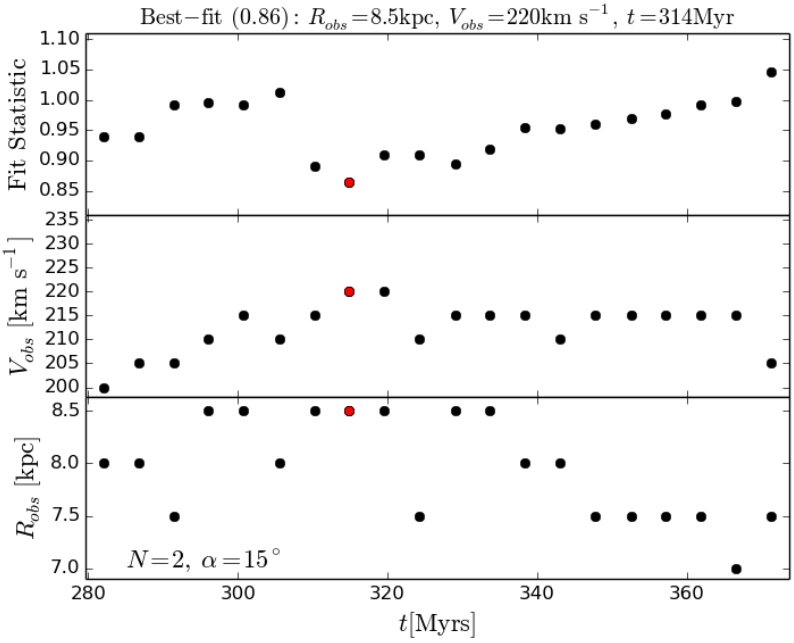

Figure 4.13: Variation of fit statistic with evolution of a barred spiral galaxy (top panel) which is used to constrain the arm-bar offset. The model here has $N = 2$, $\Omega_b = 50\mathrm{km\,s^{-1}\,kpc^{-1}}$ and $\alpha = 15°$. The best fitting time-frame is indicated by the red point. Corresponding l-v maps are shown in Figure 4.14. Middle and lower panels show the best-fitting values of R_{obs} and V_{obs} at the same epochs.

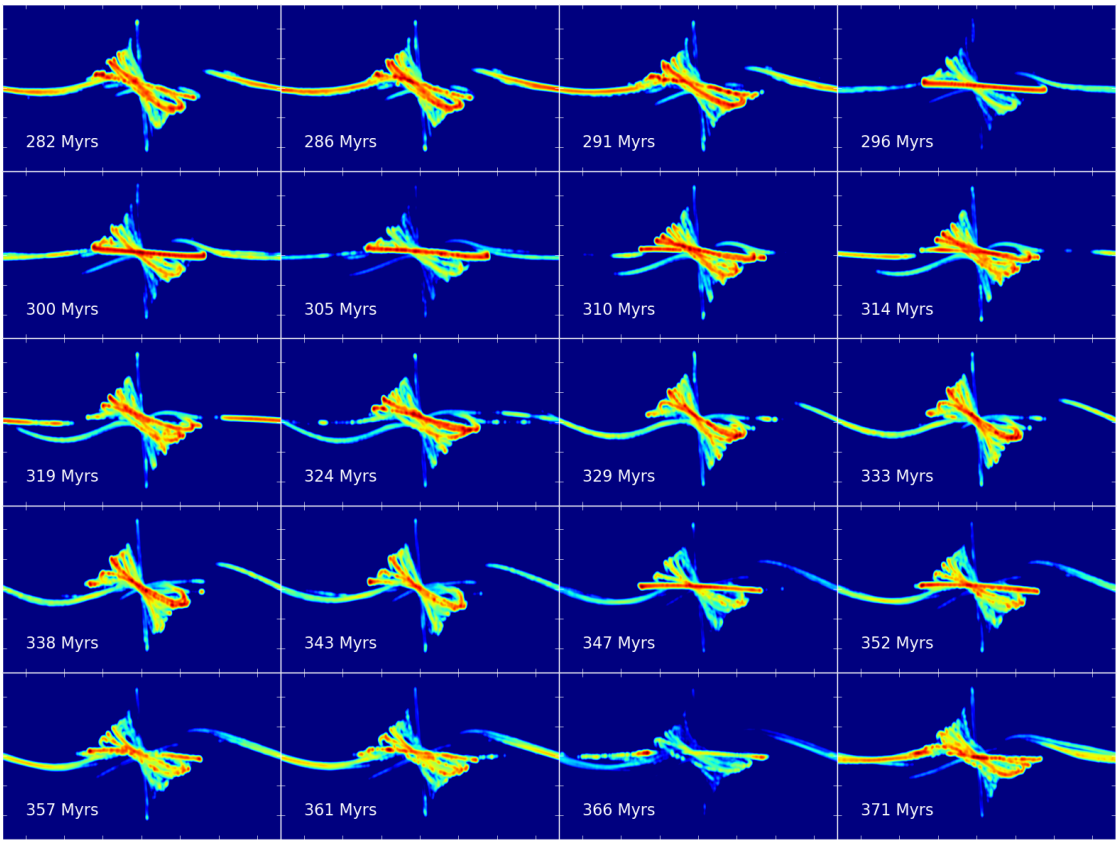

Figure 4.14: Evolution of kinematic l-v maps for a barred spiral galaxy with changing arm-bar offset. Each panel corresponds with a point shown in Figure 4.13.

maps for each point in Figure 4.13, constructed using the best-fit parameters. This figure shows the motion of arm features with respect to the bar, where individual arms can be seen to move vertically in velocity space with time. Conversely inner features caused by the bar (where $|v_{\rm los}| >> 0$) can be seen to not change. The final panel in Fig. 4.14 has the same arm-bar offset as a time between the third and fourth panels (around 294Myrs). While differences between the maps can be seen, the global structure is the same, showing that over the time-frame of 100Myrs the *l*-*v* features vary only marginally.

4.6.3 Radiative transfer maps

The TORUS emission maps for each N-Ω_b-α combination are shown in Figure 4.15 with the best fitting values of $R_{\rm obs}$, $V_{\rm obs}$ and arm-bar offset (i.e. evolution time) found using the method described in Section 3.6. The best-fitting values for each model are also given in Table 4.1. Simple by-eye comparisons between these maps shows that whilst most fit some features well ultimately none shown a perfect match to the data, suffering the same problems as the arm-only models in Chapter 3. As was the case in the arm only models, the fit statistic is uncorrelated with the pitch angle. If the fit statistic is averaged across all parameters except pitch angle then there is a marginal preference towards $\alpha = 12.5°$. There is also a preference towards a pattern sped of $\Omega_b = 50{\rm km\,s^{-1}\,kpc^{-1}}$ for $N = 2$ models and $\Omega_b = 60{\rm km\,s^{-1}\,kpc^{-1}}$ when $N = 4$.

The reasons preventing a good fit to all emission features are covered by the following examples. In Fig. 4.16 we show four different arm-bar simulations from Fig. 4.15 in both *l*-*v* and *x*-*y* space. These have been chosen to highlight the main differences between the simulations, and are not necessarily the best fits from Fig. 4.15. In the first panel we show a 2-armed spiral model with our slower bar ($50{\rm km\,s^{-1}\,kpc^{-1}}$). The *l*-*v* map in this case shows a good reproduction of the Carina arm, and Local arm material in the second quadrant (this is common to all 2-armed model fits in Fig. 4.15). The *x*-*y* map shows that the *l*-*v* Carina arm feature in this model actually joins with the Local arm material. The Carina segment branches away as it nears the Solar position, passing though $R < R_\circ$ while the Local arm feature breaks away from the spiral potential and maintains a radial distance of $R > R_\circ$ upon passage into the first quadrant. The major drawback of this and other 2-armed models is the failure to produce the Outer, Perseus and Local arms simultaneously. Two armed-models produce an inner emission ridge seen in observations (a combination of the Scutum-Centaurus-Crux, SCC, arms and possibly a molecular ring). However the ridge in this case is too shallow in *l*-*v* space, implying it is too close to the Solar position.

In the second panel we show another 2-armed model with a moderate pitch angle (12.5°) and a slow bar ($50{\rm km\,s^{-1}\,kpc^{-1}}$), but with a slower arm pattern speed than the previous model ($15{\rm km\,s^{-1}\,kpc^{-1}}$). This value of Ω_{sp} provides strong branching features that can be seen in the *x*-*y* map, driving a 4-armed gas structure from only a 2-armed potential. This model reproduces the Perseus, Outer and the Local arms. Reproducing these arm features simultaneously would be impossible for a 2-armed logarithmic structure (as in the previous model). The Local and Outer arms are actually reproduced by the branches, not the arms directly tracing the potential. The SCC arm/inner ridge is angled similarly to observations, and the 3kpc-expanding arm is very clearly seen in *l*-*v* space. The main flaw in this model is the position of the Carina arm, which does not

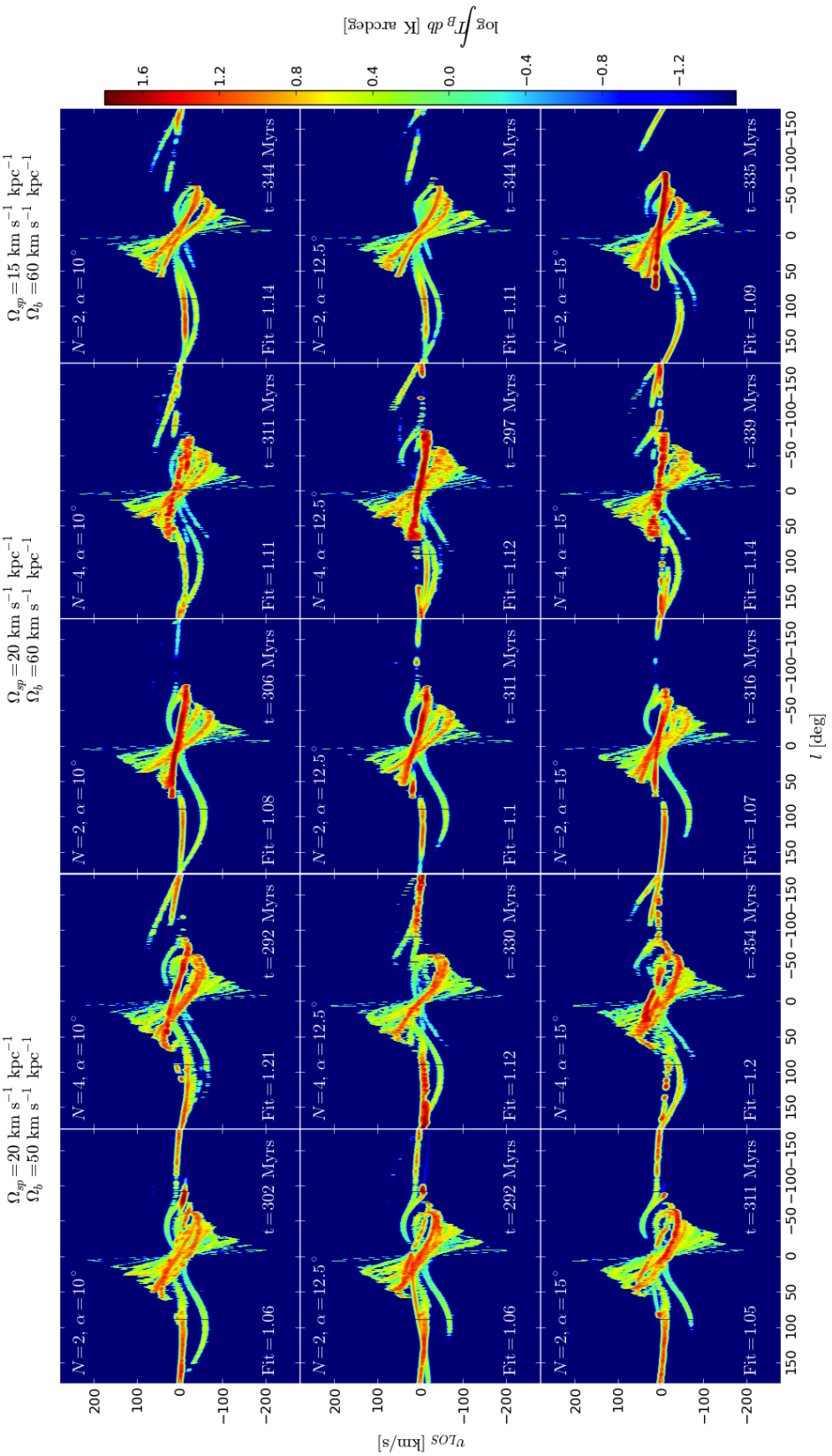

Figure 4.15: Synthetic emission maps made using TORUS for our barred-spiral models with θ_b = 45°. The arm position relative to the bar is found using the method of fitting to the observer coordinates in the isolated arm and bar cases. The first two columns show $\Omega_b = 50\text{km}\,\text{s}^{-1}\,\text{kpc}^{-1}$ with $N = 2, 4$ respectively, and the second two show $\Omega_b = 60\text{km}\,\text{s}^{-1}\,\text{kpc}^{-1}$ with $N = 2, 4$. The fifth column has a slower arm pattern speed of $\Omega_{sp} = 15\text{km}\,\text{s}^{-1}\,\text{kpc}^{-1}$. The spiral arm pitch angle increases from top to bottom.

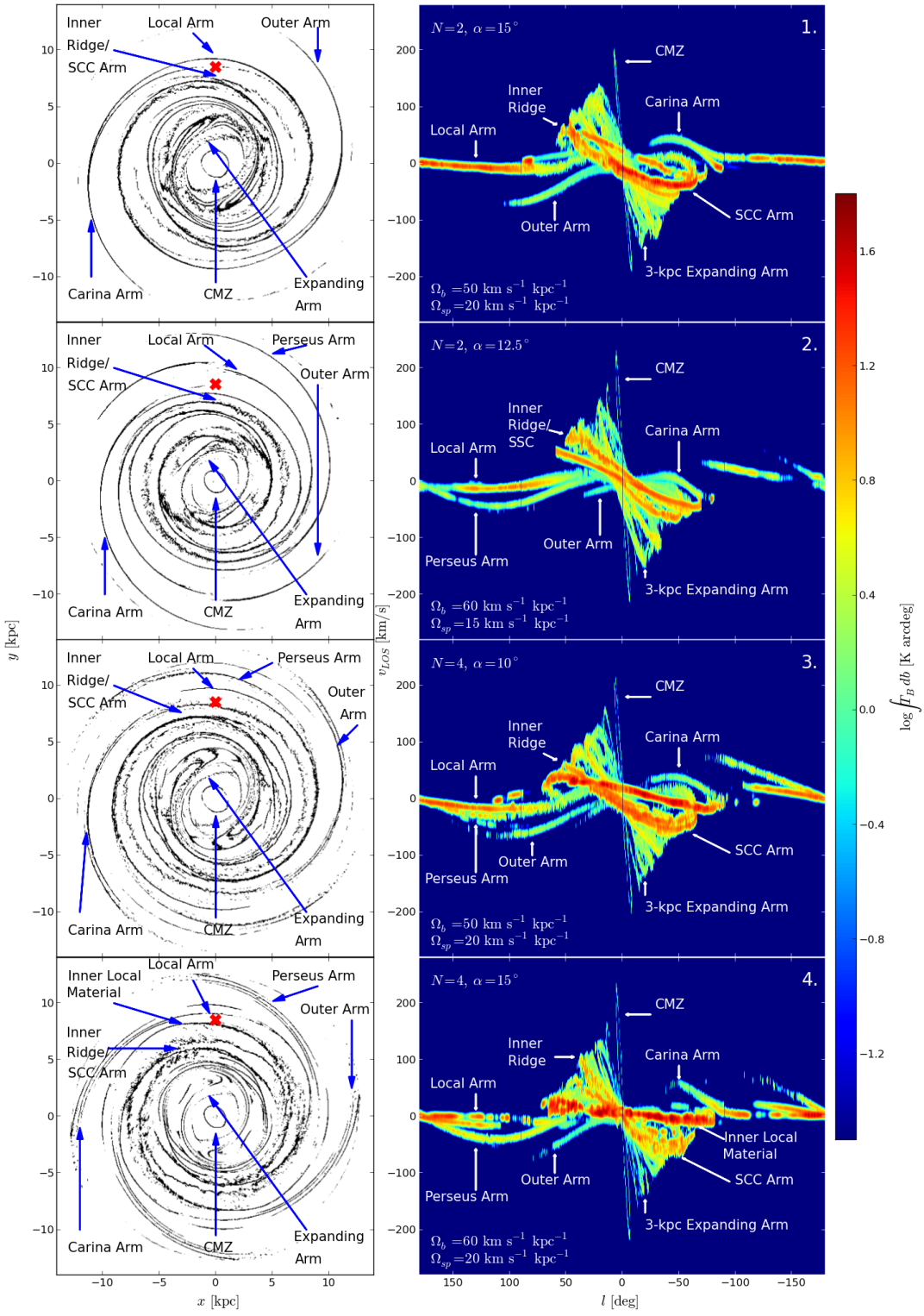

Figure 4.16: Four CO radiative transfer *l*-*v* maps with their *x*-*y* counterparts from Fig. 4.15, chosen to show a range of different morphologies. The top-down maps only show material that is seen in CO *l*-*v* space; that of the highest density. The cross indicates the observer's position (which differs between models). SCC refers to the Scutum-Centaurus-Crux arm in the 4-armed paradigm of the Milky Way, also referred to in the main text as the Inner Ridge. Arrows indicate locations of prominent features in *l*-*v* space. Models 2 and 4 reproduce the outer arm structure while 1 and 3 provide a better reproduction of the Carina arm.

reach into the $v_{los} > 0\,\mathrm{km\,s^{-1}}$region as seen in observations.

The third panel shows a 4-armed model with a shallow pitch angle (10°). In this case there is clear reproduction of the Carina arm feature, located inside the Solar radius in *x*-*y* space. As this feature passes in between the Solar position and the Galactic centre it causes a bright emission feature at near-local velocities, a feature not seen in observations. The SCC arm feature is seen behind this strong emission feature in *l*-*v* space. The second quadrant arm features are not as clear as the previous model, with the Local and Perseus features not clearly separated in *l*-*v* space. The feature here labelled as the Outer arm could equally be labelled the Perseus arm, but would leave multiple arm structures unidentified in the outer Galaxy, caused by a large amount of branching material in the 7kpc $< R <$ 11kpc region seen in *x*-*y* space.

	Mix model	
Best fit parameter	CGN2+WK	CGN4+WK
Ω_b [$\mathrm{km\,s^{-1}\,kpc^{-1}}$]	50	60
V_{obs} [$\mathrm{km\,s^{-1}}$]	220	215
R_{obs} [kpc]	8.5	8.5
α [°]	15	10

Table 4.1: Best fitting values for the barred-spiral simulations. A systematic uncertainty for each value is present due to the coarseness of the parameter space; $\Delta\Omega_{sp} = \Delta\Omega_b = 10\mathrm{km\,s^{-1}\,kpc^{-1}}$, $\Delta V_{\mathrm{obs}} = 5\,\mathrm{km\,s^{-1}}$, $\Delta R_{\mathrm{obs}} = 0.5$kpc and $\Delta\theta_b = 10°$. The parameter space for the mix models is smaller than the isolated cases and was refined in Chapter 3.

The final panel also shows a 4-armed model, with a wide pitch angle (15°), but with a faster bar than the previous panels ($60\mathrm{km\,s^{-1}\,kpc^{-1}}$). The faster bar is less extended radially, allowing the gas to trace the spiral potential to smaller radii. In the *x*-*y* map the spiral arm pitch angle is maintained to $R \approx 4$kpc, whereas in the slower, $50\mathrm{km\,s^{-1}\,kpc^{-1}}$, models in the upper panels structure is dominated by the bar until $R \approx 6$kpc. This model appears to produce all the observed features; Local arm, Perseus arm, Outer arm, SCC arms/ridge and Carina arm. The problem again is that arms must pass in front of the observer to appear in the fourth quadrant, producing emission that dominates the SCC feature in the inner Galaxy. This model in particular has little emission in the third quadrant, as seen in observations, owing to the Perseus arm disappearing as it leaves the second quadrant. The Carina arm feature is located at higher values of v_{los} than is seen in observations, however there are similar maps for the $\alpha = 12.5°$ case that provide a better match for this section, but are not shown in this figure due to the poor reproduction of other features.

Do the arms and bar have the same pattern speed?

Results presented in this and the previous chapter indicated that the bar and arms have different pattern speeds, a view that is supported by numerous other studies of our Galaxy (see the review of Gerhard 2011). This is also seen in some numerical simulations of disc galaxies, where patterns in the inner disc tend to rotate considerably faster than those in the outer disc (Sellwood & Sparke 1988; Grand et al. 2012). Observations of external galaxies however often favour a single, or smoothly decreasing pattern speed with radius (Egusa et al. 2009; Speights & Westpfahl 2011, 2012), as do some other numerical studies (Roca-Fàbrega et al. 2013). To check the validity of

a model with independent bar and spiral pattern speeds we performed calculations where both components have the same pattern speed, primarily to check whether the smaller parameter space of the previous section (where $\Omega_{sp} = 20\mathrm{km\,s^{-1}\,kpc^{-1}}$) was justified.

In Figure 4.17 we show calculations with barred, 2-armed, and 4-armed potentials, and their combinations where $\Omega_{sp} = \Omega_b$ in the range of 10-60$\mathrm{km\,s^{-1}\,kpc^{-1}}$, using the WK and CG potentials. The effect of adding a bar can clearly be seen in the third and fifth rows, with the main difference being the addition of the inner x_2 orbits. In the case of the faster bars (50, 60$\mathrm{km\,s^{-1}\,kpc^{-1}}$) the bar tends to dominate the spiral features which are confined within $R < 8$kpc where the OLR of the bar drives strong ring-like structures. The slower pattern speeds (10, 20$\mathrm{km\,s^{-1}\,kpc^{-1}}$) the bar has a minimal effect on the arm structures, only dominating the morphology within $R < 3$kpc. This is due to the OLR of the bar lying well outside the Galactic disc at these slow pattern speeds. The mid-range speeds (30, 40$\mathrm{km\,s^{-1}\,kpc^{-1}}$) show morphologies effected by the bar and spiral features now that the bar and spiral OLR is within the disc. This is clearer in the 4-armed case, where the arm OLR lies at a smaller radii than that of the bar.

The slowest pattern speed calculations do not appear to produce desirable morphological structures. In the 2-armed case the bar is barely noticeable, leaving effectively just the arms and we have already shown that the $\Omega_{sp} = 10\mathrm{km\,s^{-1}\,kpc^{-1}}$ arm models provide a poorer fit than the $20\mathrm{km\,s^{-1}\,kpc^{-1}}$ case. The 4-armed case has weak arm and bar features, which are not strong enough to maintain a sufficient CO abundance to appear in *l*-*v* emission maps. The faster models are far too radially constrained to reproduce the observed *l*-*v* features, with arms only persisting well within the Solar radius, making it impossible to reproduce the Perseus and Outer arms.

The remaining pattern speeds (20-50$\mathrm{km\,s^{-1}\,kpc^{-1}}$) display both arm and bar features. Figure 4.18 shows *l*-*v* maps of the models in Figure 4.17 with pattern speed of 20-50$\mathrm{km\,s^{-1}\,kpc^{-1}}$. These maps were made using the simple method described in Chapter 3 and are shown for the best fitting R_{obs}, V_{obs} and l_{obs} (where the bar is constrained to point towards the second quadrant). As the arm and bar features rotate with the same pattern speed, we have assumed some fixed arm-bar offset. As such the exact position of features is not expected to perfectly reproduce those seen in observations, but rather show *l*-*v* morphologies possible with single pattern speeds. The $20\mathrm{km\,s^{-1}\,kpc^{-1}}$ models allow for a large amount of spiral structure, but the bar forms some peculiar inner structures due to the large inner x_2 orbits which creates wide loop-like structures in *l*-*v* space. The faster, $50\mathrm{km\,s^{-1}\,kpc^{-1}}$, bar has ILR inside the Solar radius, so the bar-driven arms lie in the inner Galaxy, creating emission with less gaps, and central emission that better resembles observations. The $40\mathrm{km\,s^{-1}\,kpc^{-1}}$model suffers the same problems as the bar-only models of Chapter 3, where the OLR of the bar lies just inside the Solar radius. This causes very strong emission at local velocities in the inner Galaxy, which is absent in observations. Finally, the $50\mathrm{km\,s^{-1}\,kpc^{-1}}$ model has very few arm features in the outer Galaxy, as the arms are now within, or just outside for $N = 2$, the Solar radius, making it impossible to fully represent the arm features in the outer Galaxy.

None of the barred spiral models shown above with $\Omega_{sp} = \Omega_b$ seem to be able to reproduce Galactic *l*-*v* features better than models with $\Omega_{sp} \neq \Omega_b$. Bar features do a good job of fitting the central emission for fast pattern speeds, while arm models better represent the outer Galaxy with

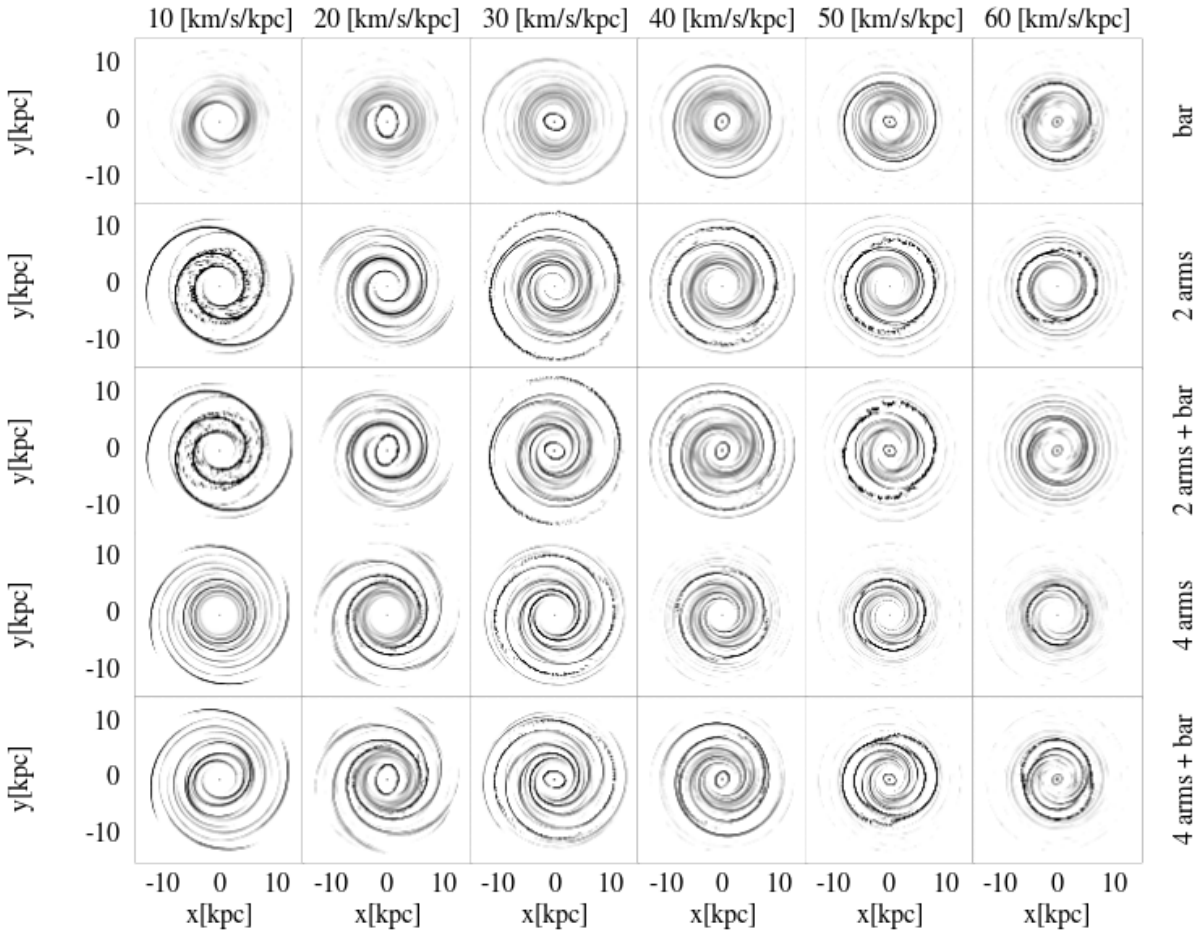

Figure 4.17: Top down views of calculation with bar and arm potentials rotating at the same pattern speed, increasing from left to right. The different rows show, in order from top to bottom, bars, 2-armed models, 2-armed and a bar, 4-armed, 4-armed and a bar, all after 380Myrs of evolution. A black and white scheme is used to highlight the minor differences in the addition of a bar to the central region.

slow pattern speeds. This leads us to the conclusion that the CO features of the Milky way are best represented with two very different pattern speeds for the arms and bar.

The central molecular zone

In all of our *l*-*v* maps we fail to reproduce the structure of the CMZ. In certain instances we do produce velocities that are comparable to the highest values seen in observations, one such example is shown in Fig. 4.19. The peak velocity structures in our models stem from the inner x_2 bar orbits perpendicular to the bar major axis, and appear as a symmetric loop structure in *l*-*v* space, while the observed CMZ is highly asymmetric. The SPH particles that are present have aligned themselves with the x_2 orbits, leaving little material available to fill in the missing emission. In order to fully capture the asymmetric emission features in the central galaxy a dedicated simulation is required of only the inner galaxy to better resolve the gaseous features. The addition of stellar feedback or a live stellar disc may also be required to break up the symmetric inner bar orbits.

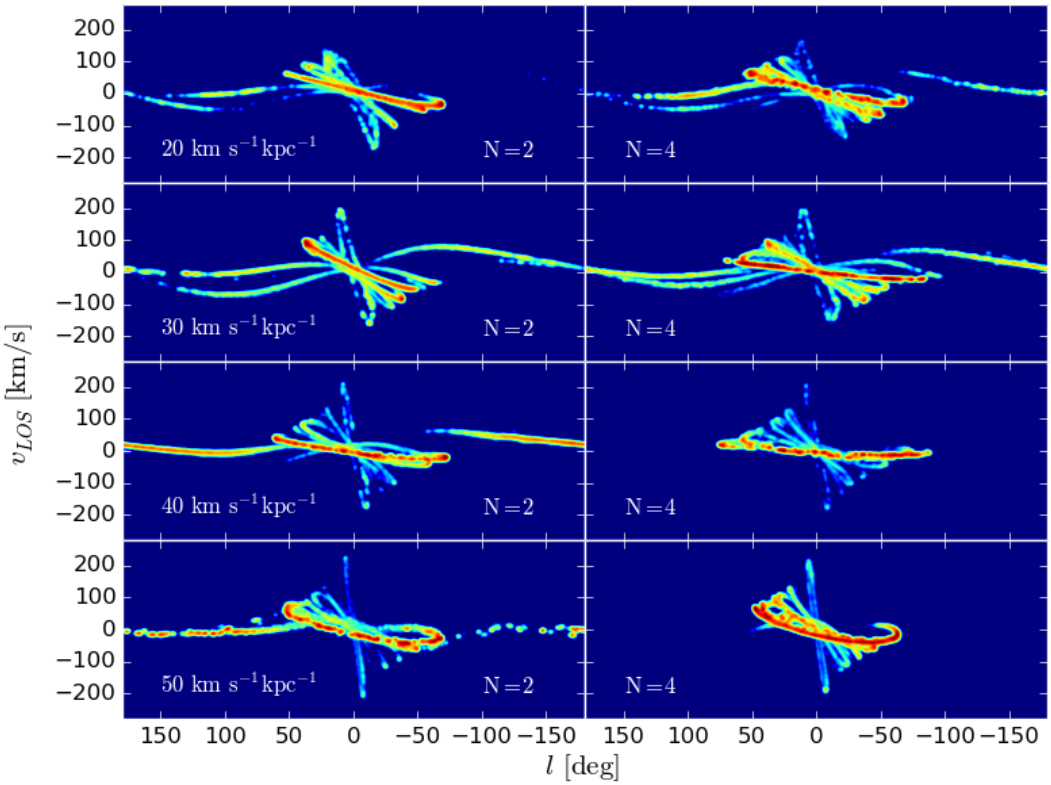

Figure 4.18: Best fitting l-v maps of the calculations shown in Fig. 4.17 with arm/bar pattern speeds of 20, 30, 40 and 50km s^{-1} kpc^{-1} (increasing from top) and $N = 2$ or $N = 4$. These are simple kinematic maps, rather than being built by TORUS, where the bar is allowed to lie anywhere within the second quadrant.

It may be the case that the bar model is correct, but the physics is too simple to correctly model the l-v features. The x_2 orbital features are aligned similarly to the CMZ. Lee et al. (1999) constrained the x_2 orbits of a barred model to the CMZ features, finding that while a wide orientation angle of $\theta_b = 50°$ provided a good reproduction of the l-v slope, the gas particles traced very thin structures in l-v space similar to those in Fig. 3.18. They did however perform a similar calculation with collisionless N-body particles, representing the stellar component, which appear much broader in l-v space similar to observations. In the next chapter we will be discussing calculations with a live stellar component, which also may provide a better match to observations.

4.7 Discussion of investigation using spiral and bar potentials

The models shown in Figures 4.15 and 4.16 show it is possible to reproduce all features of the l-v data. However, we find it difficult to produce a good match to all features simultaneously. Four armed models are more capable of fitting multiple features simultaneously, but to do so must place some arm structure just inside the Solar position. This must be within very close proximity to allow the tangent point of the Carina arm to reach out to $l \approx -90°$. While a strong emission feature is seen in the inner Galaxy in observations, it is angled much steeper in l-v space than our synthetic maps. One can conclude that the local SCC arm material is either lacking in molecular

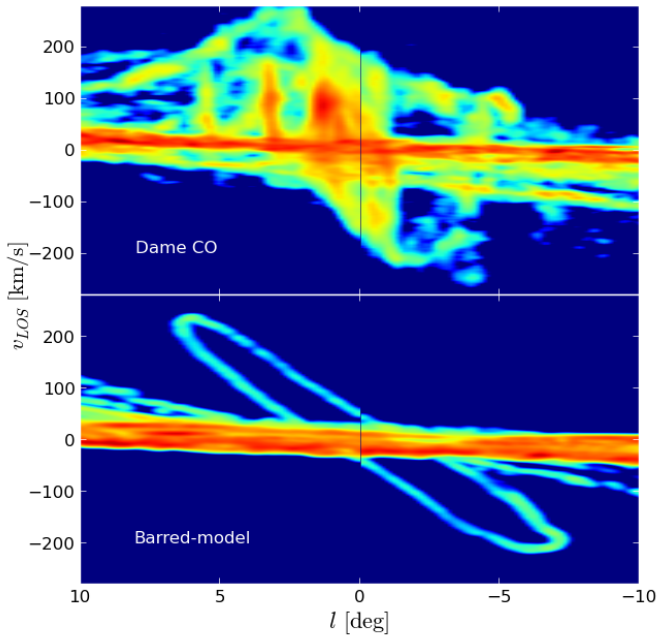

Figure 4.19: The observed CO emission in the Galactic centre (top, $|l| < 10°$) compared to that produced in the centre by the addition of a barred potential rotating at $50\mathrm{km\,s^{-1}\,kpc^{-1}}$ (bottom). The underlying model appears too simplistic to capture the large amount of structure seen in observations.

material or that the shape is far from that of a logarithmic spiral near the Solar position. If it is indeed lacking in molecular gas, then it can be expected to at least be rich in atomic gas.

Alternatively the Carina-Sagittarius arm structure could deviate significantly from a normal logarithmic-spiral structure. This is supported by other works in the literature (e.g. Georgelin & Georgelin 1976, Pandian et al. 2008). These models involve some straight section of the SCC arm as it passes in front of the observer. In Fig. 4.20 we show such a model, specifically that of Taylor & Cordes (1993), compared to a 4-fold symmetric spiral pattern similar to that used in this study. This additional distance between the observer would give the arm a greater line-of-sight velocity, pulling it up and away from the $V_{los} = 0\,\mathrm{km\,s^{-1}}$ line in our maps in Fig. 4.15, as seen in projection in the bottom left panel of Fig. 4.20. It is also seen in observations that while the Sagittarius and Carina tangents are well traced by distance determinations, there is very little material placed on these arms in the local Galaxy in the direction of the Galactic centre (e.g. Georgelin & Georgelin 1976, Fish et al. 2003, Russeil 2003, Hou et al. 2009). It also may be that the arm structure is better represented by a transient and irregular spiral structure, rather than that of a fixed grand design galaxy. These structures are reproducible in simulations through the inclusion of a live stellar disc, rather than fixed analytical potential (e.g. Baba et al. 2009; Dobbs et al. 2010; Grand et al. 2012).

In Gómez & Cox (2004) the authors construct synthetic *l*-*v* maps by simply mapping structures in *x*-*y* onto *l*-*v* co-ordinates. They too show that while the Carina "hook" is easy to reproduce, it causes a strong dense ridge angled far too shallow in *l*-*v* space compared to that seen in observa-

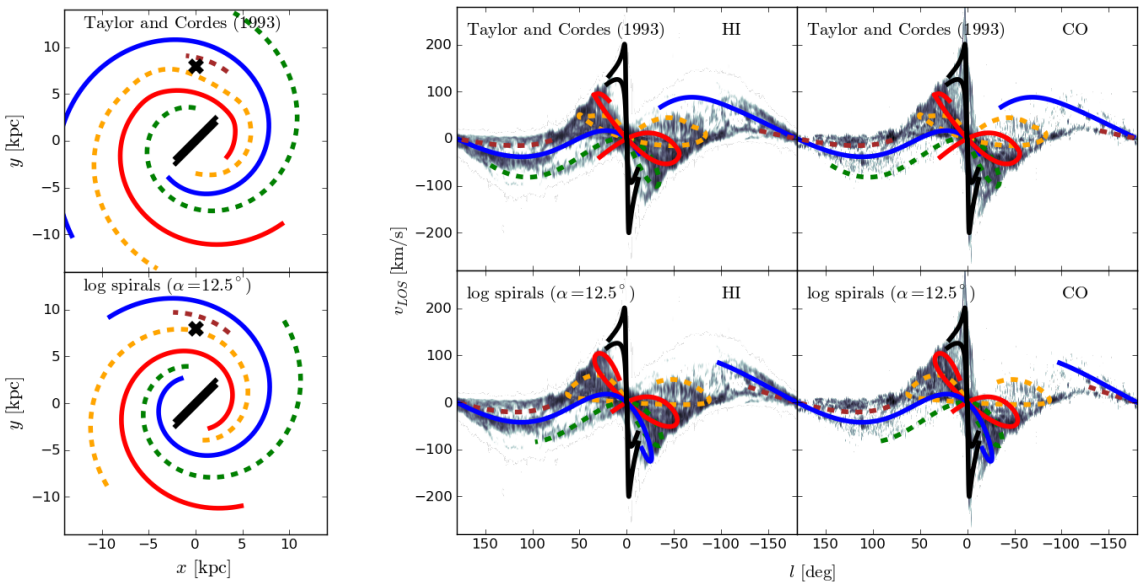

Figure 4.20: Different arm models in x-y plane (top figure) and their projection onto l-v space (bottom figure). Left panels: arm model of modified logarithmic spirals from Taylor & Cordes (1993), primarily constrained to data from Georgelin & Georgelin (1976). Right panels: simple 4-armed spiral model with each arm offset by $\pi/2$ from the previous with addition of a local arm segment. Arms only extend radially to distance required to match l-v emission features. Observed CO and H I emission data is plotted on greyscale behind the model arm features in the lower figure. Bold lines indicate the strong primary arm features in the old stellar population inferred by Churchwell et al. (2009).

tions. They also note that crowding in velocity space can cause ridges in l-v space not necessarily corresponding to high density gas regions. As CO traces high density regions only we do not have that problem here, and our l-v features correspond well with high density gas regions associated with arm and bar features. Our results are at some odds with the work by Rodriguez-Fernandez & Combes (2008), who find that a bar pattern speed of 30km s^{-1} kpc^{-1} is the best match to the l-v diagram, without the inclusion of arm potentials. Our value is more in keeping with that suggested by Fux (1999), 50km s^{-1} kpc^{-1}, and Englmaier & Gerhard (1999), 50-60km s^{-1} kpc^{-1}. Our lower pattern speed of 40km s^{-1} kpc^{-1} resulted in extremely strong emission in front of the observer, features that would not appear in the aforementioned works due to the mapping of x-y features to l-v space lacking a radiative transfer treatment.

4.8 Chapter summary

In this Chapter we have built on the work in presented in Chapter 3. We have constructed the first synthetic emission maps in CO and H I of the full Galactic plane using the radiative transfer code TORUS. Spiral and bar features can clearly be seen in l-v space, with emission of comparable strengths to that seen in observations. While CO features seemed only to scale in strength with surface density, the H I emission experiences very strong absorption at the higher surface densities

needed to observe considerable CO emission. We believe this to be a result of the simplistic nature of the physics in the calculation, with gas readily falling into a very thin plane, increasing optical depth and H I absorption. However, CO is well reproduced, which is a better tracer of spiral structure.

We then performed calculations similar to those in Chapter 3 but with the inclusion of arm and bar potentials simultaneously. While these provide a better reproduction of observations than the arm or bar models could alone, even with these we could not satisfactorily reproduce all the observed CO features. Whilst it was possible to reproduce features in emission that are seen in observations, such as the Perseus arm, Carina arm, inner ridge emission, local material and the outer arm, these features are not all reproducible simultaneously. The 2-armed models cannot reproduce all these features, yet the 4-armed models create too much emission locally. Assuming logarithmic spiral arms, in order to successfully match the Carina arm feature, an extremely strong emission feature must be placed near $v_{los} = 0\,\mathrm{km\,s^{-1}}$ in the inner Galaxy. Models which do not use radiative transfer may miss the significance of this feature. Alternatively the Carina arm would need to exhibit an irregular shape in the vicinity of the Sun. This leads us to the conclusion that while the 4-armed symmetrical model can produce many of the features seen in the *l*-*v* observations, it may be necessary to allow an irregular arm structure to convincingly match the Galaxy.

The possibility of the arm and bar components rotating at the same pattern speed was also investigated. These models did a significantly poorer job however than those with $\Omega_{sp} \neq \Omega_b$, implying the bar and arms are both morphologically and kinematically different entities.

An alternative approach to that in this and the previous Chapter is to model the Milky Way as a transient, multi-armed galaxy by the inclusion of a live *N*-body stellar disc. A study of the Milky Way ISM *l*-*v* emission using a live-stellar disc, and the comparison to the grand design case, is the topic of the subsequent Chapter.

5

Simulations and synthetic observations using live stellar systems

"The most exciting phrase to hear in science, the one that heralds new discoveries, is not 'eureka!' but 'that's funny' "
– Isaac Asimov, (1920-1992)

5.1 Introduction

In the previous two chapters we have shown the capability to create synthetic observations of the Galactic plane, specifically in CO emission. To do so we modelled the Milky Way as a grand design barred-spiral, whereby the arms and bars are fixed and have a constant pattern speed and morphology. While some of the features seen in observations could be reproduced, never were they all simultaneously. In this chapter we instead model the Milky Way stellar system as a set of discretised mass components, rather than a continuous density profile. Modelling a galaxy in this way is a tried and tested method and has been used to simulate both isolated stellar systems (Sellwood & Carlberg 1984; Sparke & Sellwood 1987; Sellwood & Sparke 1988; Shen et al. 2010; Grand et al. 2013; D'Onghia et al. 2013) and the simultaneous evolution of a gas disc (Carlberg & Freedman 1985; Elmegreen & Thomasson 1993; Clarke & Gittins 2006; Baba et al. 2009; Grand et al. 2012; Struck et al. 2011; Renaud et al. 2013; Athanassoula et al. 2013; Roca-Fàbrega et al. 2013). Simulations such as these, and many others, have shown that both bar and spiral features are surprisingly easy to reproduce, though not ones that necessarily agree with theory. For instance, spiral arms do not appear to be steady spiral density waves such as those suggested by Lin & Shu (1964), and bars are seemingly overabundant, and difficult to reproduce with accompanying spiral

structures.

In this chapter we first outline the computational method, and the procedure to generate the initial conditions of the simulations. We then show results various different simulations, and the accompanying gas morphology resulting form the evolution of the stellar system. The gas is then used to construct synthetic *l*-*v* plots similarly to Chapter 4, where we utilise a similar tool to constrain the best fitting values for $V_{\rm obs}$, $R_{\rm obs}$ and $l_{\rm obs}$. We briefly dedicate some time to quantifying the morphology of the best fitting simulations, e.g. the pitch angle and pattern speed of the arms, and compare these to the best-fitting maps of Chapters 3 and 4.

5.2 Modelling the stellar distribution with live particles in SPH

The computational method for evolving the ISM fluid is the same as that in Chapter 2. We utilise the SPH method with ISM chemistry and cooling to evolve the positions, velocities, energies and chemical abundances of the gas particles when exposed to the gravitational filed of a Milky Way-like disc galaxy. While the method is essentially the same, some of the algorithms are slightly different (see Section 2.2.12). Instead of using a fixed potential with an analytic force field, we use numerous "star" particles in an *N*-body prescription. These star particles are not stars in the traditional sense. They emit no radiation, are all of uniform mass, and are constant in number throughout the evolution of the system. Most importantly, they are much more massive than any single star. Simulating the Galaxy on an individual star-by-star basis would be computationally crippling for the calculation of the gravitational force. Instead we use star particles whose mass is closer to that of a stellar cluster, with individual particles having masses of the order 10^4 to 10^5 solar masses depending on resolution and disc mass. These will be referred to simply as "stars" for the remainder of this chapter. Star particles behave similarly to SPH particles, but experience no hydrodynamical forces (i.e. are collisionless), and have no concept of internal energy. They therefore store no chemical information either. They do store a density, but this is used only for time-stepping, to ensure they are evolved in a similar manner to SPH particles. The main difference to the SPH particles is that they exert a gravitational force upon each other, and the individual gas particles. Details on the calculation of *N*-body forces, rather than those of a smooth potential, are given in Section 2.2. Gas particles still exert no gravitational forces upon each other, or the stars (i.e. no self-gravity in the gas), this is assumed to be negligible compared to the gravitation of the stellar system. In some instances we also use a live dark matter halo rather than fixed potential. As the general properties of the dark matter are still unknown, halo particles are simply more massive star particles.

5.2.1 Setting the stellar system

The initial conditions of particles in an *N*-body simulation are paramount to the evolution of the system, specifically the initial position and momentum vectors. In the previous chapters the initial gas distribution was relatively unimportant, with positions and velocities dominated by the effect of the external potentials shortly after their activation. However, in this instance the particles also provide the gravitational forces for the calculation, and so initial conditions can cascade into the

results seen much later in the simulation.

The method of setting initial conditions is adopted from Hernquist (1993), which is also used in Baba et al. (2009). The method requires density profiles of the separate Milky Way components; bulge, disc and halo. For the calculations here we always employ a live stellar disc. A bulge is also frequently used to match the Milky Way's rotation curve, though this has adverse effects on the efficiency of bar formation (see Sec. 1.3.4 and later in this chapter). Regarding the halo, we usually use a simple potential to represent the halo, due to its gravitational effect mostly dominating the outer disc, while the disc itself appears to primarily influence the gas dynamics. We do employ a live halo in some calculations, though the additional computational resources required to evolve a live halo require an overall reduction in resolution in the other mass components.

The density profiles we use are slightly different to those used in the previous chapter. Previously all that was needed of the potentials was for them to create a rotation curve that matched that observed, in effect reducing to a single force vector for each calculation. Here however the density distribution determines the stellar distribution, and in turn how it evolves over time. The density profiles chosen are therefore ones that have been tailored to match the Milky Way's mass/luminosity profile for each component. The bulge used is a spherical Plummer profile (Plummer 1911), with corresponding density, potential and velocity profile of

$$\rho_{\rm Plum}(r) = \frac{3M_b r_b^2}{4\pi} \frac{1}{\left(r_b^2 + r^2\right)^{5/2}} \tag{5.1}$$

$$\Phi_{\rm Plum}(r) = -\frac{GM_b}{\sqrt{r_b^2 + r^2}} \tag{5.2}$$

$$V^2_{\rm Plum}(r) = +r\frac{GM_b}{\left(r_b^2 + r^2\right)^{3/2}} \tag{5.3}$$

where M_b and r_b define the characteristic mass and scale length. Initial calculations were made using a Hernquist profile bulge but due to the relatively stronger concentration at small radii, problems were encountered when setting the initial smoothing lengths of the particles. A spherical bulge is a slight simplification, as in the Milky Way the inner bar is often indiscernible from the bulge. However, we make no assumption about a bar morphology, and instead allow bars to naturally occur in the disc evolution. The stellar disc, containing the majority of stellar material, follows an exponential density profile (Binney & Tremaine 1987) so called due to the surface density profile of the form

$$\Sigma_{\rm Exp}(r) = \frac{M_d}{2\pi R_d^2} \exp\left(-r/r_d\right) \tag{5.4}$$

which can be generalised to a volume density with the inclusion of a sech^2(z) vertical scaling

$$\rho_{\rm Exp}(r,z) = \frac{M_d}{4\pi R_d^2 z_d} \exp\left(-r/r_d\right) \mathrm{sech}^{\,2}(z/z_d) \tag{5.5}$$

where characteristic masses and scale lengths are M_d, r_d and z_d. Integrating $\rho_{\rm Exp}$ over z reduces

vertical dependance to $2z_d$ and returns the disc surface density. The 2D potential and velocity profile are

$$\Phi_{\rm Exp}(r) = -\frac{GM_d r}{2r_d^2}\left[I_0\left(\frac{r}{2r_d}\right)K_1\left(\frac{r}{2r_d}\right) - I_1\left(\frac{r}{2r_d}\right)K_0\left(\frac{r}{2r_d}\right)\right] \tag{5.6}$$

and

$$V^2_{\rm Exp}(r) = \frac{GM_d r^2}{2r_d^3}\left[I_0\left(\frac{r}{2r_d}\right)K_0\left(\frac{r}{2r_d}\right) - I_1\left(\frac{r}{2r_d}\right)K_1\left(\frac{r}{2r_d}\right)\right] \tag{5.7}$$

where I_0, I_1 and K_0, K_1 are modified Bessel functions of the first and second kind respectively. A NFW dark matter halo is adopted (Navarro et al. 1996) which takes the form

$$\rho_{\rm NFW}(r) = \frac{\rho_0}{r/r_h(1 + r/r_h)^2} \tag{5.8}$$

where

$$\rho_{\rm NFW,0} = \frac{M_h}{4\pi r_{200}^3}\frac{C_{NFW}^3}{\ln(1 + C_{NFW}) + C_{NFW}/(1 + C_{NFW})}. \tag{5.9}$$

and M_h, r_h, r_{200} and C_{NFW} are constants to be set. r_{200} defines the halo viral radius, and r_h is related by $r_h = r_{200}/C_{NFW}$. The resulting potential and velocity profiles are

$$\Phi_{\rm NFW}(r) = -4\pi G\rho_{h,0}r_h^2\frac{\ln(1 + r/r_h)}{r/r_h}, \tag{5.10}$$

and

$$V^2_{\rm NFW}(r) = -GM_h\left(\frac{1}{r_h}(1 + r/r_h)^{-1} - \frac{1}{r}\ln\left[1 + \frac{r}{r_h}\right]\right)\frac{1}{\ln(1 + C_{NFW}) - C_{NFW}/(1 + C_{NFW})}. \tag{5.11}$$

In the case of a fixed halo, this is all that is needed to calculate the forces for the gas and star particles.

The density profiles for each component are used to set the positions of the star particles. The density profile effectively represents the number density of the star particles of that mass component, providing the masses are all the same. The density can thus be used as the probability distribution function (PDF) for the stars. Once correctly normalised, this can then be integrated to obtain the cumulative distribution function (CDF) in the range of 0-1. By drawing random numbers and finding the equivalent positions from equating to the CDF, the particles can be placed "randomly" in accordance with a predefined density profile. Figure 5.2 shows an example of this for the exponential disc. In the left panel is the surface density profile (red line), PDF (magenta line) and CDF (blue line). The histogram and black points correspond to the star particles position and corresponding surface density drawn from these distributions, showing good agreement with the input functions. On the right is the resulting *x*-*y* positions of the 10000 particles, once allocated a random azimuthal position is drawn from a uniform distribution.

Minor complications arise when using the density profiles above. None of the profiles are constrained to a finite volume, and so require either the radial extent to be artificially limited (but this can lead to artificial truncation of the mass distribution) or to add a ad-hoc truncation profile over some distance r_t, e.g. with an additional $\exp[-(r/r_t)^2]$ term in the density profile.

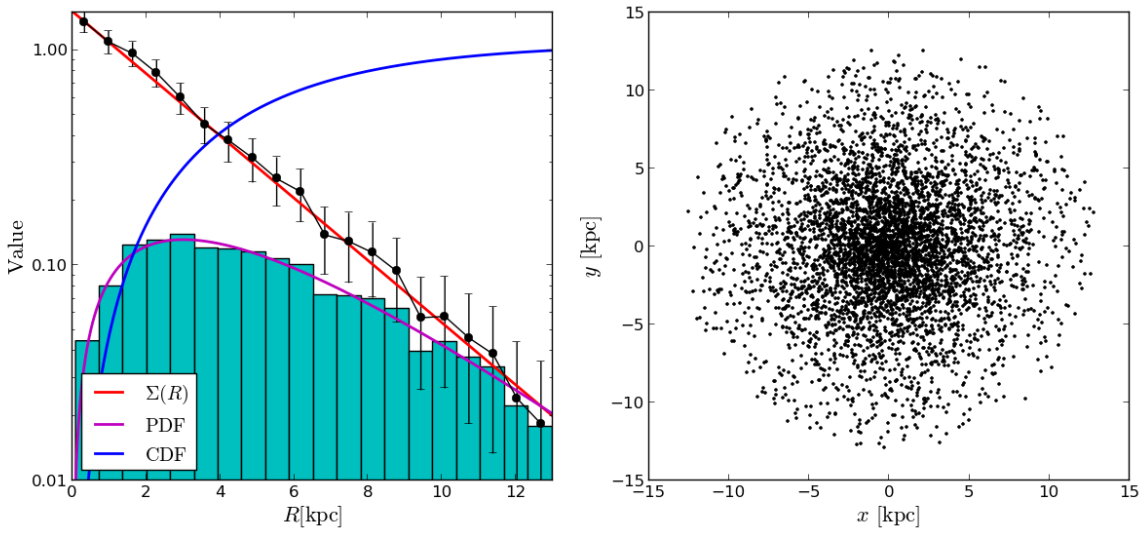

Figure 5.1: Example of setting the initial positions of particles. On the left is the surface density profile (red), resulting PDF (magenta) and CDF (blue) as a function of radius for the exponential disc. The resulting particle positions chosen from these functions is shown to match the PDF, and the underlying surface density (black points, with errors scaling as the size of histogram bins). The resulting x-y positions of the particles is shown in the right panel.

The truncation distance is chosen carefully as to ensure the total mass of the component is not significantly altered (e.g. r_t = 4kpc for the bulge). This makes calculation of the CDF for the halo sufficiently complicated that a Taylor expansion to the eighth term was used for the integration.

Drawing the velocities is significantly more complicated, but primarily requires integrating the separate moments of the collisonless Boltzmann equation, a.k.a Jean's equations (i.e. differential equations in velocity components in the R, z and θ directions with respect to R). This procedure can give mean velocity components, which can then be used with some sensible source function, such as a Gaussian, to draw actual velocities for each particle (see Hernquist 1993 for details). This process requires density, potential, velocity and mass profile functions for each component, and requires numerical integrations of combinations of Equations 5.1 to 5.11, requiring numerical integration schemes. Velocities of the disc are circular with some dispersion, while the velocities of the halo and bulge are in random orientations. Tests were made where the bulge had a non-zero streaming fraction, i.e. fraction of orbits aligned with net disc rotation, but this had minimal impact on the disc evolution. The initial value of the Toomre Q parameter must be defined for the disc to calculate the velocity dispersion. We use a value of $Q_s = 1$ to ensure the disc is borderline stable to arm formation. We experimented with other initial values of Q_s, and found 1 to be a good value for seeding spiral structure while keeping the disc from experiencing dramatic radial density waves and avoiding an over-clumpy stellar distribution. Occasionally velocities are generated nearing the escape velocity of the system, if this is the case a new velocity is drawn (Hernquist 1993).

We use the SPH code SPHNG in for the work presented in this chapter, which is described in Section 2.2.12. As with any N-body code, it is prudent to soften the gravitational force to avoid

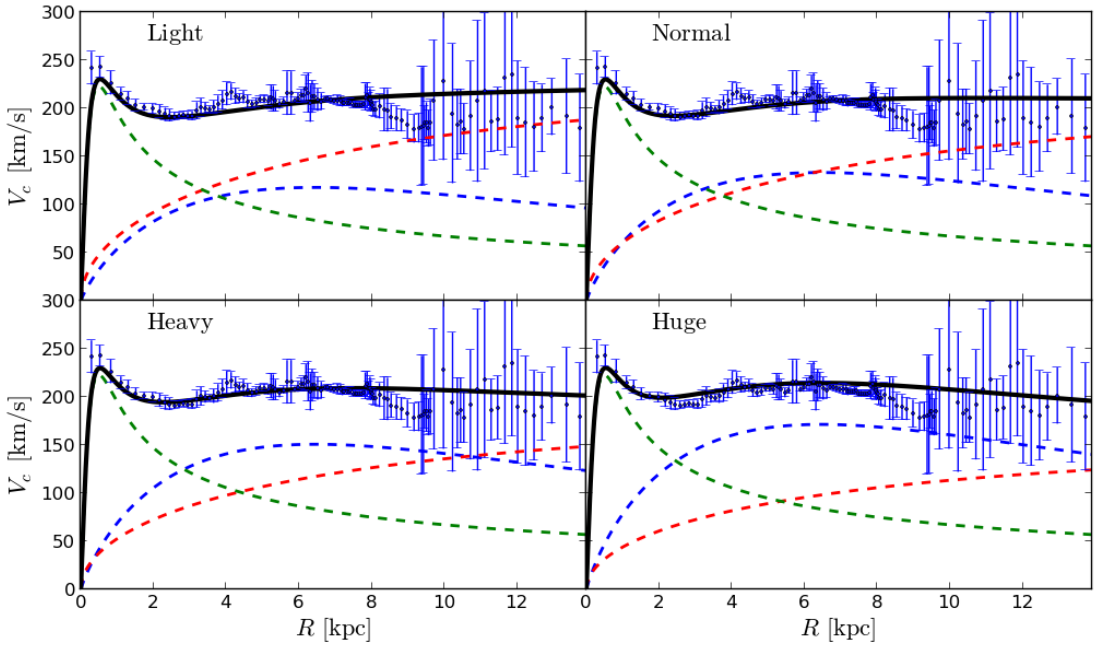

Figure 5.2: Axisymmetric rotation curves for calculations presented in this chapter. Disc, bulge and halo components are shown as the red, green and blue dashed lines respectively. Four different models are shown with labels referring to the disc mass; "light", "normal", "heavy" and "huge". The halo mass is adjusted in each case to ensure a rotation curve that is in agreement with observations (blue points, from Sofue 2012).

problems during close encounters between particles. SPHNG incorporates adaptive softening lengths for the gas and star particles. The gas particles simply use the hydrodynamical smoothing length scale. The stars use a value that is calculated from nearest neighbouring star particles, identical to the method of calculating the smoothing lengths of SPH gas particles. The difference being the smoothing length of N-body particles is not use for a hydrodynamical force. The implementation of which is described in detail in Price & Monaghan (2007). Approximate softening values for gas and star particles are 20pc and 100pc respectively, but differ greatly depending on environment.

Due to the nature of an N-body methodology imbedded in an SPH structured code, there are occasionally difficulties when setting the initial smoothing lengths of the star particles due to the large difference of masses between the gas and star particles. To overcome these problems we occasionally seed a stellar system with a resolution 1/9 lower than that desired. This relatively small number of particles, $O(10^5)$, without a gas disc is easily set by the code. This is then allowed to evolve for a very small timestep. After which the resolution is increased by simply transforming the point particle into a body-centred cubic lattice with vertices 0.6 times the smoothing length of the parent particle, and mass split between them accordingly. As setting up cubic lattices can induce spurious structure, we rotate each lattice randomly in each direction after splitting. The resulting system evolves very similarly to the original, low-resolution one. A gas disc is then imposed on the stellar distribution.

In the calculations in the previous chapter, how the mass in stars was distributed between the bulge-disc-halo system was irrelevant so long as the resulting rotation curve agreed with ob-

Term	Description	Value
M_d	Disc mass	$2.5, 3.2, 4.1, 5.3 \times 10^{10}\,\mathrm{M}_\odot$
M_h	Halo mass	$10.1, 8.3, 6.3, 4.4 \times 10^{11}\,\mathrm{M}_\odot$
M_b	Bulge mass	$1.05 \times 10^{10}\,\mathrm{M}_\odot$
r_d	Disc radial scale length	3.0 kpc
z_d	Disc vertical scale length	0.3 kpc
r_{200}	Halo radial scale length	122 kpc
C_{NFW}	Halo concentration factor	5
r_b	Bulge radial scale length	0.35 kpc

Table 5.1: Fixed galactic axisymmetric potential parameters used to reproduce the observed rotation curve in calculations with a live stellar component. The four values for M_d and M_h indicate our four configurations for the different disc to halo mass ratios. The resulting rotation curves are shown in Figure 5.2.

servations. Here this is not the case as the mass in the disc is directly delivered to the disc and bulge star particles. As there is some uncertainty regarding the mass of the Milky Way components we use four separate bulge-disc-halo configurations, the rotation curves for each are shown in Figure 5.2 with the respective parameters for the "light", "normal", "heavy" and "huge" configurations (ordered by increasing disc mass) given in Table 5.1. We keep the bulge initial conditions the same for all calculations and use different disc and halo masses to reproduce the observed rotation curve. The values for the "normal" setup are based on those from Baba et al. (2009). The bulge mass is unchanged, with the disc to halo mass ratio being the effective variable. The different disc masses also allow for greatly different swing amplified spiral modes (Equation 1.9 and Dobbs & Baba 2014) ranging from $2 \leq m \leq 5$. Thus while we do not have direct control over the spiral structures formed in these calculations, we attempt to drive a range of spiral modes induced by swing amplification.

A final point to note is the setting of gas particles. We set gas on similar orbits and positions to the star particles, only with much lower masses in accordance with a gas disc of the same mass as the previous chapters ($8 \times 10^9\,\mathrm{M}_\odot$) for consistency. Gas was not distributed according to the observed surface density profile however, but rather in an exponential disc. As the stellar disc is live, there is room for the surface density to settle itself due to the complex motions of the stellar system. We wanted to allow for the stellar distribution to drive the gas around the disc, rather than assume some profile. The resulting resolutions adopted for each set of computations is approximately 1 million disc star particles, and 0.1 million bulge particles. For simulations with a live halo 0.95 million disc, 50000 bulge and 0.5 million halo particles are used. In our high resolution calculations, 3 million gas particles are used. While 5 million was seen to be optimal in the previous chapters, we performed tests with 1 million and find the emission features are less sensitive to resolution. One million did however make weaker arm features in the edge of the disc, where particle density becomes low. We use 1 million gas particles for lower resolution tests, some of which are shown in this chapter.

We also allow for the creation of sink particles in these calculations (Bate et al. 1995). In simulations with N-body gravitational forces it is possible that the density of the gas in certain regions becomes extremely high as the gas accumulates around some point, such as a small cluster

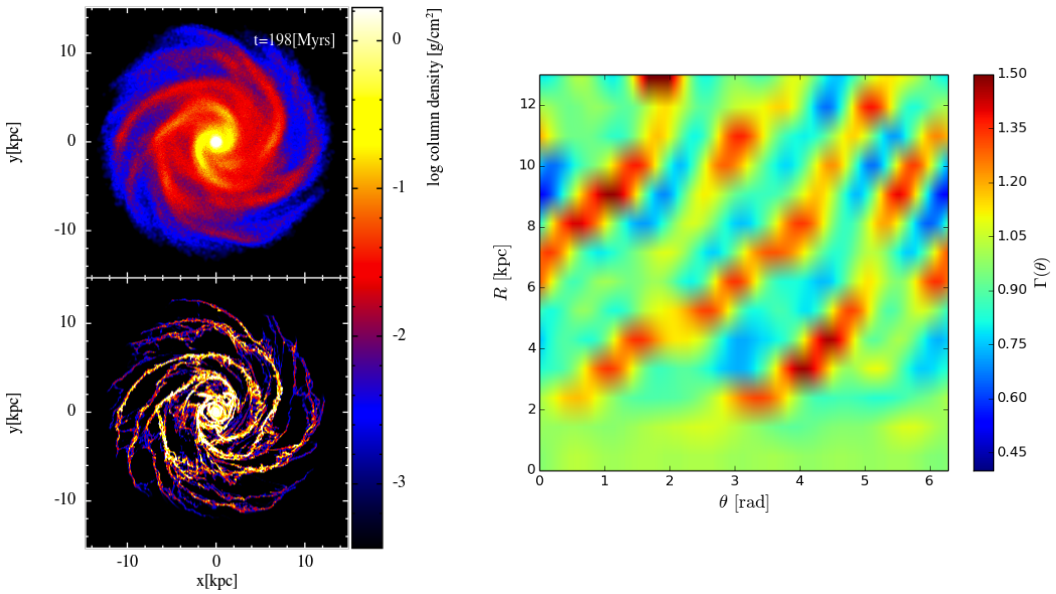

Figure 5.3: Projection of material in a simulation with a live disc and bulge into $R-\theta$ space. In the left panel the density of the stars (top) and gas (bottom) is shown. In the right panel the stellar material has been binned and normalised by surface density.

of star particles. To allow the computation to proceed further the gas clump is replaced by an accreting point-mass particle; a sink. These sinks act via gravitation with the remaining particles, and are allowed to accrete additional gas as the traverse the disc. Very few sinks are formed in these simulations (one or two, if any) and they have minimal impact on the global gas morphology.

5.3 Measuring arm number, pitch angle and pattern speed

One of the main differences between the models with a live stellar component and those with fixed analytic potentials in previous chapters is that we do not know the arm number, pitch angle, and pattern speed of features formed. While we can at least estimate a dominant arm mode from swing amplification (Equation 1.9), other values are complete unknowns until the calculation is performed. We use numerous methods to quantify these values from our calculations, so they can be compared to observational determined values, and those of the previous chapters. The methods outlined here are similar to those used in pervious studies (Dobbs et al. 2010; Fujii et al. 2011; Grand et al. 2012; D'Onghia et al. 2013), e.g. using Fourier transforms to find arm number, and will be illustrated by an example simulation. An important caveat to this and the rest of the methods below is that the arm shape is assumed logarithmic and periodic, i.e. with each arm separated by $2\pi/N$.

Arm number

The simplest way to measure arm numbers numerically is to take a Fourier transform of the Galactic material. The data is first projected into $R-\theta$ space, where logarithmic spiral arms will appear as diagonal lines. The data is binned into an $R-\theta$ grid, which is then normalised by the surface

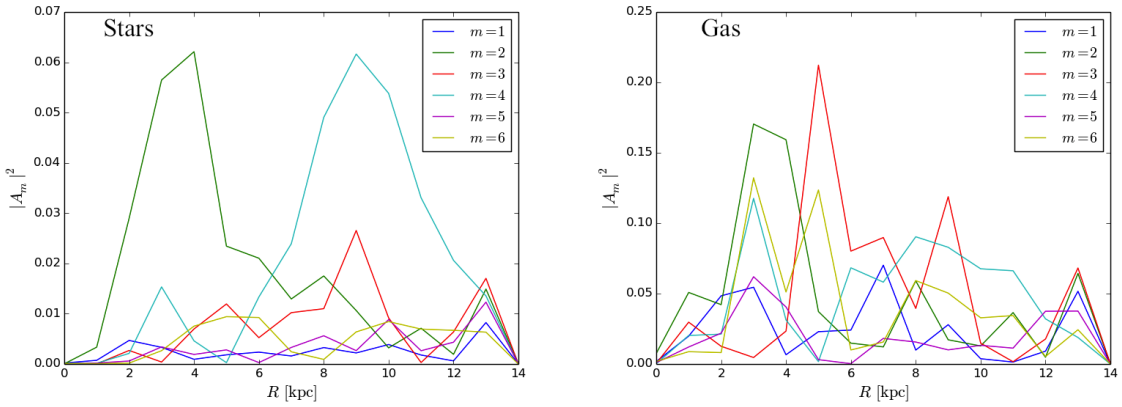

Figure 5.4: Amplitude of Fourier modes as a function of radius in stellar (left) and gaseous (right) material in the calculation shown in Figure 5.3. Different modes are shown as different coloured lines. Note the stellar material has much clearer structure than that of the gas.

density of the disc to ensure that inner arm structures do not dominate the fit. This gives the surface density contrast at a given radius: $\Gamma|_R(\theta) = \Sigma(R,\theta)/\Sigma(R)$. In Figure 5.3 we give an illustration. In the left panel is the top-down column density of the stars (top) and gas (bottom) in a simple live disc-bulge model. In the right panel is the corresponding normalised surface density of the stars in $R-\theta$ space. Notice the over-densities appearing in diagonal lines, tracing out the spiral arms. The stellar distribution tends to be much smoother than the gaseous distribution, making fitting to arm number and pitch less susceptible to being driven by small armlets or inter-arm features.

A Fourier transform is then performed on $\Gamma|_R(\theta)$ at different radii (this is done every kpc). We use the FFT module of the NUMPY PYTHON package. We then extract the dominant mode at that given radius (i.e. $\Gamma|_R(\theta)$ array) in the range $1 \leq m \leq 6$, which is then dubbed the dominant spiral mode for that calculation in that time-frame. An example of Fourier modes for the calculation in Figure 5.3 is shown in Figure 5.4. The dominant modes for the stellar and gaseous components are shown in the left and right panels respectively. For the stars it appears a 2-armed structure dominates the inner disc, which then transforms into 4-armed pattern in the outer disc (beyond the Solar position). This can also be seen by-eye in Figure 5.3, where there are two clear inner arms in the stars and a weaker, yet noticeable, 4-armed pattern further out. Again, the dominant modes are much clearer in the stars as opposed to the gas. While both show a $m = 2$ dominant mode in the inner disc, the gas has a strong $m = 3$ mode in the mid disc.

The strongest Fourier mode is taken to be the arm number, though in some instances, such as Fig. 5.4, there are two conflicting modes due to the variation as a function of radius. The location of the dominant modes that are shown in Figure 5.4 are shown in Figure 5.5 (stars only), with each panel corresponding to a different value of m. This figure confirms what is shown in Figure 5.4, that the $m = 4$ mode dominates the outer disc, and the $m = 2$ mode dominates the inner disc.

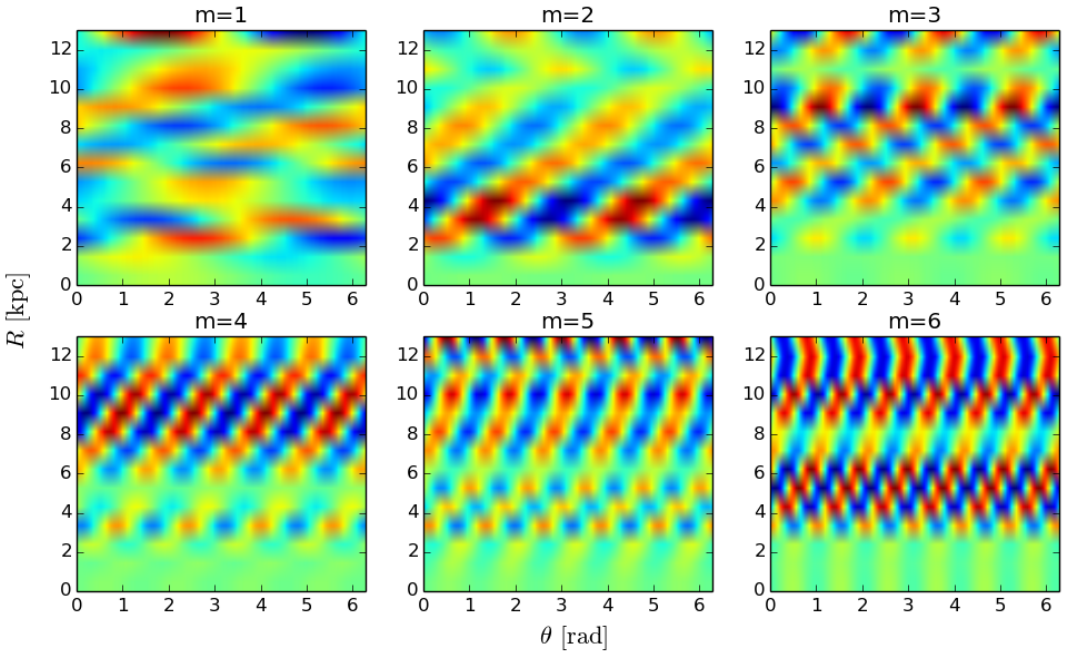

Figure 5.5: Location in $R-\theta$ space of the dominant modes in Fig. 5.4, shown for the stars only. If all modes are combined together they will approximately return the map in the left of Figure 5.3 (neglecting $m > 6$) terms).

Pitch angle

Once a dominant arm number is known (or selected) the pitch angle can be calculated. We can choose to fit to any spiral mode, i.e. any panel of Figure 5.5. This is useful for calculations where arm features are compared across multiple time-frames such as the calculation of the pattern speed, where the arm number is assumed to be time-independent. We first extract the $R-\theta$ position of the required mode. Depending on the morphology, this may only be done across a certain radial extent, such as the range in which that mode dominates (e.g. from 2kpc $\leq R \leq$ 6kpc for the $m = 2$ mode in Fig. 5.5). The pitch angle, α, of a logarithmic spiral arm is linked to the values of the constant B in the equation

$$\theta = f(R, \alpha) = B(\alpha) \ln R + C \tag{5.12}$$

where the pitch angle is $\alpha = \arctan B$ and C defines the azimuthal position of the arms. This equation is then fit to the relevant mode, and uncertainties are added at each radius (σ_Γ), proportional to the inverse of the value of $\Gamma|_R(\theta)$ thereby adding weight to the regions of greater density. The fitting is done using a downhill Nelder-Mead simplex algorithm from the SCIPY PYTHON package and minimising a chi-squared like statistic of the form

$$\chi = \frac{1}{n} \sqrt{\frac{\sum_i (f(R_i, \alpha) - \theta_i)^2}{\sigma_\Gamma^2}} \tag{5.13}$$

over all i points in the arm (n total). To perform such a fit an initial guess is needed for the B and C parameters. Usually the fit is unaffected by these values, but we test numerous values to check

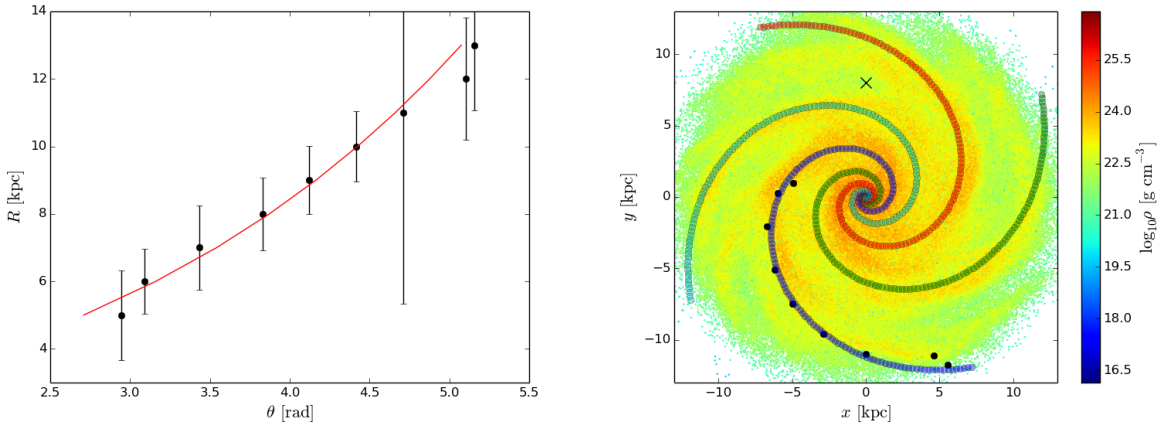

Figure 5.6: Fitting the pitch angle of an arm to a stellar disc. In the left panel are points used in the fit, shown in black, and the corresponding best-fit arm model shown as the red line ($\alpha \approx 20°$). In the right panel is the $m = 4$ model over-plotted onto the stellar disc, where particles are coloured by density.

for consistency (confirming any spurious fits by-eye).

An example of the fit to the $m = 4$ stellar mode in Figure 5.5 is shown in Figure 5.6. The left panel shown the points that trace out the arm (black points) and the best fitting logarithmic spiral arm (red line). In the right panel the top down position of the disc star particles is shown, coloured by particle density, with the same points as in the left panel over-plotted along with the best fitting $m = 4$ arm model. In this instance the best fitting model has a pitch angle of approximately $\alpha = 20°$. This can change up to $\pm 2°$ depending on the radial extent of the disc used in the fit.

Pattern speed

While there exists some complex methods of determining the pattern speed from an observers perspective (e.g. Tremaine & Weinberg 1984) we choose to simply calculate the azimuthal offset between arm features over a given time frame. This approach is often adopted in numerical works, as we are in the privileged position of knowing the morphology at different epochs (Dobbs 2011b; Grand et al. 2013).

For any given calculation we first calculate arm number and fit a pitch angle. We then take subsequent time-steps and perform the same fit to arms, only this time fixing the arm mode to fit to. Then by simply calculating the offset between arms at different epochs the pattern speed can be calculated as a function of radius. In Figure 5.7 we show such a calculation. In the left panel are the traces of the best-fitting $m = 4$ mode for the simulation shown in Figure 5.3 (again, stars only) and at four later time-steps spanning $\approx$40 Myrs. The resulting pattern speeds are shown in the right panel by the coloured points, where the speed has been calculated using adjacent time-frames only. The dashed line shows the pattern speed calculated using all time-frames (i.e. using the first and last frame). In all instances a clear decrease of pattern speed with radius can be seen, indicating the arms act as material, rather than wave-like features. The average pattern speed across all time-frames and radii in Fig. 5.7 gives a value of $\Omega_p = 24 \mathrm{km\,s^{-1}\,kpc^{-1}}$.

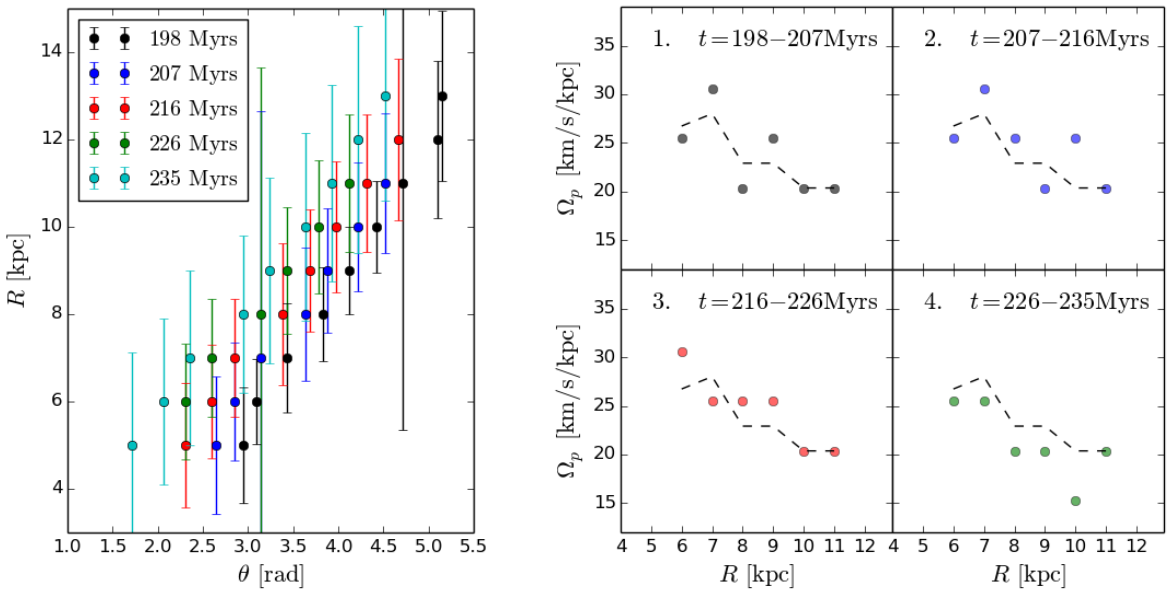

Figure 5.7: Illustration of fitting to the pattern speed in a calculation with a live stellar component. In the left panel is the tracing of best-fitting arm structures for the $m = 4$ mode across 40 Myr of evolution of the calculation shown in Figure 5.3. The offset of each arm to the neighbouring time-frame is used to calculate a pattern speed for the spiral arms as a function of R, shown in the right panel by the coloured points. The dashed line is the pattern speed across all five time-frames.

The arm structure is assumed to be constant with time using this method. This is not entirely the case, seen by the fact that best-fitting pitch angles change between time-frames in Figure 5.7, with values ranging from $22° \leq \alpha \leq 19°$. However, the dominant arm modes appear constant over this time, i.e. the general trends in Figure 5.4 remain largely unchanged (in the stars).

5.4 Results of simulations

In this section we describe the results of our simulations using a live stellar distribution for the disc, bulge and, in some instances, halo. Discussion of the *l*-*v* maps will be done in Sections 5.5 and 5.6.

The full set of simulations is given in Table 5.2. The "heavy" configuration is more of our default rather than the "normal" (so named as it matches the values of Baba et al. 2009). The "normal" setup tended to create a many armed structure ($4 < m < 5$) in test simulations, so we made our default a disc with a slightly higher mass to a drive a slightly lower arm mode. We run live disc only (D), live disc and bulge (B) and live disc, bulge and halo (H) calculations in a range of mass configurations; a,b,c and d (see Table 5.1 and Figure 5.2). The D and B calculations use a fixed analytic halo potential but we also perform two calculations using a live halo and the "heavy" mass disc, Hb. A few special case calculations were also performed. The first case is to evolve the stellar system of each type of model for 1Gyr before the addition of gas (DbG, BbG and HbG models). The aim was to see what kind of structure can be created in a settled disc.

Calculation	Description
Db	Live disc *only* in "heavy" configuration
Dc	Live disc *only* in "normal" configuration
DbG	As Db but allowing for 1Gyr of evolution before addition of gas
Ba	Live disc and bulge in "huge" configuration
Bb	Live disc and bulge in "heavy" configuration
Bc	Live disc and bulge in "normal" configuration
Bd	Live disc and bulge in "light" configuration
BbL	As Bb but with half gas disc mass
BbG	As Bb but allowing for 1Gyr of evolution before addition of gas
Hb	Live bulge, disc and halo in "heavy" configuration
HbG	As Hb but allowing for 1Gyr of evolution before addition of gas

Table 5.2: Description of different live-disc models. Refer to Table 5.1 and Figure 5.2 for the disc and halo mass ratio configurations. If halo is not listed as live then it is represented by an analytic potential. All models contain the same configuration of gas disc except BbL. All apart from DbG and HbG contain 3 million gas particles models.

Previous *N*-body work has shown that without some method dissipation, either by addition of gas or accretion, spiral arms will slowly dissipate (Sellwood & Carlberg 1984). To this end, we aimed to see if a generally featureless disc could reproduce *l*-*v* features of our Galaxy. One final calculation is our fiducial setup (Bb in Table 5.2) with half the normal gas disc mass (4×10^9 $M_\odot$) to see whether a reduced disc mass will reproduce sufficient CO emission in a live disc; BbL. It produced significantly weaker emission when using fixed potentials (Figure 4.3).

5.4.1 Live disc only

The simplest calculation performed was to calculate the evolution of a stellar disc, without the presence of a bulge but with an analytic halo to maintain outer velocity structure. The evolution of such as system (with a disc mass/halo mass of the "normal" configuration) is shown in Figure 5.8. The stellar distribution is shown in the top panels and the gas in the bottom, where all material is rotating clockwise. Arm structures can clearly be seen in the stars and gas. The nature of these arms is discussed in more detail in Section 5.4.2. These arms host a majority of the molecular gas in the simulation. As gas leaves the arm it experiences a drop in density and has a rapid decrease in molecular content, until the eventual passage into another spiral arm. Similar to the previous calculations, the vertical structure in the gas collapses into the plane rapidly, though the somewhat more turbulent nature of the stellar potential makes the disc thickness greater than when using an analytic potential. We maintain that stellar feedback may be required to substantially drive gas away from the plane.

Figure 5.8 shows a mild shockwave of material emanating from the centre at early times (also visible in the rotation curve). This is seen in other *N*-body calculations, and can be reduced by allowing for the disc to evolve for some time and periodically re-setting azimuthal positions to avoid arm growth (Fujii et al. 2011). We find these structures are resolution dependant, and in lower resolution cases the effect is much clearer. Originally we ran a "Huge" disc configuration (a would be Da model) but found these radially propagating rings having too strong an effect on

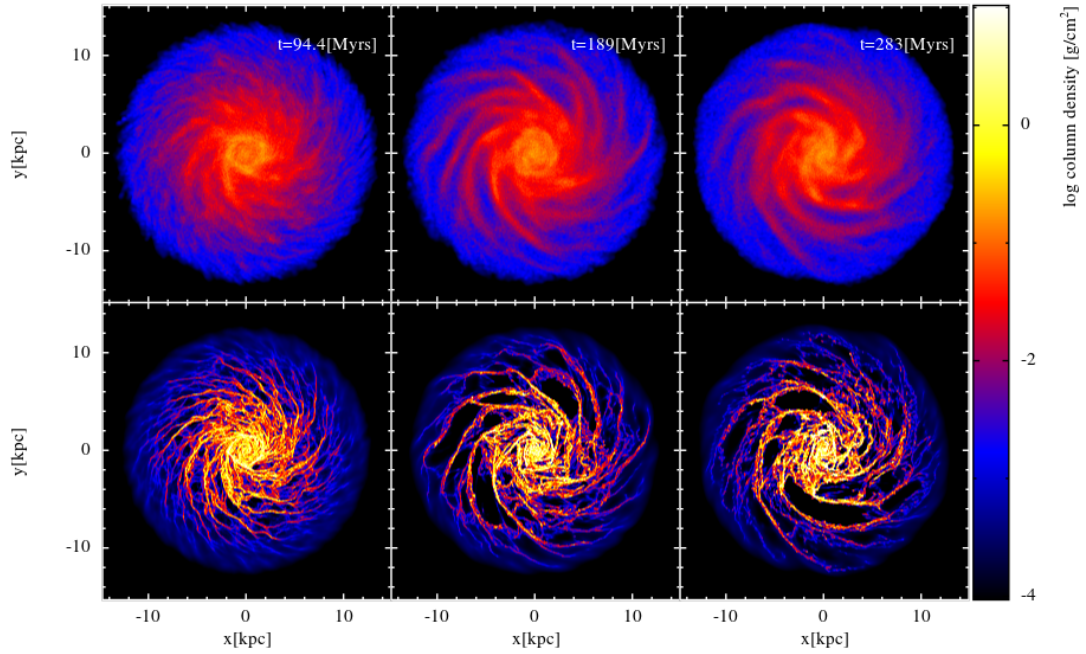

Figure 5.8: Evolution of a live stellar disc (top) and the accompanying gas disc (bottom) in the Dc model over 280Myrs. Clear spiral arms can be seen to grow with evolution of the disc.

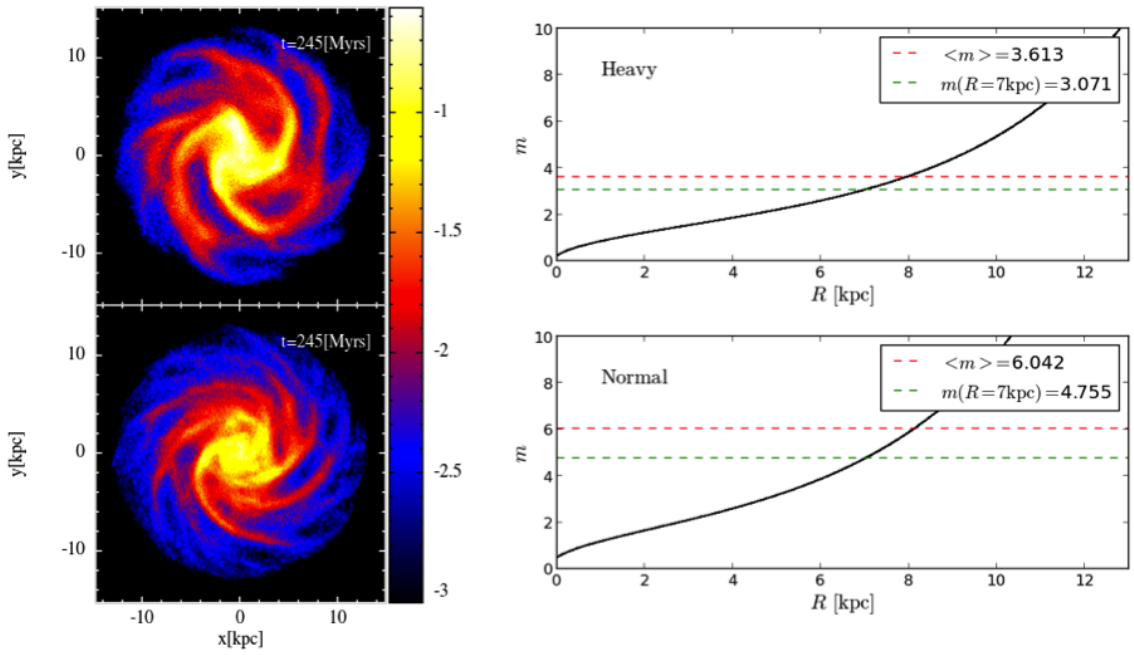

Figure 5.9: Top down views of two live disc simulations with different disc masses (Db top, Dc bottom) and their associated predicted swing-amplified modes as a function of radius (right panels). A Fourier analysis of the heavier disc model in the top panel gives a dominant arm mode of $m = 3$ which is in agreement with that predicted in the mid-disc by swing amplification. Likewise the lighter disc has a dominant mode of $m = 5$, also in good agreement with the predicted value. The predicted mode is calculated via Equation 1.9 as a function of disc mass, epicycle frequency and radius.

the gas. By 200Myrs these features are appear greatly diminished in Db and Dc, with a settled rotation curve, and so we do not analyse gas before this point.

In our two primary disc calculations, Db and Dc, there appears to be a good agreement between the number of arms formed and that predicted by swing amplification (Equation 1.9). In Figure 5.9 we show the Db and Dc models (stellar component only) in the left panels. By-eye it appears that the higher mass disc (top) has fewer individual arm features than the lower mass disc (bottom). In the adjacent panels we show the swing amplified mode predicted using the initial conditions of the gas disc. The mode increases with radius, but two useful values can be drawn, the average m over the entire disc, and the value at 7kpc (half-way and near the solar position). The values for these models predict a value of $3 < m < 4$ form the Solar position to the edge of the disc in the Db (i.e. heavy) model, and $4.5 < m < 6$ in the Dc model. We use the method of Section 5.3 to find the dominant arm mode, rather than assessing by-eye, and find values of $m = 3$ and $m = 5$ for the Db and Dc models respectively. These are in excellent agreement with those predicted in the outer disc, implying the swing amplification prediction allows for good rough estimate of resulting arm number. The pitch angle however gives extremely high values, with values of 20°and 28°for the Db and Dc models, far outside values inferred for the Milky Way and at the high end of values seen in external galaxies.

Due to the nature of the bulge-free system, the rotation curve for these models decays rapidly approaching the Galactic centre. As opposed to models with bulges, where the curve rises near $R \approx 2$kpc, keeping a near-constant rotation throughout the disc (see Fig. 5.2). This leads to the lack of an ILR, which has been theorised and seen in observations to encourage the growth of a bar in the inner disc (see Sec. 1.3.4 for a discussion). The model DbG, which we allowed to evolve for 1Gyr before the addition of gas, was found to display a clear bar structure. This bar is relatively short compared to that believed to persist in the Milky Way, with a semi-major axis of approximately 2kpc and fairly wide with axis ratio of approximately 2:1. In general, any disc model without an inner bulge formed a steady bar after around a Gyr of evolution, whereas systems with a strong inner bulge tended to be bar-free.

The evolution of such a bar is shown in Figure 5.10 for stars and gas (top and bottom panels respectively). This bar rotates at approximately $\Omega_p = 28\mathrm{km\,s^{-1}\,kpc^{-1}}$, which is slower, but not outside of uncertainties, than that of the Milky Way. In this figure the bar can be seen to generate arm structure at its ends, though these eventually de-couple from the bar and dissipate, leaving new arms to form in their wake. These arms have a wide pitch angle in the inner/mid disc, with values of 20°-28°, however, the arms stray from a logarithmic spiral at the edge of the disc where they strongly circularise making fits to α problematic. The model shown in the figure is of a lower resolution in the gas than the models presented in the rest of this chapter. There are only 0.1 million gas particles, as opposed to the fiducial 3 million. We show this model because we had tremendous difficultly maintaining the higher resolution models. The forcing time-step for the gas became detrimental to the computation time due to the effects of the gas entering and leaving the barred region.

Nevertheless, the gas in the low resolution run in Figure 5.10 can be seen to trace out the bar. In intermediate times the gas traces out a long line along the bar, tracing it's major axis.

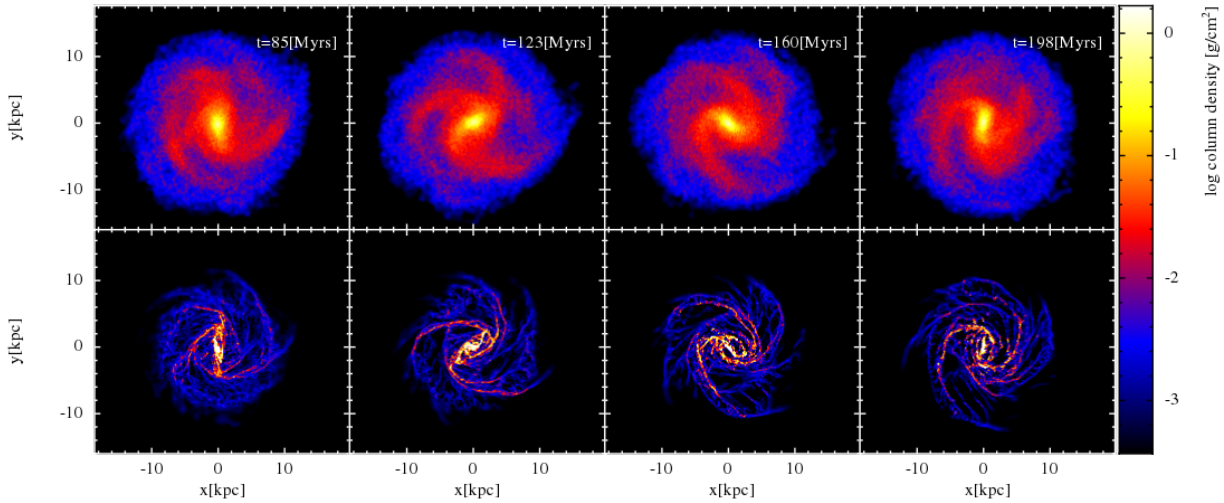

Figure 5.10: Evolution of a low-resolution disc with initial bar in the stellar disc. Shown for 200Myrs of evolution, where the bar has already been allowed to evolve for 1Gyr before inclusion of a gas disc. Stars and gas are in the left and right panels respectively.

No inner ring is seen as in the barred models of Chapter 3 due to the lack of any ILR. To asses the suitability of this model to the Milky Way we project the position of the gas particles into l-v space. The resolution is too low to properly map the emission structure, but by simply re-mapping we can gauge the similarities to our Galaxy. In Figure 5.11 we show the gas distribution with the bar angled at $\theta_b = 20°$ and the corresponding projection of gas into l-v space (the observer is at $y = 8$kpc in the top-down view). The second l-v map shows the bar at a wider orientation angle ($\theta_b = 50°$). Some structures do seem similar to observations, such as arms features that resemble Carina and Perseus arms. However, in order to obtain an l-v structure with features that resemble the Milky Way we had to lower the observers velocity to $180\,\mathrm{km\,s^{-1}}$, well outside of our normal range. This is to compensate for the lack of a bulge, and generally shallower rotation curve in the inner disc compared to our other models. While the rotation curve has indeed risen in the inner disc since the start of the simulation thanks to the inner bar, it is still low compared to the values inferred from observations ($V_c \approx 150\,\mathrm{km\,s^{-1}}$as opposed to the observed values of $V_c \approx 250\,\mathrm{km\,s^{-1}}$). While the creation of a bar is promising, we still require a bulge to match the velocity structure of our Galaxy, which inhibits bar formation (see next section).

5.4.2 Live disc and bulge

The main Galactic disc configuration investigated is the Ba-d group of models, which contain a live disc and bulge, but maintain a static dark matter halo to reduce computational effort. We show the Ba, Bb, Bc and Bd models at three separate intervals in Figures 5.12, 5.13, 5.14 and 5.15 respectively. Stars are shown in upper panels, and gas in the lower. The third time frame of the Ba model is slightly earlier than the other models. This is due to the computation taking significantly longer than the others[1]. We did not continue this calculation further as maps made from existing

[1]Run time appeared to scale with stellar disc mass due to the size of the forcing time-step experienced by the gas particles entering from regions of very low to very high density.

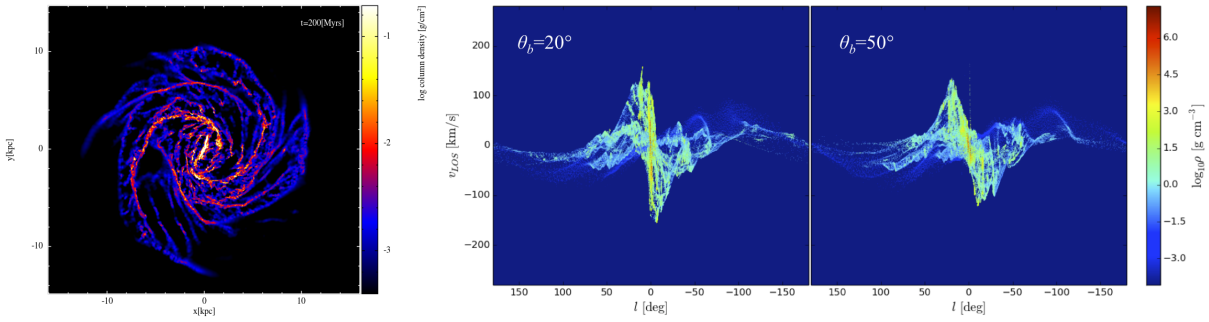

Figure 5.11: Gas embedded in a stellar disc after a bar has been allowed to form, and then evolved for 200Myrs with the gas. In the left panel the projection of the gas into l-v space is shown for bar orientations of $\theta_b = 20°$ and $\theta_b = 50°$ (left and right respectively). The observer is placed at $y = 8$kpc and given a rotation speed of $180\,\mathrm{km\,s^{-1}}$.

time-steps and lower resolution calculations that had evolved for longer showed the Ba model was a poorer fit to Galactic l-v data in general.

As with the disc-only models, the gas clearly traces the arm features in the stars. The higher density gas in the disc is the location of the majority of the molecular content. In the highest mass disc (Ba) there is very little inter-arm gas. In the arm cavities in Figure 5.12 there are effectively no gas particles, though stars are still present (seen by the non-zero density in the stars in the inter-arm regions). The gas is effectively being swept-up in an arm passage and is not released until the arm is sheared apart by rotation. The arms in the Ba model appear non-logarithmic in many places, especially so in the final panel. Various kinks, or knees, form along the spiral arms. The disc mass appears to be very large to be supported by rotation, and the stellar-gravity is producing strong local collapse into these irregular arm patterns. At the time of the middle panels of Fig. 5.12, Fourier analysis indicates that $m = 2$ is the dominant arm mode with a wide pitch angle of 20°. This only persists for $R < 9$kpc, above which there is no clear dominant mode. At the latter time the $m = 2$ mode still dominates at a similar pitch angle, but there is considerable power in the $m = 3$ and $m = 5$ spiral modes, visible by-eye. The pitch angle of the $m = 2$ mode is maintained between the second and third panels of Figure 5.12 over which time the average pattern speed is $\Omega_p = 38\mathrm{km\,s^{-1}\,kpc^{-1}}(4 < R < 9\mathrm{kpc})$. Interestingly the pattern speed here is fairly flat with radius, rather than decreasing.

The Bb model (Fig. 5.13) shows much more regular spiral structure, with some clear dominant spiral modes visible in the stars. There is also a moderate amount of inter-arm structure in the gas with features being continuously created and destroyed as arms are sheared out and re-formed. The pitch angle and pattern speed analysis for this model is used as the example in Section 5.3. The dominant arm mode (left, Fig. 5.4) appears to clearly favour a 2-armed pattern in the inner disc and a 4-armed in the outer. This is seen by inspection of the stellar distribution in Figure 5.13, where a small 2-armed feature can clearly be seen inside of $R < 5$kpc while the edge of the disc displays four arm tails. The Milky Way is also thought by some to have a higher arm number in the outer disc, and there is also confusion over whether there are 2 or 4 spiral arms (Amaral & Lepine 1997; Levine et al. 2006). The pitch angle of 4-armed pattern is approximately 20°and the pattern speed has a mean of $25\mathrm{km\,s^{-1}\,kpc^{-1}}$, though this is seen to decay with radius;

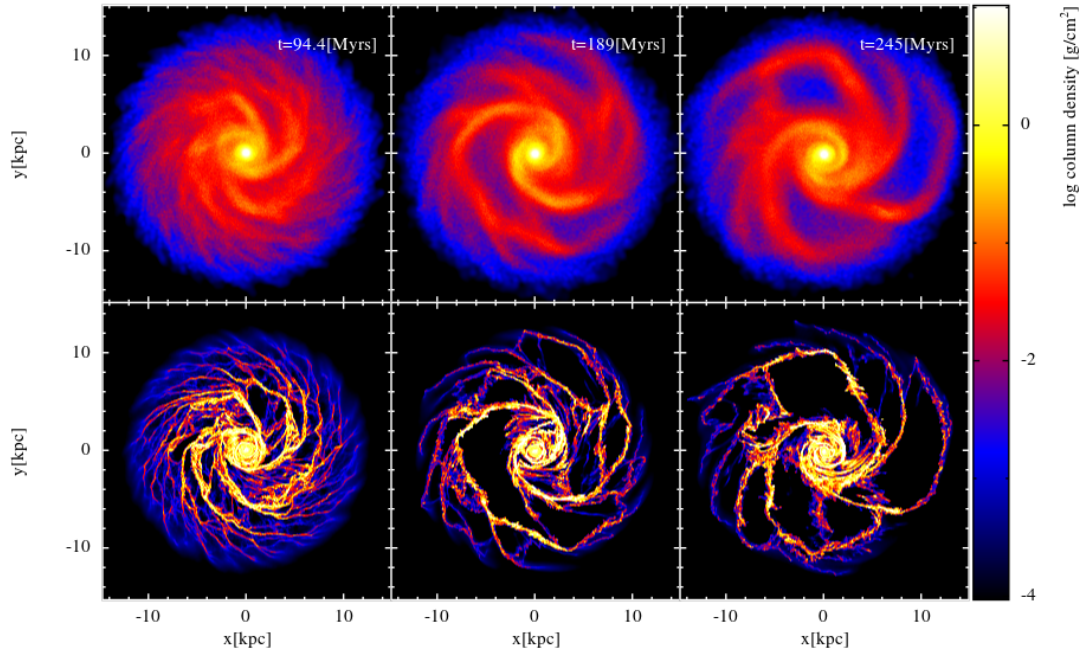

Figure 5.12: Evolution of the Ba model, with the heaviest disc mass investigated, in the stellar (top) and gaseous component (bottom). Large scale arm structures can be seen, yet appear rather irregular with many knee and kink features.

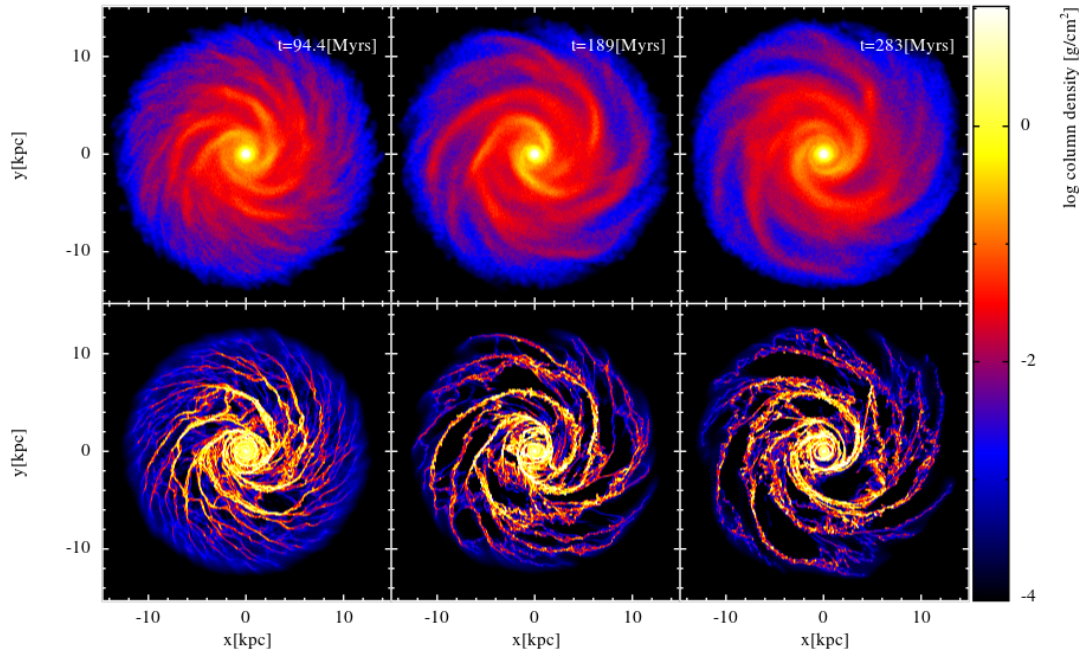

Figure 5.13: As Fig. 5.12 but for the Bb configuration. Arms appear more smooth and regular compared to the Ba model.

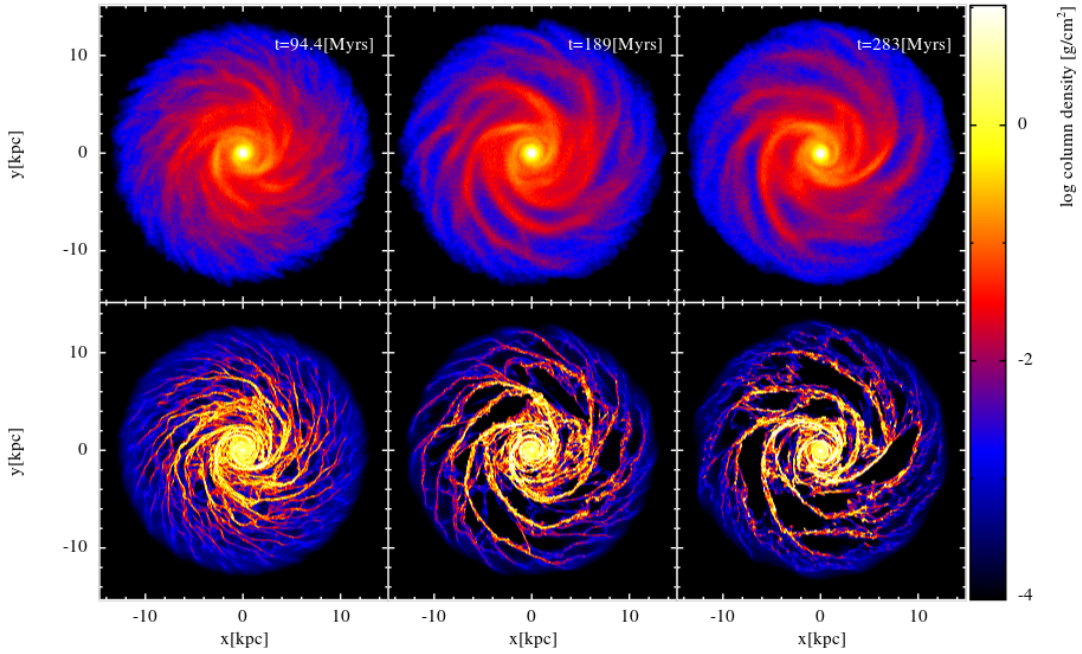

Figure 5.14: As Fig. 5.12 but for the Bc configuration. A significant amount of small arm structures are now visible compared to Ba and Bb.

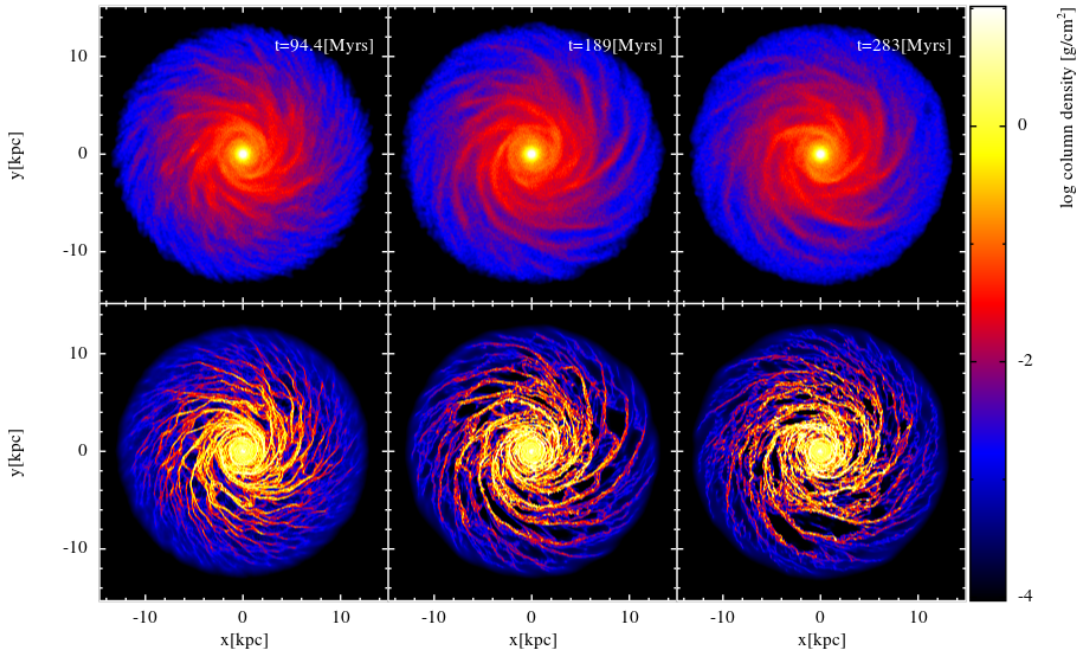

Figure 5.15: As Fig. 5.12 but for the Bd configuration. Arm structure is very small scale and flocculent with no clear dominant spiral mode visible by-eye.

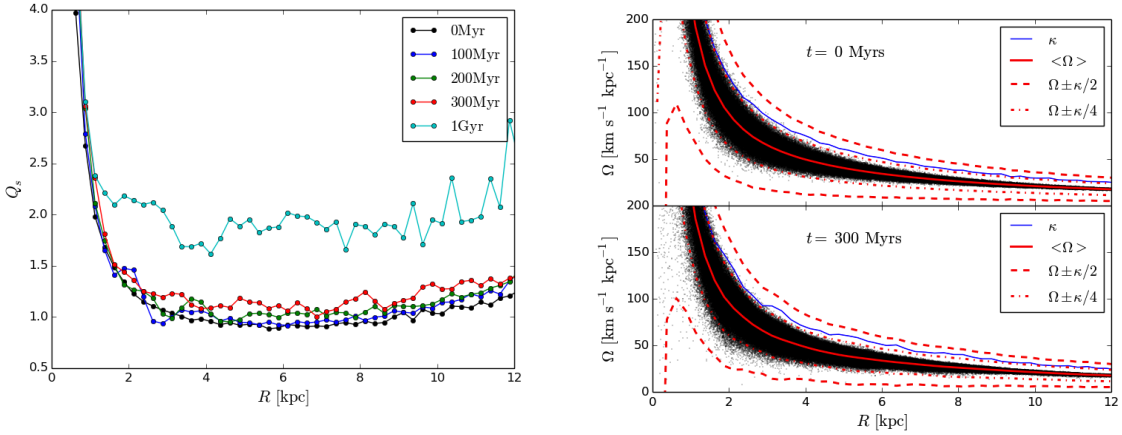

Figure 5.16: Evolution of the Toomre Q-parameter in the Bc disc-bulge calculation as a function of radius (left). In right panel the orbital frequency of gas particles is shown for the same model at initialisation (top) and after 300Myrs of evolution.

20km s^{-1} kpc^{-1}< Ω_p <30km s^{-1} kpc^{-1} in the range 4kpc < R < 11kpc indicating the arms are material in nature. If the arms are fit to the $m = 2$ component inside $R <$ 5kpc then a similar pitch angle is inferred than the $m = 4$ case.

The Bc model in Figure 5.14 is similar to the Bb model, with some clear spiral features and inter-arm material. There also appears to be a 2-armed mode in the inner disc, though this is less clearly defined than the heavier case. When fitting to the spiral arm number there are two dominant modes; $m = 4$ and $m = 5$. The latter is the strongest amplitude, but is a clear spike rather than being the prevalently strongest amplitude. Interestingly this spike occurs very near to the Solar position (7kpc) and gives a pitch of 18°. This is interesting as in many Galactic models the preferred structure is a 4-armed spiral, but with the addition of some small spur or minor Local arm which is always separate from the 4 main arms. The fact that the Bc model is preferentially a 4-armed model throughout most of the inner disc, lightly 2-armed in the centre, and seemingly 5-armed near the Solar radius makes it an excellent candidate for replicating Galactic l-v features. The pitch angle of the $m = 4$ mode is only slightly higher than the $m = 5$ mode and displays a mean pattern speed of 25km s^{-1} kpc^{-1}and a range of 22km s^{-1} kpc^{-1}< Ω_p <35km s^{-1} kpc^{-1} which is at the high end of values calculated for the arms of the Milky Way.

The lightest model (Bd) is shown in Figure 5.15. Here there appears to be a clear departure from the Bb and Bc models in that there is no clear spiral mode visible by-eye. The structure of this disc appears to mimic a flocculent spiral galaxy such as NGC 4414 with multiple small scale arms and inter-arm features. Performing a fit to the arm features tends to reveal little more information. Across numerous time frames there is no clear mode that dominates more than a couple of kpc of the disc. There appears two spikes in amplitude, one for the $m = 2$ mode in the inner disc, similar to the other models, and one for an $m = 5$ mode at $R =$ 8kpc. Beneath which is an indeterminate mess of amplitudes with $m = 4$ and $m = 6$ showing small scale peaks. Attempts to fit a pitch angle to the $m = 5$ mode result in values in the range 15° < α < 23° and the pattern is impossible to determine with values ranging from 20km s^{-1} kpc^{-1}< Ω_p <40km s^{-1} kpc^{-1} depending on the features incorporated into the fit.

Our final model of a bulge-disc system is shown in the left panel of Figure 5.17, where we have allowed the disc to evolve for 1Gyr before the addition of gas. The result is a disc that is very smooth, with no clear spiral features. Some very tightly wound arms appear in the gas, but these appear local in nature and are rapidly wound up and dispersed. At this stage the stellar disc is highly stable to perturbations, with $Q \approx 2$ in the inner disc (the 1Gyr data in Fig. 5.16). The morphology of the gas is almost ring-like, with no bar or inner $m = 2$ mode as in the previous calculations. It has been postulated that some other mechanism is needed to maintain spiral structure for 10's of galactic rotations in numerical simulations (Fujii et al. 2011). In the calculations of Sellwood & Carlberg (1984) additional forms of energy are added to maintain spirality, effectively imitating star formation, keeping the disc warm enough to maintain it's spiral structure. D'Onghia et al. (2013) instead propose that the spiral structure can be continually re-seeded simply by GMCs perturbing an otherwise featureless stellar disc. Our simulations are fairly low resolution compared to pure N-body simulations in the literature. We saw in initial test calculations that arm features become weaker and short lived as the resolution is decreased, and so we do not expect them to last longer than the order of a Gyr.

We do not show any figures of the BbL model (lighter gas disc). The morphology is very similar to that of the fiducial mass disc (Bb). This model is used to primarily gauge the effect of disc mass on the CO emission features (Sec. 5.6).

Disc stability

In all of the models presented above there is a lack of inner bar-like structure throughout. This is believed to be due to the Q-barrier caused by the inclusion of the bulge, which was absent in the disc only models. In Figure 5.16 we show the Q-parameter for the stars in the left panel as a function of radius. A clear incline can be seen near the galactic centre which acts as a boundary in stability, stopping waves from propagating through the centre (see Sec. 1.3.1). Interestingly all models show a trailing $m = 2$ mode in the inner disc. It is possible this is the disc attempting to form a bar as in the disc models, but is undermined by the increased stability inherent to the bulge dominated region. If this were the case, then it implies there is some small region of parameter space where it is possible to form a bar but also maintain a rotation curve that is near-flat, presumably by considerably reducing the bulge mass. This stability of the inner disc against arm and bar formation also causes a small disc of molecular material at the galactic centre. In the gas density renders there is a disc of material of very high density inside $R < 2$kpc where molecular gas is easily maintained. This was very much not the case in the models with fixed potentials, where the bar, and arms in some instances, swept up the gas into steady orbits and left the very centre of the disc relatively devoid of gas.

The Q-parameter is a key quantity in determining stability. In the left of Figure 5.16 the evolution of Q is shown from 0-1Gyr. Initially $Q \approx 1$ in the mid-disc, as expected from the setup conditions, making the disc barely stable. Over 300Myrs Q can be seen to slowly increase throughout the disc, raising to approximately 1.2 in the mid-disc region. At much later times, of the order of Gyr, $Q \approx 2$, implying the disc is highly stabilised. In the right panel the rotation frequencies for the stars initially and after 300Myrs are shown. The dashed lines show the resonance curves,

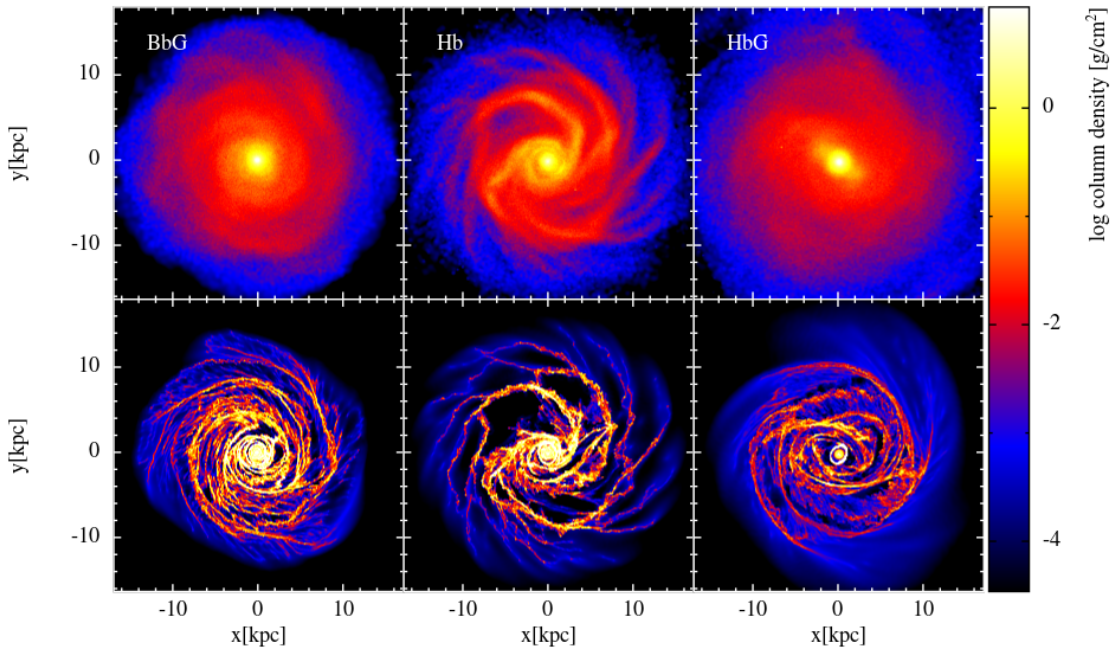

Figure 5.17: Stellar (top) and gas (bottom) densities in our three remaining models. BbG (left) has a much further evolved disc than those shown previously and the gas has formed many shallower pitch angled arms closer in morphology to rings. Hb (middle) has arm features not dissimilar to the static halo counter-part (Bb). HbG (right) has an evolved bulge-disc-halo system and has formed a bar in the centre, though weaker compared to that formed in the disc-only models. Only disc particles are plotted in the stellar density render. Note the HbG model is of slightly lower resolution, with only 1 million gas particles.

indicating the presence of the ILR and OLR. Note that the rotation structure is largely unchanged in the evolution of the system, with the main difference at later times being the existence of small scale fluctuations in κ (and hence resonances), presumably caused by asymmetries in the disc, i.e. arm features.

The rotation curve of each disc model showed a dispersion that increased with disc mass, both initially after several hundred Myr of evolution. Dispersion around the mean rotation curve ranged from $\pm 50\,\mathrm{km\,s^{-1}}$ in Ba to $\pm 20\,\mathrm{km\,s^{-1}}$ in Bd. The dispersion in the rotation curve therefore appears directly related to the number of arms formed, which in unsurprising as the dispersion is also incorporated into the value of m predicted by swing amplification ($m \propto \Sigma^{-1}$, and Σ determines the stellar velocity dispersion).

5.4.3 Live disc, bulge and halo

For the basic live halo-disc-bulge models, the morphology is not dissimilar to the static halo models. In the central panel of Figure 5.17 we show the stellar (top) and gas (bottom) morphology in the Hb model after 240Myrs of evolution. The arm structure is quite asymmetric, with some clear branching features. There appears to be a dominant 2-armed pattern in the inner/mid disc, which dissipates in the outer disc. Fitting arms to this feature gives a pitch angle of $\alpha \approx 20°$, similar to

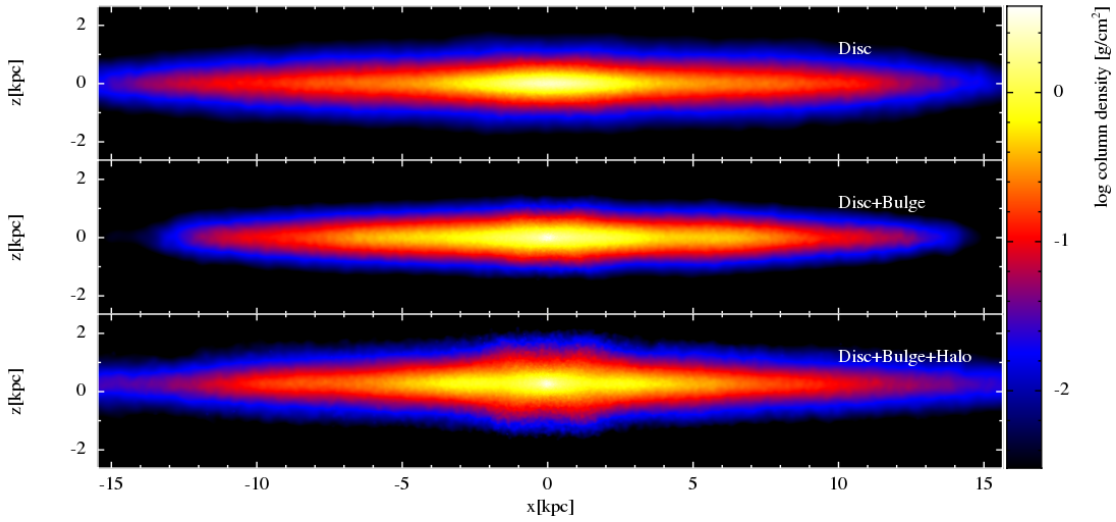

Figure 5.18: Vertical density render of the stellar distribution in three different simulations. In the top panel is a live disc calculation that had formed a bar (DbG), in the middle a live disc-bulge calculation with no bar (Bb) and in the bottom panel a live disc-bulge-halo calculation that formed a bar (HbG). Gas, bulge and halo particles have not be plotted for clarity.

values found in the previous models. There is a moderate strength $m = 4$ mode in the outer disc with $\alpha \approx 18°$, but this only dominates around $R = 8$kpc, and the fit to one of the four arms is very tenuous (evident from the top down view in Fig. 5.17). The pattern speed for the $m = 4$ mode gives a high average of $\Omega_p = 30\mathrm{km\,s^{-1}\,kpc^{-1}}$, but this is only valid for the very narrow radial range where the mode dominates.

The turbulent nature of the disc, and the irregular spirality, in the Hb model led us to perform the HbG model. Here the stellar system had been evolved for 1Gyr before the addition of the gas component. In the right panel of Figure 5.17 we show such a model after 260Myrs of evolution. An interesting development has occurred in this model. A weak bar has formed in the inner disc, with a strong spheroidal component, presumably owing to disc orbits interacting with the bulge. The density contrast between this bar and the surrounding disc is lower than that of the disc only simulations (Fig. 5.10). The gas response is extremely similar to that of the previous chapters where we utilised fixed analytic potentials for the bar (e.g. Fig. 3.13). There is a clear nuclear ring inside the bar, which did not exist in the disc-only models due to a lack of any ILR. Around which is a void of gas, and an oval-like set of orbits tracing the outer bar structure. Beyond which are a set of arms, which trail off the bar ends and wind up with rotation. The pitch is highly circular in the mid-outer disc. Tracking the motion of the bar gives a pattern speed of approximately $\Omega_p = 45\mathrm{km\,s^{-1}\,kpc^{-1}}$, which is much higher than that of the bar in the disc only calculations. The OLR of such a bar occurs near 8kpc (see Figure 3.1b). If compared to the gas distribution in Figure 5.17 there appears a significant amount of substructure at this radius, which is similar to the features seen with static potentials. As with the disc barred model, the calculations at high resolution were severely hampered by the existence of the bar. The model shown in Figure 5.17 is the lower resolution calculation (1 million gas particles).

To further asses the nature of this bar we show the edge on appearance of the stellar disc

of the DbG, Bb and HbG models in Figure 5.18 (disc that formed a bar, bar-free disc+bulge and the bar formed in the live halo). The disc-only calculation is the narrowest vertically, appearing to not have changed much since the initial setup, despite the formation of a bar. The live-bulge calculation has a slightly flatter inner region compared to the disc only case, but the difference is marginal. Note the disc is greater extended radially compared to the other two as the disc is younger by around a Gyr, over which time the other models have expanded somewhat. In the live halo run, however, there is an inner lobed structure. This is similar to seen in observations of peanut/boxy bars in external galaxies and our own Milky Way (see the NIR image of the Milky Way in Fig. 1.15). The lobes appear to also be associated with the ends of the bar. In the figure the bar is oriented at approximately 60° to the line of sight, and as the bar is rotated to lie parallel to the line of sight (pointing out of the page) these lobes disappear, leaving just a bright central concentration. The bar orientation angle has to be very wide to see such lobes, with the 60° for the figure usually lying out of range of values determined for the Galaxy (but not always; de Boer & Weber 2014). The position of these lobes is strongly coupled to the bar length and the bar in these models is approximately 3kpc long, shorter than the Long bar (with a semi-major axis of around 4.5kpc). If we could increase the bar length in our model then the lobes in Fig. 5.18 would lead to a shallower bar orientation more in keeping with observations.

5.5 Simple kinematic longitude velocity maps

5.5.1 Method

As with Chapter 3, we must take into account the uncertainty in the observer's position and velocity by varying the parameters $l_{\rm obs}$, $V_{\rm obs}$ and $R_{\rm obs}$. However, as the morphology is highly time-dependant, similar to the mixed models of Chapter 4, we must also test multiple time-stamps for each simulation. We choose to do so in the range of 200-320Myrs of evolution of the gas disc. This is enough time to allow the majority of the molecular gas to form (seen to be $t \gtrsim$150Myr in Fig. 3.10) and for the disc to settle into a spiral pattern that will persist for up to a Gyr. The range in these parameters is the same as used previously (Table 3.2). Note that we must search the full range of $l_{\rm obs}$ values, as we cannot assume the disc is symmetric.

The method is the same as that described as in Section 3.6 with one small difference. As the gas in the simulation is less strongly associated with spiral arms, with some dense material shearing away from arms but maintaining a high molecular content, there is a chance that Equation 3.18 will scale poorly due to a clump of high density gas that lies very close to observing position. To rectify this we include a limiting factor, ϵ, in the denominator to limit emission from material near the Solar position. This changes the equation for synthetic emission from Equation 3.18 to

$$I_{i,\rm synth} \propto \chi_{i,\rm CO} / \left(d_i^m + \epsilon \right) \tag{5.14}$$

where m is a factor to be determined (making ϵ of dimensions kpc^m). To find appropriate values of m, ϵ and the longitudinal smoothing length of emission (see Sec. 3.6 for meaning) we again constrain to a map created from the TORUS radiative transfer code. In Figure 5.19 we show the fit

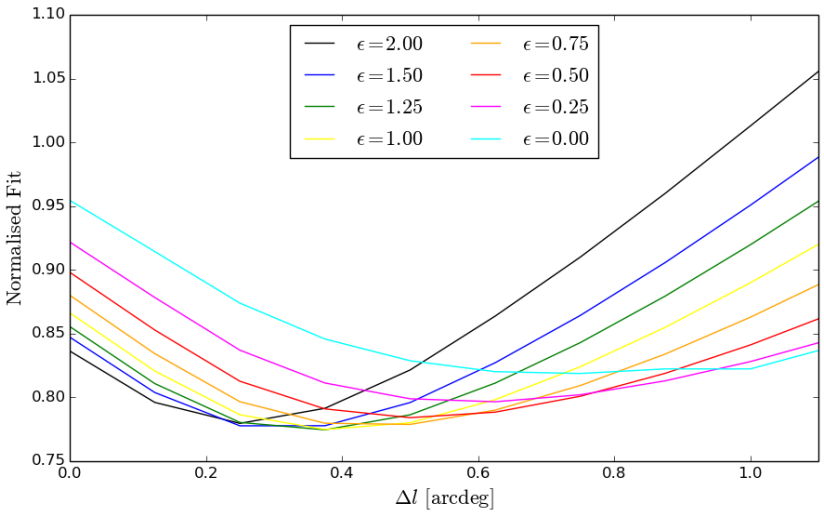

Figure 5.19: Best fitting values for the smoothing parameter (Δl, x-axis) and scaling limit factor (ϵ, different coloured curves) when fitting a simple l-v map to one created by TORUS. Best-fitting values are $\epsilon = 1$ and $\Delta l = 0.40°$, with the corresponding map and TORUS map shown in Figure 5.20.

statistic (MAE) from fitting to the ϵ (coloured lines) and Δl (x-axis) parameters. The yellow line in the figure provides the best fit to the TORUS map, giving $\epsilon = 1.0$ and $\Delta l = 0.4°$ (3 pixels). We maintain $m = 2$ from the previous section, finding it to be an equally good fit as previously (not shown). Interestingly the longitudinal smoothing parameter is somewhat smaller than the value when using analytic potentials presumably because the dispersion in the star particles already acts to smear out emission in some way, whereas much of the gas lies confined in the bottom of the potential wells when using potentials. The resolution in the gas is also somewhat lower here (3 instead of 5 million) which can also have an effect.

The corresponding best-fitting map for these values of m, ϵ and Δl is shown in Figure 5.20 (top) along with the TORUS CO map to which it was constrained. General features and emission scale is similar in both maps, though again there are some subtle differences. The gas seems over smoothed in the simple map. We tried a fit to observer's position using this and a slightly narrower smoothing, and the minima for $l_{\rm obs}$, $V_{\rm obs}$ and $R_{\rm obs}$ were found to be the same, implying this is of little consequence.

We reiterate that these maps are not to be used for a quantifiable comparison to observations, merely to fix some additional parameters before continuing with analysis, and allow a fast sweep through the many possible maps. Once best-fitting values of $l_{\rm obs}$, $V_{\rm obs}$, $R_{\rm obs}$ and time-stamp $t_{\rm bf}$, have been found for each model, we then use these to create TORUS data cubes of emission.

5.5.2 Maps of models

As an example of the fitting process to find the best fitting values of $l_{\rm obs}$, $V_{\rm obs}$, $R_{\rm obs}$ and $t_{\rm bf}$ we show l-v maps for the Bb model in Figure 5.22, across multiple time-frames spanning $200 < t < 300$Myrs. The behaviour of the fit statistic is shown in Figure 5.21 as a function of t, $V_{\rm obs}$ and $R_{\rm obs}$ where each point corresponds to a map in Figure 5.22. The red point indicates the best-fitting map

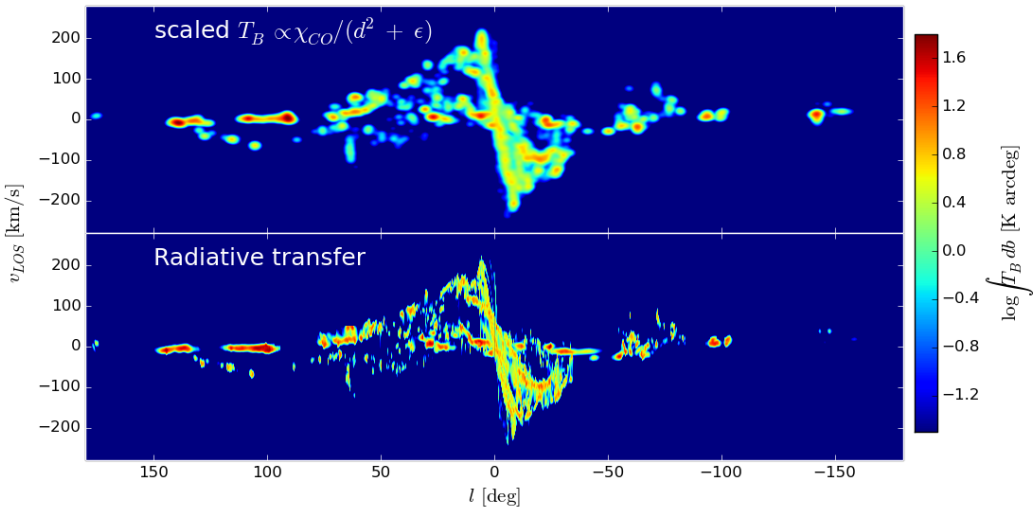

Figure 5.20: *l*-*v* maps made using the simple method outlined in the main text (top, $\epsilon = 1$) and using the TORUS radiative transfer code (bottom). The simulation contains a live bulge and disc component, and the observer is placed at $R_{\rm obs} = 7$kpc with $V_{\rm obs} = 200\,{\rm km\,s^{-1}}$.

(values indicated at the top of the figure). In this example a clear minima is seen in the fit statistic for the 226Myr time-stamp, with associated values of $V_{\rm obs} = 200\,{\rm km\,s^{-1}}$ and $R_{\rm obs} = 8.5$kpc. The $l_{\rm obs}$ parameter is not shown, as it contains little information without some clear reference point such as in barred simulations. The best-fit map in Figure 5.22 shows features that mark it out from the others, such as the Carina arm being correctly placed. The fit seems to worsen at later times. Inspection of the corresponding *l*-*v* maps indicates this is likely due to the inner disc material moving away from the position of the Inner Ridge seen in observations.

The process of fitting to $l_{\rm obs}$, $V_{\rm obs}$, $R_{\rm obs}$ and $t_{\rm bf}$ was performed for each model, with the exception of the DbG model which had not evolved sufficiently to show any features in the outer disc. The resulting best fit *l*-*v* maps are shown in Figure 5.23 with parameters for each model given in Table 5.3. The disc models (Db, Dc) have some of the poorest fit values, which appears to be due their lack of emission at high velocities in the inner disc. Some arm structures are seen in the outer disc, but these do not stray far from the local velocity ($v_{los} \approx 0\,{\rm km\,s^{-1}}$). The halo model that had formed a bar (HbG) seems to produce no emission in the outer galaxy at all, implying the spiral features seen in the top-down maps are too weak. This is similar to the analytic bar models, where outer arms rarely extended into the outer disc, and if they did were found to be too weak. The inner nuclear ring in this model produces a very strong feature in *l*-*v* space which is a strong function of bar orientation. For the best-fitting arrangement shown here the bar is angled at approximately $\theta_b = 50°$, similar to the values found in the previous chapters.

The remaining models, all with a live bulge component, provide a variety of *l*-*v* features. The heaviest disc model appears too turbulent in the inner disc. While it has an inner structure that is aligned similarly to observations, there is a large amount of material at high velocities and not matching the observed features. Coupled with the irregular arm structure seen in the top-down map, we conclude this (our heaviest disc) is a poor match to the Milky Way and do not produce any full radiative transfer *l*-*v* maps. Moderate-to-light mass discs (Bb, Bc, Bd, BbG and Hb) provide

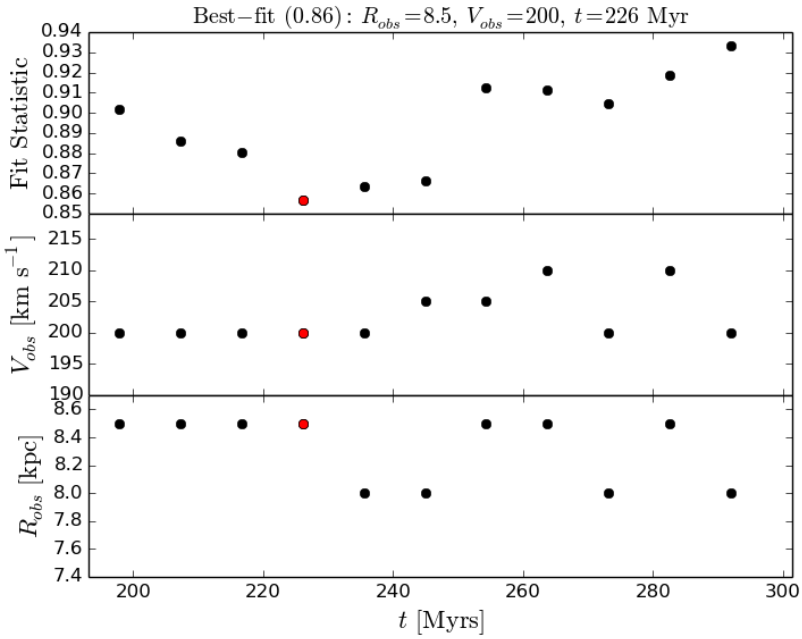

Figure 5.21: Variation of fit statistic with t, $V_{\rm obs}$ and $R_{\rm obs}$ for the Bb model. The best fitting time-frame is indicated by the red point, with values given at the top of the Figure. Corresponding l-v maps for each point are shown in Figure 5.22.

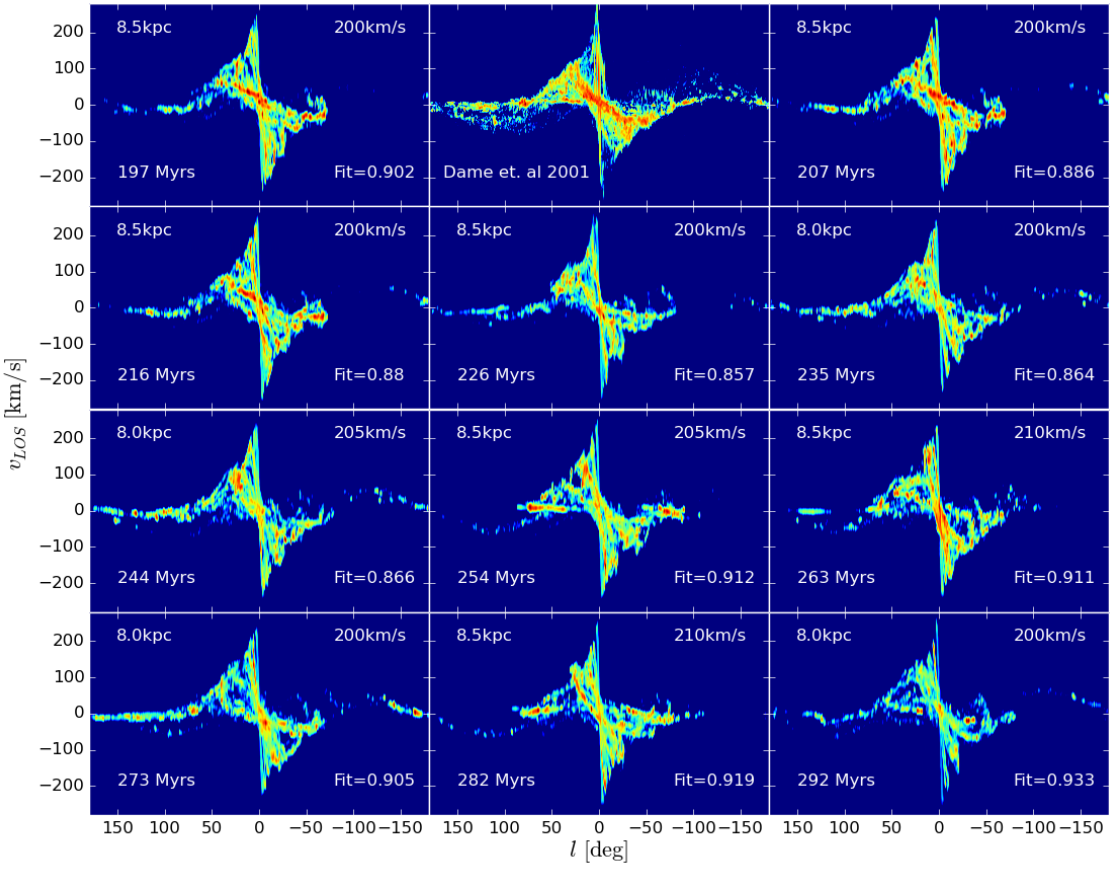

Figure 5.22: Evolution of kinematic l-v maps for the Bb model where each panel has been fit to the map of Dame et al. (2001) to find the best fitting values for $l_{\rm obs}$, $V_{\rm obs}$ and $R_{\rm obs}$ which are indicated in each panel. Each panel corresponds with a point shown in Figure 5.21. Top centre is the CO observational data for comparison.

Model	t_{bf} [Myr]	R_{obs} [kpc]	V_{obs} [km s^{-1}]	N	α [°]	$< \Omega_p >$ [km s^{-1} kpc^{-1}]	Fit stat.
Db	235	8.5	200	3	27	N/A	0.974
Dc	216	8.0	200	5	28	N/A	0.931
Ba	197	8.5	215	2	23	38	0.994
Bb	226	8.5	200	4	18	25	0.857
Bc	207	7.0	200	4	22	25	0.833
Bd	207	7.0	205	5	25	20-40†	0.768
BbG	216	8.0	200	3	13	35	0.879
Hb	216	8.0	205	4	26	30	0.925
HbG	197	7.0	200	2	8-25*	N/A	1.086

Table 5.3: Results of fitting to l_{obs}, V_{obs}, R_{obs} and t_{bf} for each model and the corresponding arm models fit. The mean pattern speed across the disc, $< \Omega_p >$, is quoted as in many cases the pattern speed was a function of radius.

* Arms are strongly wound around a bar and do not trace a logarithmic structure well

† Arm pattern is too flocculent to constrain rotation speed

a better agreement (and lower fit statistics). The lightest disc produces a near-uniform emission structure in the inner disc due to the flocculent nature of the arms. The Bb and Bc models provide good representations of the Carina and Local arms, while producing an Inner Ridge of the correct orientation. The remaining disc model, BbG, has good outer disc features but has an inner structure that reaches too high velocities. This could be due to the relatively low value of $V_{obs} = 200\,\mathrm{km\,s^{-1}}$, but this is needed to correctly place the Perseus arm. The inner feature of this model also appears straight in *l*-*v* space, as opposed to the other models where the feature curves as it moves into the fourth quadrant. This is because arm features in this model are closer in morphology to rings than to arms (left, Fig. 5.17) which show up as straight lines in *l*-*v* space.

The values in Table 5.3 show that models with the lowest fit statistic (< 0.9) have a high arm number ($3 < N < 5$). This implies the Milky Way emission features are best-fit by a high arm number, rather than the $m = 2$ value as implied by some studies. Interestingly we had some difficulty producing $N = 2$ armed structures. In the case of the Ba model the arms were highly irregular and appeared to be buckling in the outer disc, beyond the Solar position. The HbG model displayed a $N = 2$ pattern, but these arms are trailing from the bar ends and do not extend far radially. $N = 2$ arm models have been produced by studies in the literature, but tend to only be so when perturbed by some external body (Dobbs et al. 2010; Struck et al. 2011).

Pitch angles tend to be around $\alpha \approx 20°$. While high, this is not outside of the uncertainties in Milky Way models. Values as high as these were ruled out when using fixed potentials because there appeared to be voids of gas in the disc due to the large arm separation, which provided a poorer representation of *l*-*v* features. However, when using a live disc there is a considerable amount of branches and inter-arm material, which allowed for the arms to fit to additional structures in *l*-*v* space. We estimate an uncertainty of around 2° for α, gauged by varying the extent of the disc and material (gas or stars) used in the arm fit.

The pattern speeds in Table 5.3 have large uncertainty, and are only mean values as the pattern speed is seen to decrease with radius in all disc models. Regardless, the arm pattern speeds appear high compared to values inferred for the Milky Way and found when using analytic poten-

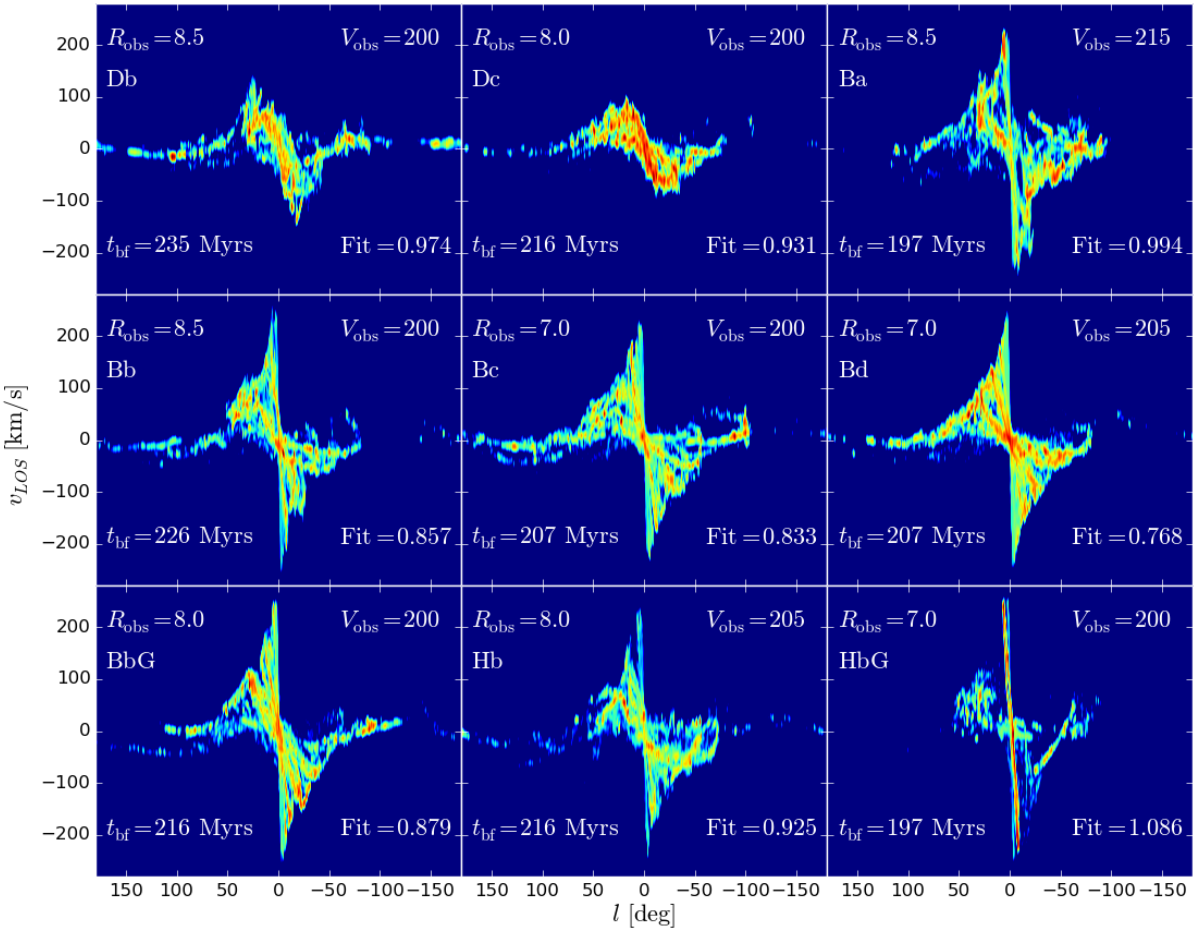

Figure 5.23: Best fitting l-v from the simple fitting procedure to find l_{obs}, V_{obs}, R_{obs} and t_{bf} for models Db, Dc, Ba, Bb, Bc, Bd, BbG, Hb and HbG. Best fitting values are given in each panel, along with the value for the fit statistic used to constrain them. V_{obs} and R_{obs} are in $\mathrm{km\,s^{-1}}$and kpc respectively.

tials ($\Omega_{sp} \approx 20\mathrm{km\,s^{-1}\,kpc^{-1}}$). Values for bars lie between $30\mathrm{km\,s^{-1}\,kpc^{-1}} < \Omega_p < 45\mathrm{km\,s^{-1}\,kpc^{-1}}$, though we could not perform any barred simulation at high resolution for more than 90Myrs due to computational difficulties. The best fitting radius, R_{obs} varies across the models, with no clear preferred value. For instance the Bb and Bc models, which both provide a good match to the l-v data, have best-fitting values of 8.5kpc and 7.0kpc respectively. The best fitting observer velocities appear systematically lower than those of the analytic potentials and the approximate value for the Solar position ($220\,\mathrm{km\,s^{-1}}$). We believe this to be due to the nature of the density distributions used to set the stellar material being slightly different to those of used in Chapter 3. By comparing the model rotation curves of Figures 5.2 and 3.1 at the Solar radius ($R \approx 8$kpc) the models in this chapter appear to pass through the data points of Sofue (2012) in the Bd, Bc and Bb models whereas the model from Chapter 3 appears to over-estimate the local velocity by $10 - 20\,\mathrm{km\,s^{-1}}$. As such, to match the velocity of local material the value of V_{obs} can be somewhat lower, in keeping with the rotation curve of the live stellar disc. The exception is the Ba model, whose rotation curve also over-estimates the local velocity, hence the higher best-fit value for V_{obs} (Table 5.3).

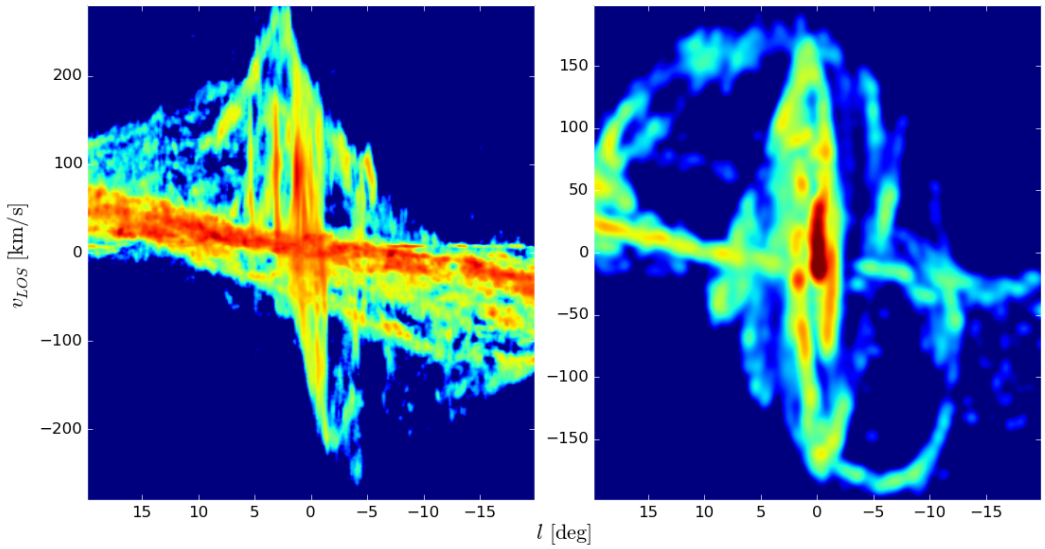

Figure 5.24: Inner structure of the gas disc in the DbG model (right) due to the creation of a bar, angled at $\theta_b = 45°$. Features are similar to those seen in observations (Dame et al. 2001, left). Note the velocity range is slightly smaller in the right panel.

We have not shown any values or maps for the BbL model as they are extremely similar to those of the Bb model, with only slight variations in the best fitting values of $l_{\rm obs}$, $V_{\rm obs}$ and $R_{\rm obs}$.

Regarding the barred models specifically, we do not perform any radiative transfer calculations using these models. They are either too low resolution, or did not run for long enough to develop sufficient structure. There is one point of merit we wish to discuss however. In the bar formed in the DbG model, that had only ran for 85Myrs with gas, there is internal structure that is very similar in l-v space to that observed in CO data. The internal structure is shown in Figure 5.24 (right) alongside that seen in observations (left). The bar is angled at $\theta_b = 45°$ and the synthetic l-v map is shown over slightly narrower velocity range (remember that without a bulge, disc-only models underestimate the velocities in the inner disc). While by no means a perfect reproduction, this is perhaps the closest to the CMZ out of all of our models. In both maps there is a bright vertical inner region that has a width of several degrees, with some emission structures falling away from the peak values as you move away from $l = 0°$. The structures directly around the CMZ in the model appear at too high velocities, indicating the structure may extend too far radially, which could be reduced with the addition of a more compact inner bulge. Different values of θ_b were investigated, but none lessened this effect. This model has the obvious drawback however of having very weak outer arms, though higher resolution calculations, where arms should be more prominent, were not feasible.

5.6 Radiative transfer emission maps

Using the methods discussed we have narrowed down the full range of models in Table 5.2 down to seven that we wish to analyse further and create emission maps, now taking into full account optical depth effects. These models are the majority of the bulge-disc calculations (Bb, Bc, Bd,

BbG, BbL) and a single live halo model (Hb). However, in instances of fitting the simple *l*-*v* maps there were some double-minima seen in the fit which gave a considerably better match than the other models. Specifically we have included another Bc time-stamp, which is taken at a much later time (292Myrs, rather than the 207Myrs of best fit model) and provided a better fit than the Bd and Hb models. Some other instances such as this occurred, but none so clearly a good fit.

The procedure for creating *l*-*v* emission maps is identical to that outlined in Section 4.3. We use the TORUS radiative transfer code to create cubes of brightness temperature as a function of latitude, longitude and line-of-sight velocity which are the integrated over latitude and quantitively compared to the CO map of Dame et al. (2001). A turbulent velocity of $4\,\mathrm{km\,s^{-1}}$ is again added to the line width to better match the observed features. Sinks and stars are all discarded before the creation of maps.

5.6.1 Column densities

In Figure 5.25 we show typical column densities as a function of latitude and longitude in the second quadrant of a live-disc calculation, which can be directly compared to the fixed potential case (Fig. 4.6). The disc has been aligned such that similar arm structures are present, with a near, mid and far arm are all present in the quadrant. The near arm appears clearly as an emission feature that is vertically extended up to $b = \pm 2^\circ$, similarly to the fixed potential case. The remainder of the material is somewhat different. There is no clear narrow band of material centred at $b = 0^\circ$ as for the fixed potential, with instead column densities appear well distributed with latitude. This is because the live stellar disc has a great many more homogeneities, and the vertical velocity dispersion in the disc keeps material away from the mid-plane which was a drawback of the previous models. The H I appears very uniform with no strong asymmetries or over-densities. Peak values of H I density are much lower than the fixed potential case, presumably because of the increased dispersion around the mid-plane. Molecular gas densities are similar however, as the densest gas is limited in molecular abundance by limiting factors (e.g. χ_{CII}) while the general gas density can continue to increase. Material is still confined to lower latitudes than that seen in our own Galaxy, where molecular and atomic gas can be seen to extent out to $b = \pm 5^\circ$ (Heyer et al. 1998; Taylor et al. 2003). Stellar feedback may be necessary to produce this extended vertical structure (Duarte-Cabral et al. in preperation).

The molecular column densities for this quadrant are shown in Figure 5.26, to be compared with similar plots for fixed potentials (Fig. 4.8). These appear to give a poorer representation of the column density profiles in observations compare to those of Fig. 4.8. This could be due to the CO is being under-produced with respect to H_2 in comparison, though this seems unlikely as the chemistry for both codes is identical. It is possible that this is a resolution effect, and that the slightly higher resolution of the fixed potential calculations allowed for a greater resolution of the denser regions, more accurately following the molecular content in these regions (5 million as opposed to 1 million particles). The other possibility is that the dense gas regions inside these live disc calculations are less efficient at creating and/or shielding molecular gas compared to smooth potentials. This may be because these transient arms are not as consistently strong as the analytic potentials and that their transient nature is disruptive to the presence of molecular gas. The column

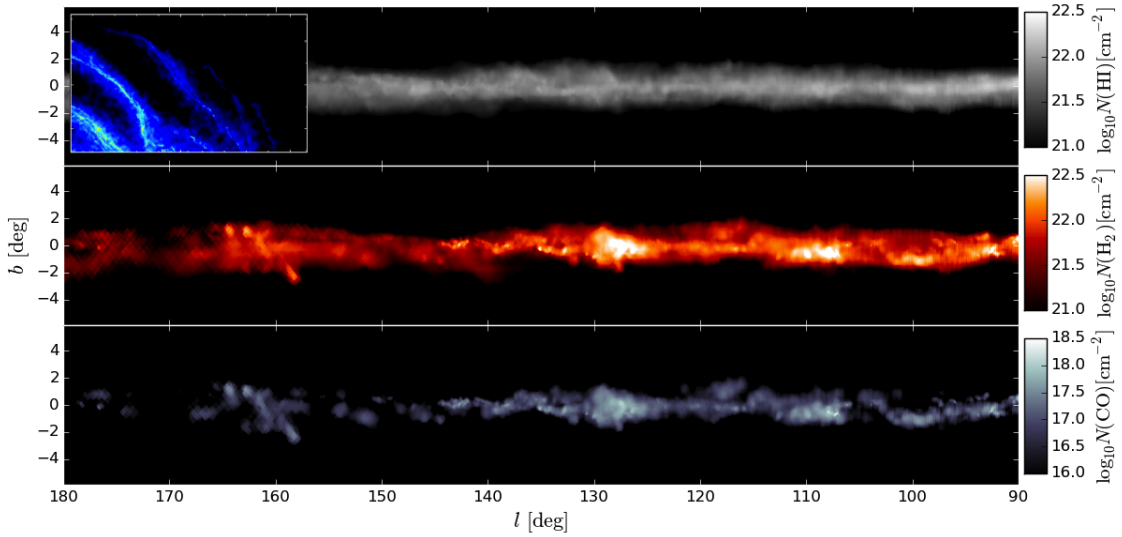

Figure 5.25: Column density of H I (top), H_2 (middle) and CO (bottom) of the second quadrant of the Bc model, shown in the insert.

densities do however provide one improvement to those of the fixed potentials. They have column densities that reach into much lower H_2 densities. The fixed potential data by comparison decayed very rapidly around $N(H_2) \approx 10^{20}\text{cm}^{-1}$.

5.6.2 Emission maps

We show all seven of our best-fitting CO emission maps in Figure 5.27, and the observational data alongside for comparison. The fit statistic has been re-calculated now that the emission correctly takes into account emission and absorption effects, and correctly computes the "size" of the features. Encouragingly, the fit statistic follows the same trends across the maps as when we used the simple map creation tool. The three best fitting maps (in order) are the Bd, Bc (both) and Bb models. The BbG and Hb models fair significantly poorer in comparison.

The lighter gas disc is now shown (BbL) where the gas had half the fiducial mass. The emission features are significantly weaker than the Bb counterpart. While the strength of the emission is weaker over-all, more in line with observational values, there are clear gaps in *l*-*v* features that are not present in the Bb model. We conclude that the fiducial disc mass (or somewhere between) is a better value for reproducing emission features.

While each model still has merits, there are clearly three that can be dropped from analysis: the BbL model (as stated above), the Hb and BbG models. The evolved disc model (BbG) provides a good reproduction of the Carina arm, Perseus arm and some of the Local arm. The inner disc however, is poorly reproduced. The inner ridge feature is angled too steeply in *l*-*v* space, and seems to be tracing the ring-like inner structure of the disc rather than spiral arms. The lack of a full Local arm, or any Outer arm feature, also undermine this model. As expected the live-halo model (Hb) is similar to the static halo case (Bb). There is some marginal outer arm emission and a seemingly complex inner structure, though this appears more complex in the Hb model. Overall the Hb model is a poorer version of the Bb model, with weaker arm features, a misshapen

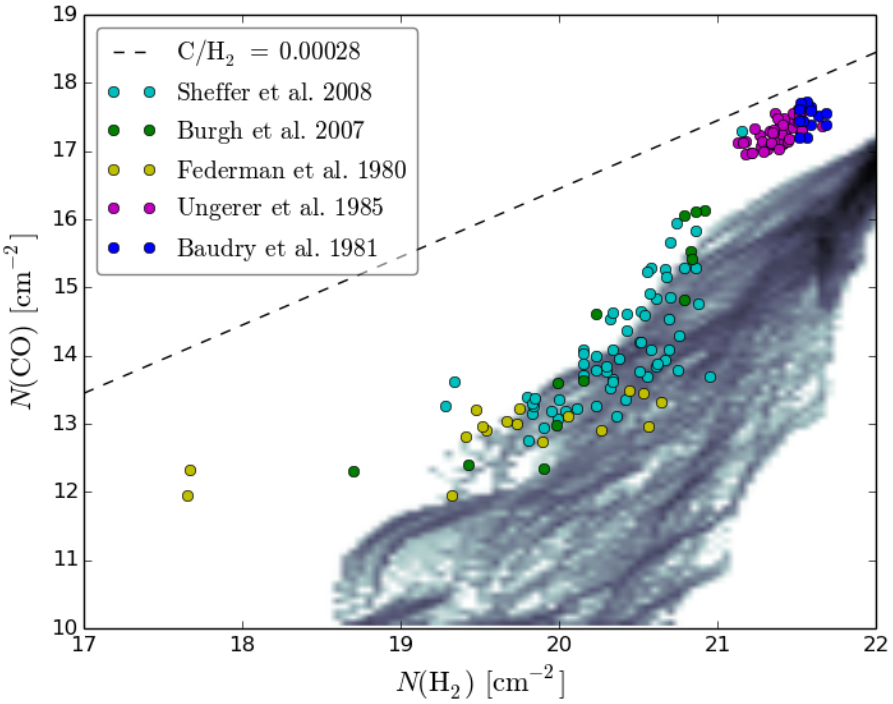

Figure 5.26: Column density of H_2 and CO for the second quadrant of the Bc calculation shown in Figure 5.25. Several sources of observational data for the second quadrant are shown for comparison.

inner structure, poor reproduction of the Carina arm and poorer fit statistic. This could be due to additional dynamical instability possibly seeded by an unresolved dark halo so we don't consider this model further.

The remaining four models; Bb, Bc(×2) and Bd, all provide a good fit to many of the observed features. All produce the Carina, Perseus, and Local arm material, though some better than others. For instance, the lightest disc model appears to show extremely weak arm structure that can be assigned to Perseus, but it is barely visible in the second quadrant. The Inner Ridge is well produced in the Bc(292Myr) and Bd models, and in the case of the former this smoothly transitions into the Carina arm. The Fourier analysis of these models favours a 4-arm fit (5 for the lightest case), indicating that Galactic structure is best fit by a higher arm number, rather than say a 2-armed one.

So far we have limited ourselves to discussing the emission structures seen in CO. We provide a single map of the H I emission for comparison, using the Bc(207Myr) model. The emission here is a much better representation of that observed (lower panel, Fig. 5.28) than the fixed potential calculations. The arm structures are traced by the emission, similarly to the CO (Fig. 5.27) though there are many more weaker arm features visible. This is very different to the analytic potentials, whose emission structure did not show any strong correlation to the location arms and CO emission for our standard surface density (Fig. 4.3). This is likely because the gas is less confined to the plane when using a live disc, and so it decreases the optical depth and hence H I absorption along lines-of-sight to the arms. The emission strength is also comparable to observed values, with peak emission features appearing near 200K. The structures here appear very fine

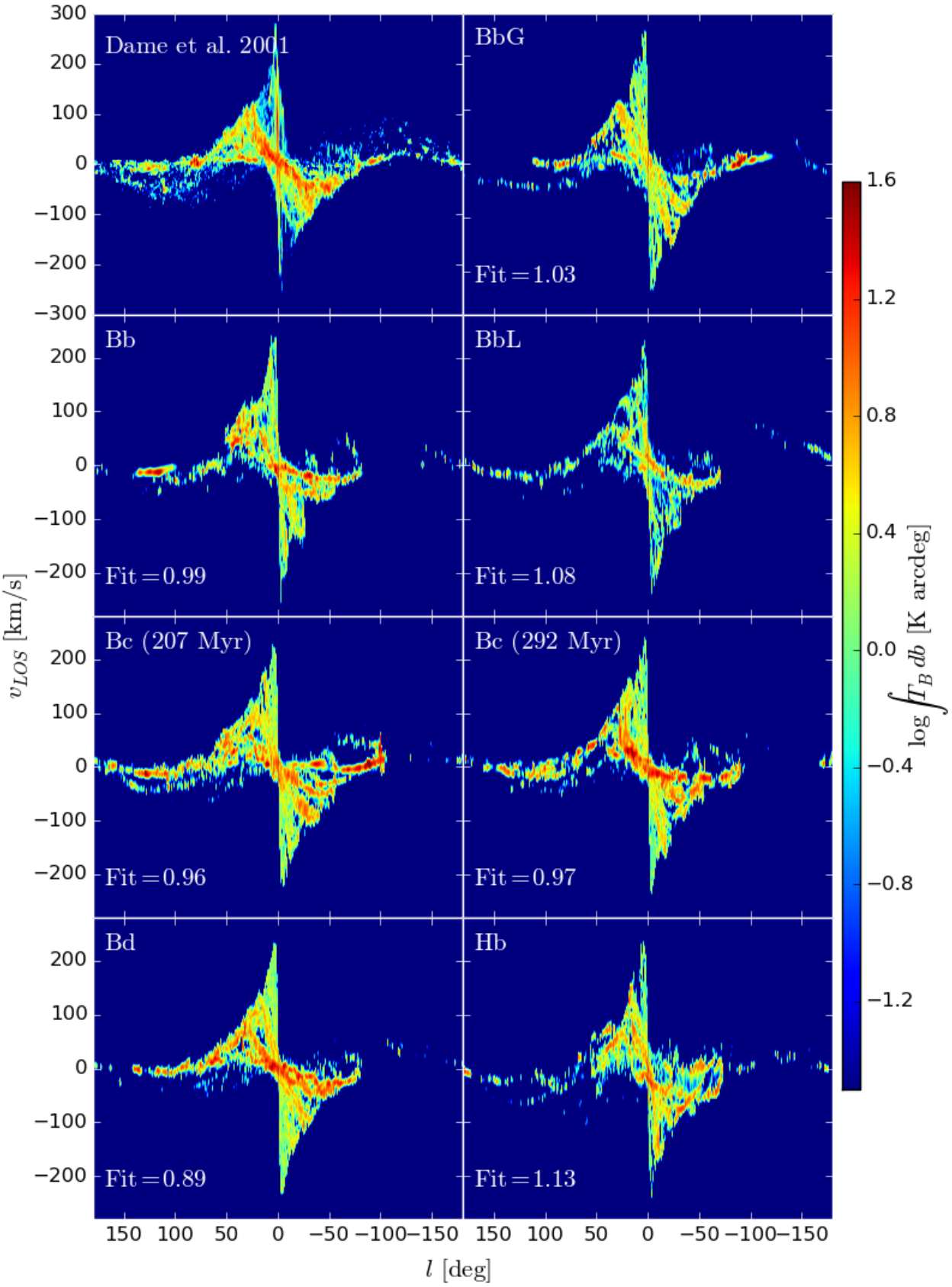

Figure 5.27: Seven CO emission maps made using TORUS where time-fame and observer coordinates have been fitted to observational data (top left for comparison, re-scaled slightly to match synthetic maps). The models include the Bb, Bc, Bd, BbL, BbG and Hb mass configurations, and an additional Bc that also provided a good match to the data.

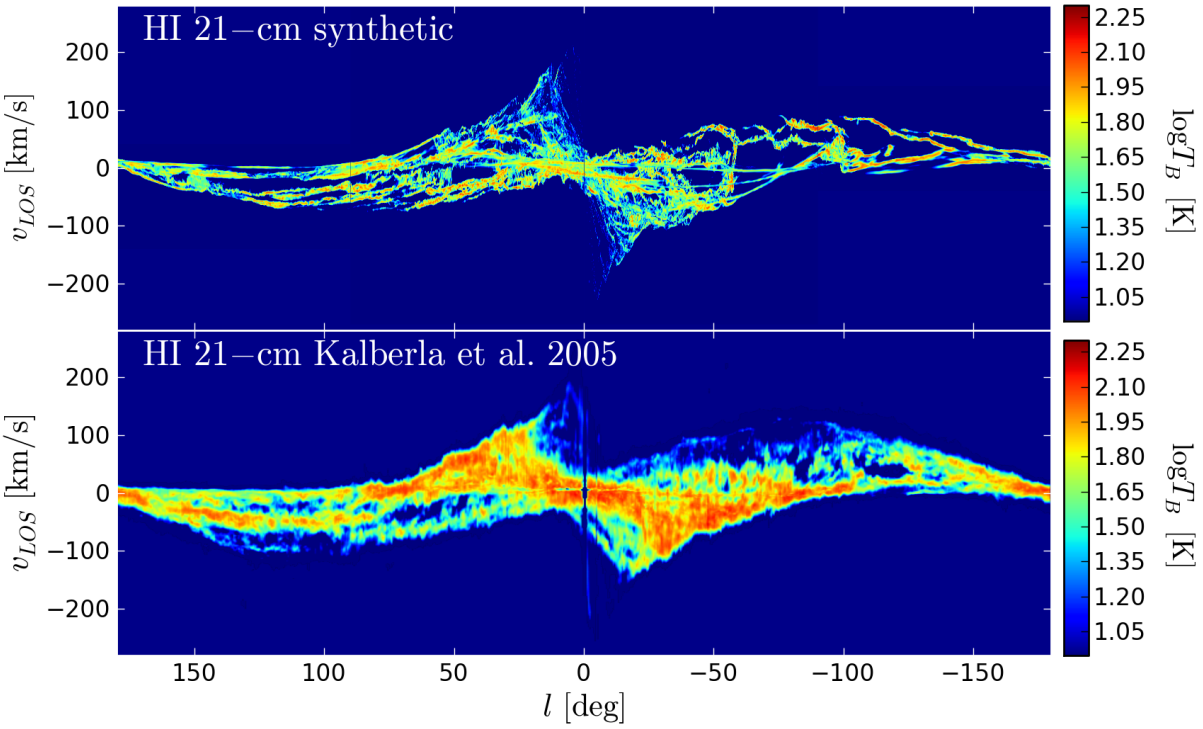

Figure 5.28: Emission map of the H I 21-cm transition created using TORUS. The input model is the 207Myr Bc model, the same as the second map in Figure 5.29. Observational data from Kalberla et al. (2005) is shown for comparison.

compared to observations as we omitted the turbulent broadening present in CO. Arm features can be clearly seen in the second quadrant, even without the broadening to smooth features. The Perseus, Local and Outer arms all appear in the synthetic map. The inner disc at the location of the CMZ shows no emission feature, similar to observations, indicating that in our simulations CMZ hosts just molecular material and a only minor traces of atomic gas.

5.7 Discussion

Through the work presented in this chapter we have shown that it is possible to produce many of the observed features of the Galactic CO emission using a system of N-body particles to represent the stellar distribution. As in Chapter 4, we will use our four best-fitting maps as a basis for our discussion. In Figure 5.29 we show four maps, from top to bottom: Bb, Bc(207Myrs), Bc(292Myrs) and Bd, organised by disc mass. In the left column we show the top-down gas distribution, and in the right the TORUS CO l-v emission maps, created at the best fitting values of $l_{\rm obs}$, $V_{\rm obs}$ and $R_{\rm obs}$. In each frame we also label significant arm features, with the same nomenclature as used for the Milky Way.

In the heavy disc (Bb, top panel) model the inner l-v features are similarly inclined to those seen in the observations, namely the Inner Ridge is present, though it is not as clearly defined. The top-down map shows this is a combination of a far and near arm feature. The near arm (labelled Carina) appears weaker than the far inner arm (labelled SCC) and so emission from the far arm can pass through the near arm. This allows for the reproduction in the Carina Arm, which requires an

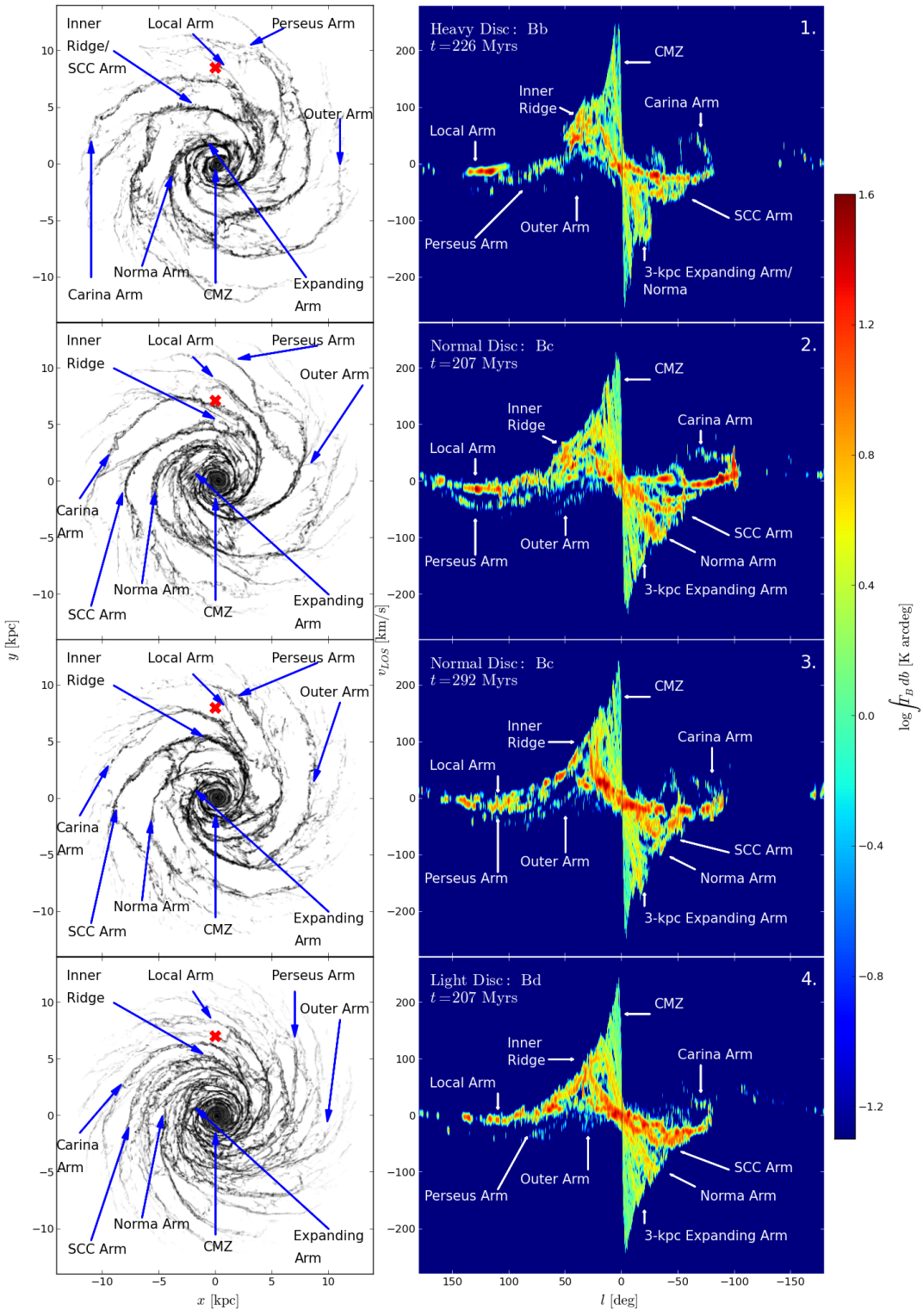

Figure 5.29: Our four best-fitting CO radiative transfer *l*-*v* maps from Fig. 5.27 with their *x*-*y* counterparts. The top-down maps only show gas material that is seen in CO *l*-*v* space; that of the highest density. The cross indicates the observers position (which differs between models). SCC refers to the Scutum-Centaurus-Crux arm in the 4-armed paradigm of the Milky Way, also referred to in the main text as the Inner Ridge when viewed in *l*-*v* space. Arrows indicate locations of prominent features in *l*-*v* space.

arm to be very close to the observers location, while avoiding large amounts of emission at local velocities in the range $|l| < 50°$. This was a persistent problem in the maps created from synthetic potentials. The uniform and unbroken nature of the arms made producing the Carina Arm and Inner Ridge impossible. This model also has a looped arm features at very low velocities similar to the 3kpc-Expanding Arm, though is angled steeper in l-v space than observations. A Local Arm feature has been produced by a spur of the Carina Arm, lying very close to the red-cross in the top-down map. This has been suggested by other studies; that the Local Arm is in fact some spur or inter-arm structure, rather than a primary arm (though the picture is still not clear; Reid et al. 2009, Xu et al. 2013). The caveat of this model is the outer arm structure. Both the Perseus and Outer arms, while clear in the top-down map, are weak or incorrectly placed in l-v space. The Perseus arm appears at velocities too similar to the local values, making it nearly indistinguishable from the Local Arm in CO emission. The Outer Arm can barely be seen in emission, its presence only given away by a couple of dense pockets of gas.

The second model (Bc) has a slightly lighter disc, and appears a much better fit for many of the l-v features. The arms in the second and third quadrant are an especially good reproduction of observations. In Figure 5.30 we show a zoom in of this region shown alongside the observational data. The Local, Perseus and Outer arm features are all reproduced and have comparable line-of-sight velocities. The emission is however still somewhat higher than that observed, a problem with all maps produced in this thesis. The top-down map shows the Local and Perseus arms are a bifurcation of the same arm. The Carina hook structure is reproduced, but is present at too great a longitude compared to the observations. This feature can be made to better match, by increasing $R_{\rm obs}$, but at the expense of the other arm features. The Inner Ridge of this model is somewhat poorer than the other models. There is even a void of emission at approximately $l = 20°$ $v_{los} = 80\,{\rm km\,s^{-1}}$where clear emission is seen in observations. The incorrect reproduction of the Inner Ridge is due to the SCC Arm tracing a near-circular arc in the inner disc, which is seen as the steep straight line in the l-v map. In the other models the SCC arm clearly "winds", i.e. has a non-circular shape, so is seen to be angled in l-v space.

The second Bc model, created at approximately 100Myrs after the first, appears to be the best reproduction by-eye (the fit-statistic favours the lightest model however). The model shows the Carina, Perseus, Outer and Local Arms as well as an Inner Ridge that is aligned similarly to observations. Local material is again formed by a spur off the Perseus Arm. The Perseus Arm itself is hard to differentiate from the Local and Outer Arm features, which is the main problem with the model. All arm structures in the second quadrant appear at too shallow velocities, implying $V_{\rm obs}$ is incorrect or that the model rotation curve is too shallow near the Solar Radius. This model offers the best reproduction of the Inner Ridge and Carina arm simultaneously. The Carina Arm appears to branch away from the SCC Arm (the source of the Inner Ridge) allowing it to be correctly placed in l-v space without it causing spurious emission in the inner disc, a problem the symmetric fixed potential models persistently encountered. There also appears to be a 4-armed outer structure, with a very strong 2- armed inner structure, which adds weight to the models arms including a strong stellar 2-armed component and weaker 4-armed one in the gas/dust and young stars (Drimmel 2000; Churchwell et al. 2009).

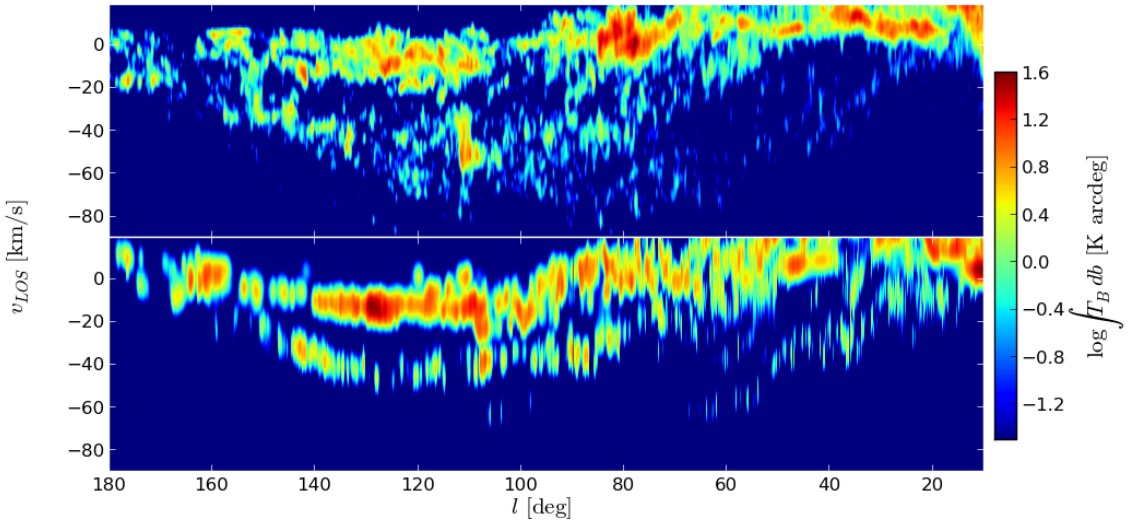

Figure 5.30: Zoom in of the first and second quadrant arm features in CO from the 207Myr Bc arm model (second row, Fig.5.29). Observational data is shown in the upper panel for comparison, the emission strength of which has been increased slightly to be on the same scale as the synthetic map.

Our final model has the lightest disc, and the lowest fit statistic. As with the previous model, there is a good reproduction of the Inner Ridge, Carina Arm and Local material. The Perseus and Outer Arms appear too weak, and there is a significant amount of emission in the inner disc ($|l| < 30°$). While common to all models, this excess emission is especially evident here due to the general flocculent nature of the spiral arms. There is no clear inner disc structure and the many smaller arm features in the inner disc are seen in molecular emission, appearing as a great swath rather than distinct arm features. The flocculent nature is also to blame for the weakness of the Perseus and Outer Arms beyond the Solar radius. It is somewhat alarming that the emission features can be well reproduced by a model with seemingly no clear dominant spiral mode (Fourier analysis indicates $m \approx 5$). While the fit statistic indicates this model is a good fit, it is likely because there is little emission seen in the incorrect place. Coupled with the correct reproduction of the Inner Ridge, Carina and Local Arms, this explains the goodness of the fit. The arm features however seem too weak in the outer disc for this model to be a correct reproduction of our Galaxy. Arms are barely visible in the outer disc, be it in CO or general gas density, meaning they would also not be visible in atomic emission which is simply not the case in observations (see the lower panel of Fig. 5.28).

Overall, the fit statistic favours the light disc model, Bd. However, the features appear too flocculent in the outer disc, and so we favour the second best fit model, Bc. The Bd model provides an excellent fit to the strongest emission regions, that of the Inner Ridge, while the Bc reproduces all other arm features. As the latter arms are weaker in emission in comparison, the fit statistic is lower for the model that fit the Inner Ridge but not the arms, Bd.

5.7.1 Comparison to calculations with fixed stellar potentials

It appears that using a live-stellar distribution does a better job than the fixed analytic potentials in many regards. The irregular arm structures created by the live stellar system are able to match emission features simultaneously, such as the Carina arm and Inner Ridge, while symmetric logarithmic spiral arms could not. For example, in the previous Chapters the second quadrant could be fit by moderate to large pitch angles, whereas a much smaller value was needed to fit the Carina feature. The arm numbers of the best fitting models are similar to those suggested by the previous chapters, favouring a 4-armed gas structure to best match the observations. The pitch angles are somewhat higher than inferred previously ($18^\circ < \alpha < 25^\circ$), which are higher than the standard Milky Way models (Vallée 2005). High pitch angles are not uncommon in N-body simulations (Wada et al. 2011a; Grand et al. 2013) whereas low values are seemingly hard to create without the arms dissipating. Pattern speeds appear to be a function of radius in nearly all cases, with mean values for arms ranging from $25\mathrm{km\,s^{-1}\,kpc^{-1}} < \Omega_p < 35\mathrm{km\,s^{-1}\,kpc^{-1}}$, also similar to values found in other studies (Grand et al. 2012; Baba et al. 2013) but higher than those found in the previous chapters. The arms appear material, unlike the steady density waves implied by theories, and material tends to reside in the arms until they shear apart. It may be the case that the Galaxy has no fixed pattern speed, and its spiral arms are also material in nature. It is not unheard of for other galaxies to have pattern speed that decrease with increasing radius (Meidt et al. 2008; Speights & Westpfahl 2012). Bar features that were produced displayed pattern speeds of $30\mathrm{km\,s^{-1}\,kpc^{-1}}$ (for the disc only, thin bars) and $45\mathrm{km\,s^{-1}\,kpc^{-1}}$ (peanut/boxy bars).

The total strength of CO emission is more in line with that seen in observations (i.e. weaker) than the previous models, which tended to create extremely bright arm emission structures. The increase in inter-arm features also makes lower strength features corresponding to moderate density material more common. The fit statistic for the emission maps of models is calculated in exact same way as in Chapter 4 and the best-fitting models here provide a systematically better fit than those with fixed potentials (best fitting values give ≈ 1.05 for potentials and ≈ 0.95 for live discs).

There are some drawbacks to this method however. Each model has far too much emission in the inner disc. This is due to all models here having an inner bulge, which creates high density gas flow around the centre. The initial gas profile, that increases towards the centre, may also be a flaw in the models. The fixed potential calculations effectively had a hole in the inner disc, which resulted in a large dearth of emission at high velocities inside of $|l| < 20^\circ$. High gas density was still seen in the inner disc however, but was solely aligned on the x_2 orbits of the bar. As such we believe either an inner bar structure is needed to sweep up molecular material in the inner disc, or that gas density is greatly reduced by some other mechanism. Bars were reproduced however, both in cases with and without an inner bulge. The bulge-free models displayed tentatively good features in the CMZ, but unfortunately were computationally difficult and produced weak outer arm features. The other family of bars reproduced the weak boxy/peanut nature of the Milky Way's bar, but had similar problems as the analytic bars of the previous section (tightly wound arms and very strong nuclear rings at the ILR).

5.8 Chapter summary

In this chapter we have shown simulations of the stellar and gaseous components of the Milky Way, rather than using a set of fixed analytic potentials to represent the stars as in Chapters 3 and 4. Various arm and bar morphologies were formed in the stars, with arms appearing transient and material in nature rather than as density waves. The arm number is seen to increase as the disc to halo mass ratio decreases, with arm numbers found to range from $2 \leq N \leq 5$. We perform fits to logarithmic spiral features, finding pitch angles in of $18^\circ < \alpha < 25^\circ$ and pattern speeds in the range of $20\mathrm{km\,s^{-1}\,kpc^{-1}} < \Omega_p < 38\mathrm{km\,s^{-1}\,kpc^{-1}}$ which decreases with radius rather than maintaining a constant value. Both pattern speed and pitch angle are within the range of values inferred from observations, though in the higher range.

Using the molecular gas in these simulations we then created synthetic *l*-*v* emission maps. A simple method is used to find a best-fitting time-frame and observers coordinates, which are used to reject some outlying models and provide input parameters for the full radiative transfer maps. We find moderate mass discs with a live bulge-disc component provide a good match to the observations, with 4-armed spiral patterns that reproduce many of the arm features. These arms provide a better fit than those using fixed potentials (Chapter 4) and provide a lower fit statistic. The arm features of the Milky Way are thus found to be best-fit by a dynamic and transient disc, displaying a 4-armed pattern in the gas with a pitch angle of approximately 20°.

Some models also formed inner bars, though not in the case of our best fitting models due to the strong inner bulge. We believe a bar is necessary to amend the main flaw in these models; the excess emission at the Galactic centre. It may be that a calculation with a smaller bulge is needed to allow for a bar to form while keeping a distinct outer arm structure.

6

Conclusions and future work

"From out there on the Moon, international politics look so petty. You want to grab a politician by the scruff of the neck and drag him a quarter of a million miles out and say, 'Look at that, you son of a bitch'."
– Edgar Mitchel, Apollo 14 astronaut, People magazine, 8 April 1974

6.1 Thesis conclusions

This thesis has focussed on lifting the veil on the shape of our Galaxy, a problem that has plagued observers and theorists alike for decades. The method to do so was to utilise numerical SPH simulations to model the ISM evolution in a Milky Way-like disc. Many different Milky Way models were employed, investigating a wide variety of morphologies of the bar and spiral arms. Using these simulations, synthetic observations (primarily of CO emission) were then created using a radiative transfer code which could be directly compared to observational data. By finding models that provide a good representation of the emission features of our Galaxy it was inferred whether the morphology of the input Galaxy model was a good representation of the Milky Way's morphology. Whilst other authors have produced individual synthetic maps from simulations, here we extend this idea to using multiple simulations to carry out a systematic study of the available parameter space and use a full radiative transfer treatment to replicate observations.

In Chapters 1 and 2 we set the scene of the problem at hand and present the primary numerical tool used throughout this work; SPH. This includes the specialised physics and chemistry incorporated that allows for ISM cooling and molecular gas formation, which is key for creation of the synthetic observations.

In Chapter 3 results are presented where the Galaxy is assumed to be grand design in nature,

i.e. that the morphology is fixed and unchanging in nature with distinct arm and bar features. The gas in a Galactic disc is subjected to a variety of different analytic potentials designed to represent the stellar gravitational field of the main morphological components. Separate simulations using arms or bars are first performed, investigating the effect of pattern speeds, bar orientation, arm number and arm pitch angle on structures seen in longitude-velocity space. Best-fitting values for the bar favour pattern speeds of $50 - 60 \mathrm{km\,s^{-1}\,kpc^{-1}}$ and orientations of $\approx 45°$, while the best-fitting values for the arms are a pattern speed of $20 \mathrm{km\,s^{-1}\,kpc^{-1}}$ and a pitch angle from $10° - 15°$. Some of the parameters showed clear best fits, such as arm pattern speed, while others were harder to constrain, such as the pitch angle. Bars and arms on their own could not provide a good match for observations, with the position of resonances limiting the radial extent structures could be sustained in the gas. Specifically, a fast bar was needed to produce features in the inner disc, while arms of a much slower pattern speed were needed to observe arms beyond the Solar radius. The observer's position and velocity were also variables in the modelling as they could heavily impact the position of emission features. While not the subject of our investigation, best-fitting models showed a good agreement with literature values.

Synthetic observations in Chapter 3 were calculated in a very simple manner. In Chapter 4 this is greatly improved by use of a radiative transfer code which explicitly calculated the emissivity and opacity throughout the model galaxies. Synthetic observations showed that molecular emission features were highly sensitive to the surface density of the gas, which directly determines its column density and optical thickness. Emission from arms and bars was visible in our fiducial gas disc, though the peak brightness temperatures were somewhat greater than those observed. H I emission on the other hand did not trace the morphology well. This is believed to be caused by the gas settling into a very narrow range of latitudes, which causes very high atomic gas column densities, a problem induced by the simplistic nature of the potentials. This was not an issue with CO, as the molecular gas density is so much lower than that of the H I. Simulations were then performed with the best-fitting arms and bars from Chapter 3. Many of the emission features from the Milky Way were reproducible, such as various individual spiral arms. There was however no model that could fit all features simultaneously. The primary difficulty was in reproducing the Carina arm in the fourth quadrant and the inner molecular ridge of material with the correct orientation in l-v space inside $|l| < 50°$. In order to match Carina using fixed logarithmic spirals the arm must pass in between the observer and the Galactic centre, creating a great swath of emission and local velocities ($v_{los} \approx 0 \mathrm{\,km\,s^{-1}}$), which is not seen in observations. Either the molecular gas in this arm must be greatly reduced, by this arm perhaps being weaker in general to others, or the shape must stray from logarithmic in the Solar vicinity. The arm number, perhaps the key parameter in mapping the Galaxy, was not clearly constrained. Two armed models provided a better fit numerically, but could not fit all observed features simultaneously. Conversely four armed models could reproduce all features, but inadvertently produced spurious emission where it was not required, worsening the quality of the fit. A such we conclude a four armed barred model is a good representation of our Galaxy, but a key ingredient is needed to remove or amend some of the spurious emission features.

In Chapter 5 a different approach is taken where the analytic potentials representing the

stellar component are replaced with a system of N-body "star" particles, whose evolution determines the gravitational forces experienced by the gas. The resulting arm features are transient and vary greatly in shape, displaying multiple branches, inter-arm features, and kinks. The number of arms created is strongly correlated to the disc to halo mass ratio, with arm numbers ranging from two to five and in some cases producing effectively a flocculent disc. Pitch angles tend to be rather wide compared to those found using analytic potentials, with values around 20°. These arms tend to have a pattern speed that decreases with radius, implying they are material in nature rather than standing density waves. While some bar features are also created, these are either a poor match for the inner velocity structure or do not create sufficient emission in the outer disc. The CO emission maps for our best-fitting calculations appear a much better match to the observed map than the analytic potentials, with a select few maps reproducing many of the arm structures. These best fitting models favour a four-armed structure, though interestingly a highly flocculent disc with no clear dominant spiral mode can also provide a reasonable match. The main detriment of these models is the over-abundance of emission in the Galactic centre. This may require an inner bar, absent in most of these models but present in the models using analytic potentials, to sweep up this excess molecular material in the $|l| < 20°$ region. The H I emission also provides a closer match to observations that than of the fixed potentials, due to the live-disc being greater dispersed around the Galactic plane.

In the Introduction we proposed 5 key questions we sought the answers to in this work. These questions and direct answers are as follows.

- Can we create synthetic molecular emission maps of our own Galaxy sufficient for the purpose of constraining morphology? The longitude velocity emission maps indeed proved very capable of highlighting what could be deemed a good and a poor spiral model of the Galaxy. The addition of a radiative treatment over previous studies helped to highlight the dangers of simply matching up arm features as material very near the observer can produce extremely bright emission features not seen in observations.
- Can a grand design spiral perturbation sufficiently reproduce the observed features in l-v space? The barred and armed models made using fixed potentials failed to provide a full match to observed features. While individual arm structures could be reproduced, the symmetric grand-design models proved incapable of matching all structures simultaneously.
- Is a 2-armed structure sufficient to reproduce all the features, or is a 4-armed model needed? A four armed pattern is required, both seen in the fixed potentials and live disc simulations. There is simply not enough structure in the gas to match the l-v data with two arms.
- Does a 2-armed stellar distribution produce a 4-armed gas morphology sufficient to match l-v features? We found that a 2-armed stellar spiral can produce 4-armed gas features, but that these are too tightly wound to match the observations. Interesting the live disc simulations produced strong $m = 2$ modes in the inner disc and strong $m = 4$ modes in the outer disc, which could be the best way to reconcile the 2 and 4-armed paradigms inferred by observations.
- Can instead a transient spiral structure better fit the observations? The material and recurrent spiral structure of the live disc simulations produced much better matches to the observa-

tional data. The more irregular arm structure coupled with more discontinuous emission along individual arms allowed for more realistic *l*-*v* maps, and allowed for different arm numbers to dominate different Galactic radii.

The synthetic observations in this thesis show that a four-armed morphology is needed to reproduce the observed gas emission features. The theory that a two-armed stellar morphology can drive a four-armed structure in the gas is only supported by a small amount of models with fixed potentials, and none of the calculations with a live disc. Fixed analytic potentials tend to be a poorer representation of the disc, with a live stellar distribution creating a better range of features that can match the observed arm emission implying the arms of the Milky Way may not be in a steady state driven by spiral density waves. A bar feature does seem required however in the inner disc. The inclusion of a bar in the analytic models gave a better match to inner features than the arm only models created using a live disc, which display an over-abundance of emission towards the Galactic centre. As such, modelling the Galaxy a live-stellar disc and transient arms with the inclusion of a small, rapidly rotating inner bar, would provide the best reproduction of our Galaxy.

6.2 Future work

The work outlined in this thesis has some clear and obvious avenues for extension. In following subsections we discuss directions we have already begun working in to either further understand the morphology of the Milky Way, or constrain some other Galactic scale features.

6.2.1 Perturbing bodies driving spiral structure

A mechanism of spiral structure generation that we have not investigated thus far in detail is that caused by passage of some massive perturbing body. The tidal forces on a galactic disc are believed to be very effective at seeding spiral arms, bridges and tails (Toomre & Toomre 1972; Dobbs et al. 2010). There are many examples in the literature of the effect of a perturbing mass, be it point mass or a many-body system, on a Milky Way-like disc (Toomre & Toomre 1972; Donner et al. 1991; Barnes & Hernquist 1996; Oh et al. 2008; Dobbs et al. 2010; Purcell et al. 2011; Struck et al. 2011). However, as far as we are aware there has been no in-depth study on wether these tidal effects could produce morphologies that are a good representation of our own Galaxy.

By using an *N*-body and SPH prescription, similar to Chapter 5 it is possible to simulate such a perturbing scenario. This was done so by Dobbs et al. (2010), who used a point mass perturber to simulate the interaction between a galactic disc and the creation of spiral structure that showed a striking resemblance to M51. We have already performed numerous test calculations on the effects of a point mass perturber on the discs presented in Chapter 5, an example of which is shown in Figure 6.1. Here a point mass perturbing particle with approximately a third of the mass of the stellar disc approaches the disc on a hyperbolic orbit and induces a two armed spiral feature in the disc. This spiral structure persists for about three rotations of the disc, in which time the perturber has continued on it's orbital path. This interaction also seems to have bolstered the inner bar, it appearing much longer and than in the initial time-stamp. An advantage of this

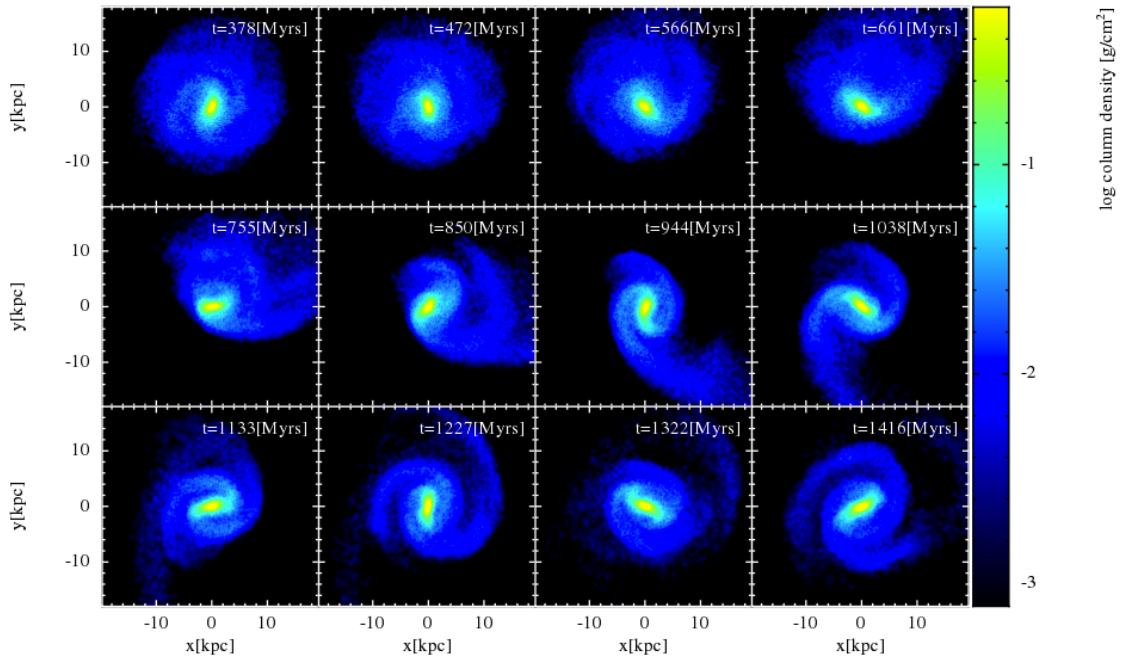

Figure 6.1: Effect of point-mass perturber on a disc galaxy composed of 1 million star particles that have formed a weak barred structure. The perturber is initially located at the top of the first panel, and moves on a hyperbolic orbit clockwise (off-panel). Its passage induces arms in the stars, which persist for three full rotations after periastron passage.

method is that it is an easy way of reproducing $m = 2$ features in the disc, which was difficult to do in the isolated galaxy case in Chapter 5. The next step is to include gas particles with active chemistry, and then construct synthetic CO emission maps to assess the validity of the models. Preliminary tests show that the velocity structure is quite different from the isolated case, with the tides caused by the perturber inducing large scale velocity structures in the disc. It may therefore be prudent to allow the disc to settle somewhat after the passage of the perturber, though this will also result in a weakening of spiral features. Extension of this method would involve replacing the point-mass perturber by an N-body companion, though the increase in computational cost would be considerable.

6.2.2 The effects of stellar feedback and self-gravity on global *l*-*v* features

In terms of the physics incorporated into the models in this thesis, we have taken a practically simple approach. The forces experienced by the gas are reduced to the stellar gravitational field and hydrodynamical forces, with additional ISM heating and cooling mechanisms. The main omission is the gravitational effect of the gas upon itself, which we have assumed to be negligible compared to that of the stellar system. The addition of self-gravity results in creation of clumps in the gas, and acts to create inhomogenities in the global gas flow (Dobbs 2008). To maintain a calculation involving self-gravity in the gas it is prudent to include some method of breaking up these dense clumps. To this end stellar feedback can be employed to insert energy into the ISM. This approach has been employed by numerous galactic-scale studies in the past, both in grid-based and SPH

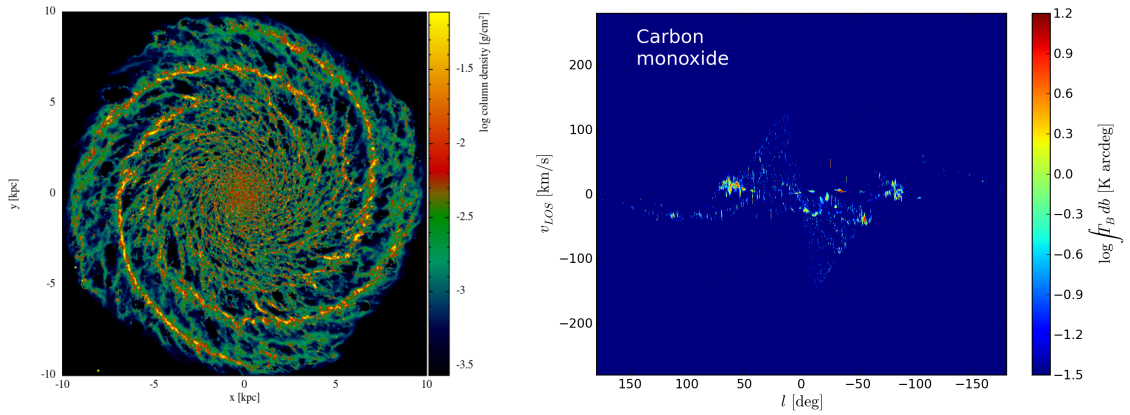

Figure 6.2: The effect of supernovae feedback and self-gravity on the evolution of the ISM disc with a 4-armed spiral potential and resulting CO emission features. The left panel shows the top-down surface density after 250Myrs of evolution and the right panel the CO emission map created using TORUS with the observer placed at y = 7kpc in the top-down view. SPH calculation performed by C. Dobbs using SPHNG with 8 million particles and is described in Dobbs et al. (2011).

codes; Wada et al. (2000); Scannapieco et al. (2006); Tasker & Bryan (2006); Dobbs et al. (2011); Kawata et al. (2014). Stellar feedback comes in variety of forms, be it radiation pressure, stellar winds or supernova feedback. In galactic-scale calculations this is usually solely represented by the strongest contribution; that of supernovae. These feedback events occur when the gas becomes sufficiently dense, i.e. forming a GMC. The activation of such a feedback event in the code is a costly one, and requires neighbour lists to be re-called in order to ascertain where the energy of the supernova must be deposited. Coupled with the inclusion of self-gravity, these calculations can be extremely more computationally expensive than those presented in this thesis.

The inclusion feedback can act to greatly change the global morphology of galactic simulations. As such the effect on the synthetic observations, such as those presented in this thesis, could be great. The effect of such physics has already been investigated to a degree by Duarte-Cabral et al. (in preperation) and Acreman et al. (2012), where the emission structures from fixed analytic potentials are greatly disrupted and provide a much better resemblance to observations. These studies, however, were focused solely on the second quadrant using some assumed spiral model. As an extension to the work of this thesis we intend on taking our best fit models and including the effects of self-gravity and feedback in hopes of producing an even match to observations. The code SPHNG (utilised in Chapter 5) has already been adapted by C. Dobbs to include supernova feedback (Dobbs et al. 2011), so utilising it with the models in Chapters 3 and 5 would be relatively straight forward. It has also been used with a live-stellar system (Dobbs et al. 2012).

As a simple test of this approach, we have taken a calculation from Dobbs et al. (2011) that includes self-gravity, feedback and four-armed potential and created a synthetic plane survey of CO emission, shown in Figure 6.2. The top-down map of the gas is shown in the left, and the TORUS CO l-v map in the right. Emission features are greatly dispersed compared to those in Chapters 4 and 5 and arm features can be seen away from the local velocity plane (note the Perseus and Carina arm analogues). The surface density of the gas is somewhat lower than our

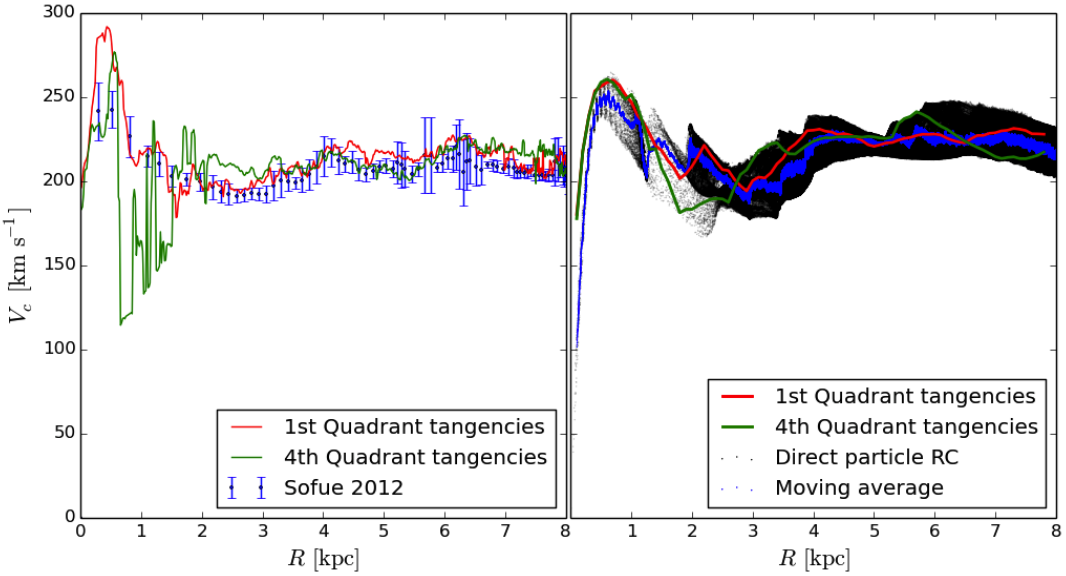

Figure 6.3: Different rotation curves from observational data of the Milky Way (left) and a barred-spiral simulation (right). In the left panel we show the rotation curve data from Sofue (2012) and rotation curves calculated from the terminal velocities of the CO l-v map of Dame et al. (2001) in using longitudes $0° < l < 180°$ and $180° < l < 360°$. In the right panel are similar rotation curves for the SPH calculation. The green and red lines are from 4th and 1st quadrant tangencies respectively. Black points are the circular velocities of individual SPH particles, and the blue points are these moving averages of the individual values.

calculations, which results in reduced emission overall (see Fig. 4.3). Note also the lack of any clear resonance features caused by the arms in the top down plot, which appeared clearly visible in our calculations.

An obvious question is why we did not include these effects in the first place. The answer is that self-gravity and feedback greatly increase computational time. With a vast parameter space to explore and a moderately high resolution required to produce CO emission, this would simply not have been computationally feasible.

6.2.3 Further tests of Galactic structure

Longitude-velocity emission maps are complex structures with which to fit our models to. The data product is effectively a 4-dimensional object, and as such the fitting procedure is quite complicated. As such it is prudent to use other observations of our Galaxy with which to constrain our models. This could involve a study specifically focussed on reproducing the l-v features of H I in the full Galactic plane and using a live-stellar system or feedback which would drive material away form $b = 0°$ and avoiding the problems in Section 4.4. The models already created for this thesis could also be re-used to create further synthetic observations. Arm tangency maps such as those of Drimmel (2000) or Benjamin et al. (2005) could be easily created for both static and live stellar systems. Doing so for the calculations in Chapter 5 could be compared to the studies that find significant differences in the tangencies observed in the stars and the gas (Drimmel 2000; Steiman-

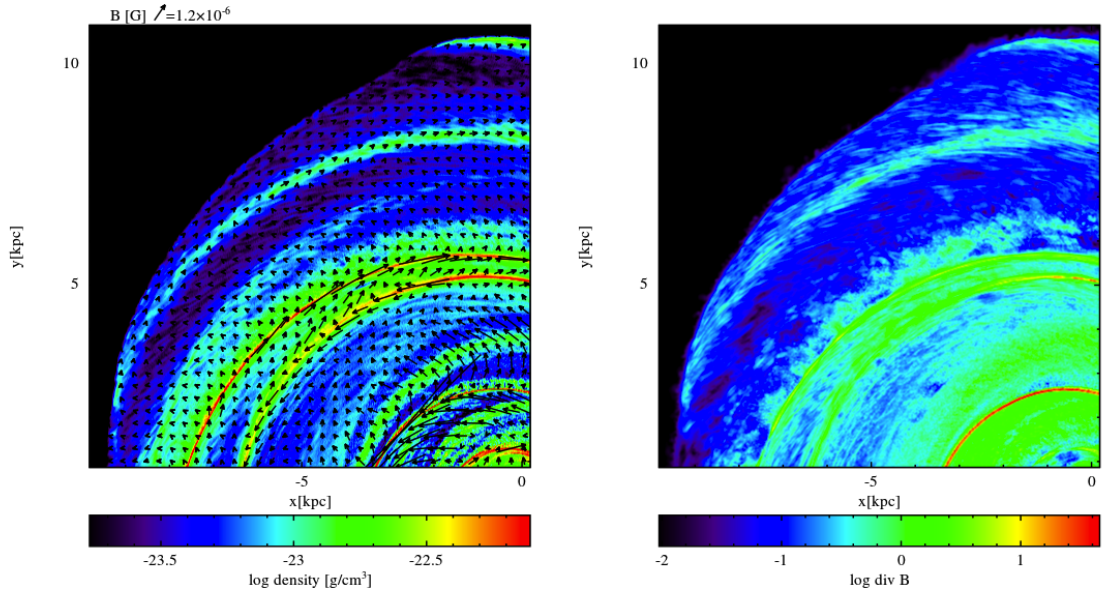

Figure 6.4: Simulation of ISM gas in a 2-armed spiral galaxy with an active magnetic field. An initial toroidal field with a strength of $B_\circ = 10^{-7}$G can be seen to be enhanced and flip directions in the left panel, where arrows indicate the direction and strength of field. In the right panel the divergence of the magnetic field is shown in the same region ($\vec{\nabla} \cdot \vec{B}$). This computation was performed using PHANTOM and 8 million SPH particles.

Cameron et al. 2010).

A simple additional comparison to make with observations is to compare the various rotation curves that can be computed from our models to those measured for our Galaxy. In Figure 6.3 we show various rotation curves for our Galaxy (left) and from a barred-spiral calculation (right). Rotation curves can be calculated directly from the terminal velocities of l-v maps, with various dips and bumps highlighting morphological features. By simply comparing the different rotation curves, such as for example those created from the fourth quadrant tangencies from models and observations, we can infer additional information regarding Galactic morphology.

6.2.4 Galactic magnetic field reversal

A feature of our Galaxy that we have so far over-looked is the topology of the galactic-scale magnetic field. The existence of some field has been known for some time due to the observation of rotation measures (pulsar observations), which require some finite magnetic field. The magnetic field in disc galaxies is believed to originate either from some dynamo action on small scale turbulent field lines, or due to some primordial magnetic field. Regardless of its origin, magnetic fields have been observed in external disc galaxies with field strengths of the order of μG (Beck et al. 1996).

The topology of the magnetic field of the Milky Way is as shrouded in doubt as the arm morphology. Studies seem to present a divided opinion on whether the direction of the magnetic field lines reverse at every spiral arm passage (Sofue & Fujimoto 1983; Han et al. 2006), experience just a single reversal at Sagittarius arm (Brown 2010) or reverse in a series of Galactocentric rings (Vallée 2011). Numerical simulations on the subject have shown that an initial small scale

field can be greatly magnified and ordered by the differential rotation in the disc (Kotarba et al. 2009; Pakmor & Springel 2013). Other work has shown that the field can be disordered from the global symmetry by pockets of cold ISM gas (Dobbs & Price 2008).

An application of the best fitting spiral models presented in this thesis is to introduce a Galactic-scale magnetic field and study the effect of the field on the disc evolution. A specific goal would be to assess the plausibility of the reversal of magnetic field lines in the passage of spiral arms. Is a reversal reproducible in the Best-fitting Galactic models? If so, how is this dependant on arm number and pattern speed?

Many techniques already exist for including magnetic fields in SPH (see Price 2012a for a review). We have performed numerous preliminary simulations in collaboration with D. Price and C. Dobbs involving an active magnetic field in disc galaxies similar to those in shown in Chapter 3. In Figure 6.4 we shown one such calculation of ISM gas in a two-armed spiral galaxy. In the left panel is the density render of a single quadrant with magnetic field vectors overplotted. In the right panel the divergence of the magnetic field is shown for the same region. The calculation is performed using PHANTOM with 8 million SPH particles and an isothermal equation of state ($T = 100$K). An initial toroidal magnetic field is applied with a strength of $B_\circ = 10^{-7}$G. Somewhat promisingly, the magnetic field can clearly be seen to change orientations in the passage through the spiral arms. In the two-armed brach region the field seems to swap from being directed towards then opposite to the disc rotation. The right panel illustrates a problem with these calculations. The divergence of the field is clearly non-zero throughout the disc, with values in the inner arms especially reaching considerable magnitudes. While methods such as additional divergence cleaning can improve matters, these calculations usually crash in an explosion of $\vec{\nabla} \cdot \vec{B}$. A possible work-around is to allow the disc to settle considerably before the activation of a magnetic field, and preliminary tests show this allows for simulation of the magnetic field for many Gyr without incident.

Bibliography

Abel, T., Anninos, P., Zhang, Y., & Norman, M. L. 1997, NA, 2, 181

Acreman, D. M., Dobbs, C. L., Brunt, C. M., & Douglas, K. A. 2012, MNRAS, 422, 241

Acreman, D. M., Douglas, K. A., Dobbs, C. L., & Brunt, C. M. 2010a, MNRAS, 406, 1460

Acreman, D. M., Harries, T. J., & Rundle, D. A. 2010b, MNRAS, 403, 1143

Agertz, O., Moore, B., Stadel, J., et al. 2007, MNRAS, 380, 963

Allen, C. & Santillan, A. 1991, RMxAA, 22, 255

Amaral, L. H. & Lepine, J. R. D. 1997, MNRAS, 286, 885

Araya, E., Hofner, P., Churchwell, E., & Kurtz, S. 2002, ApJS, 138, 63

Arp, H. 1966, ApJS, 14, 1

Athanassoula, E. 1992a, MNRAS, 259, 328

Athanassoula, E. 1992b, MNRAS, 259, 345

Athanassoula, E., Machado, R. E. G., & Rodionov, S. A. 2013, MNRAS, 429, 1949

Avedisova, V. S. & Palous, J. 1989, Bulletin of the Astronomical Institutes of Czechoslovakia, 40, 42

Baba, J., Asaki, Y., Makino, J., et al. 2009, ApJ, 706, 471

Baba, J., Saitoh, T. R., & Wada, K. 2010, PASJ. , 62, 1413

Baba, J., Saitoh, T. R., & Wada, K. 2013, ApJ, 763, 46

Bailey, M. E., Butler, C. J., & McFarland, J. 2005, Astronomy and Geophysics, 46, 020000

Balkowski, C. 1973, A&A, 29, 43

Bally, J., Stark, A. A., Wilson, R. W., & Henkel, C. 1987, ApJS, 65, 13

Barnes, J. & Hut, P. 1986, Nature, 324, 446

Barnes, J. E. 1992, ApJ, 393, 484

Barnes, J. E. & Hernquist, L. 1996, ApJ, 471, 115

Bate, M. R., Bonnell, I. A., & Price, N. M. 1995, MNRAS, 277, 362

Bate, M. R. & Burkert, A. 1997, MNRAS, 288, 1060

Battaglia, G., Helmi, A., Morrison, H., et al. 2005, MNRAS, 364, 433

Baudry, A., Perault, M., de La Noe, J., Despois, D., & Cernicharo, J. 1981, A&A, 104, 101

Beck, R., Brandenburg, A., Moss, D., Shukurov, A., & Sokoloff, D. 1996, ARAA, 34, 155

Becker, W. & Fenkart, R. 1971, A&AS, 4, 241

Benjamin, R. A. 2008, in Astronomical Society of the Pacific Conference Series, Vol. 387, Massive Star Formation: Observations Confront Theory, ed. H. Beuther, H. Linz, & T. Henning, 375

Benjamin, R. A., Churchwell, E., Babler, B. L., et al. 2005, ApJL, 630, L149

Benz, W. 1988, Computer Physics Communications, 48, 97

Benz, W. 1990, in Numerical Modelling of Nonlinear Stellar Pulsations Problems and Prospects, ed. J. R. Buchler, 269

Benz, W., Cameron, A. G. W., Press, W. H., & Bowers, R. L. 1990, ApJ, 348, 647

Bergin, E. A., Hartmann, L. W., Raymond, J. C., & Ballesteros-Paredes, J. 2004, ApJ, 612, 921

Binney, J., Gerhard, O., & Spergel, D. 1997, MNRAS, 288, 365

Binney, J. & Merrifield, M. 1998, *Galactic Astronomy*, Princeton, NJ, Princeton University Press

Binney, J. & Tremaine, S. 1987, *Galactic Dynamics*, Princeton, NJ, Princeton University Press

Bissantz, N., Englmaier, P., & Gerhard, O. 2003, MNRAS, 340, 949

Blitz, L. & Spergel, D. N. 1991, ApJ, 379, 631

Bloemen, J. B. G. M., Deul, E. R., & Thaddeus, P. 1990, A&A, 233, 437

Bohlin, R. C., Savage, B. D., & Drake, J. F. 1978, ApJ, 224, 132

Böhm-Vitense, E. 1989, Introduction to stellar astrophysics. Vol. 2. Stellar atmospheres.

Boissier, S. & Prantzos, N. 1999, MNRAS, 307, 857

Bovy, J., Rix, H.-W., Liu, C., et al. 2012, ApJ, 753, 148

Bowyer, S., Lieu, R., Sidher, S. D., Lampton, M., & Knude, J. 1995, Nature, 375, 212

Brand, J. & Blitz, L. 1993, A&A, 275, 67

Brinks, E. & Bajaja, E. 1986, A&A, 169, 14

Brown, J. C. 2010, in Astronomical Society of the Pacific Conference Series, Vol. 438, Astronomical Society of the Pacific Conference Series, ed. R. Kothes, T. L. Landecker, & A. G. Willis, 216

Brunt, C. M., Heyer, M. H., Vázquez-Semadeni, E., & Pichardo, B. 2003, ApJ, 595, 824

Bryan, G. L., Norman, M. L., O'Shea, B. W., et al. 2014, ApJS, 211, 19

Burgh, E. B., France, K., & McCandliss, S. R. 2007, ApJ, 658, 446

Burton, W. B. 1973, PASP, 85, 679

Burton, W. B. & Shane, W. W. 1970, in IAU Symposium, Vol. 38, The Spiral Structure of our Galaxy, ed. W. Becker & G. I. Kontopoulos, 397

Buta, R. & Combes, F. 1996, Fund. Cosmic Physics, 17, 95

Carlberg, R. G. & Freedman, W. L. 1985, ApJ, 298, 486

Caswell, J. L. & Haynes, R. F. 1987, A&A, 171, 261

Chakrabarti, S., Laughlin, G., & Shu, F. H. 2003, ApJ, 596, 220

Chakrabarty, D. 2007, A&A, 467, 145

Chemin, L., Carignan, C., & Foster, T. 2009, ApJ, 705, 1395

Churchwell, E., Babler, B. L., Meade, M. R., et al. 2009, PASP, 121, 213

Cioffi, D. F., McKee, C. F., & Bertschinger, E. 1988, ApJ, 334, 252

Clarke, C. & Gittins, D. 2006, MNRAS, 371, 530

Cohen, R. S., Cong, H., Dame, T. M., & Thaddeus, P. 1980, ApJL, 239, L53

Combes, F. 1991, Annual Review of Astronomy and Astrophysics, 29, 195

Combes, F., Boisse, P., Mazure, A., Blanchard, A., & Seymour, M. 1995, *Galaxies and Cosmology*, Springer-Verlag Berlin Heidelberg New York.

Combes, F., Debbasch, F., Friedli, D., & Pfenniger, D. 1990, A&A, 233, 82

Combes, F. & Sanders, R. H. 1981, A&A, 96, 164

Contopoulos, G. & Papayannopoulos, T. 1980, A&A, 92, 33

Cordes, J. M. & Lazio, T. J. W. 2002, ArXiv Astrophysics e-prints

Cossins, P. J. 2010, PhD thesis, University of Leicester

Courant, R., Friedrichs, K., & Lewy, H. 1928, Mathematische Annalen, 100, 32

Cox, D. P. 2005, ARAA, 43, 337

Cox, D. P. & Gómez, G. C. 2002, ApJS, 142, 261

Cox, D. P. & Smith, B. W. 1974, ApJL, 189, L105

Dale, J. E., Ngoumou, J., Ercolano, B., & Bonnell, I. A. 2013, MNRAS, 436, 3430

Dalgarno, A. & McCray, R. A. 1973, ApJ, 181, 95

Dame, T. M., Elmegreen, B. G., Cohen, R. S., & Thaddeus, P. 1986, ApJ, 305, 892

Dame, T. M., Hartmann, D., & Thaddeus, P. 2001, ApJ, 547, 792

Dame, T. M. & Thaddeus, P. 2008, ApJL, 683, L143

Dame, T. M. & Thaddeus, P. 2011, ApJL, 734, L24

Dame, T. M., Ungerechts, H., Cohen, R. S., et al. 1987, ApJ, 322, 706

de Avillez, M. & Breitschwerdt, D. 2004, Ap&SS, 292, 207

De Becker, M. 2013, Bulletin de la Societe Royale des Sciences de Liege, 82, 33

de Boer, W. & Weber, M. 2014, ArXiv e-prints

de Vaucouleurs, G. 1948, Annales d'Astrophysique, 11, 247

Debattista, V. P., Gerhard, O., & Sevenster, M. N. 2002, MNRAS, 334, 355

Dehnen, W. 1999, ApJL, 524, L35

Dehnen, W. 2000, AJ, 119, 800

Dehnen, W. 2002, Journal of Computational Physics, 179, 27

Dehnen, W. & Binney, J. J. 1998, MNRAS, 298, 387

Dias, W. S. & Lépine, J. R. D. 2005, ApJ, 629, 825

Dib, S., Bell, E., & Burkert, A. 2006, ApJ, 638, 797

Dobbs, C. L. 2008, MNRAS, 391, 844

Dobbs, C. L. 2011a, in IAU Symposium, Vol. 270, Computational Star Formation, ed. J. Alves, B. G. Elmegreen, J. M. Girart, & V. Trimble, 459–466

Dobbs, C. L. 2011b, Memorie della Societa Astronomica Italiana Supplementi, 18, 109

Dobbs, C. L. & Baba, J. 2014, ArXiv e-prints

Dobbs, C. L. & Bonnell, I. A. 2006, MNRAS, 367, 873

Dobbs, C. L. & Bonnell, I. A. 2008, MNRAS, 385, 1893

Dobbs, C. L., Bonnell, I. A., & Pringle, J. E. 2006, MNRAS, 371, 1663

Dobbs, C. L. & Burkert, A. 2012, MNRAS, 421, 2940

Dobbs, C. L., Burkert, A., & Pringle, J. E. 2011, MNRAS, 417, 1318

Dobbs, C. L., Glover, S. C. O., Clark, P. C., & Klessen, R. S. 2008, MNRAS, 389, 1097

Dobbs, C. L. & Price, D. J. 2008, MNRAS, 383, 497

Dobbs, C. L., Pringle, J. E., & Burkert, A. 2012, MNRAS, 425, 2157

Dobbs, C. L., Theis, C., Pringle, J. E., & Bate, M. R. 2010, MNRAS, 403, 625

Domínguez, J. M., Crespo, A. J. C., Gómez-Gesteira, M., & Marongiu, J. C. 2011, International Journal for Numerical Methods in Fluids, 67, 2026

D'Onghia, E., Vogelsberger, M., & Hernquist, L. 2013, ApJ, 766, 34

Donner, K. J., Engstrom, S., & Sundelius, B. 1991, A&A, 252, 571

Douglas, K. A., Acreman, D. M., Dobbs, C. L., & Brunt, C. M. 2010, MNRAS, 407, 405

Downes, D., Wilson, T. L., Bieging, J., & Wink, J. 1980, A&AS, 40, 379

Draine, B. 2003, Annual Review of Astronomy and Astrophysics, 41, 241

Draine, B. T. & Bertoldi, F. 1996, ApJ, 468, 269

Drimmel, R. 2000, A&A, 358, L13

Drimmel, R., Cabrera-Lavers, A., & López-Corredoira, M. 2003, A&A, 409, 205

Drimmel, R. & Spergel, D. N. 2001, ApJ, 556, 181

Duarte-Cabral, A., Dobbs, C., & Acreman, D. in preperation

Dwek, E., Arendt, R. G., Hauser, M. G., et al. 1995, ApJ, 445, 716

Efremov, Y. N. 2011, Astronomy Reports, 55, 108

Efstathiou, G., Lake, G., & Negroponte, J. 1982, MNRAS, 199, 1069

Egusa, F., Kohno, K., Sofue, Y., Nakanishi, H., & Komugi, S. 2009, ApJ, 697, 1870

Elmegreen, B. G. & Thomasson, M. 1993, A&A, 272, 37

Elmegreen, D. M. 1985, in IAU Symposium, Vol. 106, The Milky Way Galaxy, ed. H. van Woerden, R. J. Allen, & W. B. Burton, 255–270

Elmegreen, D. M., Sundin, M., Sundelius, B., & Elmegreen, B. 1991, A&A, 244, 52

Englmaier, P. & Gerhard, O. 1999, MNRAS, 304, 512

Ewen, H. I. & Purcell, E. M. 1951, Nature, 168, 356

Federman, S. R., Glassgold, A. E., Jenkins, E. B., & Shaya, E. J. 1980, ApJ, 242, 545

Fehlberg, E. 1985, NASA TR, R-287

Ferland, G. J., Peterson, B. M., Horne, K., Welsh, W. F., & Nahar, S. N. 1992, ApJ, 387, 95

Fernández, D., Figueras, F., & Torra, J. 2001, A&A, 372, 833

Ferrers, N. M. 1887, Quart. J. Pure Appl. Math, 14

Ferrière, K. M. 2001, Reviews of Modern Physics, 73, 1031

Fich, M. & Tremaine, S. 1991, ARAA, 29, 409

Field, G. B., Goldsmith, D. W., & Habing, H. J. 1969, ApJL, 155, L149

Field, G. B., Somerville, W. B., & Dressler, K. 1966, ARAA, 4, 207

Fish, V. L., Reid, M. J., Wilner, D. J., & Churchwell, E. 2003, ApJ, 587, 701

Freeman, K. C. 1966, MNRAS, 134, 1

Freeman, K. C. 1970, ApJ, 160, 811

Frenk, C. S., White, S. D. M., Bode, P., et al. 1999, ApJ, 525, 554

Freudenreich, H. T. 1998, ApJ, 492, 495

Fryxell, B., Olson, K., Ricker, P., et al. 2000, ApJS, 131, 273

Fujii, M. S., Baba, J., Saitoh, T. R., et al. 2011, ApJ, 730, 109

Fujimoto, M. 1968, in IAU Symposium, Vol. 29, Non-stable Phenomena in Galaxies, 453

Fux, R. 1999, A&A, 345, 787

Gabbasov, R. F., Repetto, P., & Rosado, M. 2009, ApJ, 702, 392

Georgelin, Y. M. & Georgelin, Y. P. 1976, A&A, 49, 57

Gerhard, O. 2002, in Astronomical Society of the Pacific Conference Series, Vol. 273, The Dynamics, Structure & History of Galaxies: A Workshop in Honour of Professor Ken Freeman, ed. G. S. Da Costa, E. M. Sadler, & H. Jerjen, 73

Gerhard, O. 2011, Memorie della Societa Astronomica Italiana Supplementi, 18, 185

Gies, D. R. & Helsel, J. W. 2005, ApJ, 626, 844

Gilmore, G. & Reid, N. 1983, MNRAS, 202, 1025

Gingold, R. A. & Monaghan, J. J. 1977, MNRAS, 181, 375

Gingold, R. A. & Monaghan, J. J. 1982, Journal of Computational Physics, 46, 429

Gittins, D. M. & Clarke, C. J. 2004, MNRAS, 349, 909

Glover, S. C. O. & Clark, P. C. 2012, MNRAS, 421, 116

Glover, S. C. O., Federrath, C., Mac Low, M.-M., & Klessen, R. S. 2010, MNRAS, 404, 2

Glover, S. C. O. & Jappsen, A.-K. 2007, ApJ, 666, 1

Glover, S. C. O. & Mac Low, M.-M. 2007, ApJS, 169, 239

Goldsmith, P. F. & Langer, W. D. 1978, ApJ, 222, 881

Gómez, G. C. 2006, The Astronomical Journal, 132, 2376

Gómez, G. C. & Cox, D. P. 2004, ApJ, 615, 758

Gómez, G. C., Pichardo, B., & Martos, M. A. 2013, MNRAS, 430, 3010

Gould, R. J. & Salpeter, E. E. 1963, ApJ, 138, 393

Grabelsky, D. A., Cohen, R. S., Bronfman, L., & Thaddeus, P. 1988, ApJ, 331, 181

Grabelsky, D. A., Cohen, R. S., Bronfman, L., Thaddeus, P., & May, J. 1987, ApJ, 315, 122

Grand, R. J. J., Kawata, D., & Cropper, M. 2012, MNRAS, 426, 167

Grand, R. J. J., Kawata, D., & Cropper, M. 2013, A&A, 553, A77

Grimm, H.-J., Gilfanov, M., & Sunyaev, R. 2002, A&A, 391, 923

Güver, T. & Özel, F. 2009, MNRAS, 400, 2050

Hammersley, P. L., Garzón, F., Mahoney, T. J., López-Corredoira, M., & Torres, M. A. P. 2000, MNRAS, 317, L45

Han, J. L., Manchester, R. N., Lyne, A. G., Qiao, G. J., & van Straten, W. 2006, ApJ, 642, 868

Han, J. L., Manchester, R. N., & Qiao, G. J. 1999, MNRAS, 306, 371

Han, J. L. & Qiao, G. J. 1994, A&A, 288, 759

Harries, T. J. 2000, Monthly Notices of the Royal Astronomical Society, 315, 722

Hartmann, D. & Burton, W. B. 1997, Atlas of Galactic Neutral Hydrogen

Heiles, C. & Troland, T. H. 2003, ApJ, 586, 1067

Helfer, T. T., Thornley, M. D., Regan, M. W., et al. 2003, ApJS, 145, 259

Henderson, A. P. 1977, A&A, 58, 189

Hernquist, L. 1993, ApJS, 86, 389

Hernquist, L. & Katz, N. 1989, ApJS, 70, 419

Hernquist, L. & Ostriker, J. P. 1992, ApJ, 386, 375

Herschel, W. 1785, Philosophical Transactions of the Royal Society of London, 75, 213

Heyer, M. H., Brunt, C., Snell, R. L., et al. 1998, ApJS, 115, 241

Hollenbach, D. & McKee, C. F. 1989, ApJ, 342, 306

Hollenbach, D. & Salpeter, E. E. 1971, ApJ, 163, 155

Hollenbach, D. J., Werner, M. W., & Salpeter, E. E. 1971, ApJ, 163, 165

Holmberg, E. 1941, ApJ, 94, 385

Hoskin, M. A. 1976, Journal for the History of Astronomy, 7, 169

Hou, L. G., Han, J. L., & Shi, W. B. 2009, A&A, 499, 473

Hubber, D. A., Batty, C. P., McLeod, A., & Whitworth, A. P. 2011, A&A, 529, A27

Hubble, E. P. 1936, Realm of the Nebulae

Indrani, C. & Deshpande, A. A. 1999, NA, 4, 33

Irrgang, A., Wilcox, B., Tucker, E., & Schiefelbein, L. 2013, A&A, 549, A137

Jenkins, E. B. & Savage, B. D. 1974, ApJ, 187, 243

Kalberla, P. M. & Kerp, J. 2009, Annual Review of Astronomy and Astrophysics, 47, 27

Kalberla, P. M. W., Burton, W. B., Hartmann, D., et al. 2005, A&A, 440, 775

Kalberla, P. M. W., Dedes, L., Kerp, J., & Haud, U. 2007, A&A, 469, 511

Kalnajs, A. J. 1965, PhD thesis, Harvard University

Kalnajs, A. J. 1973, Proceedings of the Astronomical Society of Australia, 2, 174

Kant, I. 1755, Allgemeine Naturgeschichte und Theorie des Himmels

Kapteyn, J. C. 1922, ApJ, 55, 302

Kawata, D., Gibson, B. K., Barnes, D. J., Grand, R. J. J., & Rahimi, A. 2014, MNRAS, 438, 1208

Kerr, F. J. 1962, MNRAS, 123, 327

Kerr, F. J. 1969a, Australian Journal of Physics Astrophysical Supplement, 9, 3

Kerr, F. J. 1969b, ARAA, 7, 39

Keto, E. & Caselli, P. 2008, ApJ, 683, 238

Khoperskov, S. A., Vasiliev, E. O., Sobolev, A. M., & Khoperskov, A. V. 2013, MNRAS, 428, 2311

Kim, W.-T., Seo, W.-Y., & Kim, Y. 2012, ApJ, 758, 14

Kolpak, M. A., Jackson, J. M., Bania, T. M., Clemens, D. P., & Dickey, J. M. 2003, ApJ, 582, 756

Kotarba, H., Lesch, H., Dolag, K., et al. 2009, MNRAS, 397, 733

Kritsuk, A. G. & Norman, M. L. 2002, ApJL, 569, L127

Larson, R. B. 1981, MNRAS, 194, 809

Le Bourlot, J., Pineau des Forêts, G., & Flower, D. R. 1999, MNRAS, 305, 802

Lee, C. W., Lee, H. M., Ann, H. B., & Kwon, K. H. 1999, ApJ, 513, 242

Lee, H.-H., Herbst, E., Pineau des Forets, G., Roueff, E., & Le Bourlot, J. 1996, A&A, 311, 690

Lépine, J. R. D., Mishurov, Y. N., & Dedikov, S. Y. 2001, ApJ, 546, 234

Lépine, J. R. D., Roman-Lopes, A., Abraham, Z., Junqueira, T. C., & Mishurov, Y. N. 2011, MNRAS, 414, 1607

Levine, E. S., Blitz, L., & Heiles, C. 2006, Science, 312, 1773

Lin, C. C. & Shu, F. H. 1964, ApJ, 140, 646

Lin, C. C. & Shu, F. H. 1966, Proceedings of the National Academy of Science, 55, 229

Liszt, H. 2002, A&A, 389, 393

Liu, M. & Liu, G. 2003, Smoothed particle hydrodynamics: a meshfree particle method (World Scientific, Singapore)

Liu, M. & Liu, G. 2010, Archives of Computational Methods in Engineering, 17, 25

Lockman, F. J. 1979, ApJ, 232, 761

Lodato, G. & Price, D. J. 2010, MNRAS, 405, 1212

Long, K. & Murali, C. 1992, ApJ, 397, 44

López-Corredoira, M., Cabrera-Lavers, A., & Gerhard, O. E. 2005, A&A, 439, 107

López-Corredoira, M., Cabrera-Lavers, A., Mahoney, T. J., et al. 2007, AJ, 133, 154

Lucy, L. B. 1977, AJ, 82, 1013

Mac Low, M.-M. & Klessen, R. S. 2004, Reviews of Modern Physics, 76, 125

Majewski, S. R. 2008, in IAU Symposium, Vol. 248, IAU Symposium, ed. W. J. Jin, I. Platais, & M. A. C. Perryman, 450–457

Marshall, D. J., Joncas, G., & Jones, A. P. 2009, ApJ, 706, 727

Martos, M., Hernandez, X., Yáñez, M., Moreno, E., & Pichardo, B. 2004, MNRAS, 350, L47

McClure-Griffiths, N. M., Dickey, J. M., Gaensler, B. M., et al. 2012, ApJS, 199, 12

McCray, R. & Kafatos, M. 1987, ApJ, 317, 190

McElroy, D., Walsh, C., Markwick, A. J., et al. 2013, A&A, 550, A36

McKee, C. F. & Ostriker, J. P. 1977, ApJ, 218, 148

McWilliam, A. & Zoccali, M. 2010, ApJ, 724, 1491

Meidt, S. E., Rand, R. J., Merrifield, M. R., Shetty, R., & Vogel, S. N. 2008, ApJ, 688, 224

Mel'Nik, A. M. & Rautiainen, P. 2009, Astronomy Letters, 35, 609

Minchev, I., Nordhaus, J., & Quillen, A. C. 2007, ApJL, 664, L31

Mishurov, Y. N. & Zenina, I. A. 1999, A&A, 341, 81

Miyamoto, M. & Nagai, R. 1975, PASJ, 27, 533

Moisés, A. P., Damineli, A., Figuerêdo, E., et al. 2011, MNRAS, 411, 705

Monaghan, J. J. 1992, A&AAn. Rev., 30, 543

Monaghan, J. J. 1997, Journal of Computational Physics, 136, 298

Monaghan, J. J. 2005, Reports on Progress in Physics, 68, 1703

Monaghan, J. J. & Gingold, R. A. 1983, Journal of Computational Physics, 52, 374

Monaghan, J. J. & Lattanzio, J. C. 1985, A&A, 149, 135

Morris, J. & Monaghan, J. 1997, Journal of Computational Physics, 136, 41

Muller, C. A. & Oort, J. H. 1951, Nature, 168, 357

Nakanishi, H. & Sofue, Y. 2003, PASJ. , 55, 191

Nakanishi, H. & Sofue, Y. 2006, PASJ. , 58, 847

Narayanan, D., Krumholz, M. R., Ostriker, E. C., & Hernquist, L. 2012, MNRAS, 421, 3127

Navarro, J. F., Frenk, C. S., & White, S. D. M. 1996, ApJ, 462, 563

Nelson, R. P. & Langer, W. D. 1997, ApJ, 482, 796

Nelson, R. P. & Langer, W. D. 1999, ApJ, 524, 923

Oh, S. H., Kim, W.-T., Lee, H. M., & Kim, J. 2008, ApJ, 683, 94

Ollongren, A. 1967, AJ, 72, 474

Oort, J. H. 1932, Bull. Astron. Inst. Netherlands, 6, 249

Oort, J. H., Kerr, F. J., & Westerhout, G. 1958, MNRAS, 118, 379

O'Shea, B. W., Nagamine, K., Springel, V., Hernquist, L., & Norman, M. L. 2005, ApJS, 160, 1

Ostriker, J. P. & Peebles, P. J. E. 1973, ApJ, 186, 467

Ostriker, J. P., Peebles, P. J. E., & Yahil, A. 1974, ApJL, 193, L1

Pakmor, R. & Springel, V. 2013, MNRAS, 432, 176

Paladini, R., Davies, R. D., & De Zotti, G. 2004, MNRAS, 347, 237

Pandian, J. D., Momjian, E., & Goldsmith, P. F. 2008, A&A, 486, 191

Pasha, I. I. 2004a, ArXiv Astrophysics e-prints

Pasha, I. I. 2004b, ArXiv Astrophysics e-prints

Patsis, P. A. & Athanassoula, E. 2000, A&A, 358, 45

Patsis, P. A., Grosbol, P., & Hiotelis, N. 1997, A&A, 323, 762

Patsis, P. A., Hiotelis, N., Contopoulos, G., & Grosbol, P. 1994, A&A, 286, 46

Pichardo, B., Martos, M., & Moreno, E. 2004, ApJ, 609, 144

Pichardo, B., Martos, M., Moreno, E., & Espresate, J. 2003, ApJ, 582, 230

Piontek, R. A. & Ostriker, E. C. 2005, ApJ, 629, 849

Plummer, H. C. 1911, MNRAS, 71, 460

Press, W. H. 1986, in Lecture Notes in Physics, Berlin Springer Verlag, Vol. 267, The Use of Supercomputers in Stellar Dynamics, ed. P. Hut & S. L. W. McMillan, 184

Price, D. 2005, ArXiv Astrophysics e-prints

Price, D. J. 2008, Journal of Computational Physics, 227, 10040

Price, D. J. 2012a, Journal of Computational Physics, 231, 759

Price, D. J. 2012b, in Astronomical Society of the Pacific Conference Series, Vol. 453, Advances in Computational Astrophysics: Methods, Tools, and Outcome, ed. R. Capuzzo-Dolcetta, M. Limongi, & A. Tornambè, 249

Price, D. J. & Federrath, C. 2010, MNRAS, 406, 1659

Price, D. J. & Monaghan, J. J. 2004, MNRAS, 348, 139

Price, D. J. & Monaghan, J. J. 2007, MNRAS, 374, 1347

Purcell, C. W., Bullock, J. S., Tollerud, E. J., Rocha, M., & Chakrabarti, S. 2011, Nature, 477, 301

Quillen, A. C. & Minchev, I. 2005, AJ, 130, 576

Rachford, B. L., Snow, T. P., Tumlinson, J., et al. 2002, ApJ, 577, 221

Raha, N., Sellwood, J. A., James, R. A., & Kahn, F. D. 1991, Nature, 352, 411

Rautiainen, P. & Salo, H. 1999, A&A, 348, 737

Rautiainen, P., Salo, H., & Laurikainen, E. 2008, MNRAS, 388, 1803

Reid, M. J. 1993, ARAA, 31, 345

Reid, M. J., Menten, K. M., Zheng, X. W., et al. 2009, ApJ, 700, 137

Renaud, F., Bournaud, F., Emsellem, E., et al. 2013, MNRAS, 436, 1836

Roberts, W. W. 1969, ApJ, 158, 123

Roca-Fàbrega, S., Valenzuela, O., Figueras, F., et al. 2013, MNRAS, 432, 2878

Rodriguez-Fernandez, N. J. & Combes, F. 2008, A&A, 489, 115

Roman-Duval, J., Jackson, J. M., Heyer, M., et al. 2009, ApJ, 699, 1153

Rosswog, S. 2009, NAR, 53, 78

Rosswog, S. & Price, D. 2007, MNRAS, 379, 915

Rots, A. H. & Shane, W. W. 1975, A&A, 45, 25

Rubin, V. C., Ford, W. K. J., & . Thonnard, N. 1980, ApJ, 238, 471

Rundle, D., Harries, T. J., Acreman, D. M., & Bate, M. R. 2010, MNRAS, 407, 986

Russeil, D. 2003, A&A, 397, 133

Rybicki, G. B. & Lightman, A. P. 1979, Radiative processes in astrophysics

Sandage, A. 2005, ARAA, 43, 581

Savage, B. D., Bohlin, R. C., Drake, J. F., & Budich, W. 1977, ApJ, 216, 291

Scannapieco, C., Tissera, P. B., White, S. D. M., & Springel, V. 2006, MNRAS, 371, 1125

Schinnerer, E., Meidt, S. E., Pety, J., et al. 2013, ApJ, 779, 42

Schmidt, M. 1956, B. A. N., 13, 15

Schöier, F. L., van der Tak, F. F. S., van Dishoeck, E. F., & Black, J. H. 2005, A&A, 432, 369

Schwarz, M. P. 1981, ApJ, 247, 77

Scoville, N. Z., Yun, M. S., Sanders, D. B., Clemens, D. P., & Waller, W. H. 1987, ApJS, 63, 821

Sellwood, J. A. 2011, MNRAS, 410, 1637

Sellwood, J. A. & Carlberg, R. G. 1984, ApJ, 282, 61

Sellwood, J. A. & Carlberg, R. G. 2014, ApJ, 785, 137

Sellwood, J. A. & Sparke, L. S. 1988, MNRAS, 231, 25P

Sewilo, M., Watson, C., Araya, E., et al. 2004, ApJS, 154, 553

Shapley, H. 1918a, ApJ, 48, 89

Shapley, H. 1918b, ApJ, 48, 154

Shapley, H. 1918c, ApJ, 48, 279

Shaviv, N. J. 2003, NA, 8, 39

Sheffer, Y., Rogers, M., Federman, S. R., et al. 2008, ApJ, 687, 1075

Shen, J., Rich, R. M., Kormendy, J., et al. 2010, ApJL, 720, L72

Shetty, R. & Ostriker, E. C. 2006, ApJ, 647, 997

Shu, F. 1982, The Physical Universe: An Introduction to Astronomy, Series of Books in Astronomy (Univ Science Books)

Shull, J. M. & Beckwith, S. 1982, ARAA, 20, 163

Shull, J. M. & van Steenberg, M. E. 1985, ApJ, 294, 599

Simard-Normandin, M. & Kronberg, P. P. 1980, ApJ, 242, 74

Simonson, III, S. C. 1970, A&A, 9, 163

Simonson, III, S. C. 1976, A&A, 46, 261

Slavin, J. D. & Cox, D. P. 1993, ApJ, 417, 187

Smith, R. J., Glover, S. C. O., Clark, P. C., Klessen, R. S., & Springel, V. 2014, MNRAS, 441, 1628

Sofue, Y. 2012, PASJ. , 64, 75

Sofue, Y. & Fujimoto, M. 1983, ApJ, 265, 722

Sofue, Y. & Rubin, V. 2001, ARAA, 39, 137

Solomon, P. M., Sanders, D. B., & Rivolo, A. R. 1985, ApJL, 292, L19

Sparke, L. S. & Sellwood, J. A. 1987, MNRAS, 225, 653

Speights, J. C. & Westpfahl, D. J. 2011, ApJ, 736, 70

Speights, J. C. & Westpfahl, D. J. 2012, ApJ, 752, 52

Spitzer, L., Drake, J. F., Jenkins, E. B., et al. 1973, ApJL, 181, L116

Springel, V. 2005, MNRAS, 364, 1105

Springel, V. 2010a, MNRAS, 401, 791

Springel, V. 2010b, A&AAn. Rev., 48, 391

Springel, V., Yoshida, N., & White, S. D. M. 2001, NA, 6, 79

Stark, A. A. & Lee, Y. 2006, The Astrophysical Journal Letters, 641, L113

Steiman-Cameron, T. Y., Wolfire, M., & Hollenbach, D. 2010, ApJ, 722, 1460

Strasser, S. T., Dickey, J. M., Taylor, A. R., et al. 2007, AJ, 134, 2252

Strong, A. W., Bloemen, J. B. G. M., Dame, T. M., et al. 1988, A&A, 207, 1

Struck, C., Dobbs, C. L., & Hwang, J.-S. 2011, MNRAS, 414, 2498

Sutherland, R. S. & Dopita, M. A. 1993, ApJS, 88, 253

Tasker, E. J., Brunino, R., Mitchell, N. L., et al. 2008, MNRAS, 390, 1267

Tasker, E. J. & Bryan, G. L. 2006, ApJ, 641, 878

Taylor, A. R., Gibson, S. J., Peracaula, M., et al. 2003, AJ, 125, 3145

Taylor, J. H. & Cordes, J. M. 1993, ApJ, 411, 674

Teyssier, R. 2002, A&A, 385, 337

Thacker, R. J., Tittley, E. R., Pearce, F. R., Couchman, H. M. P., & Thomas, P. A. 2000, MNRAS, 319, 619

Tielens, A. G. G. M. 2008, ARAA, 46, 289

Timmermann, R., Bertoldi, F., Wright, C. M., et al. 1996, A&A, 315, L281

Toomre, A. 1964, ApJ, 139, 1217

Toomre, A. 1969, ApJ, 158, 899

Toomre, A. 1981, in Structure and Evolution of Normal Galaxies, ed. S. M. Fall & D. Lynden-Bell, 111–136

Toomre, A. & Toomre, J. 1972, ApJ, 178, 623

Toro, E. F. 1992, Royal Society of London Philosophical Transactions Series A, 341, 499

Tremaine, S. & Weinberg, M. D. 1984, ApJL, 282, L5

Tremblin, P., Anderson, L. D., Didelon, P., et al. 2014, ArXiv e-prints

Tricco, T. S. & Price, D. J. 2012, Journal of Computational Physics, 231, 7214

Trimble, V. 1987, ARAA, 25, 425

Trumpler, R. J. 1930, Lick Observatory Bulletin, 14, 154

Ungerer, V., Nguyen-Quang-Rieu, Mauron, N., & Brillet, J. 1985, A&A, 146, 123

Valcke, S., de Rijcke, S., Rödiger, E., & Dejonghe, H. 2010, MNRAS, 408, 71

Vallee, J. P. 1988, AJ, 95, 750

Vallée, J. P. 1995, ApJ, 454, 119

Vallée, J. P. 2002, ApJ, 566, 261

Vallée, J. P. 2005, AJ, 130, 569

Vallée, J. P. 2008, AJ, 135, 1301

Vallée, J. P. 2011, NAR, 55, 91

Vogt, D. & Letelier, P. S. 2011, Monthly Notices of the Royal Astronomical Society, 411, 2371

Vogt, N. & Moffat, A. F. J. 1975, A&A, 39, 477

Von Neumann, J. & Richtmyer, R. D. 1950, Journal of Applied Physics, 21, 232

Wada, K. 2008, ApJ, 675, 188

Wada, K., Baba, J., Fujii, M., & Saitoh, T. R. 2011a, in IAU Symposium, Vol. 270, Computational Star Formation, ed. J. Alves, B. G. Elmegreen, J. M. Girart, & V. Trimble, 363–370

Wada, K., Baba, J., & Saitoh, T. R. 2011b, ApJ, 735, 1

Wada, K. & Koda, J. 2001, PASJ. , 53, 1163

Wada, K. & Koda, J. 2004, MNRAS, 349, 270

Wada, K., Spaans, M., & Kim, S. 2000, ApJ, 540, 797

Wada, K., Taniguchi, Y., Habe, A., & Hasegawa, T. 1994, ApJL, 437, L123

Wadsley, J. W., Stadel, J., & Quinn, T. 2004, NA, 9, 137

Wadsley, J. W., Veeravalli, G., & Couchman, H. M. P. 2008, MNRAS, 387, 427

Walter, F. & Brinks, E. 1999, AJ, 118, 273

Wang, Y., Zhao, H., Mao, S., & Rich, R. M. 2012, MNRAS, 427, 1429

Watson, C., Araya, E., Sewilo, M., et al. 2003, ApJ, 587, 714

Weaver, H. 1970, in IAU Symposium, Vol. 38, The Spiral Structure of our Galaxy, ed. W. Becker & G. I. Kontopoulos, 126

Weiland, J. L., Arendt, R. G., Berriman, G. B., et al. 1994, ApJL, 425, L81

Weiner, B. J. & Sellwood, J. A. 1999, ApJ, 524, 112

Weingartner, J. C. & Draine, B. T. 2001, ApJ, 563, 842

Whitehouse, S. C., Bate, M. R., & Monaghan, J. J. 2005, MNRAS, 364, 1367

Wilson, P. A., Colón, K. D., Sing, D. K., et al. 2014, MNRAS, 438, 2395

Wolfire, M. G., Hollenbach, D., McKee, C. F., Tielens, A. G. G. M., & Bakes, E. L. O. 1995, ApJ, 443, 152

Wolfire, M. G., McKee, C. F., Hollenbach, D., & Tielens, A. G. G. M. 2003, ApJ, 587, 278

Xu, Y., Li, J. J., Reid, M. J., et al. 2013, ApJ, 769, 15

Yang, J., Jiang, Z., Wang, M., Ju, B., & Wang, H. 2002, ApJS, 141, 157

Yin, J., Hou, J. L., Prantzos, N., et al. 2009, A&A, 505, 497

Young, J. S. & Scoville, N. Z. 1991, ARAA, 29, 581

Yuan, C. & Grosbol, P. 1981, ApJ, 243, 432

Zhao, H., Rich, R. M., & Spergel, D. N. 1996, MNRAS, 282, 175

Zwicky, F. 1933, Helvetica Physica Acta, 6, 110

A

SPH equations with adaptive spatial resolution

"Computer, compute to the last digit the value of pi. "
– Spock, Star Trek: *Wolf in the Fold*, 1967

In this Appendix we provide some additional details on the derivation of the SPH equations for momentum, energy and density in the "grad-h" formalism where particles have variable smoothing lengths. The deviations are somewhat different to those in Chapter 2 where h is fixed.

A.1 Density equation

This Lagrangian method makes it much easier to pull out the variable h parameterisation. If resolution is indeed adaptive then we must re-compute the density gradients. By taking the time-derivative of the density gradient you obtain an equation similar to Equation 2.16;

$$\begin{aligned}\frac{D\rho_a}{Dt} &= \frac{D}{Dt}\sum_b m_b W_{ab}(h_a) = \sum_b m_b \left[\frac{\partial W_{ab}}{\partial r_{ab}}\frac{Dr_{ab}}{Dt} + \frac{\partial W_{ab}}{\partial h_a}\frac{Dh_a}{Dt}\right] \\ &= \sum_b m_b v_{ab} \cdot \nabla_a W_{ab}(h_a) + \frac{D\rho_a}{Dt}\frac{\partial h_a}{\partial \rho_a}\sum_b m_b \frac{\partial W_{ab}(h_a)}{\partial h_a}\end{aligned} \tag{A.1}$$

then by extracting the density derivatives you obtain an expression similar to the fixed h case (Equation 2.16)

$$\frac{D\rho_a}{Dt} = \frac{1}{\Omega_a}\sum_b m_b \vec{v}_{ab} \cdot \nabla_a W_{ab}(h_a) \tag{A.2}$$

where the correction for the spatially varying smoothing length is

$$\Omega_a = 1 - \frac{\partial h_a}{\partial \rho_a}\sum_b m_b \frac{\partial W_{ab}(h_a)}{\partial h_a}, \tag{A.3}$$

where $\partial h_a/\partial \rho_a = -h_a/3\rho_a$ in 3D. We also have the spatial derivative of the density as

$$\begin{aligned}\frac{\partial \rho_b}{\partial r_a} &= \frac{\partial}{\partial r_a}\sum_k m_k W_{bk}(h_b) = \sum_k m_k \left[\frac{\partial W_{bk}}{\partial r_{bk}}\frac{\partial r_{bk}}{\partial r_a} + \frac{\partial W_{bk}}{\partial h_b}\frac{\partial h_b}{\partial r_a}\right] \\ &= \sum_k m_k \nabla_a W_{bk}(h_b) + \frac{\partial \rho_b}{\partial r_a}\frac{\partial h_b}{\partial \rho_b}\sum_k m_k \frac{\partial W_{bk}(h_b)}{\partial h_b} \\ &= \frac{1}{\Omega_b}\sum_k m_k \nabla_a W_{bk}(h_b)\end{aligned} \tag{A.4}$$

A.2 Velocity equation

We will use instead a Lagrangian formulation of the SPH equations to get the correct formulation. Remember $L = T - V$, here $V = U$, i.e. potential energy comes from thermal energy. The EoM then comes the from principle of least action, whereby if we define $S = \int L dt$ then solving for $\delta S = \int \delta L dt = 0$ gives us the EoM (the Euler Lagrange equations)

$$L_{sph} = \sum_b m_b \left[\frac{1}{2}v_b^2 - u_a(\rho_b, s_a)\right] \tag{A.5}$$

by minimising the action we get;

$$\frac{d}{dt}\frac{\partial L}{\partial \vec{v_a}} - \frac{\partial L}{\partial \vec{r_a}} = 0. \tag{A.6}$$

The first term is then (as all terms in the summation vanish apart from the a term)

$$\frac{d}{dt}\frac{\partial L}{\partial \vec{v_a}} = m_a \frac{d\vec{v_a}}{dt} \tag{A.7}$$

and the second (assuming constant entropy);

$$\frac{\partial L}{\partial \vec{r_a}} = -\sum_b m_b \left.\frac{\partial u_b}{\partial \rho_b}\right|_s \frac{\partial \rho_b}{\partial \vec{r_a}} = -\sum_b m_b \frac{P_b}{\rho_b^2}\frac{\partial \rho_b}{\partial \vec{r_a}} \tag{A.8}$$

where we have used the first law of thermodynamics (for constant entropy $du = PdV = Pd\rho/\rho^2$). Between these two we can find a solution for the rate of change of momentum. We can insert the density spatial gradient from above to give;

$$m_a \frac{D\vec{v_a}}{Dt} = -\sum_b \sum_k m_b \frac{P_b}{\rho_b^2}\frac{1}{\Omega_b} m_k \nabla_a W_{bk}(h_b) \tag{A.9}$$

and using the identity[1] $\nabla_a W_{bk} = \nabla_b W_{kb}(\delta_{ba} - \delta_{ka})$ we can remove the k summation by

$$\begin{aligned} m_a \frac{D\vec{v_a}}{Dt} &= -\sum_b \sum_k m_b \frac{P_b}{\rho_b^2}\frac{1}{\Omega_b} m_k \nabla_b W_{kb}(h_b)(\delta_{ba} - \delta_{ka}) \\ &= -\sum_k m_a m_k \frac{P_a}{\rho_a^2}\frac{1}{\Omega_a}\nabla_a W_{ka}(h_a) + \sum_b m_b m_a \frac{P_b}{\rho_b^2}\frac{1}{\Omega_b}\nabla_b W_{ab}(h_b) \end{aligned} \tag{A.10}$$

[1] Taken form Rosswog (2009) using the identity $\partial r_{bk}/\partial r_a = \hat{e}_{bk}(\delta_{ba} - \delta_{ka})$. This also implies the identity $\nabla_a W_{ba} = \nabla_{ab} W_{ab}(\delta_{ba} - \delta_{aa}) = -\nabla_b W_{ab}$ and $\nabla_a W_{ba} = \nabla_a W_{ab}$.

If we then change the index from a sum over k to b in the left hand terms and re-arrange we obtain the momentum equation for variable smoothing lengths

$$\frac{D\vec{v}_a}{Dt} = -\sum_b m_b \left(\frac{P_a}{\Omega_a \rho_a^2} \vec{\nabla}_a W_{ab}(h_a) + \frac{P_b}{\Omega_b \rho_b^2} \vec{\nabla}_a W_{ab}(h_b) \right). \tag{A.11}$$

If the variable smoothing terms are removed then we obtain the same result as Equation 2.26, showing that the momentum equation can be derived from the Lagrangian or the Navier-Stokes equations.

A.3 Energy equation

By using the adiabatic energy equation (Equation 2.28). Gives the very simple solution for the energy equation with adaptive resolution of;

$$\frac{Du_a}{Dt} = \frac{P_a}{\rho_a^2} \frac{D\rho_a}{Dt} = \frac{P_a}{\rho_a^2} \frac{1}{\Omega_a} \sum_b m_b \vec{v}_{ab} \cdot \vec{\nabla}_a W_{ab}(h_a) \tag{A.12}$$

after some hefty re-arrangement we can obtain the split-operator form of the above. However, we do not provide this as it is not included in either of the codes used in this thesis, due to the unfortunate side effect of possible negative particle energies when using this formalism.

B

Galactic potential ancillaries

"You win again gravity!"
– Capt. Zapp Brannigan, Futurama: *Amazon Women in the Mood*, 2001

In this Appendix we outline the derivation of the forces experienced by the potential used in Pichardo et al. (2003), who, despite complexity, do not present it in their work. This potential is utilised in Chapters 3 and 4, either by direct force calculation or finite difference of the potential.

B.1 Forces due to a superposition of Schmidt spheroids with a linear internal density profile

We want the density profile inside the spheroids of $\rho = p_0 + p_1 a$ where a is the semi-major axis of the spheroid layer in question. The equations for the forces resulting from a homogeneous spheroid are in Schmidt (1956); Ollongren (1967), and the general solution for the inhomogeneous spheroid is given by,

$$F_\varpi = 4\pi e^{-3}\sqrt{1-e^2}\varpi \int_0^\gamma \rho \sin^2\beta d\beta \tag{B.1}$$

and

$$F_z = 4\pi e^{-3}\sqrt{1-e^2} z \int_0^\gamma \rho \tan^2\beta d\beta \tag{B.2}$$

where γ is the limiting size of the spheroid, where $a = a_0$ and a_0 is the maximum spheroid semi-major axis. These terms are related by,

$$\sin\beta = e_0, \text{ inside} \tag{B.3}$$

and

$$\varpi^2 \sin^2\beta + z^2 \tan^2\beta = a_0^2 e_0^2, \text{ outside.} \tag{B.4}$$

An in-plane solution to B.1 and B.2 can be easily found by setting $z = 0$ in B.4, substituting in ρ and solving the integral. but we want the general off-plane solution, so our density is given by,

$$\rho = p_0 + \frac{p_1}{e_0}\sqrt{\varpi^2 \sin^2\beta + z^2 \tan^2\beta}. \tag{B.5}$$

Our different density profile to that of Schmidt (1956) means we must solve for F_ϖ and F_z ourselves. This gives two rather nasty integrals to solve,

$$F_\varpi = 4\pi e^{-3}\sqrt{1-e^2}\varpi \int_0^\gamma \left[p_0 + \frac{p_1}{e_0}\sqrt{\varpi^2 \sin^2\beta + z^2 \tan^2\beta}\right] \sin^2\beta d\beta \tag{B.6}$$

and

$$F_z = 4\pi e^{-3}\sqrt{1-e^2} z \int_0^\gamma \left[p_0 + \frac{p_1}{e_0}\sqrt{\varpi^2 \sin^2\beta + z^2 \tan^2\beta}\right] \tan^2\beta d\beta. \tag{B.7}$$

The p_0 terms are simple enough using standard integral solutions;

$$\int \sin^2 x\, dx = \frac{1}{2}(x - \sin x \cos x) \tag{B.8}$$

and

$$\int \tan^2 x\, dx = \tan x - x. \tag{B.9}$$

This leaves us with

$$I_\varpi = \int_0^\gamma \sin^2\beta \sqrt{\varpi^2 \sin^2\beta + z^2 \tan^2\beta} d\beta \tag{B.10}$$

and

$$I_z = \int_0^\gamma \tan^2\beta \sqrt{\varpi^2 \sin^2\beta + z^2 \tan^2\beta} d\beta \tag{B.11}$$

left to solve. Beginning with the first integral, remove a tan from the square-root.

$$I_\varpi = \int_0^\gamma \sin^2\beta \frac{\sin\beta}{\cos\beta}\sqrt{\varpi^2 \cos^2\beta + z^2} d\beta = \tag{B.12}$$

Now substitute $u = \varpi^2 \cos^2\beta$ and using,

$$\frac{du}{d\beta} = -2\varpi^2 \sin\beta\cos\beta = -2u\frac{\sin\beta}{\cos\beta} \tag{B.13}$$

so that we can substitute $d\beta \sin\beta/\cos\beta = -du/(2u)$ into the integral, along with $\sin^2\beta = 1 - \cos^2\beta = 1 - u/\varpi^2$ to give,

$$I_\varpi = -\frac{1}{2}\int_{\beta=0}^{\beta=\gamma}\left(\frac{1}{u} - \frac{1}{\varpi^2}\right)\sqrt{u + z^2} du \tag{B.14}$$

The rest was computed with the help of MATLAB using the substitutions of in $v = \sqrt{1/u - 1/\varpi^2}$, $s = v - z$ and $p = v + z$ for separate parts of the integral. The solution is given as,

$$I_\varpi = \frac{1}{3\varpi^2}\left(u+z^2\right)^{3/2} - \sqrt{u+z^2} + \frac{z}{2}\ln\left(\frac{\sqrt{u+z^2}+z}{\sqrt{u+z^2}-z}\right)\Bigg|_{\beta=0}^{\beta=\gamma} \tag{B.15}$$

$$= \frac{1}{3\varpi^2}\left(\varpi^2\cos^2\beta+z^2\right)^{3/2} - \sqrt{\varpi^2\cos^2\beta+z^2} + \frac{z}{2}\ln\left(\frac{\sqrt{\varpi^2\cos^2\beta+z^2}+z}{\sqrt{\varpi^2\cos^2\beta+z^2}-z}\right)\Bigg|_{\beta=0}^{\beta=\gamma}. \tag{B.16}$$

Then simply evaluating at the limits gives,

$$\begin{aligned} I_\varpi =& \left[\frac{1}{3\varpi^2}\left(\varpi^2\cos^2\gamma+z^2\right)^{3/2} - \sqrt{\varpi^2\cos^2\gamma+z^2} + \frac{z}{2}\ln\left(\frac{\sqrt{\varpi^2\cos^2\gamma+z^2}+z}{\sqrt{\varpi^2\cos^2\gamma+z^2}-z}\right)\right] \\ &- \left[\frac{1}{3\varpi^2}\left(\varpi^2+z^2\right)^{3/2} - \sqrt{\varpi^2+z^2} + \frac{z}{2}\ln\left(\frac{\sqrt{\varpi^2+z^2}+z}{\sqrt{\varpi^2+z^2}-z}\right)\right] \end{aligned} \tag{B.17}$$

so

$$\begin{aligned} I_\varpi =& \frac{1}{3\varpi^2}\left[\left(\varpi^2\cos^2\gamma+z^2\right)^{3/2} - \left(\varpi^2+z^2\right)^{3/2}\right] + \sqrt{\varpi^2+z^2} - \sqrt{\varpi^2\cos^2\gamma+z^2} \\ &+ \frac{z}{2}\ln\left[\frac{\left(\sqrt{\varpi^2\cos^2\gamma+z^2}+z\right)\left(\sqrt{\varpi^2+z^2}-z\right)}{\left(\sqrt{\varpi^2\cos^2\gamma+z^2}-z\right)\left(\sqrt{\varpi^2+z^2}+z\right)}\right]. \end{aligned} \tag{B.18}$$

We can now evaluate the radial force as,

$$F_\varpi = 4\pi e_0^{-3}\sqrt{1-e^2}\varpi\left\{\frac{p_0}{2}\left(\gamma - \sin\gamma\cos\gamma\right) + \frac{p_1}{e_0}I_\varpi\right\} \tag{B.19}$$

Then we must return to our second integral, B.11. Using the same substitution for u;

$$I_z = -\frac{1}{2}\int_0^\gamma \frac{\tan\beta}{u}\sqrt{u+z^2}d\beta = -\frac{1}{2}\int_0^\gamma\left(\frac{\varpi^2}{u^2} - \frac{1}{u}\right)\sqrt{u+z^2}du \tag{B.20}$$

Using MATLAB again, we obtain,

$$I_z = \left(1+\frac{\varpi^2}{2u}\right)\sqrt{u+z^2} + \frac{1}{4z}\left(\varpi^2-2z^2\right)\ln\left(\frac{\sqrt{u+z^2}+z}{\sqrt{u+z^2}-z}\right)\Bigg|_{\beta=0}^{\beta=\gamma}, \tag{B.21}$$

$$= \left(1+\frac{1}{2\cos^2\beta}\right)\sqrt{\varpi^2\cos^2\beta+z^2} + \frac{1}{4z}\left(\varpi^2-2z^2\right)\ln\left(\frac{\sqrt{\varpi^2\cos^2\beta+z^2}+z}{\sqrt{\varpi^2\cos^2\beta+z^2}-z}\right)\Bigg|_{\beta=0}^{\beta=\gamma}. \tag{B.22}$$

Evaluating the integral limits gives,

$$\begin{aligned} I_z =& \left[\left(1+\frac{1}{2\cos^2\gamma}\right)\sqrt{\varpi^2\cos^2\gamma+z^2} + \frac{1}{4z}\left(\varpi^2-2z^2\right)\ln\left(\frac{\sqrt{\varpi^2\cos^2\gamma+z^2}+z}{\sqrt{\varpi^2\cos^2\gamma+z^2}-z}\right)\right] \\ &- \left[\frac{3}{2}\sqrt{\varpi^2+z^2} + \frac{1}{4z}\left(\varpi^2-2z^2\right)\ln\left(\frac{\sqrt{\varpi^2+z^2}+z}{\sqrt{\varpi^2+z^2}-z}\right)\right] \end{aligned} \tag{B.23}$$

so

$$I_z = \left(1 + \frac{1}{2\cos^2\gamma}\right)\sqrt{\varpi^2\cos^2\gamma + z^2} - \frac{3}{2}\sqrt{\varpi^2 + z^2} + \frac{1}{4z}\left(\varpi^2 - 2z^2\right)\ln\left[\frac{\left(\sqrt{\varpi^2\cos^2\gamma + z^2} + z\right)\left(\sqrt{\varpi^2 + z^2} - z\right)}{\left(\sqrt{\varpi^2\cos^2\gamma + z^2} - z\right)\left(\sqrt{\varpi^2 + z^2} + z\right)}\right] \tag{B.24}$$

giving the force in the z-direction as,

$$F_z = 4\pi e_0^{-3}\sqrt{1 - e^2}z\left\{p_0\left(\tan\gamma - \gamma\right) + \frac{p_1}{e_0}I_z\right\}. \tag{B.25}$$

The potential itself is given in the general form of $\rho = q/a + p_0 + p_1 a$ in Ollongren (1967), and by simply discarding the q terms.

B.2 Rotating potentials and changing co-ordinate systems

The potentials utilised vary between being specified in Cartesian and cylindrical co-ordinate systems. The transformation matrix relating the two co-ordinate systems is defined as;

$$\begin{pmatrix}\hat{e}_x\\ \hat{e}_y\\ \hat{e}_z\end{pmatrix} = \begin{pmatrix}\cos\theta & -\sin\theta & 0\\ \sin\theta & \cos\theta & 0\\ 0 & 0 & 1\end{pmatrix}\begin{pmatrix}\hat{e}_r\\ \hat{e}_\theta\\ \hat{e}_z\end{pmatrix}. \tag{B.26}$$

The grad operator also takes a different form in cylindrical polars,

$$\vec{\nabla} = \left[\frac{\partial}{\partial x}, \frac{\partial}{\partial y}, \frac{\partial}{\partial z}\right] = \left[\frac{\partial}{\partial r}, \frac{1}{r}\frac{\partial}{\partial\theta}, \frac{\partial}{\partial z}\right]. \tag{B.27}$$

These equations easily enables us to switch between co-ordinate systems. So if our potential is in polars we can easily evaluate a force in Cartesian co-ordinates by applying the matrix above to the grad operator, giving us the following transformations:

$$\frac{\partial}{\partial x} = \cos\theta\frac{\partial}{\partial r} - \frac{\sin\theta}{r}\frac{\partial}{\partial\theta} \tag{B.28}$$

$$\frac{\partial}{\partial y} = \sin\theta\frac{\partial}{\partial r} + \frac{\cos\theta}{r}\frac{\partial}{\partial\theta} \tag{B.29}$$

$$\frac{\partial}{\partial z} = \frac{\partial}{\partial z}. \tag{B.30}$$

Some of the potentials we utilise are in cylindrical co-ordinates, but must be rotated to allow for the simulation of a non zero pattern speed. To do so we first rotate the particular SPH particle to the reference frame of the rotating potential, using the rotation matrix above (z_i is unchanged),

$$x_i' = x_i\cos\left(t_i\Omega_p\right) - y_i\sin\left(t_i\Omega_p\right), \tag{B.31}$$

$$y_i' = x_i\sin\left(t_i\Omega_p\right) + y_i\cos\left(t_i\Omega_p\right). \tag{B.32}$$

At this position the forces are calculated in the reference frame of the potential (f'_x and f'_y) and then the force vector is rotated back to the reference frame of the particle and the forces are applied,

$$f_{x,i} = f'_{x,i} \cos\left(-t_i \Omega_p\right) - f'_{y,i} \sin\left(-t_i \Omega_p\right) \tag{B.33}$$

$$f_{yi} = f'_{x,i} \sin\left(-t_i \Omega_p\right) + f'_{y,i} \cos\left(-t_i \Omega_p\right). \tag{B.34}$$